Photometric techniques for Exoplanet detection: The construction and deployment of the KELT-South telescope

Rudolf Bruwer Kuhn

October 2014

A project submitted in partial fulfilment of the requirements for the degree PhD.
in the Department of Astronomy
UNIVERSITY OF CAPE TOWN

Supervisors: Prof. P. A. Whitelock and Dr. J. W. Menzies
In Collaboration with Dr. J. A. Pepper at Lehigh University
and Prof. K. G. Stassun at Vanderbilt University

Abstract

In this thesis I present the work I performed during the initial construction and deployment of the second telescope in the KELT project and I report the results of the search for transiting exoplanets and variable stars using one of the first commissioning datasets obtained with the telescope. The KELT-South telescope is located in Sutherland, South Africa and construction started in 2008. The telescope has been operating at full capacity since 2010, after two commissioning seasons from late 2008 to early 2010. I developed all the code that allows it to be fully automatic and robotic and over the last 5 years I have been responsible for the observing operations and general maintenance of the telescope. I also developed many other software tools that help with the identification of the exoplanet candidates.

The **K**ilodegree **E**xtremely **L**ittle **T**elescope (KELT) project at present consists of two robotic, wide field, small aperture telescopes that are designed primarily to find transiting exoplanets around bright stars in the magnitude range $8 < V < 11$. Transiting planets orbiting bright stars can be studied with intense follow-up programs with relative ease on larger telescopes, making them favourable targets to determine the atmospheric composition of the planet as well as a host of other properties that cannot be obtained from planets orbiting fainter stars. Of the known 1811 (August 2014) exoplanets only 60 are transiting stars with $V < 11$ and only 16 of those have been found from the southern hemisphere. The discovery of more of these exoplanets will help constrain the theories of formation and evolution of short period, gas giant exoplanets.

Data reduction on one of the commissioning datasets was completed in 2012. The dataset spans 46 days and lightcurves for 78297 objects were obtained. I performed a search for periodicities in the lightcurves and found that 1411 stars showed clear signs of variability and these objects were compiled into a catalogue of possible variable stars. 1018 of the catalogue members were not previously known to be variable. I searched for planetary transits and eight possible exoplanet candidates were identified. Photometric follow-up observations of two targets eliminated them as exoplanet candidates, each being a blended eclipsing binary system. The remaining six candidates are awaiting follow-up observations at present. Although the commissioning dataset served primarily to refine the data reduction pipeline and the procedures I used to find variable stars, I have demonstrated that the KELT-South telescope is capable of detecting the kinds of signals required for exoplanet discovery.

Acknowledgements

I would like to thank the many individuals who assisted me in all aspects of this thesis and those that helped me through the rough times without being directly involved with the work.

Firstly, and most importantly, I would like to thank my parents for the love and support throughout my entire life. A special thanks to my Dad who taught me the names of the planets in our Solar System before I could read, which is probably the initial seed that sparked my lifelong fascination with astronomy. To my Mom, thanks for listening to my endless questions, always trying to understand what I was struggling with and encouraging me to find the answers myself when no one else was able to provide them. This thesis is dedicated to both of you.

I would like to express my appreciation for all the love and support I received from Stephanie, my soon to be wife. You might not have been part of this thesis from the start, but you were instrumental in its completion. Your words and deeds of encouragement made the last few months much easier and I cannot imagine how I would have been able to finish this task without you. I am truly blessed to have someone as “ama–zing” as you in my life.

I was fortunate to have supervisors that allowed me the freedom to explore my own interests and offered support and guidance whenever I needed it. Patricia and John, you have made the last couple of years much easier by letting me do my own thing, but getting me back on the right path when I strayed too far.

A huge thank you has to go to my unofficial supervisor on this project, Josh. Without you the KELT-South project would never have happened and I would never have had the opportunity to work on an amazing project like this. I appreciate all the time and guidance you provided even though I wasn’t officially your student to mentor. I would really like to thank Keivan for giving me the opportunity to visit the USA on three occasions and providing all the financial support that enabled those trips. I learned so much about being the best possible scientist from all the people at Vanderbilt and I thank you for all the insightful discussions.

To my sister (and your four amazing kids) I would like to extend a special thank you. You’ve been there from the start and you always believed in your “big brother”, you’ve been a true inspiration to me over these last few years. To all my school friends, although we’ve not had much time to chat in the last few years, you’ve been supportive every time we did have a change to meet and I really appreciate the encouragement.

A very special mention to all my office mates at SAAO over the last couple of years, thanks for all the encouragement, guidance, sharing of ideas and many unforgettable trips to Sutherland. Cold nights fixing telescopes were much easier knowing that a nice hot coffee (and a laugh) was always available when I needed it. I would never have made it through to the end without you. Thanks to my colleagues (that became life long friends) Marissa, Enrico and Paul, you have been vital in the completion of this thesis and I cannot thank you enough for all the support.

To all my friends and colleagues at Vanderbilt University, thanks for making me feel at home the minute I arrived in Nashville for the very first time. Y'all made the second and third trips so much easier knowing that I had friends I could call on. To Joey, thanks for taking over the telescope operations and maintenance duties over the last few months while I concentrated all efforts on typing up this thesis. KELT-South is in good hands and I look forward to working with you in future on all aspects related to KELT-South.

Everybody at SAAO should also get a mention, especially Piet, Willie, Gareth, Simon, Nimrod, Chantal, Hamish and Amanda. All of you were willing to help in all aspects of the KELT-South project and provided enormous amounts of advice on telescope hardware, electrical systems, computers, code and so much more. I would also like to thank the amazing ladies at the Sutherland observing hostel that provided awesome meals three times a day (and sometimes so extras) during my eight month stay in Sutherland during the construction of KELT-South. Thanks to John, Jaci, Hennie, Michael, and all other members of the support staff in Sutherland that were always available with extra hands when one pair just wasn't enough to get things done.

With a project such as KELT-South, there are far more people that I need to thank than there is space in this thesis*. I appreciate all the help I received and will never forget your contributions that allowed KELT-South to evolve from a pile of bricks to a fully automated machine capable of finding other worlds.

---

*This research made use of data products from:

- The Two Micron All Sky Survey, which is a joint project of the University of Massachusetts and the Infrared Processing and Analysis Centre/California Institute of Technology, funded by the National Aeronautics and Space Administration and the National Science Foundation.
- The VizieR catalogue access tool and the SIMBAD database, operated at CDS, Strasbourg, France.
- The International Variable Star Index (VSX) database, operated at AAVSO, Cambridge, Massachusetts, USA.
- The NASA Exoplanet Archive, which is operated by the California Institute of Technology, under contract with the National Aeronautics and Space Administration under the Exoplanet Exploration Program.
- The Exoplanet Orbit Database and the Exoplanet Data Explorer at http://www.exoplanets.org.
- The Exoplanet Encyclopaedia at http://www.exoplanets.eu.
- The Transiting Exoplanet Catalogue at http://www.astro.keele.ac.uk/jkt/tepcat/tepcat.html.

Plagiarism Declaration

I, Rudolf B. Kuhn, know that plagiarism is wrong. Plagiarism is the use of another person's ideas or published work and to pretend that it is one's own. This therefore amounts to theft. Each significant contribution to, and quotation in this work that I have obtained from other people's published works or unpublished sources has been attributed, and has been cited and fully referenced. This research report is my own original work and I expect reviewers to regard it as such and that I alone am responsible for any incomplete references that may remain in my work.

Contents

List of Figures

List of Tables

Chapter 1

Introduction

"Scientists have calculated that the chance of anything so patently absurd actually existing are millions to one. But magicians have calculated that million-to-one chances crop up nine times out of ten." - Mort by Terry Pratchett

The search for planets outside our solar system, called extrasolar planets (exoplanets), has seen a very large number of unbelievable worlds discovered in the last 20 years. The first announcement of a confirmed exoplanet discovery in 1992, from the studies of the changes in the millisecond pulse arrival times from the pulsar PSR 1257+12 (Wolszczan & Frail 1992), forced the scientific community to think differently about the formation and types of planetary systems that might exist. The planets orbiting the pulsar were calculated to be 2.8 and 3.4 times the mass of the Earth ($M_\oplus$) with orbital periods of 98.2 and 66.6 days respectively. Although the planets in this system were very different to the planets in our solar system, it provided the first conclusive proof of planets orbiting other stars.

Earlier radial velocity (RV) work by Campbell and Walker done in the 1980's hinted at a possible exoplanet with a mass of $\sim$1.7 times that of Jupiter (M_{J}) orbiting the star γ Cep A, with a 25 m s^{-1} amplitude and a period of 2.7 years (Campbell et al. 1988). For many years the true nature of the signal was debated with the discovery of a 2.5 year activity period of the star casting doubt on the 2.7 year signal detected earlier (Walker et al. 1992). Only in 2003 was the original discovery verified to be of planetary in origin (Hatzes et al. 2003). In 1989 a team lead by Latham announced a possible 11 M_{J} substellar companion orbiting the star HD 114762 in a 84 day orbit and they referred to the object as "a brown dwarf" or "a possible giant planet" and is now considered the first true exoplanet ever discovered (Latham et al. 1989). For many years after the initial announcement, the astronomical community still debated the true nature of the object. It was not until 1995 when similar objects were being discovered around other stars that the companion to HD 114762 was considered to be a real planet, although doubt still remained due to the large mass of the object. It was not until the early 2000's when the mass distribution of exoplanets became apparent that HD 114762b was considered a true exoplanet (Latham 2012).

The search for planets around Sun-like stars, using the RV method, revealed that the star 51 Pegasi had a planet of about 1 $M_{\rm J}$ orbiting it at a distance of 0.052 Astronomical Units (AU), resulting in an orbital period of only 4.2 days (Mayor & Queloz 1995). This placed the large planet closer to its parent star than Mercury is to our own Sun. Similar to the discovery of HD 114762b by Latham in 1989, the companion of 51 Pegasi was doubted as a planet. This time the doubt arose due to the short orbital period. Theories of planetary formation at the time could not explain how a system like this had formed. The theories needed serious revision and have continually evolved along with the discovery of more and more exoplanets. It was soon realised that some planetary systems found using the RV technique might have the system in the right configuration for the planet to pass between us and the parent star. The first planet observed to pass in front of its parent star, a transiting exoplanet, was discovered in 1999 around the star HD209458 (Henry et al. 2000, Charbonneau et al. 2000). The first exoplanet discovered by the transit method first and then confirmed by RV was OGLE-TR-56b (Konacki et al. 2003). The first few transiting planets to be discovered were all classified as “Hot-Jupiters”, planets with masses similar to Jupiter and orbital radii less than 0.1 AU resulting in orbital periods between 3 and 20 days. As more and more transiting exoplanets have been discovered the classification now includes objects called “Very-Hot-Jupiters” (Beatty & Gaudi 2008), planets with orbital periods less than 3 days and orbital radii less than 0.025 AU (Ragozzine & Wolf 2009), “Hot-Neptunes”, planets with similar masses to Neptune (17 $M_{\oplus}$) and short orbital periods, “Super-Earths”, planets with masses slightly larger than the Earth mostly composed of rocky elements, and “Earth-like”, planets that have masses comparable to Earth and are found in orbits that make the possibility of liquid water on their surfaces very likely.

At present the number of known exoplanets is well over 1800[*] with masses ranging from 7×10^{-5} to 47 $M_{\rm J}$ (planets with masses larger than 13 $M_{\rm J}$ are now considered not to be planets, see Section 1.1 below) and orbital periods as short as 0.09 days and as long as 730000 days. Along with the extreme diversity of exoplanets have come the many methods of finding these exotic worlds. There are a large number of exoplanet search programmes at present with many more planned for the near future, which include specialised space-based observatories dedicated to the discovery of Earth-like planets in Earth-like orbits. The KELT project is a ground based survey that searches for the brightest transiting exoplanets with two dedicated small aperture wide field telescopes, one in the northern hemisphere and one in the southern hemisphere.

1.1 Definition of a Planet

The current definition, established in 2006, for a planet according to the International Astronomical Union’s (IAU) is:

1. A planet is a celestial body that (a) is in orbit around the Sun, (b) has sufficient mass for its self-gravity to overcome rigid body forces so that it assumes a hydrostatic

---

[*] Data obtained from http://www.exoplanet.eu on 2014 August 1

equilibrium (nearly round) shape, and (c) has cleared the neighbourhood around its orbit.

2. A “dwarf planet” is a celestial body that (a) is in orbit around the Sun, (b) has sufficient mass for its self-gravity to overcome rigid body forces so that it assumes a hydrostatic equilibrium (nearly round) shape, (c) has not cleared the neighbourhood around its orbit, and (d) is not a satellite.

3. All other objects, except satellites, orbiting the Sun shall be referred to collectively as “Small Solar System Bodies”.

However, the current IAU definition for planet only accounts for our own solar system and all exoplanets were excluded from this definition for now. The “working” definition for exoplanets was established in 2001 (and last modified in 2003) by the Working Group on Extra Solar Planets[*] (WGESP) with the following criteria:

1. Objects with true masses below the limiting mass for thermonuclear fusion of deuterium (currently calculated to be 13 M_J for objects of solar metallicity) that orbit stars or stellar remnants are “planets” (no matter how they formed). The minimum mass/size required for an extrasolar object to be considered a planet should be the same as that used in our solar system.

2. Substellar objects with true masses above the limiting mass for thermonuclear fusion of deuterium are “brown dwarfs”, no matter how they formed nor where they are located.

3. Free-floating objects in young star clusters with masses below the limiting mass for thermonuclear fusion of deuterium are not “planets”, but are “sub-brown dwarfs” (or whatever name is most appropriate).

The above statements are not purely based on deuterium-burning mass or on the formation process of the planet and as such are not universally accepted. The Extrasolar Planets Encyclopaedia[†] includes objects up to 20 M_J and larger with the statement “*The basic criterion is, in principle, the mass limit: 13* M_J*. This criterion (based on absence of a thermonuclear source of energy) is somewhat arbitrary since a companion could start its formation by dust accretion in a disk and end up with a mass* $> 13\ M_J$*. But, due to the lack of precision in the definition of a planet, this criterion has to be made more flexible. For instance, if the star has a planetary companion, other companions with masses less than 20 Jupiter masses are included. An additional difficulty comes from the uncertainty in the mass value (for instance an object with a mass* $19 \pm 3\ M_J$ *could have a true mass value* $< 13\ M_J$ *with a* 2σ *statistical deviation (= 12% probability). We thus finally include planets with masses* $< 20\ M_J$ *up to* 2σ”. The Exoplanet Data Explorer[‡] includes objects up to 24 M_J

---

[*] http://www.dtm.ciw.edu/users/boss/iauindex.html

[†] http://exoplanet.eu/

[‡] http://exoplanets.org/

with the advisory "*We have retained the generous upper mass limit of 24 Jupiter masses in our definition of a planet, for the same reasons as in the catalogue: at the moment, any mass limit is arbitrary and will serve little practical function, both because of the sin i ambiguity in RV masses and because of the lack of physical motivation.*". The NASA Exoplanet Archive* follows a similar reasoning and adopted a policy of including all objects as planetary where: "*(a) the mass (or minimum mass) is equal to or less than 30 Jupiter masses, (b) sufficient follow-up observations and validation have been undertaken to deem the possibility of the object being a false positive unlikely and (c) further orbital and/or physical properties are available in peer-reviewed publications.*".

The exact criterion for distinguishing between planets and brown dwarfs is not clear. Studies by Spiegel et al. (2011) suggest that the exact point at which deuterium fusion occurs depends on a number of factors including the helium abundance, the initial deuterium abundance, and the metallicity of the object in question. They conclude that although 13 $M_{\rm J}$ is a reasonable estimate of the mass at which deuterium burning begins, it can range from $\sim$11 $M_{\rm J}$ (for objects with three times solar metallicity) to $\sim$16 $M_{\rm J}$ (for objects with zero-metallicity).

The WGESP does agree that these statements are adequate for a reasonable working definition of an exoplanet at this time. The definition is likely to change as the knowledge of exoplanets improves. It should be noted that the WGESP ended its existence in August 2006, with the decision of the IAU to create a commission dedicated to exoplanets as part of Division III† of the IAU. The new commission is Commission 53 on Extrasolar Planets and the founding president is Michel Mayor.

1.2 Exoplanet Nomenclature

The IAU adopted the naming convention for exoplanets as an extension to the naming convention used by the Washington Multiplicity Catalogue for multiple-star systems, whereby the brightest member of the star system receives the letter "A" and other stars in the system that are distinct from A are labelled "B","C", etc. In the case of exoplanets, the name is formed by taking the name of its parent star and adding a lower case letter. The first planet discovered in a system is given the designation "b" and later planets are given subsequent letters. If several planets in the same system are discovered at the same time, the closest one to the star receives the next letter, followed by the other planets in order of orbital size. Since most planets are found in single star systems the "A" was simply omitted, leaving the exoplanet name with the lower case letter only (as in HD209458b). The name of the parent star can follow many different systems, with most exoplanet search projects naming the host star in order of their chronological exoplanet discovery rather than by catalogue names (as in the case of WASP-1b, where the host star is catalogued as TYC 2265-107-1). If a planet orbits one member of a binary star system, then an upper case letter for the star

---

[*] http://exoplanetarchive.ipac.caltech.edu/

[†] http://www.iau.org/science/scientific_bodies/commissions/53/

will be followed by a lower case letter for the planet (as in KELT-2Ab).

This convention works for almost all exoplanets discovered to date, but fails when applied to exoplanets in circumbinary star systems. The two exoplanets discovered orbiting the close compact binary system NN Ser (Beuermann et al. 2010) were initially called NN Ser (ab)c and NN Ser (ab)d, but this placed the planets and stars on the same hierarchical level and contradicted the convention of naming the first planet to be discovered in the system with a lower case b. The exoplanets found orbiting the compact binary system HW Vir (Lee et al. 2009, Beuermann et al. 2012) were initially named HW Vir 3 and HW Vir 4, contradicting the system used to name the planets in pulsar systems whereby the first planet in the pulsar system is given the #1 designation, e.g. PSR 1257+12#1 (although recent studies by Horner et al. (2012) suggest that the planets present in the HW Vir system are dynamically unstable, the issue of naming the possible planets is still relevant to this discussion). For this purpose Hessman et al. (2010) proposed a new naming convention for exoplanets that preserved as many of the names as possible at the time while introducing a physically informative description into the name of the exoplanet. The following rules were proposed:

1. The formal name of an exoplanet is obtained by appending the appropriate suffixes to the formal name of the host star or stellar system. The upper hierarchy is defined by upper-case letters, followed by lower-case letters, followed by numbers, etc. The naming order within a hierarchical level is for the order of discovery only.

2. Whenever the leading capital letter designation is missing, this is interpreted as being an informal form with an implicit "A" unless otherwise explicitly stated.

3. As an alternative to the nomenclature standard in rule#1, a hierarchical relationship can be expressed by concatenating the names of the higher order system and placing them in parentheses, after which the suffix for a lower order system is added.

4. When in doubt (i.e. if a different name has not been clearly set in the literature), the hierarchy expressed by the nomenclature should correspond to dynamically distinct (sub-)systems in order of their dynamical relevance. The choice of hierarchical levels should be made to emphasize dynamical relationships, if known.

Using the new proposed rules would require the renaming of planets in only four systems, HW Vir and NN Ser. HW Vir 3 would become HW Vir (AB)b, HW Vir 4 would be renamed to HW Vir (AB)c, NN Ser c would be renamed to NN Ser (AB)b, NN Ser d would be renamed to NN Ser (AB)c, PSR B1620-26 b (Thorsett et al. 1993) would become PSR B1620-26 (AB)b and DP Leo b (Beuermann et al. 2011, Qian et al. 2010) would be renamed to DP Leo (AB)b.

With the new convention it is possible to distinguish clearly between the dynamical status of planets around single stars, stars in multiple systems, and circumbinary (or higher order) planets.

1.3 Methods of Finding Exoplanets

Although there are a number of methods for discovering exoplanets, some techniques are, given the current technological standard, easier to implement than others and have thus been responsible for the vast majority of exoplanet discoveries. The different techniques also yield different amounts of information from the planetary systems discovered. The RV technique for instance is very good at finding massive exoplanets, but in most cases will only yield the minimum mass of a planet and the orbital period. The transit method on the other hand will be able to determine the size of the planet and along with the information from the RV method will be able to determine the density of the planet. Transiting exoplanets also present the opportunity to study the atmosphere of the planet as it passes in front of the parent star by using spectroscopy. The different methods for exoplanet detection that have successfully detected exoplanets include:

- Direct Imaging
- Astrometry
- Pulsar Timing
- Gravitational Microlensing
- Radial Velocity
- Eclipse Timing Variations
- Transit Method
- Relativistic Beaming

The above methods can be divided into two broad categories; direct and indirect. The direct method relies on the premise that one can actually take an image of the planet directly. This technique is extremely difficult because the planet is of order 10^{10} times fainter than the star it orbits. Planets are also so close to their parent stars that separating planet and star when taking an image is extremely difficult. Despite these difficulties, 49 objects with masses ranging between 3 M_J (Kalas et al. 2008) and 47 M_J (Aller et al. 2013) have been discovered using this technique. Some of these objects are separated from their parent stars by only 2.6 AU (Liu et al. 2011), while others have much larger separation distance of 3200 AU (Aller et al. 2013). There are even some multiple object systems that have been imaged directly (Marois et al. 2008). Whether these objects should be considered true exoplanets is still a matter of debate, even though many are below the traditional ∼13 M_J deuterium burning limit boundary used to distinguish between planets and brown dwarfs (Spiegel et al. 2011). The disadvantage of discovering objects using this technique is that very little information about the object can be determined. With orbital periods as long as thousands of days, observations need to be taken many years apart to ensure that the initial detections were real and not an artefact of the data reduction procedure. It should also be noted that this technique is biased toward finding young (< 0.2 Gyr), self-luminous objects that emit radiation at infrared wavelengths.

The indirect method relies on gathering data from the parent star itself and by making precise observations one is able to deduce the presence of a planet in orbit around the star. The planet will exert a gravitational pull on the star, which can be measured by astrometry or spectroscopy, and the planet may pass in front of it causing the amount of light from the star to decrease by a small amount. In the case of microlensing, a foreground star acts as a lens and amplifies the light from a background star. This increase in brightness can be predicted very accurately and by observing an "extra" unforeseen increase in brightness, the presence of a planet orbiting the lensing star can be inferred.

Discussed below are the methods that are relevant to the KELT-South project only, namely the RV and transit methods. The reason for this is that although the methods listed above have all been successful in discovering exoplanets, the transit methods is the main focus of the KELT-South project and the RV method is used to confirm the discovery. Of particular interest to the KELT-South project is the possibility of using the Southern African Large Telescope (SALT) to do the RV confirmation or using the new High Resolution Spectrograph (commissioned in early 2014) to study the atmospheric composition of the transiting exoplanet similar to studies by Redfield et al. (2008).

1.3.1 Radial Velocity

The RV technique has been the most efficient at finding exoplanets. Of the more than 900 confirmed exoplanets (excluding the recent bulk announcement by the Kepler group of ∼850 new "validated" exoplanets) 538 have been discovered by this method. The first unambiguous discovery of a planet using the RV technique was announced in 1995 October and published in Nature (Mayor & Queloz 1995) in the same year. The planet was found to have a minimum mass of 0.47 $M_{\rm J}$ and a period of 4.23 days. The discovery was confirmed shortly after and the mass and period were improved to 0.41 $M_{\rm J}$ and 4.21 days respectively (Marcy & Butler 1995).

The RV method relies on the very small Doppler shift in the spectrum of a star caused by the gravitational pull of the planet orbiting it. The two objects orbit around the barycentre of the system and the periodic Doppler shift can be monitored closely from earth. The amount of shift in the spectrum is directly proportional to the mass of the planet and inversely proportional to the square of the distance between the star and the planet. The more massive the planet and the closer it is to the parent star the easier it will be to detect. This selection effect is unavoidable. It also means that systems that have inclination angles close to 90°, edge-on, will show the largest effect and the planets that have very low inclinations, face-on, will show no effect. The RV of the star can be measured from the wavelength shift using:

$$\frac{v_r}{c} = \frac{\delta\lambda}{\lambda_0} = \frac{(\lambda - \lambda_0)}{\lambda_0} \tag{1.1}$$

where λ_0 is the rest wavelength, λ is the measured wavelength and c is the speed of light.

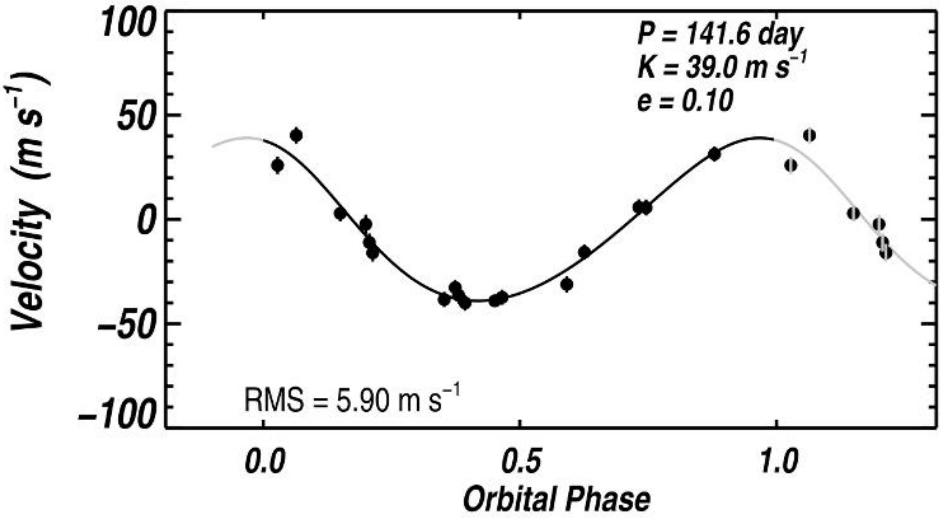

Figure 1.1: The radial velocity curve of the exoplanet HD231701b showing almost perfect sinusoidal behaviour. This indicates that the exoplanet has an almost perfectly circular orbit. Image taken from Fischer et al. (2007).

Current technology allows the detection of RV shifts of ~1 m s^{-1} from ground based telescopes with instruments like HARPS (**H**igh-**A**ccuracy **R**adial velocity **P**lanetary **S**earcher) (Mayor et al. 2003). A RV curve can be obtained by taking a spectrum of the star throughout an entire orbit of the planet (see Figure 1.1). One thing that can be determined by studying the RV curve is the eccentricity of the orbit. Fully circular orbits will produce RV curves that have perfect sinusoidal shapes. Highly eccentric orbits will produce RV curves with distinct shapes (see Figure 1.2) To determine the separation between the planet and the star, Kepler's third law of planetary motion can be used. By measuring the period P from the RV curve, the semi-major axis a can be determined:

$$a = \sqrt[3]{\frac{P^2 G(M_* + M_p)}{4\pi^2}} \tag{1.2}$$

where M_* is the mass of the star, M_p is the mass of the planet and G is the gravitational constant.

When calculating the mass of the planet, only the mass function $f(M_*, M_p)$ of the system can be found:

$$f(M_*, M_p) = \frac{M_p^3 \sin^3 i}{(M_* + M_p)^2} = \frac{K^3 P (1 - e^2)^{\frac{3}{2}}}{2\pi G} \tag{1.3}$$

where K is the semi-amplitude of the RV shift determined from the RV curve and e is the eccentricity of the orbit. By estimating the mass of the star using its spectral type the minimum mass of the planet, M_p sin i, can be calculated.

As stated previously, the problem with the RV technique is that it only provides limited

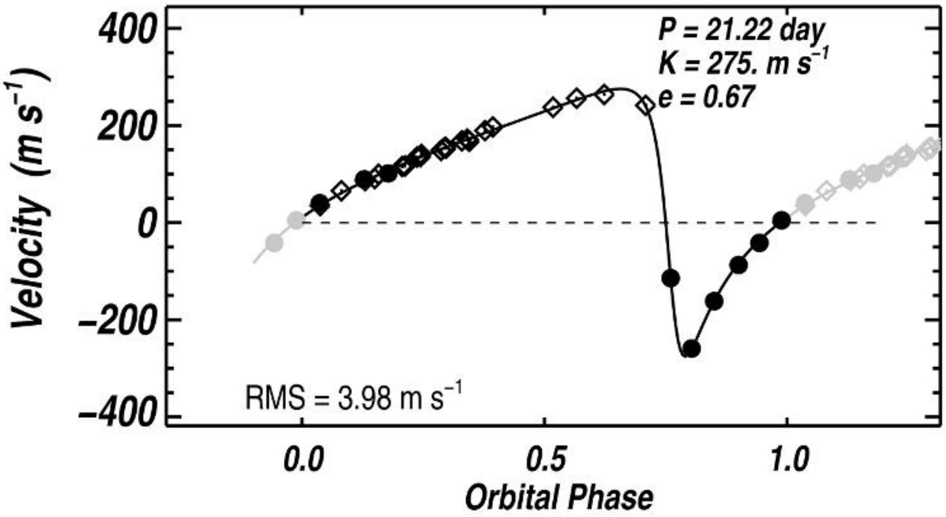

Figure 1.2: The radial velocity curve of the exoplanet HD17156b showing non-sinusoidal behaviour. This indicates that the orbit of the exoplanet is highly eccentric. Image taken from Fischer et al. (2007).

information about the planet. Only a minimum mass can be calculated due to the fact that the orbital inclination is unknown. However, the eccentricity and period of the orbit can be determined very accurately. To determine more properties of the system it would require the planet to transit the face of the star from our line of sight. This would then give the inclination angle and the true mass of the planet could be determined. This is the strength of the Transit Method of exoplanet detection.

1.3.2 Transit Method

When a planet passes in front of a star along our line of sight (as shown in Figure 1.4), the light from that star will show a small but measurable decrease in brightness, provided that the object that passed in front of it is large enough. The probability of this geometric alignment (if the planet is in a circular orbit) is given by:

$$p = \frac{R_* + R_p}{a} \tag{1.4}$$

where R_* is the radius of the star, R_p is the radius of the planet and a is the distance between them (Borucki & Summers 1984, Sackett 1999). Assuming $R_p << R_*$, the probability for transits range from 10% to 0.1% for planets that are between 0.05 and 5 AU away from their parent stars respectively. From this it can be seen that the transit technique will be most effective at finding large planets in close orbits.

Transiting exoplanets also provide us with the opportunity to study other interesting features like the presence of rings or moon in orbit around the gas giant planet (Brown

2001), their internal structure (Guillot 2005), the chemical composition of the atmosphere (Charbonneau et al. 2002) and the spin-orbit alignment (Queloz et al. 2000a, Gaudi & Winn 2007, Winn 2007, Triaud et al. 2010).

The transit method is very good at finding candidate exoplanets, but there are other astronomical phenomena that can produce a lightcurve almost identical to a transiting exoplanet lightcurve (see Section 1.3.3 for a detailed discussion). The astrophysical false positive fraction was shown to be as high as 35% for planet candidates in the Kepler sample (Santerne et al. 2012). Although the transit method yields fundamental parameters not obtainable by RV studies (e.g. the radius of the exoplanet), the confirmation of an exoplanets is still done by the RV method to ensure that the mass of the transiting object is in the planetary regime. Late M dwarfs ($M > 80\ M_{\rm J}$), brown dwarfs ($13\ M_{\rm J} < M < 80\ M_{\rm J}$) and gas giant planets ($M < 13\ M_{\rm J}$) are all very similar in size due to the balance between gravitational collapse and electron degeneracy pressure (Perryman 2000). The two methods work together to determine all the system parameters.

1.3.3 Common Types of False Positives and Follow-up Strategies

Many configurations of astronomical phenomena can produce a lightcurve very similar to one produced by a transiting exoplanet and it becomes increasingly important to discard obvious false positive identifications before submitting the candidates for observation on larger telescopes (Seager & Mallén-Ornelas 2003, Poleski et al. 2010, Morton 2012, Cameron 2012, Santerne et al. 2013). Time on large telescopes is extremely valuable and competition for that time is also increasing. The four most common false positives include:

- Stellar pulsations.
- Star spots.
- An eclipsing binary systems on grazing incidence orbits.
- Small stars that transit larger stars.
- An eclipsing binary system blended with a brighter star.

The first false positive comes from active stars either through certain types of pulsations or magnetically induced star spot activity. Certain types of variable stars pulsate at a multitude of frequencies. When these pulsation modes interact with one another in the right manner, the resulting lightcurve of the pulsating star can look very similar to the lightcurve of a transiting exoplanet. One easy way to remove this type of false positive is to calculate a Lomb-Scargle periodogram and check for multiple pulsation frequency modes (see Section 5.6). If a strong periodicity is identified, one can remove that from the lightcurve (essentially performing a pre-whitening) and check that the original “transit” feature survives the subtraction of pulsation (this can be repeated multiple times). If it does not, then it is a very good indication that the pulsations were the cause of this feature and the candidate can be removed from any follow-up strategy.

Star spots are regions of high magnetic activity on the surface of the star that produce areas of cooler gas than the surrounding material. These regions of cooler gas can cause lowering in the apparent brightness of the surface of the star to such an extent that the change is detectable by transit surveys. Star spots can grow to huge sizes, sometimes covering large fractions of the stellar surface. The period at which this dimming of the starlight is measured is dependent on the rotational period of the star and the latitude at which the star spot was formed. In cases of differential rotation, star spots at different latitudes have different periods. Star spots are not a constant feature on most stars though, so any changes in the brightness, period, depth or shape of the transit feature seen in the lightcurve of the candidate is usually a good indication that a transiting exoplanet is not the cause.

In the case of the grazing eclipsing binary system, the true period of the orbit is actually twice as long as the photometrically determined period. A common way to check for this type of false positive is to double the determined period, plot the resulting lightcurve and check the lightcurve for slightly different eclipse depths. The primary eclipse is when the cooler (or smaller) star eclipses the hotter (or larger) star and a secondary eclipse occurs when the hotter (or larger star) star eclipses the cooler (or smaller) star. Since the same surface area is obscured during both eclipses, the deeper of the two eclipses is called the primary. Different eclipse depths indicate that two different objects with different luminosities are orbiting one another.

However, if the two eclipsing stars are of the same spectral type and have similar properties, it might not be possible to see a difference in the depths of the two eclipses. In some cases it is possible to identify this type of false positive by analysis of the shape of transit event. Stellar binary eclipsing events are generally more V-shaped than the flat-bottomed transit events of exoplanets. If the shape of the transit is consistent with a flat-bottom, medium resolution spectroscopic observations taken at 0.25 or 0.75 orbital phase (usually at the point of highest RV signal assuming a circular orbit) will be able to determine the amplitude of the RV variation and also determine the mass of the eclipsing object. If the mass is determined to be above the exoplanet limit, the candidate can be safely disregarded. Medium resolution spectroscopic observations will not be able to determine the exact mass of the planet, but it will at least be able to identify a system that cannot be planetary in nature.

In situations where a smaller star eclipses a larger star (examples include a late M dwarf orbiting an A or F star or a sun like star orbiting a giant star), the secondary eclipse might not be visible in the lightcurve of the candidate star at all. A low resolution spectroscopic observation usually provides a rough estimate of the effective temperature and surface gravity of the host star. This can then be used to determine the spectral type and using appropriate models, the radius of the star can be determined. If the radius or surface gravity indicates that the star is a giant or evolved star, then the transiting object will need a radius too large to be a planet ($R_p > 2R_{\mathrm{J}}$) for it to produce a transit depth consistent with the transit depth seen in real transiting exoplanets (see Equation 1.5). In cases where the host star is not a giant star and is not an evolved star, the transiting object could be a late M dwarf or brown dwarf, and the only way to determine the true nature of the eclipsing object is to take medium resolution spectroscopic observations at 0.25 or 0.75 phase, determine the amplitude of the RV variation and determine the mass of the eclipsing object.

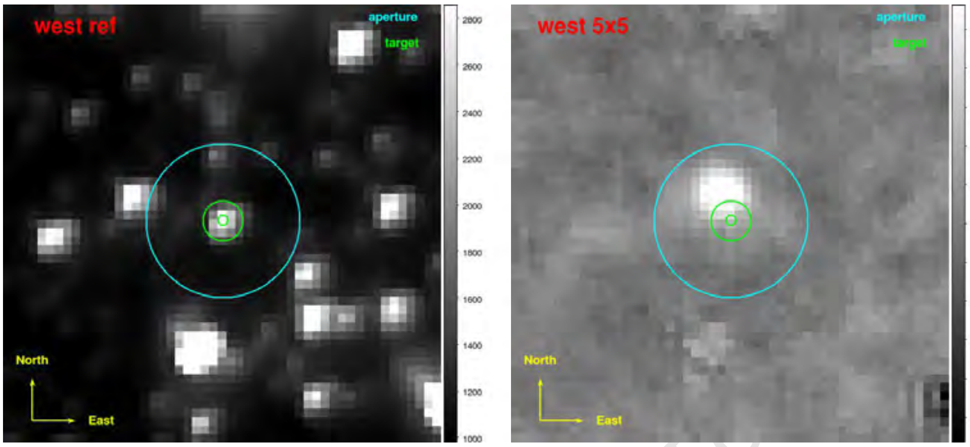

(a) (b)

Figure 1.3: Two images used in the KELT-South transiting exoplanet candidate vetting process to discarded blended eclipsing binary systems. The image on the left (1.3a) shows the original KELT-South reference image. The green circle shows the position of a star identified as a possible transiting exoplanet system during the data reduction process and the blue circle indicates the size of the photometric aperture used. The image on the right (1.3b) is the result of subtracting the median combined in-transit image from the median combined out-of-transit image. It is clear that the signal for the transit event is no longer centred on the target star, indicating that a fainter eclipsing binary to the north is most probably the cause of the transit event.

Probably the most common type of false positive is where an eclipsing system is blended with another foreground or background brighter star. In this type of line-of-sight configuration, the eclipsing binary can be physically associated with the brighter star (leading to a hierarchical triple system) or simply be a chance alignment occurrence. In most transit survey telescopes, the pixel scale of the telescope is fairly large and as a consequence many stars can be blended together within the same photometric aperture of the telescope, and what looks like a single bright target star is usually a number of fainter stars blended with the brighter one. If one of these fainter stars is in fact an eclipsing binary system, the eclipse depth will be diluted down by the light of the brighter star and the shape and depth of the eclipsing event looks very similar to that of a transiting exoplanet. One of the easiest ways to test for this type of configuration is to perform high precision photometric follow-up observations on slightly larger telescopes. Larger telescopes will have better angular resolution and will be able to determine the exact star in which the eclipsing event is taking place (see Section 5.6.2 for examples of where this applied to KELT-South transiting exoplanet candidates). In extreme cases, adaptive optics on very large telescopes can be used to identify and separate the light of the close neighbouring star from the target star and any changes in brightness in the neighbour could indicate that it was the cause of the transit signal.

In many cases the fainter neighbour cannot be separated from the target system due to it being so close to the target star that any photometric aperture size used will include some light from the faint neighbour. A common method to determine which of the two close neighbours is the cause the transit event is to median combine a set of median out-of-transit images and median combine a set of in-transit images. Subtracting the median combined in-transit image from the median combined out-of-transit image should remove all the non-variable stars from the subtracted image. Changes in the position of the peak of brightness of the target system could indicate that an eclipsing binary system is blended with the target star (see Figure 1.3).

High precision photometric observations in multiple wavebands can also be used to determine the nature of the eclipse event (Tingley 2004). The depth of a planetary transit event is not colour dependent since the planet is not a self-luminous object. However, the depth of the eclipse event in stellar binary systems is colour dependent if the blended stellar components have slightly different temperatures (colours). By monitoring the transit event in different filters, it is possible to exclude the event as a planet if different depths are recorded in each waveband.

By careful consideration of the probability that the data is not due to any of the false positive scenarios listed above and the probability that the data can only be reproduced by a transiting exoplanet has been used to "validate" exoplanets (Fressin et al. 2011). This type of analysis is usually done when the transit event is around a star too faint or the period is too long to be observed with RV instruments (also see Section 1.5.2).

1.4 Transiting Exoplanet Lightcurves

It is possible to extract five observable quantities from the lightcurve of a transiting exoplanet:

- The period, P
- The transit depth, ΔF
- The total duration of the transit, t_T
- The total duration of the flat bottom of the transit, t_F
- The time of mid-transit, t_0

In Figure 1.4, t_T is defined as the time it takes the planet to move from point 1 to point 4 (or point of first contact to point of last contact) and t_F is defined as the time it takes for the planet to move from point 2 to point 3 (or point of second contact to point of third contact). The point where ΔF is indicated is also the midpoint, t_0, of both transit lightcurves.

Seager & Mallén-Ornelas (2003) showed that there are five parameters that need to be determined to fully characterise a planetary system. These five parameters are:

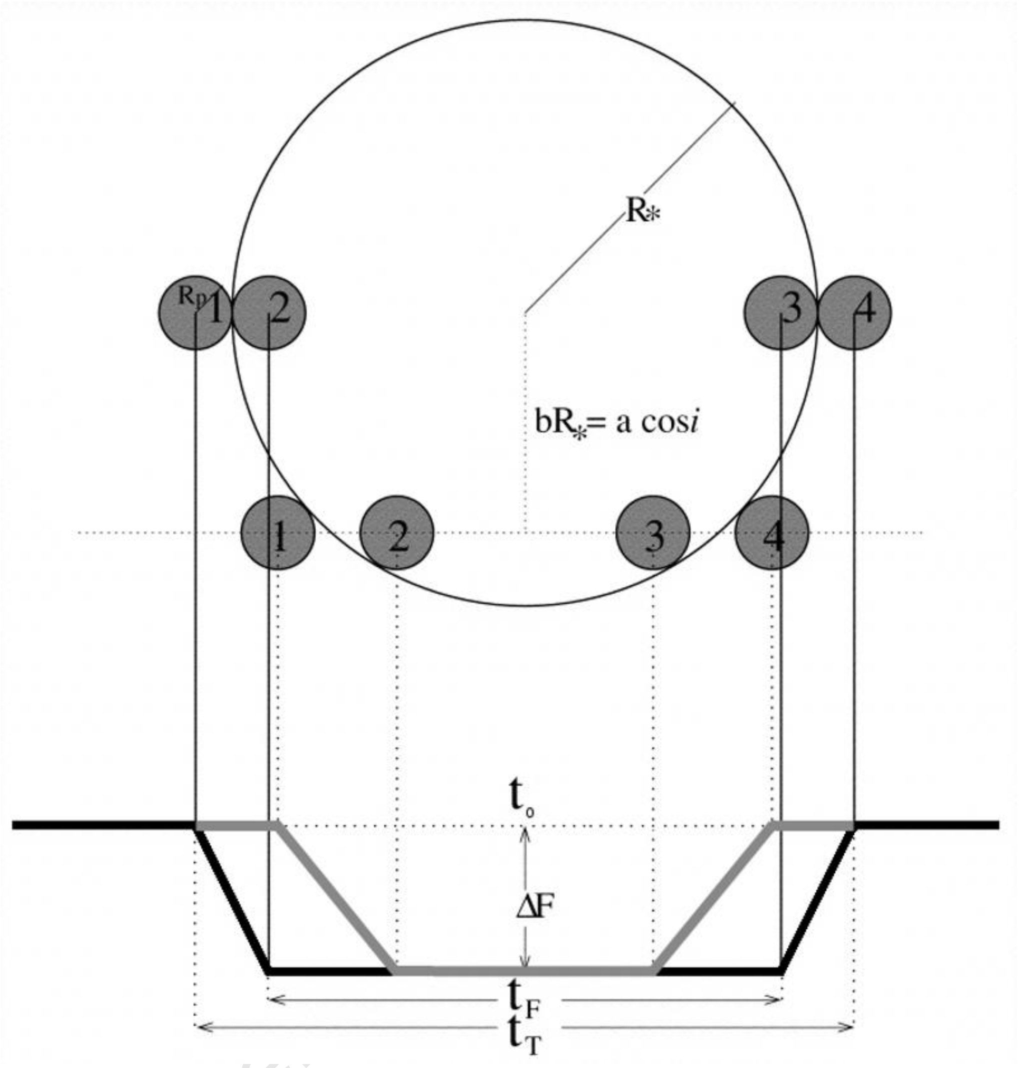

Figure 1.4: Two schematic lightcurves are shown at the bottom (solid black and grey lines) and the corresponding geometry of the star and planet is shown on the top. The original image was taken from Seager & Mallén-Ornelas (2003) and slightly modified to make the observable quantities more clear.

1. The orbital radius, a
2. The orbital inclination, i
3. The mass of the star, M_*
4. The radius of the star, R_*
5. The radius of the planet, R_p

By using the observable quantities, information about the spectral type of the star and Kepler's third law of planetary motion it is possible to derive values for these parameters and obtain a unique solution to the planetary system.

1.4.1 Geometric Equations of the System

From the observables quantities it is possible to construct 3 geometrical equations that describe the features seen in the lightcurve.
The first equation relates the depth of the transit to the radii of the exoplanet and star

$$\Delta F = \left(\frac{R_p}{R_*}\right)^2 \tag{1.5}$$

from which the absolute radius of the planet can be determined if the radius of the star can be estimated using spectral identification and stellar modelling.

The second equation describes the shape of the transit lightcurve by considering the ratio of the duration of the "flat bottom" of the transit to the total duration of the transit:

$$\frac{\sin(t_F \pi/P)}{\sin(t_T \pi/P)} = \sqrt{\frac{[(1 - R_p/R_*)]^2 - [(a/R_*)\cos i]^2}{[(1 + R_p/R_*)]^2 - [(a/R_*)\cos i]^2}} \tag{1.6}$$

The third equation describes the total duration of the transit:

$$\sin(t_T \pi/P) = \frac{R_*}{a}\sqrt{\frac{[1 + (R_p/R_*)]^2 - [(a/R_*)\cos i]^2}{1 - \cos^2 i}} \tag{1.7}$$

Equations (1.6) and (1.7) are results obtained by considering the geometry of two spheres passing in front of one another and follows from the fraction of the orbital period during which the projected distance between the centres of the exoplanet and star is less than the sum of their radii (Sackett 1999). However, these three equations are degenerate and require a physical scale of the two spheres to break the degeneracy. Fortunately, two additional equations can provide the physical scale length of the problem.

1.4.2 Physical Scale Equations of the System

The first is Kepler's third law of planetary motion:

$$P = \sqrt{\frac{4\pi^2 a^3}{G(M_* + M_p)}} \tag{1.8}$$

where G is the gravitational constant, M_* is the mass of the star and M_p is the mass of the exoplanet.

The second equation is obtained from stellar modelling and is known as the mass-radius relation:

$$R_* = kM_*^x \tag{1.9}$$

where k is a constant coefficient for each stellar sequence (main sequence, giants, etc.) and x describes the power law of the sequence.

1.4.3 Dimensionless Quantities

It is now possible to construct 3 dimensionless quantities that will help to fully characterise the planetary system. The first is the planet-star radius ratio, obtained from equation (1.5):

$$R_p/R_* = \sqrt{\Delta F} \tag{1.10}$$

The second is the impact parameter b, defined as the projected distance between the planet and the star centres during mid transit in units of R_*, obtained by combining equations (1.6) and (1.10):

$$b \equiv \frac{a}{R_*}\cos i = \sqrt{\frac{(1-\sqrt{\Delta F})^2 - [\sin^2(t_F\pi/P)/\sin^2(t_T\pi/P)](1+\sqrt{\Delta F})^2}{1-[\sin^2(t_F\pi/P)/\sin^2(t_T\pi/P)]}} \tag{1.11}$$

The third quantity is the ratio a/R_*, directly found from equation (1.7):

$$\frac{a}{R_*} = \sqrt{\frac{(1+\sqrt{\Delta F})^2 - b^2[1-\sin^2(t_T\pi/P)]}{\sin^2(t_T\pi/P)}} \tag{1.12}$$

An expression for the stellar density ρ_* can be constructed by combining (1.12) and Kepler's third law and assuming $M_p << M_*$:

$$\rho_* \equiv \frac{M_*}{R_*^3} = \left(\frac{4\pi^2}{P^2G}\right)\left\{\sqrt{\frac{(1+\sqrt{\Delta F})^2 - b^2[1-\sin^2(t_T\pi/P)]}{\sin^2(t_T\pi/P)}}\right\}^3 \tag{1.13}$$

Equation (1.13) can also be rewritten in terms of solar density as follows:

$$\frac{\rho_*}{\rho_\odot} \equiv \left(\frac{M_*}{M_\odot}\right)\left(\frac{R_*}{R_\odot}\right)^{-3} \tag{1.14}$$

1.4.4 Analytical Solution of the Planetary System

It is now possible to relate the dimensionless quantities, geometric and physical scale equations to one another to obtain the 5 unknown parameters and fully characterise the system. From equation (1.8) and again assuming $M_p << M_*$, the orbital radius is given by:

$$a = \sqrt[3]{\frac{P^2GM_*}{4\pi^2}} \tag{1.15}$$

From equation (1.7) the orbital inclination is given by:

$$i = \cos^{-1}\left(\frac{bR_*}{a}\right) \tag{1.16}$$

It is often easier to express R_*, M_* and R_p in terms of solar equivalents to facilitate direct comparison. This can be done by combining equation (1.14) and the mass-radius relation.

The expression for the mass of the star can then be written as:

$$\frac{M_*}{M_\odot} = \sqrt[(1-3x)]{k^3 \frac{\rho_*}{\rho_\odot}} \tag{1.17}$$

The radius of the star can be found either by using the mass-radius relation or equation (1.14):

$$\frac{R_*}{R_\odot} = k\left(\frac{M_*}{M_\odot}\right)^x = \left(\sqrt[(1-3x)]{k^{\frac{1}{x}} \frac{\rho_*}{\rho_\odot}}\right)^x \tag{1.18}$$

and the radius of the planet can be derived by combining equations (1.5) and (1.18):

$$\frac{R_p}{R_\odot} = \left(\sqrt{\Delta F}\right)\left(\frac{R_*}{R_\odot}\right) = \sqrt{\Delta F}\left(\sqrt[(1-3x)]{k^{\frac{1}{x}} \frac{\rho_*}{\rho_\odot}}\right)^x \tag{1.19}$$

1.4.5 Simplified Dimensionless Quantities

Under further approximations, the equations (1.11), (1.12) and (1.13) can be simplified even further. The approximation is $R_* << a$, which is roughly the same as $t_T\pi/P << 1$ and leads to:

1. $\frac{\sin(t_F\pi/P)}{\sin(t_T\pi/P)} \approx \frac{t_F}{t_T}$
2. $1 - \sin^2\left(\frac{t_T\pi}{P}\right) \approx 1$

With these assumptions, the impact parameter can be rewritten as:

$$b = \sqrt{\frac{(1-\sqrt{\Delta F})^2 - (t_F/t_T)^2(1+\sqrt{\Delta F})^2}{1-(t_F/t_T)^2}} \tag{1.20}$$

The ratio a/R_* can be rewritten as:

$$\frac{a}{R_*} = \frac{2P}{\pi}\frac{\sqrt[4]{\Delta F}}{\sqrt{(t_T^2 - t_F^2)}} \tag{1.21}$$

by using the new impact parameter from equation (1.20) and under the assumptions outlined above $\sin x \approx x$ and $\sin^2 x \approx x^2$.
The stellar density can be rewritten as:

$$\rho_* = \frac{32P}{G\pi}\frac{\sqrt[4]{\Delta F^3}}{\sqrt{(t_T^2 - t_F^2)^3}} \tag{1.22}$$

by a similar reasoning.

Solving these 3 equations allows for a first order estimate of the physical properties of the system from measurements of the transit lightcurve alone. An estimate of the stellar density using the lightcurve can be used to distinguish between a main sequence star and a giant star, which makes it possible to ascertain the nature of the companion that caused the transit feature. If the stellar density implies that the star is a giant, then the companion is most likely stellar in nature, as the transit feature could only be measured for larger objects around giant stars. If the stellar density implies that the star is in fact a main sequence star, then the companion is most likely a sub-stellar object and worthy of further investigation.

1.4.6 Limb Darkening

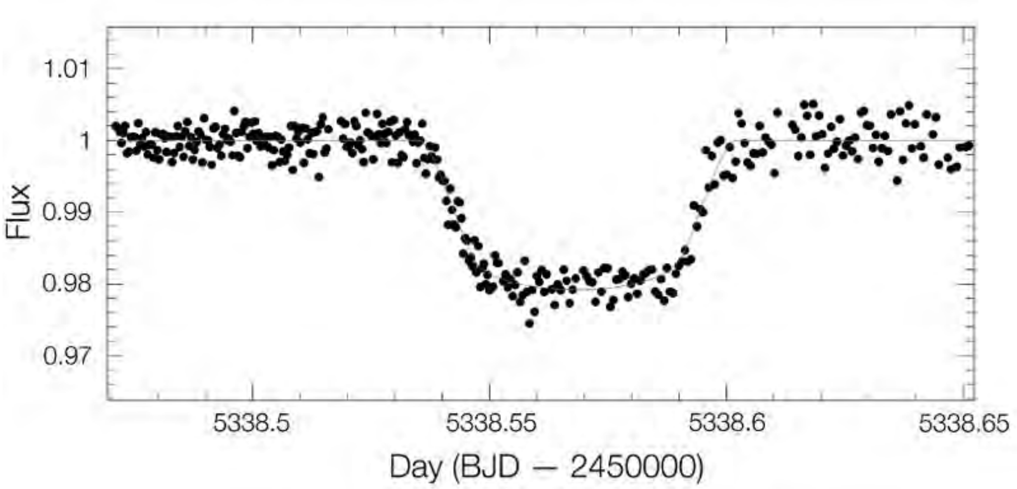

Figure 1.5: The observed lightcurve of an exoplanet passing in front of its star obtained with the **TRA**nsiting **P**lanets and **P**lanetes**I**mals **S**mall **T**elescope (TRAPPIST) in 2010 May. This is a lightcurve of the exoplanet WASP-19b and clearly shows the change in flux seen by the star as the planet passes in front of it. Figure credit: TRAPPIST / M. Gillon / ESO. Figure source: http://www.eso.org/public/images/eso1023f/

The transit lightcurve shown in Figure 1.4 and the derivation of the physical system parameters in the previous section is of course the ideal case where the orbit is circular, the surface of the star is uniform in brightness and the exoplanet is dark when compared to the star. The real transit lightcurves shown in Figures 1.5 and 1.6 differ slightly, but in significant ways. The major difference is that the "sharp" edges are in fact slightly rounded and the "flat bottom" of the lightcurve isn't actually flat. This is due to a phenomenon known as *limb darkening*. Limb darkening manifests itself as a decrease in flux as one moves from the centre of the star towards the edges (or limbs). In Figure 1.7 the effect is easily observed in images acquired by the **So**lar and **H**eliospheric **O**servatory[*] (SOHO) spacecraft. The cause of limb darkening is largely due to the depth into which one can see into the photosphere of the Sun (or stars), known as the optical depth. The physical depth into which one can see into photosphere is limited to an optical depth of unity. When looking at the centre of the Sun, the optical depth allows one to "see" to the base of the photosphere, which is much hotter than the layers above it. When viewing the surface of the Sun at an angle (towards the limb), the optical depth allows one to see only the upper, much cooler layers of the

---

[*] http://sohowww.nascom.nasa.gov/about/

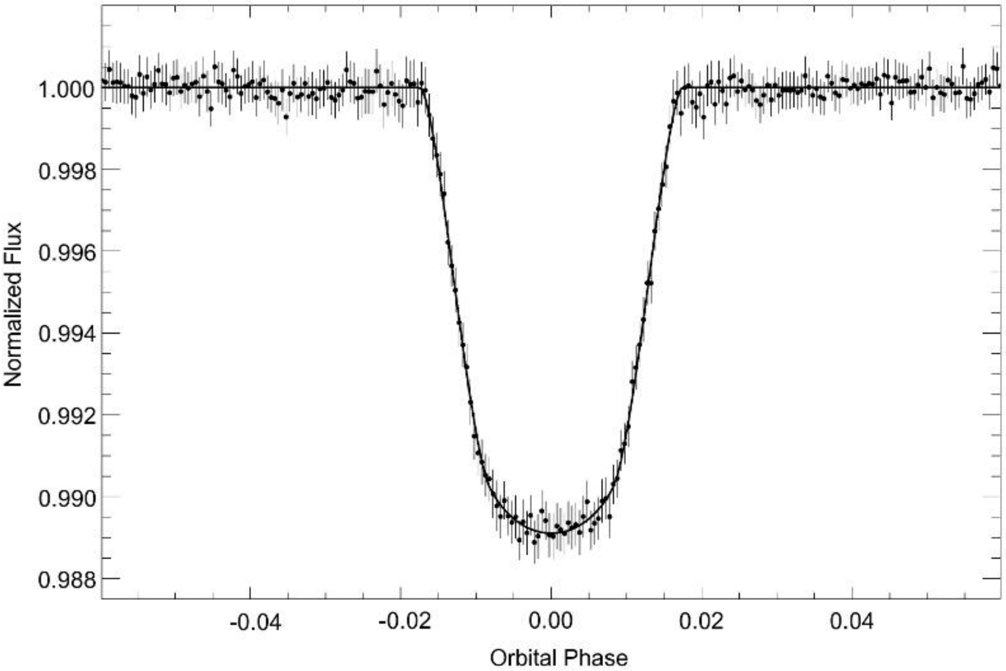

Figure 1.6: The phase folded lightcurve of an exoplanet passing in front of its star obtained from 2008 April 15 to September 7 with the CoRot Spacecraft. This lightcurve clearly shows the decrease in the measured flux as the planet CoRot-11b passes in front of it. The rounded "edges" and rounded "flat bottom" due to limb darkening is clearly visible. Figure taken from Gandolfi et al. (2010).

photosphere. The intensity of the radiation emitted is strongly dependent on temperature and the cooler parts of the Sun photosphere are thus lower in intensity.

In the case of a transiting exoplanet, the lightcurve of the transit reveals a gradual decrease in flux from second contact until the planet is in the centre of the disc of the star where the flux level is at its lowest point. The flux gradually starts to increase again as the exoplanet moves toward the other limb of the star. This causes the "rounded" shape seen during the transit in Figures 1.5 and 1.6. Limb darkening is also wavelength dependent, with the effect becoming smaller with increasing wavelength, which in turn makes the determination of the observable quantities much easier as the lightcurve will exhibit shaper edges and flatter bottoms. The intensity of the star, I, can be described as a function of $\mu = \cos\theta_*$, where θ_* is the angle between the observer and the normal vector on the surface of disc of the star. This means that $\mu = 1$ at the centre of the disc and $\mu = 0$ at the edge. In most situation for ground based telescopes, the quadratic limb darkening law is used to describe the intensity of the star:

$$\frac{I(\mu)}{I(1)} = 1 - \mu_1(1-\mu) - \mu_2(1-\mu)^2 \tag{1.23}$$

where μ_1 and μ_2 are limb darkening coefficients (Claret 2000; 2004). This law is sufficient to

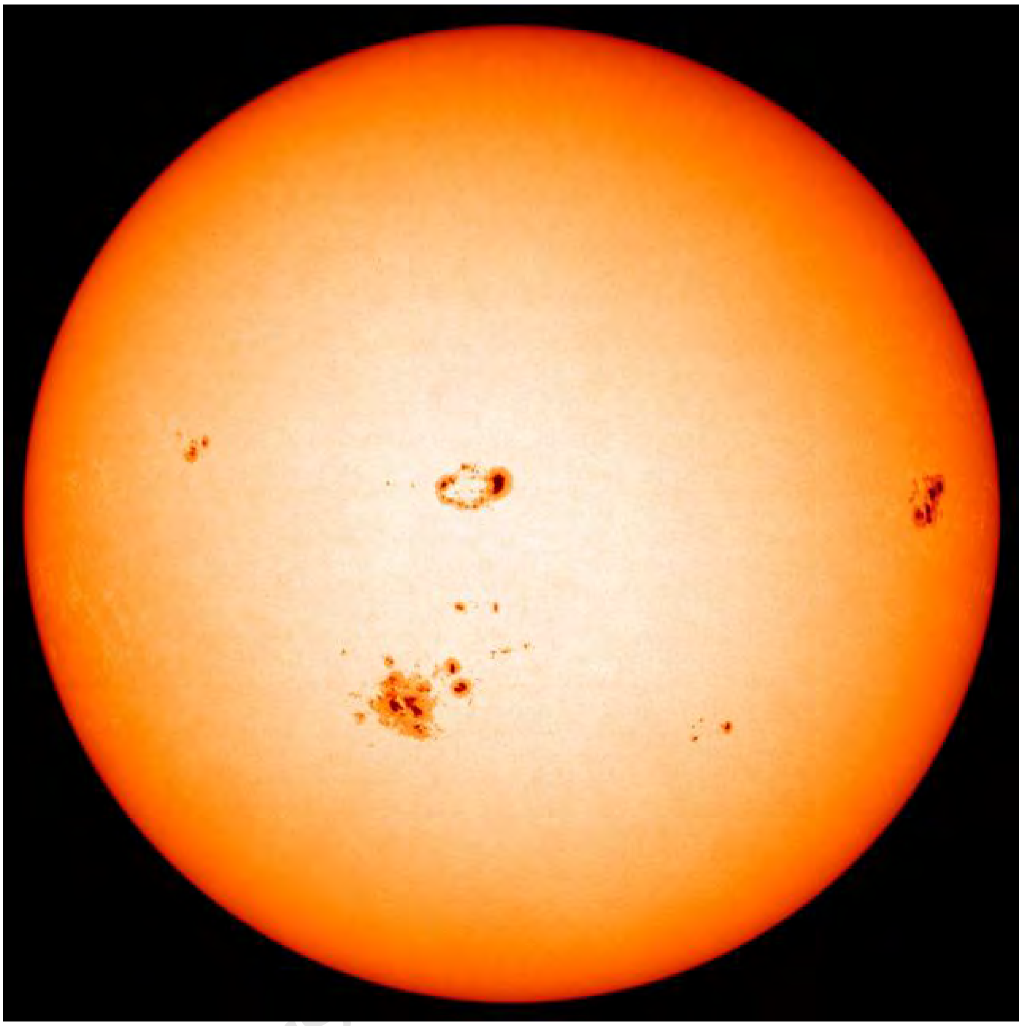

Figure 1.7: Image of the Sun taken with the SOHO spacecraft showing the effect known as limb darkening (decrease in intensity of light as ones moves from the centre of the Sun toward the edges) very clearly. Image courtesy of SOHO NASA.

describe the lightcurve of a transiting exoplanet to a much higher degree of precision than is actually achievable from the ground (Mandel & Agol 2002, Southworth 2008). The limb darkening coefficients are in most cases interpolated to the correct effective temperature and metallicity from the tables found in Claret (2004) and Claret & Bloemen (2011).

1.4.7 Numerical Solution of Exoplanet System Parameters

The RV observations of promising exoplanet candidates can be used to determine a number of properties of the host star, including the effective temperature T_{eff}, the stellar surface gravity log g, the metallicity [Fe/H], the projected stellar rotational velocity $v\sin i$ and macro-turbulence v_{mac}. From these values the mass and radius of the host star can be determined using appropriate stellar evolutionary models (Yi et al. 2001, Torres et al. 2010). These quantities along with the values determined from the transit lightcurve can then be used to obtain the physical parameters of the system through a χ^2 search for the unknown quantities. The Markov Chain Monte Carlo (MCMC) method and more recently the Differential Evolution MCMC (DE-MC) is now an invaluable tool used in the characterisation of exoplanet systems. There are a number of publicly available programs using variations of the MCMC and DE-MC algorithms to solve the physical parameters of the exoplanet system. These programs include TAP (Gazak et al. 2012), JKTEBOP (Southworth 2008), VARTOOLS (Hartman et al. 2008), EXOFAST (Eastman et al. 2013) and others, with all of these codes fitting the transit lightcurves using the analytical model of Mandel & Agol (2002). A number of recent transiting exoplanets, including HATS-3b (Bayliss et al. 2013), HAT-P-44b, HAT-P-45b and HAT-P-46b (Hartman et al. 2013), KELT-6b (Collins et al. 2013) and WASP-65b and WASP-75b (Gómez Maqueo Chew et al. 2013), have been characterised using variations of these codes with each team using slightly different approaches to determine the system parameters.

1.5 Known Exoplanets

1.5.1 Exoplanet Formation Theories

The formation of exoplanets is still a matter of debate at present. Planets are thought to be formed in the disc of material that surrounds the protostar either through the processes of core-accretion (Pollack et al. 1996) or gravitational collapse caused by instabilities in the disc (Boss 1997). The trend of metal-rich stars (see Section 1.5.4 below) being more likely to host planets suggests that the core-accretion model is the more likely explanation for planetary formation. However, the core-accretion model predicts that all the planets in the system should be well aligned with the rotational axis of the star. The mounting evidence that hot Jupiter planets fall into two classes, one with aligned orbits and one with very misaligned orbits, suggests that core-accretion alone cannot account for the diversity of exoplanets. Chaotic migration of the hot Jupiter through processes like Kozai migration (Kozai 1962), planet-planet scattering (Rasio & Ford 1996) or a combination of these processes need to be invoked to explain the types of exoplanets and the orbits that are observed.

1.5.2 Current Status of Exoplanets

As of 2014 August there are 1811 exoplanets included in the catalogue provided by **The Extrasolar Planets Encyclopaedia**[*]. This catalogue makes no distinction between *confirmed* and *validated* planets. Confirmation of an exoplanet requires that the mass of the planet be determined because, as discussed in Section 1.3.2, late M dwarfs, brown dwarfs and gas giant planets are all very similar in size and produce transit events that look very similar. Unfortunately, most of the candidate transiting exoplanet systems (of which there

---

[*] http://www.exoplanets.eu

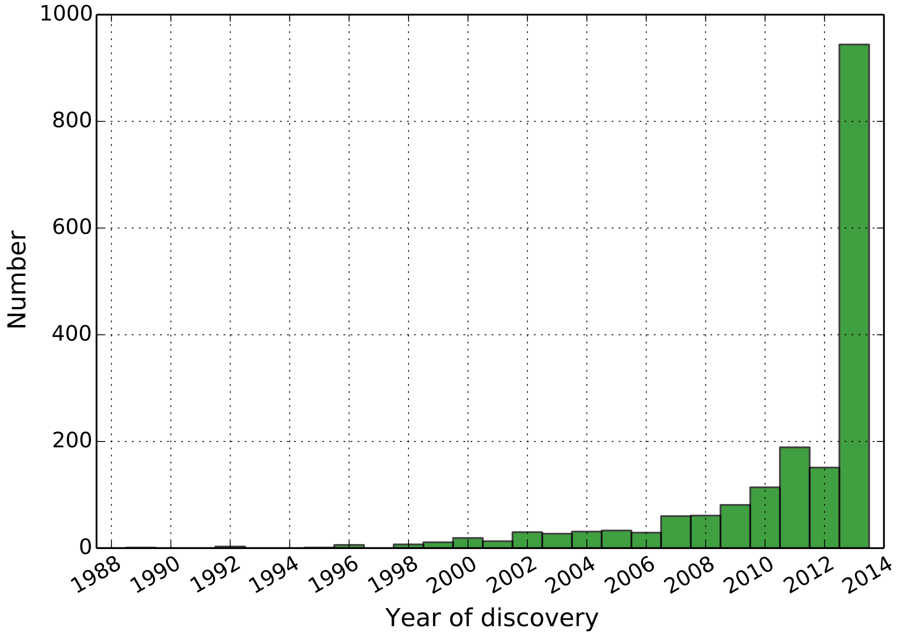

Figure 1.8: Histogram showing the number of exoplanets discovered by year.

are well over 4000) found by the Kepler spacecraft are much too faint (V > 13) for current RV surveys to determine the mass of the transiting object, leaving many candidate systems as unconfirmed or even unconfirmable. This situation is not likely to change in the near future. The HARPS-N spectrograph (Cosentino et al. 2012) was specifically built to follow-up the Kepler candidates, but even with the large amounts of time allocated to the confirmation of the candidate exoplanets, it will be impossible to confirm them at a rate of more than 20 per year. Faigler et al. (2013) showed that for a small number of the Kepler candidates it is possible to determine the mass of the transiting object via the relativistic effect known as “Doppler Beaming” (DB). This effect causes a very slight increase (or decrease) in the brightness of any light source moving toward (or away) from the observer as a consequence of the radial velocity variation caused by a planet orbiting the star. By careful analysis of the amplitude of this brightness modulation (which is estimated to be between 2 and 50 parts per million for most exoplanets), the mass of the planet can be determined.

When the mass of the candidate exoplanet system cannot be determined by RV or DB due to the faintness of the target star, other methods have been developed to exclude all other possibilities for the transit event seen in the lightcurve. These planets are known as “validated” planets. The first planets to be validated were all shown to be 100 times more likely to be a planet than any other false positive scenarios by making use of the results of the BLENDER code (Torres et al. 2011, Lissauer et al. 2011, Fressin et al. 2011). The

BLENDER code compares a number of false positive scenarios and compares the lightcurve that would have been produced by the false positive to the actual data obtained with the Kepler spacecraft. It validates a planet when the probability that the lightcurve is produced by a planet strongly outweighs any other false positive scenario.

Studies of candidate exoplanets systems with multiple transit events (caused by different objects due to different transit depths) have led to the validation of ∼850 new exoplanets (Rowe et al. 2014, Lissauer et al. 2014, Alonso et al. 2014) via analysis similar to the BLENDER code.

The histogram in Figure 1.8 shows the number of exoplanets discoveries per year and shows the rapid increase in detections over the last 5 years. Transiting exoplanet surveys have now discovered more exoplanets than RV surveys (2012 was the first year in which more transiting exoplanets were discovered than RV planets). Focus of the RV surveys have moved into characterisation of the discovered exoplanets rather than the discovery of new ones. The increased rate of discovery by the transiting exoplanets surveys is largely due to the increase in affordability of the technology that allows the detection of smaller and smaller planets as well as the advances in efficiency of the instruments used to detect exoplanets.

1.5.3 Transiting Exoplanets

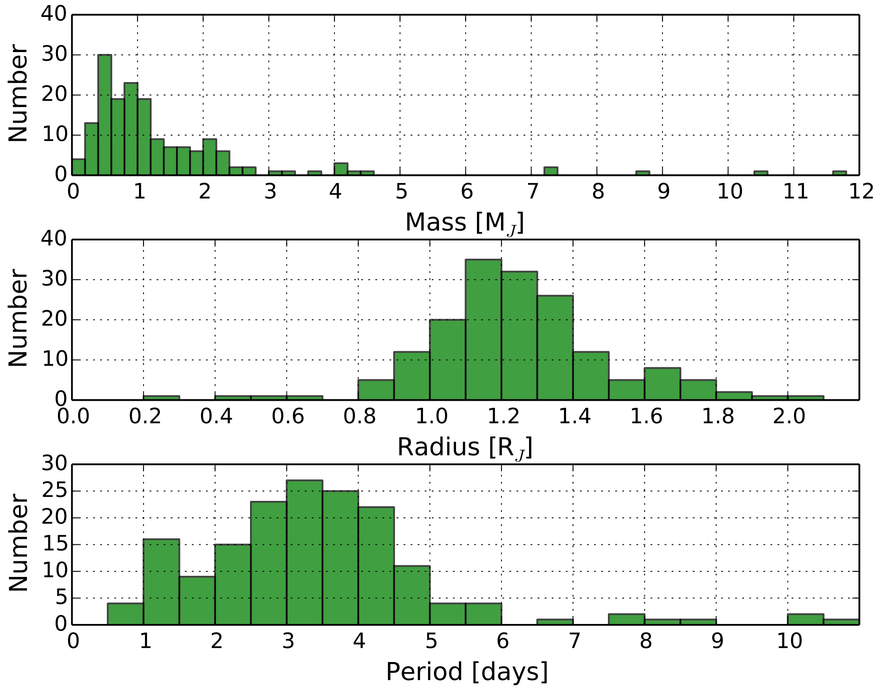

Figure 1.9: The histograms of mass, radius and period distribution for exoplanets discovered by ground based telescopes only.

As of 2014 August the number of exoplanets discovered by the transit method is 1141. Ground based telescopes have discovered 170 exoplanets and 962 have been discovered by space based telescopes. Nine of the exoplanets listed as being discovered by the transit technique were initially discovered via the RV technique and only later found to transit in follow up observations. A number of these exoplanets are classified as being discovered by the transit method, but are in actual fact RV discoveries as these exoplanets were identified as additional planets in the RV data used to confirm the original transit discovery. Some of these systems include HAT-P-44c, HAT-P-46c (Hartman et al. 2013). Other exoplanets listed as being found using the transit method are inferred via transit timing variations and are found in a large number of multiple systems (Xie 2013). The Kepler and CoRoT spacecraft are responsible for the majority of small planets discovered to date, while the larger radii and more massive exoplanets have been found largely by ground based surveys. Transiting exoplanets have periods ranging from as short as a few hours, in the case of Kepler-42c (also known as KOI-961.02) (Muirhead et al. 2012), to 303 days, in the case of Kepler-47(AB)c (Orosz et al. 2012).

If only the exoplanets discovered by ground based telescopes are considered, the distribution of mass, radius and period (seen in Figure 1.9) shows most exoplanets discovered from the ground have masses similar to Jupiter with a few almost twice the mass of Jupiter. However, the radii of these exoplanets are in most cases about 30% larger than the radius of Jupiter, with some planets having radii almost twice that of Jupiter (Hartman et al. 2011b, Anderson et al. 2011, Smalley et al. 2012). This “inflated radius” problem is a very active area of research at present with many theories trying to explain this observed phenomenon and whether a single mechanism or a combination of various processes are responsible. The best studied exoplanet with an “inflated” radius is WASP-12b (Hebb et al. 2009). At the time of its discovery, WASP-12b had the largest radius of any known exoplanet, had the shortest period of any known transiting exoplanet and the relative brightness of the host star made it an ideal candidate to study the atmospheric composition of the planet. Recent studies have shown that the exoplanet transits the brightest member of a triple star system (Bergfors et al. 2013, Bechter et al. 2014) and measurements of the secondary eclipse indicate that the atmosphere is very carbon rich, having a carbon-to-oxygen ration almost twice that of the Sun (Stevenson et al. 2014).

Some of the first theories to try and explain the larger than expected radii of hot Jupiters involved stellar radiation being absorbed by the upper atmosphere of the exoplanet and transported to the deep interior (Showman & Guillot 2002), which effectively increases the amount of energy in the exoplanets resulting in increased radii. Other mechanisms that can add energy to the interior are tidal dissipation of orbital eccentricity (Bodenheimer et al. 2001, Jackson et al. 2008), dissipation of thermal tides (Arras & Socrates 2010, Socrates 2013) and ohmic heating where ionized material in the atmosphere interacts with the magnetic field of the exoplanet (Perna et al. 2010, Batygin & Stevenson 2010, Batygin et al. 2011). More detailed studies of the problem have shown that the exact depth at which the “extra” energy is deposited in the atmosphere of the exoplanet is vitally important to explain the increased radius and that the loss of heat through the night-side (most hot Jupiter exoplanets are thought to be tidally locked to their host stars with one side permanently irradiated and the other in perpetual darkness) and polar regions of the exoplanet require additional energy sources in the deep interior of these exoplanets to explain the inflated radii observed (Spiegel & Burrows 2013).

The distribution of periods for the transiting exoplanets also shows an interesting feature. Figure 1.9 shows the distribution of the periods up to 11 days (the longest period transiting exoplanet discovered from the ground has a period of ∼10.7 days). There are very few planets with orbital period longer than 5 days, which is a well known selection effect of the ground based surveys which favours the discovery of large exoplanets in short period orbits. However, there is no selection effect that will cause the "pile-up" of exoplanets with periods between three and four days (planets with orbital periods of between one and two days are just as likely to be found). This pile-up of planets has been noted before (Udry & Santos 2007, Latham et al. 2011), with hot Jupiters discovered by space based telescopes confirming this trend. Hot Jupiters with periods shorter than one day are thought to be relatively short lived systems and the exoplanets are spiralling inward due to tidal decay (Matsumura et al. 2010). Hot Jupiter exoplanets that experience gravitational interaction through a third body in the system can be scattered into highly eccentric orbits that are then tidally captured and circularised at short periods has also been proposed to explain the period distribution (Ford & Rasio 2006, Naoz et al. 2011). The period distribution of hot Jupiters is most likely the result of many different mechanisms and many more observations of these systems will be needed to fully explain the diversity currently observed.

1.5.4 Host Star Properties and Exoplanet Frequency Trends

With the large number of exoplanets now discovered some interesting trends have started to become clear. One of the first observations was that metal-rich stars are more likely to host gas-giant planets than metal-poor stars (Gonzalez 1998, Gonzalez et al. 2001, Santos et al. 2001; 2003; 2004, Fischer & Valenti 2005, Sousa et al. 2008, Neves et al. 2009, Johnson et al. 2010, Sousa et al. 2011, Adibekyan et al. 2012b). However, this correlation was shown to not be valid for smaller Neptune and super-Earth type planets (Udry & Santos 2007, Sousa et al. 2011, Ghezzi et al. 2010, Mayor et al. 2011, Buchhave et al. 2012). Studies of lithium abundances have shown that planet-hosting solar type stars are severely depleted in lithium (Israelian et al. 2009, Sousa et al. 2010) compared to solar type stars with no planets. The exact role of other heavier elements like Mg, Al, Si, Sc and Ti in the host star and the frequency of planets is also under constant research, with claims that the stars with overabundances in these elements are more likely to have planets than low metallicity stars (Adibekyan et al. 2012a). The ratio of refractory elements (those with condensation temperatures $T_C > 900$K) to volatile elements ($T_C < 900$K) was studied by Ramírez et al. (2010) and it was found that the stars with an under abundance of refractory elements are more likely to host planets (of which the Sun is also an example). This trend was brought into question recently by studies of 61 late F- and early G-type main-sequence stars with high-quality HARPS and UVES spectra (González Hernández et al. 2013). Metal-rich stars have also been shown to host shorter period planets (Queloz et al. 2000b, Sozzetti 2004, Santos et al. 2003, Beaugé & Nesvorný 2013, Dawson & Murray-Clay 2013). There is also mounting evidence that systems containing hot Jupiters generally don't have outer planets, but systems that don't contain hot Jupiters are more likely to be multi-planets systems (Latham et al. 2011, Steffen et al. 2012, Hartman et al. 2013). This suggests completely different formation and dynamical evolution theories for these systems. There are also suggestions that the temperature and age of the host star has some correlation with the spin-orbit alignment (measured through the Rossiter-McLaughlin effect) of the planet with stars with $T_{eff} > 6250$K having a larger fraction of misaligned planets (Winn et al. 2010, Triaud 2011, Albrecht et al. 2012) and the older a star, the more likely the orbit is aligned with the spin axis (Albrecht et al. 2012). This misalignment fraction has been used to support the theory that these systems did not migrate inward smoothly from their formation position via disc migration, instead being scattered through the Kozai mechanism (Kozai 1962) or planet-planet scattering (Rasio & Ford 1996, Ford & Rasio 2008) into their current orbits. Some planets like WASP-79b (Addison et al. 2013) have a stellar spin-orbit misalignment that places the planet in a near polar orbit. Other system like HAT-P-7b (Narita et al. 2009, Winn et al. 2009), WASP-17b (Anderson et al. 2010) and HAT-P-6b (Hébrard et al. 2011) have been shown to have retrograde orbits. All these systems lend support to the notion that core-accretion and disc-migration are not the only process responsible for the formation and current location of gas giant planets. More recently Beaugé & Nesvorný (2013) have found correlations between the period and the radius of the planets. They suggest there is an under abundance of small radius planets ($3\ R_{\oplus} < \mathrm{R} < 10\ R_{\oplus}$) in short orbits ($\mathrm{P} < 3$ days). They have also found a lack of small planets ($\mathrm{R} < 4\ R_{\oplus}$) with $\mathrm{P} < 5$ days around metal-poor stars as well as an under abundance of small planets ($4\ R_{\oplus} < \mathrm{R} < 8\ R_{\oplus}$) with $\mathrm{P} < 100$ days around metal-poor stars.

By studying all these correlations the theories of planetary formation and dynamical evolution can be constrained and might eventually lead to a complete description of how these planetary systems formed and why they exist in their current configuration. This is a very active research area at present and the eventual aim is to place the formation and evolution of the solar system in context within the greater Universe.

1.6 Transiting Exoplanet Surveys

1.6.1 Ground Based Surveys

Although many dedicated surveys for transiting exoplanets are in operation*, there are a few that have been responsible for the vast majority of discoveries. The transit surveys can be classified into two main types.

The first type makes use of existing telescopes with fairly large apertures of 50 cm and

---

*A full list of teams and telescopes can be found at http://www.exoplanet.eu/research/

larger. These surveys have a relatively small field of view and are referred to as "pencil-beam surveys". These surveys generally target fainter stars making use of longer exposures. Most of these surveys were originally intended for other types of survey work, but have become invaluable tools for the discovery of exoplanets. Examples of these types of surveys include the **O**ptical **G**ravitational **L**ensing **E**xperiment (OGLE) (Udalski et al. 1992) and **MA**ssive **C**ompact **H**alo **O**bjects (MACHO) (Alcock et al. 1993) of which only the former is still active. OGLE has found eight transiting exoplanets and the distances to these systems make them some of the furthest known exoplanets.

The second type of transit survey makes use of dedicated small aperture telescopes designed and optimized exclusively to find exoplanets around the brightest stars. Most of the known transiting exoplanets have been discovered using these dedicated instruments. The more successful groups are discussed below with particular emphasis placed on the hardware systems of each telescope and the magnitudes of the stars targeted for exoplanet discovery.

HATNet/HATSouth

The original **H**ungarian **A**utomated **T**elescope (HAT) initiated by Bohdan Paczynski in 1999 was designed to find the brightest variable stars. The prototype instrument HAT-1 was decommissioned in 2002 and the hardware was upgraded to form the next generation HAT, with substantial modifications to the allow the new telescope to search for transiting exoplanets. The second generation prototype HAT-5 telescope (Bakos et al. 2004) was installed at Fred Lawrence Whipple Observatory (FLWO) atop Mt. Hopkins in Arizona, USA and observed the skies from 2003 March to 2003 July, after which it formed part of the new HATNet (Bakos et al. 2004, Hartman et al. 2004) network of telescopes. This network now consists of 4 telescopes located at FLWO and 2 more telescopes located at the Smithsonian Astrophysical Observatory's Submillimeter Array site on Mauna Kea, Hawaii. All 6 telescopes have similar hardware with Apogee AP10 2K × 2K CCDs, Canon 200 mm f/2.8 lenses and friction driven horseshoe mounts inside clamshell domes. Each telescope has an effective $8^\circ \times 8^\circ$ field of view which gives an effective pixel scale of $\sim 14''$ pixel^{-1}. Measurements of the lightcurves revealed that a precision of between 3 and 10 mmag for stars between $8 < I < 11$ can be achieved.

From 2009 to 2013 the project was expanded with 6 more telescopes in the southern hemisphere (Bakos et al. 2013), with 2 telescopes at each station located at Las Campanas, Chile; Siding Spring, Australia; and the High Energy Stereoscopic System (H.E.S.S.) Gamma-Ray site, Namibia. They form part of the HATSouth network. These telescopes are longitudinally separated in such a manner that it permits almost continuous 24 hour coverage of selected fields, increasing the probability of finding longer period transiting exoplanets as well as smaller radii planets. Each one consists of four 18 cm diameter f/2.8 focal ratio optical tube assemblies, four Apogee U16M 4K × 4K CCDs, all on a Fornax F150 equatorial fork mount. This produces an $8^\circ \times 8^\circ$ field of view and a pixel scale of $\sim 3.7''$ pixel^{-1}. With this system the precision attained is $\sim$6 mmag for stars with $r \approx 10.5$.

The number of exoplanets discovered by both the HATNet and HATSouth teams totals 54 with only 4 host stars having a V magnitude < 10. Of the more notable discoveries are HAT-P-15 b (Kovács et al. 2010) and HAT-P-17 b (Howard et al. 2012a) with orbital periods of 10.86 and 10.34 days respectively, making them among the longest period exoplanets to be discovered by ground based telescopes.

WASP/SuperWASP

The **W**ide **A**ngle **S**earch for **P**lanets (WASP) Project (Pollacco et al. 2006, Collier Cameron et al. 2009) consists of two wide-field camera array telescopes, one located at the Observatorio del Roque de los Muchachos in the Canary Islands and the other at the Sutherland Observing Station of the South African Astronomical Observatory (SAAO) in South Africa. Each telescope is equipped with 8 cameras (in a 2 by 4 layout) attached to a robotic equatorial fork mount manufactured by Optical Mechanics. Each camera consists of a 200mm f/1.8 Canon camera lens and an Andor DW436 2K × 2K CCD producing an $8^\circ \times 8^\circ$ field of view with a pixel scale of $\sim 14''$ pixel^{-1}. The combined field of view for all 8 cameras covers roughly one hour in right ascension and 30 degrees in declination.
Photometric precision of better than 1 mmag for stars with $7 < V < 11.5$ is obtained and of the 88 exoplanets discovered by the WASP consortium, only 9 host stars have $V < 10$. More notable discoveries include WASP-79 b (Addison et al. 2013, Smalley et al. 2012) a planet in an almost polar and retrograde orbit and WASP-19 b (Hebb et al. 2010) a planet with the shortest orbital period discovered by ground based telescopes at only 0.79 days.

XO

The **XO** Project (McCullough et al. 2005, Poleski et al. 2010) operates one telescope with two cameras at Haleakala summit in Hawaii, USA. Each camera consists of a 200 mm f/1.8 Canon EF200 lens attached to an Apogee Ap8p 4K × 4K back illuminated CCD and a field of view of approximately $7^\circ \times 7^\circ$, resulting in a pixel scale of $\sim 25''$ pixel^{-1}. Both cameras are mounted on a Paramount ME robotic German-equatorial mount manufactured by Software Bisque Inc. Photometric precision of 10 mmag for stars with brightness of $V < 12$ are reported and the brightest stars of $V < 8.5$ are saturated and are not analysed. Of the 5 exoplanets discovered by the XO Project, only one has a host star with $V < 10$. One of the more notable discoveries is XO-3b (Johns-Krull et al. 2008) with a mass of 11.79 $M_{\rm J}$, making it the most massive transiting exoplanet discovered by ground based telescopes.

TrES

The **Tr**ans-Atlantic **E**xoplanet **S**urvey (TrES) network consists of four telescopes in the northern hemisphere. These telescopes are **S**tellar **A**strophysics and **R**esearch on **E**xoplanets (STARE) (Brown & Charbonneau 2000, Rabus et al. 2007), **P**lanet **S**earch **S**urvey **T**elescope (PSST) (Dunham et al. 2004), Sleuth (O'Donovan et al. 2004) and the **W**ide **A**ngle **T**elescope **T**ransit **S**earch (WATTS) (Oetiker et al. 2010). Each telescope in the network has slightly different hardware, but almost the same field of view of about 6° × 6° with a pixel scale of $\sim$11$''$ pixel^{-1}. All of the 5 discoveries to date have V > 11. TrES-3b (O'Donovan et al. 2007) has a period of only 1.30619 days, making it one of the shortest period transiting exoplanet discovered by ground based telescopes.

QES

The **Q**atar **E**xoplanet **S**urvey (QES) (Alsubai et al. 2011, Bryan et al. 2012) consists of five cameras attached to a single mount located in New Mexico. The QES telescope images the same 11° × 11° part of the sky at two different pixel scales. One camera is a 200 mm f/2.0 Cannon lens attached to an FL1 ProLine PL6801 KAF-1680E 4K × 4K CCD detector that is capable of imaging the entire field at a pixel scale of 9.26$''$ pixel^{-1}. The other four cameras are 400 mm f/2.8 Cannon lenses attached to four more ProLine CCDs, arranged in a 2 × 2 mosaic pattern that each cover the original field in a 5.5° × 5.5° field of view at a pixel scale of 4.64$''$ pixel^{-1}. QES was designed to complement the SuperWASP sites in the Canary Islands and South Africa. The 200 mm camera targets stars in the magnitude range 8 < V < 12, while the 400 mm cameras target fainter stars at magnitude 11 < V < 15. To date QES has discovered two exoplanets Qatar-1b (Alsubai et al. 2011) and Qatar-2b (Bryan et al. 2012) with host star magnitudes of 12.84 and 13.3 respectively. Data obtained to characterise the Qatar-2 planetary system also showed evidence for a second planet at a much wider separation from the host star.

MEarth

MEarth (Nutzman & Charbonneau 2008, Irwin et al. 2009) was specifically designed to find transiting exoplanets around M dwarf stars in the solar neighbourhood and consists of 8 Ritchey-Chrétien robotic telescopes, each with an aperture size of 40 cm mounted on a German Equatorial mount located at FLWO. Each telescope is equipped with a back illuminated e2v 2K × 2K CCD with a pixel scale of 0.76$''$ pixel^{-1} for a 26$'$ × 26$'$ field of view. The MEarth telescopes make use of a custom 715 nm longpass filter which, in combination with the wavelength response of the detectors, produces a response function that is roughly equivalent to the Sloan i + z filters (Fukugita et al. 1996). The broad wavelength range was designed to maximise the photon flux from M dwarf stars of which there are 2000 in the MEarth target list. The one discovery to date is a 2.7 $R_\oplus$, 6.6 $M_\oplus$ exoplanet in a 1.6 day orbit around the star GJ1214. With numerous publications exploring this planet[*], it has proved to be one of the most useful in understanding and characterisation of exoplanet atmospheres and the formation and evolution of Super-Earth planets.

1.6.2 Space Based Surveys

Ground based transiting exoplanet surveys have been able to push the limit on lightcurve precision down to 0.1% using different observing and advanced reduction techniques. The

---

[*] See http://exoplanet.eu/catalog/gj_1214_b/ for a list of publications associated with GJ1214b

earth's atmosphere further limits the attainable precision to 0.01% through variable extinction and scintillation. This places a limit on the size of the exoplanets that are able to be detected using these telescopes. To find exoplanets smaller than Neptune in size or planets the size of earth, the only option is to place a telescope in space beyond the atmosphere.

CoRoT

The **Co**nvection, **Ro**tation and planetary **T**ransits (CoRoT) (Baglin 2003, Auvergne et al. 2009) satellite was launched on 2006 December 27 with first light reported on 2007 January 7. It was a joint venture by the French Space Agency and European Space Agency along with other international partners. The satellite was designed with two objectives in mind. The first was to perform astroseismology by studying oscillations and pulsations in stars. The second objective was to find and characterise small radii exoplanets (ones with radii approaching earth radius). Consisting of a 27 cm diameter off-axis afocal telescope attached to four 2K × 2K CCDs manufactured by E2V Technologies, the field of view was roughly $2.7^\circ \times 3.05^\circ$ with a pixel scale of $2.3''$ pixel^{-1}. Photometric precision of 7.1×10^{-4} was obtained for stars with R = 15 mag.

Of the 26 exoplanet discoveries, none have $V < 11$. CoRot-1b (Barge et al. 2008) was the first exoplanet to have the secondary eclipse measured in the optical waveband due to the extremely high precision lightcurve produced by the satellite. Other notable discoveries include CoRoT-2b (Alonso et al. 2008), a planet orbiting a star with significant semi-periodic stellar flux variations due to star spots, and CoRoT-7b (Queloz et al. 2009, Léger et al. 2009), a planet with a radius of only 1.7 $R_\oplus$.

The satellite's on-board instrument stopped communicating with ground stations in 2012 November and it was announced in 2013 June that the satellite had been placed in an orbit that would destroy it in the earth's atmosphere.

Kepler

The Kepler spacecraft (Borucki et al. 2009) which was launched in 2009 March has been the most successful spacecraft at discovering transiting exoplanets. With the primary goal of determining the frequency of exoplanets with radii as small as the earth or smaller in the habitable zone (the range of orbital radii at which liquid water could exist on the surface of a planet) $\eta_\oplus$, the satellite has found many other interesting objects and completely reshaped the understanding of exoplanet formation.

Studies, using the Kepler data found the occurrence rate of Earth-sized (0.5 - 1.4 $R_\oplus$) planets, orbiting stars with $T_{eff} < 4000$K, to be $0.48^{+0.12}_{-0.24}$ per star and for slightly larger planets (0.5 - 2 $R_\oplus$) the occurrence rate increase to $0.51^{+0.10}_{-0.20}$ (Kopparapu 2013).

The satellite consisted of a 95 cm aperture telescope with 42 2K × 1K CCDs with a field of view of about 115 square degrees. The telescope pointed at the same part of the sky toward the constellation of Cygnus for the entire duration of the mission. Stars in that region were pre-selected for observations, as the entire field of view contained too much data for the spacecraft to be able to process and store the data on board the satellite systems. Altogether $\sim$ 150000 stars were monitored with a measurement of the brightness of the star taken every 6 minutes.

To date the Kepler spacecraft has found over 960 exoplanets and over 4000 possible exoplanet candidates still need to be confirmed. Most of the Kepler candidates are faint (V $>$ 13) making them beyond the capabilities of the current RV surveys and as such cannot be confirmed to be planetary in nature as the true mass cannot be determined at present. Fressin et al. (2012) found that the false positive rate for all size exoplanets in the Kepler dataset for quarters 1 - 6 was $\sim$10%. This would mean that the number of candidates being actual planets could be as high as 2700. Noteworthy discoveries include Kepler-9 (Holman et al. 2010), the first system to have multiple transiting planets, Kepler-16b (Doyle et al. 2011), the first planet to be discovered orbiting a binary system, Kepler-20e (Fressin et al. 2012), the first planet with a radius smaller than the earth, Kepler-22b (Borucki et al. 2012), the first potentially habitable earth-like planet and Kepler-37b (Barclay et al. 2013), the smallest planet yet discovered, with a radius that makes it slightly smaller than Mercury.

In 2012 July the Kepler spacecraft reported the failure of one of the four reaction wheels the satellite uses to point the telescope. Although only 3 reaction wheels are required to point the telescope, a failure of another reaction wheel at the end of 2013 May effectively ended the scientific operations of the Kepler Spacecraft. Attempts to recover from the failure of the last reaction wheel finally failed in 2013 August and NASA reported that Kepler would no longer be able to do exoplanet discovery, but the spacecraft was capable of doing other types of science and enlisted suggestions by the scientific community for possible avenues of research for the “crippled” spacecraft.

1.6.3 Future Transit Surveys

Although there are many surveys planned to search for transiting exoplanets in the future, the space based **T**ransiting **E**xoplanet **S**urvey **S**atellite (TESS) (Ricker et al. 2010, Ricker 2014) and **PLA**netary **T**ransits and **O**scillations of stars (PLATO) (Rauer & Catala 2011) are most relevant to the current discussion. Both are planned to start operations in 2017 and are designed to find earth sized exoplanets around the closest and brightest stars across the entire sky.

TESS

In 2013 April NASA selected the TESS project for a planned launch in 2017 as part of their “Explorer Program” which allows small university based research groups to carry out forefront space science. The satellite will consist of an array of wide-field cameras to perform an all-sky survey to discover transiting exoplanets, ranging from earth-sized planets to gas giants, in orbit around the brightest stars in the sun’s neighbourhood. The cameras will each have a field of view of 23° × 23° with each camera offset from the other by just under 23°, yielding an effective field of view of 90° × 23° per pointing. Each camera has at its focal plane four 2K × 2K CCDs, resulting in a pixel scale of $\sim 20''$ pixel^{-1}. The lifetime of the spacecraft is expected to be 2 years and it will survey the entire northern sky in the first year, flipping the telescope over to survey the southern sky in the second year. TESS will aim to monitor all F, K, G, and M dwarf stars with magnitude $4 < V < 12$. This amounts to approximately 500000 stars across the entire sky and the team behind TESS hope to find $\sim$300 earth-like planets.

PLATO

The PLATO spacecraft will attempt to find transiting exoplanets around relatively bright stars which makes the confirmations using follow-up RV measurements much easier. This is in contrast to the CoRoT and Kepler missions, which targeted stars beyond the capabilities of most RV ground based telescopes. PLATO will consist of 32 normal cameras operating at a cadence of 25 s, and 2 fast cameras operating at a cadence of 2.5 s. The normal cameras will target stars with $V > 8$ and the fast cameras will target stars with $4 < V < 8$. The normal cameras are arranged into 4 groups of 8 cameras, with each camera in the group having the same field of view of $\sim$1100 square degrees. Each group is offset from the other by 9.2° resulting in a total field of view of about 2250 square degrees for the entire spacecraft. Each camera also has its own focal plane array which consists of four 4K × 4K CCDs working in full frame mode for the normal cameras and frame-transfer mode for the fast cameras. The pixel scale for each focal plane array will be $15''$ pixel^{-1}.

Table 1.1: Summary of the transiting exoplanet surveys (Data retrieved from The Exoplanet Encyclopedia on 2014 August 1).

Survey Name	Number of telescopes	Approx. Target Magnitude	FOV (degrees^2)	Pixel Scale (arcsec pixel^{-1})	Number of Planets found
HAT[a]	12	$8 < I < 11$	64	3.7	54
WASP[b]	2	$7 < V < 12$	450	14	88
XO	1	$8 < V < 12$	49	25	5
TrES	4	$11 < V < 14$	36	11	5
Qatar	1	$8 < V < 15$	121	9.3	2
MEarth[c]	1	??	0.2	0.8	1
KELT[d]	2	$8 < V < 10$	676	23	4
CoRoT	1	$12 < R < 17$	8	2.3	26
Kepler	1	$9 < V < 16$	115	4	934[e]

NOTES

[a] This is for the combined HATNet and HATSouth network of telescopes.

[b] This is for the combined WASP-North and SuperWASP South network of telescopes.

[c] MEarth is included in the table for completeness but their strategy differs considerably to the other surveys in that targeted observations of M Dwarf stars with distances less than 33 parsec are undertaken.

[d] This is for the KELT-North and KELT-South telescopes combined.

[e] This number includes objects originally identified as **K**epler **O**bjects of **I**nterest (KOI), **K**epler **I**nput of **C**atalog (KIC) and also includes Kepler-64b which was discovered through the Planet Hunter citizen science project.

1.7 KELT-South Motivation

The KELT project initially consisted of only the KELT-North telescope. Studies by Pepper et al. (2003) suggested that the optimum telescope design to discover transiting exoplanets, with host stars in the magnitude range 8 < V < 10, was given by:

$$\gamma = \frac{KEL^2T}{4\pi F^2} \tag{1.24}$$

where γ is the total number of photons collected, K is a constant that depends on the telescope, filter and detector throughput, E is the fraction of time spent exposing the telescope on the sky, L is the size of the detector, T is the total duration of the telescope operations and F is the focal ratio of the optical system. As a direct result of this, the KELT-North telescope was constructed in 2004 to search for bright transiting exoplanets (Pepper et al. 2007).

The reason for targeting this particular magnitude range was that RV surveys typically targeted stars brighter than V = 8 and most of the other exoplanet transit surveys targeted stars with V = 10 or fainter. Figure 1.10 shows the distribution of exoplanet host star brightness and the gap between the RV and transit surveys is clearly evident. Additional

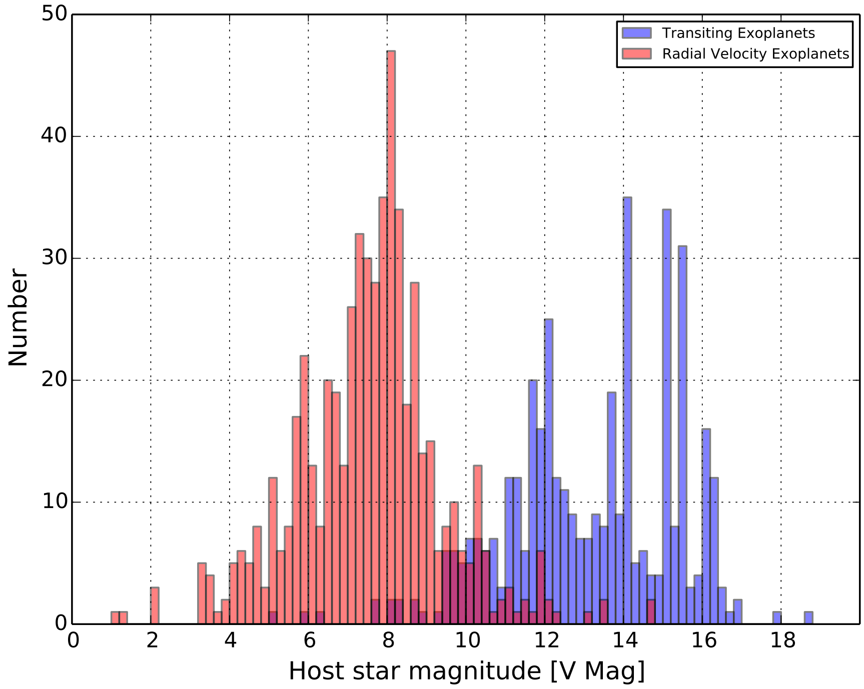

Figure 1.10: Distribution of brightness of the exoplanet host stars.

funding provided by Vanderbilt University in 2007 allowed the KELT project to build another telescope in the southern hemisphere to compliment the existing KELT-North telescope located at Irvin M. Winer Memorial Mobile Observatory near Sonoita, Arizona, which had been operating since 2004.

At the start of the planning phase of the KELT-South project in 2008, only 37 exoplanets were known to transit their host stars; of that sample only 7 had magnitude $V < 10$ and none was discovered from the southern hemisphere. KELT-South would differ slightly from KELT-North in that it would be fully robotic and autonomous (KELT-North at the time required an operator to cancel the observing operations in situations of unfavourable weather as the telescope did not have access to the status of the roof of the enclosure it was hosted in) and the observing strategy would allow it to observe slightly more of the sky (KELT-North observed a set of 13 fields evenly spaced in right ascension at a declination of $+31.7°$). KELT-South is well positioned to extend the knowledge of bright transiting exoplanets as the current number of $V < 10$ exoplanet host stars in the southern hemisphere is only 5.

The bright transiting exoplanets are arguably the most scientifically valuable. One of the brightest and best studied transiting exoplanet is HD 209458b with over 50 papers published on various properties of the exoplanet[*]. More information can be gathered from the bright transiting exoplanets due to the greater amount of flux from the host stars and follow-up observations are easier and faster to accomplish. The more information one is able to obtain from an exoplanetary system, the better one can constrain models of formation and evolution. This is the reason surveys like the **T**ransit **E**phemeris **R**efinement and **M**onitoring **S**urvey (TERMS) (Kane et al. 2009, Dragomir et al. 2012) specifically targeted known RV host stars to determine whether or not the RV planets transit their host star as well, and by combining both techniques the most accurate measurements are made possible. The combination of the transit and RV technique is able to provide constraints on more parameters than either technique alone.

The KELT-North telescope has already found 4 low-mass transiting companions to host stars with $V < 11$. KELT-1b (Siverd et al. 2012) is a 27 M_J brown dwarf and is the brightest star to host a transiting brown dwarf, KELT-2Ab (Beatty et al. 2012) is a 1.5 M_J hot Jupiter that orbits the brighter component of a binary system and is one of the 10 brightest stars known to host a transiting exoplanet, KELT-3b (Pepper et al. 2013) is a typical hot Jupiter planet and another typical hot Jupiter KELT-6b (Collins et al. 2013) orbits a star that can be considered the metal poor analogue of HD 209458b. Transiting exoplanets with similar properties offer the opportunity to compare how the properties of the host star might influence the evolution and composition of the planets. KELT-South has been collecting data since 2010 January and the data reduction on the most promising fields started in 2013 August with follow-up of the more promising candidates to follow soon thereafter (see Chapter 6 for more details).

---

[*] See http://exoplanet.eu/catalog/hd_209458_b/ for a complete list of all publications.

1.8 Thesis Outline

In Chapter 1 I introduced the concepts of exoplanets and the short history surrounding the discovery and characterization of the alien worlds. I also provided a broad overview of the current transiting exoplanet surveys to place the KELT-South project fits into context when compared to these surveys. I also highlighted some future space based transiting surveys and the discussed the kinds of results that can be expected from them in the near future.

Chapter 2 focuses on the construction and deployment of the KELT-South telescope at Sutherland, South Africa, in which I was extensively involved. I show some data we obtained from the weather monitoring software I developed to sow how well the observing site is suited to the operations of KELT-South. I also describe the hardware systems that constitute the KELT-South telescope and all the software applications that KELT-South uses on a daily basis to accomplish the goals set out in Chapter 1

In Chapter 3 I will discuss the KELT-South observational operations, the locations of the fields and the area on the sky that the telescope observes. I provide detailed descriptions of the code I developed that makes KELT-South a fully robotic and automatic telescope. The more complex observational procedures are accompanied by flowcharts to help illustrate their functions and how they accomplish the tasks required for automatic observations and exoplanet discovery.

Chapter 4 provides a detailed discussion of how well the telescope hardware has performed when compared to the specifications listed by the manufacturer of the various parts. I also include an overview of the telescope performance in terms of number of images observed since the start of the regular observing program in 2010.

In Chapter 5 I will report on the search for variable stars and transiting exoplanets from the second commissioning dataset obtained with the KELT-South telescope and show the procedure I followed to find transiting exoplanets. Although some of the candidates turned out not to be exoplanets, the demonstration that exoplanet transit-like events were identified should serve as encouragement for future searches for transiting exoplanets using the large datasets obtained in the regular observing survey mode. I will also present a catalogue of new variables stars discovered in the commissioning dataset, of which 1018 are newly identified as variable stars.

Chapter 6 will summarise the current status of the KELT-South project and discuss some of the future work needed to help the project discover its first bright transiting exoplanet. I will also discuss some of the other potential science outcomes using the KELT-South dataset and highlight some recent papers published using KELT-North datasets that show the potential for KELT-South. I will conclude with a discussion of the current status of the project and what the future has in store.

In Appendix A I will show the known transiting exoplanets that the KELT-South team have been able to independently “rediscover” during the data reduction and candidate vetting procedures of the main survey. The data reduction and identification of potential transiting exoplanet candidates in the main survey started in January 2014. This sections demonstrates that we are able to find transiting exoplanets. I also compare the published parameters to the parameters we are able to obtain by using the KELT-South lightcurves alone.

Chapter 2

KELT-South Construction, Facilities, Hardware and Software

2.1 Introduction

In the previous chapter I discussed the state of exoplanets at present and described all the transiting exoplanet survey telescopes to get an idea of where the KELT-South telescope fits into the picture and the scientific motivation for building the telescope. In this chapter I will describe the KELT-South hardware and provide an overview of the entire construction process in which I was extensively involved. I will also briefly discuss all the software packages installed on the control computer that are required for robotic and autonomous operations. Currently KELT-South is one of a few dedicated robotic telescopes in the southern hemisphere that are searching for extrasolar planets using the transit method and as far as we know is the only telescope capable of filling the magnitude gap between RV surveys for exoplanets and the current generation transiting exoplanet surveys.

The construction of the KELT-South telescope started in 2008 July, and first light images were obtained in September 2008. The telescope entered the first commissioning phase in 2008 November and ended in 2009 March. During this time the various systems were tested for stability, image quality and performance and the robotic observations were tested. At the end of this phase the optical system was taken apart and the camera was sent to Apogee Instruments for an upgrade to the cooling system. The telescope was reassembled and a second commissioning phase started in 2009 September and ended in 2010 February. Full operation of the telescope started in 2010 March, with continuous refinements to the observing procedure on a yearly basis to make the telescope as efficient as possible.

Parts of the material in this chapter has appeared in a previously published paper by J. Pepper, R. Kuhn, R. Siverd, D. James and K. Stassun as "The KELT-South Telescope" in

Publications of the Astronomical Society of the Pacific, Vol. 124, No. 913, pp. 230-241 in March 2012.

2.2 Observing Site

The KELT-South telescope is located at the South African Astronomical Observatory site (32°22′46″ S, 20°38′48″ E, Altitude 1768 m) near Sutherland, South Africa, which is also the location for the Southern African Large Telescope* (SALT) as well as numerous other optical and infrared telescopes. Sutherland is located in the western interior of South Africa about 370 km to the north-east of Cape Town on the semi-arid Karoo plateau. Sutherland is possibly the coldest place in South Africa and during the construction of the telescope, it was not uncommon for the daytime temperature to reach well below freezing. August is the middle of the winter in South Africa and generally the coldest month of the year.

KELT-South started collecting weather data from the SuperWASP weather station (see Section 2.3.1 and 3.5.2 for more details on the weather stations and the data extraction process) shortly after the initial construction of the telescope. The dataset spans the time period 2008 September 25 to 2013 August 30 with a few gaps in the dataset due to the weather station being offline or the KELT-South control computer not functioning properly (with the longest gap in data being about 2 weeks). From this dataset it was determined that wind speeds less than 45 km h^{-1} occur 97% of the time throughout the year and the median relative humidity is ∼54% (includes day and night time relative humidity levels). Table 2.1 provides an overview of the weather conditions for the Sutherland observing site. The median seeing at the site is ∼1.32″ (Catala et al. 2013). The point-spread function (PSF) of a star is dependent on the position of the star on the CCD sensor (see Section 4.8 for more details) and is characterised by a full width at half maximum (FWHM) value of between 3 and 6 pixels. The KELT-South telescope operates slightly defocused to avoid undersampling of the stars. The telescope focus is not adjusted on a nightly basis and is kept at a fixed position throughout the lifetime of the telescope. Strict photometric conditions are required for optimal photometry, but a benefit of the large pixel scale (∼23″ pixel^{-1}, see Section 4.2.2 for a detailed discussion of the plate scale) of KELT-South is that atmospheric seeing variations on the order of 5″ do not affect our ability to observe and good seeing conditions are not necessary. The Sutherland site was chosen to host the KELT-South telescope because the separation in longitude from the KELT-North telescope was not too large. During the planning phase of the project, it was envisioned that KELT-South and KELT-North could observe the same fields and provide almost 16 hours of full coverage on certain parts of the sky.

---

[*] http://www.salt.ac.za

Table 2.1: Weather conditions for the Sutherland site divided into seasons[1].

Condition	Summer 1 Dec - 28/29 Feb	Autumn 1 Mar - 31 May	Winter 1 June - 31 Aug	Spring 1 Sept - 30 Nov
Average Temperature (°C)	17.65 ± 5.72	12.60 ± 6.23	5.97 ± 4.87	11.55 ± 6.55
Average Relative Humidity (%)	49.23 ± 27.78	55.30 ± 27.22	61.41 ± 27.67	49.32 ± 28.55
Average Windspeed (km/h)	17.41 ± 9.91	17.66 ± 11.02	21.77 ± 12.68	19.84 ± 11.94
Average Day Temperature (°C)	20.21 ± 5.31	14.61 ± 6.49	7.67 ± 5.09	14.59 ± 6.29
Average Day Relative Humidity (%)	39.04 ± 24.96	47.68 ± 23.36	55.86 ± 27.84	37.61 ± 24.65
Average Day Windspeed (km/h)	18.83 ± 10.26	19.13 ± 11.11	23.03 ± 13.00	21.78 ± 12.43
Average Night Temperature (°C)	14.07 ± 4.15	10.60 ± 5.25	4.70 ± 4.27	8.53 ± 5.30
Average Night Relative Humidity (%)	63.47 ± 25.13	62.89 ± 25.90	65.35 ± 26.86	60.94 ± 28.00
Average Night Windspeed (km/h)	15.42 ± 9.02	16.21 ± 10.74	20.87 ± 12.37	17.93 ± 11.11
Good[2] Night Time (%)	66.11	64.80	59.67	63.39
Good Night Time (hours)	6.61	7.78	8.35	7.61

[1] Seasons follow the recommendations of the South African Weather Service as noted at: http://www.weathersa.co.za/web/index.php/corporate/education?id=216. Day time was defined as 06:00 to 20:00 SAST in Summer, 07:00 to 19:00 SAST in Autumn/Spring and 08:00 to 18:00 SAST in Winter. Night time was defined as 20:00 to 06:00 SAST in Summer, 19:00 to 07:00 SAST in Autumn/Spring and 18:00 to 08:00 SAST in Winter.

[2] Good weather is defined by the conditions set out in Section 3.2.

2.3 The KELT-South Observatory

KELT-South, funded by Vanderbilt University, was assembled using as many off-the-shelf components as possible to speed up the development process as well as ensure that replacing any part of the telescope would be relatively quick and easy. KELT-South consists of an optical assembly (CCD, lens, filter and hood) mounted on a robotic telescope mount. The mount is housed inside an enclosure that was specifically built for the telescope (See Figure 2.1). Inside the dome there is a climate controlled cabinet that houses the control computer and backup power sources. This control computer is responsible for controlling the robotic mount, CCD camera, observing operations, image processing and data archiving. Even though KELT-South was a copy of the KELT-North telescope, some aspects would make it significantly different. KELT-South was planned to be fully robotic and as such required the creation of new operational code. Using existing code from the KELT-North telescope was not an option as KELT-North was (and still is) housed in a building it shares with other telescopes and does not have the ability to open or close the roof by itself. At the time of the KELT-South construction the KELT-North telescope relied on an operator to open the roof, start the observing operations and shut down the telescope at the end of the run or when bad weather interrupted observing. Constructing and deploying a telescope like KELT-South involves a great number of steps and I was privileged enough to be part of all them. I now have a much better understanding of the process involved in building and operating a telescope. I lived and worked on the Sutherland observing site from 2008 July to 2009 February during the initial construction and deployment, playing a major part in testing and setting up various parts of the equipment and writing the software to make the telescope fully robotic. Many follow-up visits to the telescope throughout the following years of operation were required to either perform regular maintenance, upgrade pieces of equipment, fix broken parts (caused by lightning strikes) or make changes to observing procedures. Below is a short summary, presented in roughly chronological order, of the steps that I have been involved with. The list contains many various tasks, ranging from seemingly minor tasks to major undertakings. I have not attempted to group the tasks into any specific categories, as this type of grouping is, in general, rather subjective. Instead the list is presented in its entirety and the various tasks are discussed in greater detail in later sections of this thesis. The tasks are as follows:

- Build the dome and install the roof.
- Connect the electricity and network communications.
- Install and test the roof motor for operating the roof.
- Assemble and configure the uninterruptible power supplies (UPS) and a power distribution module (PDM).
- Assemble and configure the air-conditioned cabinet that houses the control computer, UPS and PDM.

- Install the climate controlled cabinet and connect to electricity supply.
- Program the climate controlled cabinet to keep the inside temperature at 20°C.
- Install UPS and PDM in cabinet.
- Install control computer in cabinet.
- Connect control computer to local network and check connections.
- Install steel pier and telescope mount base plate.
- Install telescope mount.
- Install telescope camera and lens.
- Attach counterweights to balance the telescope and reduce stresses on the mount motors when moving.
- Connect all devices to control computer.
- Perform focussing of the camera.
- Set-up the mount software to operate the telescope in the southern hemisphere.
- Align the telescope to the south celestial pole.
- Create pointing model for telescope.
- Install dome programmable logic controller (PLC).
- Interface control computer with PLC.
- Create scripts that will control roof operations, dome lights and flat field lights via PLC.
- Create scripts to obtain weather information from various weather stations on the observing plateau.
- Integrate weather information into observing code.
- Create shutdown procedure in UPS software in case of power failure.
- Install flat field screen on the underside of the dome roof.
- Create, install and tweak scripts that perform observing operations.
- Install and configure the internal security camera (accessible from the internet).
- Create website to monitor all aspects of the telescope[*].
- Refine pointing model and polar alignment.

---

[*] http://keltsouth.saao.ac.za

- Fully test the scripted operation and begin supervised observations in full robotic mode.

Many of the steps above were performed more than once. As systems changed and components were upgraded, the process of making the telescope efficient and reliable required many tasks to be revisited and refined. These refinements and upgrades are a continuous process and the maintenance of the telescope hardware is required to keep the telescope as efficient as possible. Detailed descriptions of all the hardware parts that make up the KELT-South telescope are presented in the following sections.

2.3.1 The Enclosure and PLC

Figure 2.1: A collection of images taken during construction of the enclosure and the installation of the roof as well as the final completed building.

The KELT-South telescope is located in a custom-built building to protect it from the elements as well as hold the various system components. Construction of the foundation and walls, done by a local contractor in Sutherland, started in 2008 July and was completed at the end of 2008 August. The building is a brick construction with a steel roll-off roof. The roof and rollers on which the roof runs were constructed in Wellington, South Africa and shipped in parts to Sutherland where they were reassembled. The installation of the roof took place over a week period that was continually disrupted by high winds preventing the lifting of the roof. Parts of the roof rail system were installed during a snowstorm. Figure

2.1 shows a collection of images taken during the construction of the enclosure and the final completed building with the telescope inside. The building is large enough for the telescope to move about freely without ever being able to slew into the walls and cause damage. The separation between the top of the telescope and the bottom of the roof is also large enough to allow the roof to close regardless of the the telescope orientation. Metal wall vents on either side of the building and an extractor fan system allow air to flow through the building and keep components inside at a reasonable temperature. The extractor fan only activates if the temperature inside the dome reaches 40°C or above. Before the fan system was installed the day time temperatures inside the enclosure could reach as high as 45°C, but with the fan installed temperatures vary between -5°C during winter and 35°C at the height of summer. The roll-off roof is moved by a regular DC motor and takes just 10 seconds to move from fully closed to fully open. Initially the roof rail system consisted of hardened plastic teeth that would mesh with a gear attached to the motor allowing the roof to be moved. In the winter of 2009, these plastic teeth broke due to the extremely cold temperatures and prevented the roof from being able to open. Steel teeth replacement rails were constructed by the support staff in Sutherland and installed to prevent a similar failure in future and this new system has performed without any incident since installation. The inside of the roof is covered by a sponge like material that absorbs moisture and prevents condensation from forming droplets of water that might fall onto the telescope. The building is north-south aligned with the roof opening towards the north of the telescope. This prevents the telescope from viewing targets above a declination +20° and below a declination -80°, as either the roof or the frame of the building above the door (on the southern side of the telescope) is in the way. Due to the telescope being slightly taller than the walls on either side of the building, the limit in right ascension is ∼5° above the horizon.

The flat field screen is bolted to the underside of the roll-off roof and interior lights can be turned on remotely to check on the condition of the telescope via an IP camera attached to the inside of the building. The IP camera takes an image of the telescope once every 5 minutes and the control computer then uploads that image to the KELT-South website. This allows us to keep an eye on the telescope during idle times and make sure that it is still functioning correctly. An external rain sensor is attached to the building and serves as an extra safety feature. This rain sensor is connected directly to the programmable logic controller (PLC) and will close the roof in the case of rain being detected. In normal operation the control computer monitors the weather via feeds provided by the SALT weather station[*], SuperWASP[†] weather station[‡], GFZ[§] weather station[¶] and Las Cumbres Observatory Global Telescope Network[‖] (LCOGT) weather stations[**] (LCOGT have three weather stations bundled together on the same mast and information is collected from the first avail-

---

[*] http://http://www.salt.ac.za/html/weather.php

[†] http://www.superwasp.org/waspsouth.htm

[‡] http://wasp.astro.keele.uk/live/

[§] http://www.gfz-potsdam.de/

[¶] The GFZ weather page can only be accessed from the local network in Sutherland

[‖] http://lcogt.net/

[**] http://lcogt.net/weather/cpt/

able station) to ensure that there is no danger of rain. Initially weather information was only collected from SALT and SuperWASP, with the GFZ weather station being added in 2011 and the LCOGT weather station added in 2013. Should the information collected by the control computer be wrong or the control computer not respond fast enough to oncoming bad weather, the rain sensor will trigger and close the roof to prevent damage. This action cannot be stopped and the roof can only be opened once the “rain detected” flag is acknowledged and reset by the control computer. The rain sensor is located on the side of the building that faces west as this is the direction from which storms typically approach the Sutherland observing site. The PLC and control computer are connected via an RS-232 (serial) cable and instruction can be sent to the PLC (in hexadecimal bytes) to perform various functions. The PLC can for example turn on the flat field lights when required to illuminate the flat field screen attached to the underside of the roof directly above the telescope mount. Together the control computer and the PLC are responsible for the roof, interior lights and flat field illumination lights. The PLC has two modes that it can operate in, one called the “remote” mode which allows the control computer to give it instructions and the other is called the “local” mode which allows a local person inside the dome to take control and open/close the roof and turn on/off various lights by buttons provided on the front face of the PLC. The PLC is connected to the mains power supply as well as an uninterruptible power supply (UPS). In the event of power failure on the main power supply that is not restored within 20 minutes, the PLC will instruct the roof to close (the roof motor is connected to the UPS, so even during a mains power failure it is still able to close the roof). This action cannot be stopped and the roof can only be opened once the “power failure” flag is acknowledged and reset by the control computer. The PLC has a hard coded trigger that will close the roof of the building and switch off any lights when no commands have been received from the control computer in a set amount of time. This is known as the “watchdog” and is currently set to 900 seconds. If this event should happen, the “watchdog triggered” flag needs to be reset before normal operations can be continued. This ensures that the enclosure is closed and set to an off state in the event that the control computer fails or crashes during an observing run when the roof is open.

2.3.2 Telescope Pier and Mount

The pier is a custom designed steel barrel construction with a steel baseplate attached to four large bolts that are embedded in the concrete floor (see the top two images in Figure 2.2). The baseplate is adjustable using four nuts on the underside and allows the steel barrel to be levelled by either tightening or loosening the bolts on the four corners of the baseplate. A steel rod running through the middle of the steel barrel is used to attach the mount base to the top of the barrel. The mount is a Paramount ME Robotic Telescope mount manufactured by Software Bisque in Colorado, USA. The Paramount ME is a research-grade German Equatorial Mount design capable of supporting a payload of up to 70 kg. The optical system, as it is configured at the moment, weighs just over 15 kg. The Paramount ME has integrated telescope and camera control but the camera control feature

Figure 2.2: A collection of images taken during assembly of the pier, mount and optical components.

is not used in the KELT-South configuration. The KELT-North telescope initially used the integrated telescope and camera control features, but after a few months it was found that the cables (that run on the inside of the mount) had become damaged by the gears of the mount as a consequence of the constant slewing. We decided to remove the cables and prevent the problem from occurring on the KELT-South telescope. This involved opening the entire mount and removing the cables. The camera is controlled through a USB cable connected to the control computer directly. The periodic tracking error of the mount before correction is ±5″ as stated by the manufacturer. This is much smaller than the large pixels of the CCD and does not affect our observations. The mount has 2 predefined points that are used extensively during observing operations. The first is called the "home" position and is defined by the manufacturer. This position is a mechanically fixed position near an hour angle of two and a declination of zero. When the telescope is homed, the built-in circuitry on the axes of the mount knows the orientation of the mount and prevents the mount from slewing into the pier. The second position is called the "park" position and can be set by the user. For the KELT-South telescope the park position was chosen to be on the east of the pier facing north and slightly downward. This ensures that during idle periods the lens and filter are oriented such that dust accumulation is minimised. As a consequence of the way the camera and lens are attached to the mount, the telescope needs to perform a meridian flip when taking images on either side of the meridian. This means that images taken east of the meridian are rotated by 180° when compared to images of the same field taken west of the meridian (a more detailed explanation of how the meridian flip is dealt with can be found in Section 5.2.2). The Paramount ME has performed extremely reliably since the construction of the telescope, with only greasing of the gears required roughly every 12 months. On a maintenance trip to the telescope in 2013 May, it was found that the mount was not slewing at the same rate in both directions, but a good cleaning, regrease and rebalance solved the problem.

2.3.3 Camera and Cooling System

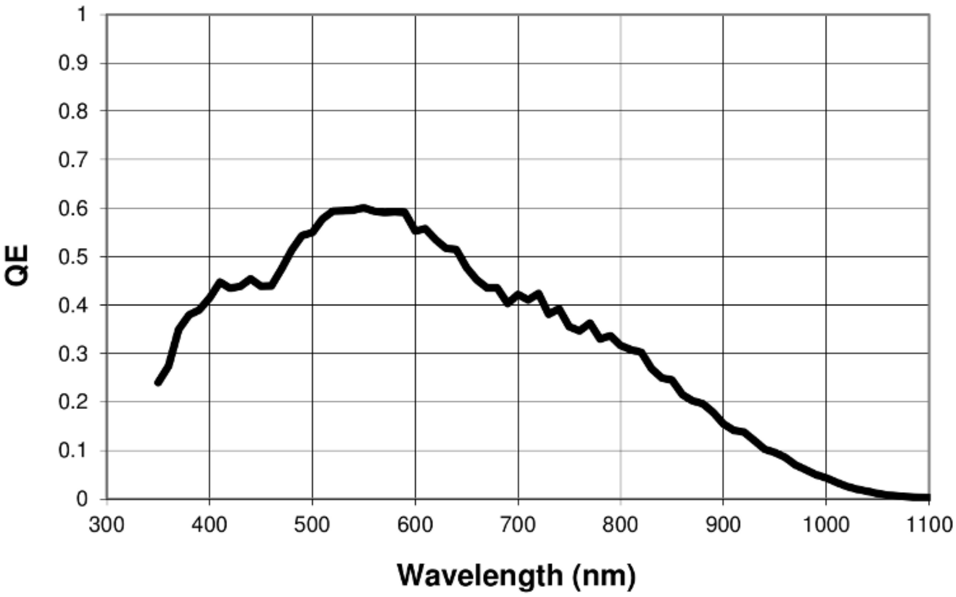

Figure 2.3: The theoretical response function of the CCD as provided by Kodak.

The KELT-South detector is an Apogee Instruments AltaU16 thermoelectrically cooled CCD camera. The camera uses the Kodak KAF-16803 front illuminated CCD with 4096 × 4096 9 μm pixels (36.88 × 36.88 mm detector area) and has a peak quantum efficiency of ∼60% at 550 nm[*] (See Figure 2.3). The interface between the AltaU16 and the computer is a standard USB 2.0 cable that has a maximum length of 5 m. For the purpose of KELT-South the CCD, which has a programmable, intelligent cooled housing (D09F type housing), is maintained at -20°C to reduce random thermal noise. During the first commissioning phase it was found that the two-stage thermoelectric Peltier cooling system was not able to maintain a stable temperature of -20°C throughout the daytime (temperatures inside the dome enclosure reached 35°C on a regular basis during the summer), and required many hours to cool to the observing temperature at night delaying observing. At the end of the first commissioning phase the camera was removed from the mount and shipped back to

---

[*] http://www.truesenseimaging.com/products/full-frame-ccd/61-KAF-16803

Apogee Instruments to upgrade the cooling system. The new upgraded air forced three-stage thermoelectric Peltier cooling system, that is capable of maintaining a temperature of 65 – 70°C below ambient temperature, was installed in 2009 June and in testing performed much better than the previous system at maintaining the low temperatures required for observation. The new three-stage cooling system was able to maintain -20°C with only a 20% load reported on the cooling system software. The cooling system typically reaches the operating temperature from ambient temperature (after power failures for example) in ∼30 minutes, with an additional 10 minutes required for temperature stabilisation.

The device is read out at 16 bit resolution at 1 MHz, giving a full-frame readout time of ∼30 s. The typical system noise for the CCD is given by the manufacturer as $\sim 9\ e^{-}$ at 1 MHz readout speed. In laboratory testing the nominal dark current was < 1.4 e^{-} pixel^{-1} s^{-1} at a temperature of -20°C and the CCD has temperature stability of ±0.1°C. The CCD operates at a conversion gain of $1.4\ e^{-}$ ADU^{-1}. The CCD specifications list the full-well depth as ∼100000 e^{-}, but the analogue-to-digital converter (ADC) saturates at 65535 ADU ($\sim 92000\ e^{-}$). The linear dynamic range, which is a measure of how much signal can be collected above the read noise and is usually represented as a decibel scale, is listed as 80 dB. The photoresponse non-linearity and non-uniformity are given as 1% (See Chapter 4 for a detailed discussion on the telescope performance, which includes a verification of the CCD specifications listed by the manufacturer). The CCD also has anti-blooming protection. The anti-blooming gate acts as a charge drain that is designed to drain off excess charge from a saturated pixel and prevent the charge from flowing into neighbouring pixels. While this has the advantage of reducing the area affected by overexposed pixels, the anti-blooming structure can consume up to 30% of the pixel area which leads to a reduction in the *fill factor* of the CCD sensor (Des Jardin & Kosman 1999). This reduction in fill factor in turn leads to an overall reduction in the quantum efficiency of the sensor. To compensate for the reduced quantum efficiency, the KAF16803 CCD sensor combines the transparent gate technology developed by Kodak (Des Jardin & Kosman 1999) and the microlens technology used on most interline CCD sensors (Ciccarelli et al. 2002). The transparent gate technology replaces one of the two polysilicon gate electrodes with a more transmissive indium-tin-oxide (ITO) gate and the microlens technology adds tiny lenses to each pixel that direct light preferentially toward the ITO gate. The shutter on the camera became stuck in 2013 April which halted the observing operations. The stuck shutter meant that the CCD was always exposed to light and to prevent damage to the CCD the entire system was shut down. A replacement part was sent from Apogee Instruments along with instruction on how to open the camera housing and replace the broken part. Replacement of the shutter took place in 2013 May.

2.3.4 Lens and Filter

KELT-South is equipped with a Mamiya 645 80 mm f/1.9 medium-format manual focus lens with a 42 mm aperture. At the time the KELT-South telescope was in the planning phase, the manufacturer of the Mamiya lens did not produce that particular model any more. We were able to purchase a lens from a vendor via the online auction site Ebay.

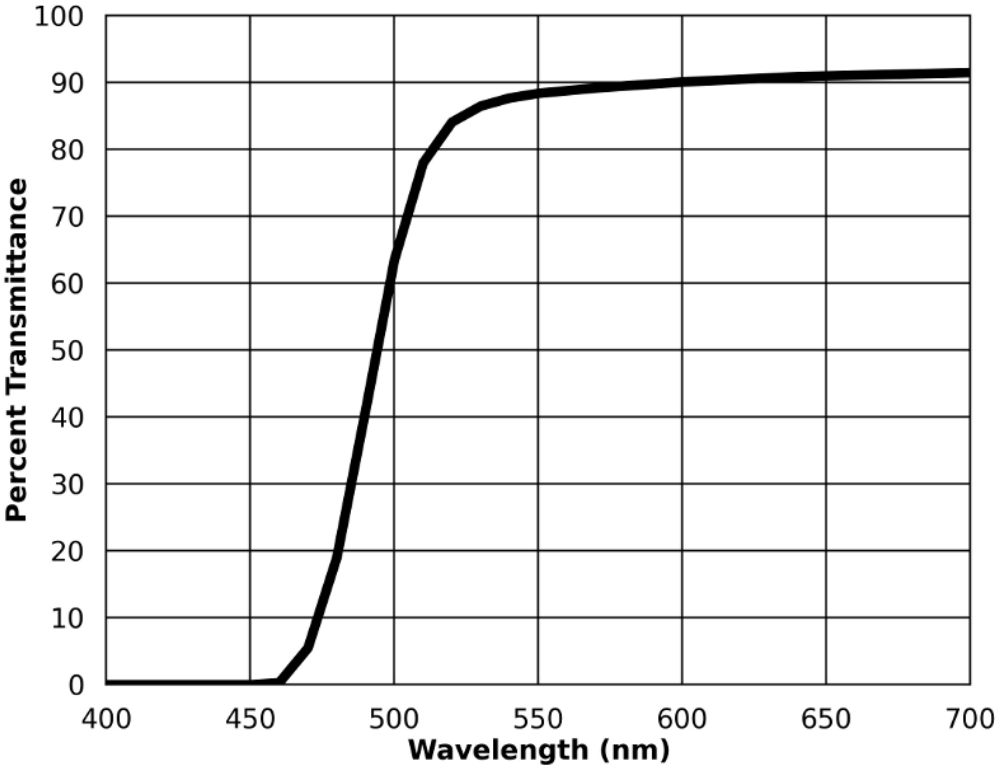

Figure 2.4: The theoretical transmission curve of the Kodak Wratten No. 8 Filter. Data used to produce the plot was taken from Lide (1994).

The lens and camera are attached together using a custom built metal bracket. In initial testing at Vanderbilt University in Nashville (before the telescope was shipped to South Africa), it was found that the cooling system was unable to keep the temperature of the CCD stable enough for astronomical observing purposes. The CCD unit was returned to Apogee Instruments and upgrades to the cooling system were performed. The metal housing of the CCD cooling unit was consequently changed slightly and the metal bracket holding the lens and CCD together had to be retooled for it to fit correctly. The entire camera unit was then shipped to South Africa, before being tested again. On the first attempt to focus the lens in Sutherland, it was found that the distance between the lens and the CCD was too short. It became clear that the retooling that had been done to the metal bracket removed too much metal and shortened the spacing between the lens and CCD. A quick search on the internet revealed that the flange focal distance (the distance between the last lens element and the CCD chip plane) for the Mamiya 645 lens should be 63.3 mm. The measured distance between the lens and CCD was ∼60 mm. A new metal spacer (manufactured by the machine shop dedicated to making parts for SALT in Sutherland) was inserted to provide the extra few mm required to focus the telescope. There are no other glass elements between the last lens element and the CCD chip (like chamber window or CCD window) that can affect the flange focal distance calculations.

The entire field of view of the detector using this lens is 26° × 26° and provides roughly $\sim 23''$ pixel^{-1} image scale. This allows us to monitor around 60000 stars in typical high Galactic latitudes, increasing to around 150000 when observing close to the Galactic plane. We avoid the extremely crowded areas of the Galactic plane, as the pixel scale makes it extremely difficult to get reliable positional information for individual stars (see Section 3 for a detailed discussion on the observing procedure). The medium-format image size is much larger than the CCD detector which reduces the severity of vignetting that is typical for large field of view observations like ours (see 4.3.6 for more details). To reduce the amount of scattered blue light from the atmosphere, the KELT-South telescope uses a Kodak Wratten No. 8 red-pass filter with a 50% transmission point at ∼490 nm (See Figure 2.4). A rubber lens hood attached to the front of the lens prevents stray light from entering the system and causing unwanted flares. The filter is mounted between the Mamiya lens and the rubber lens hood.

2.3.5 Control Computer and Climate Controlled Cabinet

The computer that controls all aspects of the telescope operation is a Dell Optiplex 755 small-form-factor running the Windows XP operating system. Regular upgrades to the operating system and the software packages were disabled as there was no need for changing a working system. Software packages (TheSky 6 Professional [version 6.0.0.60], CCDSoft [version 5.00.188] with the integrated TPoint telescope pointing model software) provided by Software Bisque*, enable the control computer to operate the CCD and mount via a script-accessible interface. Two external hard drives are connected to the control computer via USB cables and are used to backup the data obtained during a normal observing run. An identical computer was purchased and acts as a backup to the original machine in the case of a hardware failure. The backup machine is located in a different building and all changes to the observing parameters are first tested on this machine and verified to work correctly before making changes to the regular control computer. The software provided by Software Bisque allows for a mode called “simulation” where even though the computer is not attached to the mount or camera, all the functions of these devices are simulated. In the case of an unresponsive control computer, the IT support staff in Sutherland are notified and the computer is restarted or the appropriate action taken. The control computer is housed in a Rittal Top Therm Plus Cooling Unit cabinet (type 8845.500) that also contains the UPS (originally this unit also contained the transformer). The cabinet has been set up to keep the inside of the cabinet at around 20°C to ensure that the computer does not fail due to excessively high temperatures. A large duct attached to the front of the cabinet allows the hot air to be exhausted outside of the building through one of the air vents, preventing a build up of hot air inside the dome during the day time and also ensuring that hot turbulent air does not affect the seeing conditions during observations at night.

---

[*] Information available on the Software Bisque website at: htt://www.bisque.com

2.3.6 Temperature Probes

Two temperature probes record the temperatures inside and outside the computer cabinet. These probes are connected to the control computer through a USB interface and software on the computer simply logs the temperatures at one minute intervals. The probes were manufactured by Quality Thermistor Inc[*] (Qti) and provide absolute accuracy of up to ±0.1°C. At present the temperatures are simply recorded and no actions are taken if the temperatures are outside the control limits. In future the control computer will alert the technical staff in Sutherland if this situation should happen. The data from the temperature probes are displayed on the KELT-South webpage and in the five years of operation the temperatures inside the climate controlled cabinet have not been outside of the operating temperatures we set at the start of the telescope construction.

2.3.7 UPS and Transformer

The KELT-South telescope initially operated with two uninterruptible power supplies (UPS) and a power distribution module (PDM). The first UPS was an Eaton Powerware 9125 UPS with an Eaton PowerPass Distribution Module attached. Together these two systems were responsible for providing surge protection to the telescope as well as stepping down the power from 220V (South African standard) to 110V (American standard). Both these pieces of equipment were also inside the climate controlled cabinet. The 110V output power was required to operate the mount, camera and control computer (all these components were bought in the USA). The second UPS was an Eaton Powerware 9120 UPS that provided backup power to the enclosure only. The roof motor, interior lights (including flat field lights) and internal IP camera were connected to this UPS. A lightning strike close to the KELT-South dome in early 2011 caused the UPS and transformer that supplied power to the telescope to fail. The wiring for the mount, CCD and control computer was changed to allow all the telescope systems to use the 220V UPS as the main power supply. The Eaton Powerware 9120 UPS is now connected to the control computer via a USB cable and software on the computer monitors all aspects of the UPS. If a power failure should occur, the UPS will communicate that to the control computer and a script will activate that shuts down the telescope in a controlled manner to ensure minimal damage to the CCD and mount. If power is not restored to the UPS in a timely manner, the control computer will also shut down, and can only be powered up by a member of the support staff in Sutherland. Fortunately this situation has never occurred as the Sutherland site has its own diesel backup generator to provide power in case of an extended power outage.

2.4 KELT-South Software

There are a large number of software packages installed on the control computer that perform various tasks during regular operations of the telescope. Many packages were built from the

---

[*] http://www.thermistor.com/productsDirecTemp.html

source code using the compilers provided in the CYGWIN environment while others were installed using the downloadable packages from the internet (links to the locations of the packages is provided below). Compiling packages from the source code ensures that the programs are optimized for the specific hardware architecture of the control computer. Below is a short description of each package and how it is used in the KELT-South operations.

2.4.1 Fling File Transport

The FLING FILE TRANSPORT program is set up to monitor a specific folder on the hard drive of the control computer and upload any files to the SAAO webserver that are copied into this folder. During normal operations of the telescope a lot of information is collected on a scheduled basis and to monitor all aspects of the telescope more easily, a monitoring website was created that can be accessed from any internet enabled device. All files required to display the information on the KELT-South monitoring website are copied into the "watched" folder and uploaded. FLING FILE TRANSPORT makes the process of uploading files much easier and once it has been set up with the username and password for the webserver, the updating of the website is completely automatic. If the network connection form Sutherland to Cape Town is offline, the program will simply store the files and upload them when the connection is established again.

2.4.2 WCSTools

Parts of the WCSTOOLS[*] (Mink 1999) software package are used during the image analysis process of the telescope operation. The image manipulation utility GETFITS is used to extract cut out sections of the original FITS images. Some basic statistical quantities of the cutout is determined and based on the values obtained, the original FITS image is either classified as a good or bad image (a more detailed explanation of the image processing can be found in Section 3.6). GETFITS is extremely fast and memory efficient when performing tasks and the newly created FITS image retains the header information from the original image file.

2.4.3 Fpack

FPACK[†] is a program that KELT-South uses to compress the raw FITS images obtained during observations. The program is run during the data archiving part of the telescope operations and is called by a VBSCRIPT program to perform the compression. FPACK uses the tiled image compression convention[‡] to store the compressed images. FPACK is generally faster than similar programs like gzip and offers better compression levels. FPACK also keeps the FITS file header intact when compressing, making it possible to extract information from the file without having to uncompress the entire file. It is also possible to use other FITS

---

[*] http://tdc-www.harvard.edu/wcstools/index.html

[†] http://heasarc.nasa.gov/fitsio/fpack/

[‡] http://fits.gsfc.nasa.gov/registry/tilecompression.html

software utilities to manipulate the compressed file as it is still stored as a valid FITS image. A variety of compression algorithms are implemented with the program. The Rice compression algorithm is used by KELT-South as it was found to be the best algorithm for speed and compression levels of the KELT-South images.

2.4.4 ImageMagick

IMAGEMAGICK[*] is an extremely powerful and versatile software suite that enables the creation, manipulation and conversion of a wide variety of image files. In the KELT-South operations, the program is used during the image analysis process to convert images from the raw FITS format into JPEG format that can be displayed on the KELT-South monitoring website. The specific images that are converted are identified by the VBScript that performs the image analysis and the IMAGEMAGICK program used to annotate the images with the name of the file and the number of the image. With the date and file number the image has a unique identifier that is later used to make a visual inspection and determine the quality of the images for that particular night.

2.4.5 GNUPlot

GNUPLOT[†] is used extensively in the KELT-South operations by providing a scripted interface that allows the plotting of data files very easily. The weather script relies on GNUPLOT to produce graphs of the temperature and other weather conditions on site in Sutherland. These graphs are then uploaded to the KELT-South monitoring website where it allows the KELT-South team to keep an eye on all telescope activities and any problems with the telescope can be addressed in a timely manner.

2.4.6 Cygwin

CYGWIN[‡] is a collection of tools that give the Windows XP operating system similar functionality to a Linux based operating system. CYGWIN is used primarily to copy the data on the local hard drive of the control computer to the two external hard drives using an rsync command. It is also used to copy the data from the constrol computer in Sutherland to the data reduction computer at Vanderbilt University. CYGWIN was also used to build various applications from source code to ensure that they would work in the Windows environment. Most of these applications are used in the image analysis procedure and include part of the CFITSIO[§] library that is capable of manipulating FITS files.

---

[*] http://www.imagemagick.org/script/index.php

[†] http://www.gnuplot.info/

[‡] http://www.cygwin.com/

[§] http://heasarc.gsfc.nasa.gov/fitsio/

2.4.7 DirecTemp

DirecTemp is an application written and distributed by Quality Thermistor Inc (Qti) as part of the USB temperature probe hardware package. The software is set up to request the temperature measurements of the USB probes every minute and the information is recorded in a file that can be accessed by various VB Scripts. The temperature probes are used to ensure that the telescope is not exposed to temperatures outside of the operating range as suggested by the manufacturer of the various components.

2.4.8 Dimension4

The computer clock is synchronised using the free software package Dimension 4[*] to keep the clock time accurate. The system clock is synchronised once every 10 minutes and the average error/drift recorded by the Dimension 4 utility is ∼2 ms, which indicates that even if the internet connection should fail, the system clock is accurate enough to continue with observations. Timing accuracy of ∼1 s is well within the limits for normal KELT-South observations.

2.4.9 SnapShot Utility

The SnapShot Utility is part of the software package provided by ACTi[†] with the IP camera. The program is set up to connect to the IP camera over the local area network and request that an image be taken every five minutes. The image is then saved in the folder monitored by Fling File Transport for upload to the KELT-South monitoring website. The IP camera is pointed at the telescope and during the daytime the image is used to see if the telescope is correctly parked or not.

2.4.10 LANSafe

LanSafe is part of the power protection software suite that provides UPS monitoring, control and preventive measures against power failures. The control computer is connected to an Eaton Powerware 9120 UPS via a USB cable and the Lansafe software is responsible for the monitoring of all aspects of the UPS functionality. The program was set up to shut down the computer using a script if the regular mains power is unavailable for an extended period of time. This controlled shut down is done by first halting all observing programs if present, closing the enclosure roof if open, parking the telescope and turning off the temperature regulation of the CCD camera to gradually increase the CCD temperature over a long period of time. This prevents sudden changes in temperature that might damage the camera. The safe shut down procedure also prevents data corruption on the local computer.

---

[*] http://www.thinkman.com/dimension4/

[†] http://www.acti.com/home/index.asp

2.4.11 CCDSoft

CCDSoft[*] is a Windows based CCD camera control application that provides a powerful object model for scripting. Custom written Visual Basic scripts can be used to control the CCD camera and integration with TheSky6 allows the FITS images obtained with CCDSoft to contain information about the pointing position of the KELT-South mount in the headers. All aspects of the KELT-South CCD are controlled by scripts written in Visual Basic to facilitate the autonomous and robotic nature of the telescope.

2.4.12 TheSKY6

TheSky6[†] provides the interface between the control computer and the Paramount ME, allowing the mount to be controlled by VB scripts that interact with TheSky6. Exposure of the program functionality via the Component Object Model, allows scripted operation and greatly facilitates the automation and robotic operation of KELT-South. All aspects of the Paramount ME can be controlled by scripts and information about the state of the mount can also be returned.

2.4.13 TPoint

The version of Tpoint[‡] employed by KELT-South is an add-on feature of TheSky6 package. Tpoint is a software package that integrates with TheSky6 and provides the ability to determine the amount of pointing and tracking error for a telescope and then using mathematical formulae to compensate for the errors associated with the KELT-South telescope hardware. By logging the coordinates of the telescope control system when the telescope was pointed at known celestial coordinates, allowed the Tpoint software to learn about the geometry of system and after enough points were recorded, the TPoint software made adjustments to the algorithms used during pointing and tracking.

---

[*] http://www.bisque.com/help/ccdsoft%20info/welcome.htm

[†] http://www.bisque.com/Products/TheSky6/

[‡] http://www.bisque.com/sc/shops/store/tpoint-add-on-win.aspx

Chapter 3

KELT-South Observing and Operational Scripts

3.1 Introduction

In the previous chapter I discussed the facilities, hardware and software that make up the KELT-South telescope. In this chapter I will focus on the scripted operations that make KELT-South work in a fully autonomous manner. KELT-South was designed and built to be fully robotic and to achieve this, new observing operating code needed to be developed. Although KELT-South is an identical copy of KELT-North, the way the telescopes work is completely different. KELT-North is housed in a roll-off roof building along with a number of other telescopes and does not have access to the systems that would allow it to open and close the roof itself. At the start of the construction phase of the KELT-South telescope, KELT-North was not fully automated. The nightly observing scripts for KELT-North were created at Ohio State University using a custom written PERL program and uploaded to the KELT-North computer every afternoon, where they were used by a program called "Orchestrate" to direct the telescope to observe specific fields for that night. Orchestrate was used to interface the telescope hardware with the software on the KELT-North computer, but it had severe limitations in that it did not provide built-in control loop functionality or conditional branching. This made it impossible for the telescope to function autonomously, as it simply executed a list of instructions from top to bottom. If weather conditions were unfavourable for observing, on site personnel were required to abort the script. If weather conditions started out good and became unsuitable later, the observatory computer closed the roof, but the KELT-North telescope would still be observing and personnel needed to abort the script. The KELT-South telescope was planned to be fully robotic and as such a new method for controlling the telescope needed to be developed. The observing strategies would also differ slightly as KELT-South was designed to observe a slightly larger part of the sky than KELT-North (KELT-North observed a set of 13 fields evenly spaced in right ascension at a declination of +31.7°) and it would be allowed to prioritize certain fields above others (avoiding fields that were close to the Moon for instance). It would also need to collect weather information and make decisions on whether to close the roof without the need for on-site personnel to do it manually. KELT-South also needed some way of classifying images as good or bad and separate them before the images were used for data reduction, as it was found by the KELT-North team that this process was an extremely human intensive process.

In this chapter I will start by giving an overview of the telescope operations and the observing strategy. I will provide details of the different scripts I created over the last five years that enables KELT-South to search for exoplanets[*].

Parts of the material in this chapter have appeared in a previously published paper by J. Pepper, R. Kuhn, R. Siverd, D. James and K. Stassun as "The KELT-South Telescope" in *Publications of the Astronomical Society of the Pacific*, Vol. 124, No. 913, pp. 230-241 in March 2012.

3.2 Observing Overview

Any references to "telescope" in the following sections refers to all the components described in Chapter 2. The KELT-South telescope is completely robotic with no remote real-time observations undertaken. The telescope is controlled by various Visual Basic Script (VBS) programs that are executed by the Windows Scheduler at specific times. Observations are carried out every night with suitable weather conditions and observing operations start at 17:00 South African Standard Time (SAST) every day. The first thing the telescope does is to assess the current weather conditions and if any of the following are true, the weather is considered unsuitable for observing to take place:

- Outside temperature is less than -10°C.
- Relative humidity is over 90%.
- The difference between the outside temperature and the dew point temperature is less than 2°C (at this point condensation is likely to occur on the optical components of the telescope).
- Wind speed is over 60 km h^{-1}.
- It is raining (or snowing).
- It is cloudy.

If conditions are not good for observing, a series of dome flat field, bias and dark images are taken. The telescope then enters a standby mode, in which it checks the weather conditions every five minutes until astronomical dawn. If the weather conditions become favourable for

---

[*] The code I developed can be requested from Dr. John Menzies at SAAO in Cape Town: jwm@saao.ac.za

observing at any point during the night, the telescope will exit the standby mode and start observations.

If the weather conditions are determined to be good for observations the telescope reads a file that contains all the relevant information for observing operations to start. At sunset, the roof opens, the telescope is pointed at the zenith and a series of flat field images are taken. The roof is then closed and a series of dark and bias images are taken while the telescope waits for astronomical twilight to end whereupon the observing starts. Observations continue until astronomical dawn, at which point the roof closes and a series of dark and bias images are obtained in alternating order. This is done before sunrise to prevent light leaks in the dome from artificially boosting the dark current counts. The roof is then opened once more and another series of flat field images (called the morning flats) are taken. The roof is then closed and this ends the observing procedures for the night.

KELT-South has operated in both a commissioning mode and a survey mode. In both modes all images were taken with 150 second exposures, selected to get optimal photometric precision for stars in the target range $8 < V < 10$ (30, 60 and 90 second exposures were also tested in the commissioning mode). In the commissioning mode, the telescope observed a single preselected target field for the entire night. In the regular survey mode the telescope observes a number of fields located around the sky throughout the night and tiles between the available fields for as long as they are observable. A field will not be observed if it is within 50° (slightly less than two field widths) of the Moon. The typical cadence for a survey field is between 15 and 20 minutes, since only a few fields are visible at any given time and most fields are not visible throughout the entire night. This means that the number of images per field can vary wildly, but even at the highest possible cadence, KELT-South does not obtain enough signal over a single transit to positively identify that transit event. The data reduction and analysis process relies on phase-folding of the full lightcurves over one or more years to build up the required signal for an exoplanet transit detection. Doing observations in this manner, the major factor in finding transits is not the number of points acquired per night, but rather the total number of observations made.

KELT-South performs a rough image quality check of the images obtained the previous night to ensure that images contaminated by cloud cover are removed and stored separately from the regular images used for data reduction. Data acquired by the telescope throughout the night are stored on the hard drive of the control computer and after the image quality check has isolated the bad quality images, the data are compressed and copied to two external 200 GB USB hard drives that act as backup storage devices. Using Rice compression software (Pence et al. 2009; 2010b;a), the raw images are compressed to $\sim$40% of their original size (calibration images are compressed to $\sim$30% of their original size). Once the compression of the data is done, the telescope enters a sleep mode, effectively ending observations for the night. Data is transferred on a weekly basis to Vanderbilt University where it is verified to be complete before the local copy in Sutherland is deleted.

3.3 Locations of the Observed Fields

3.3.1 Commissioning Fields

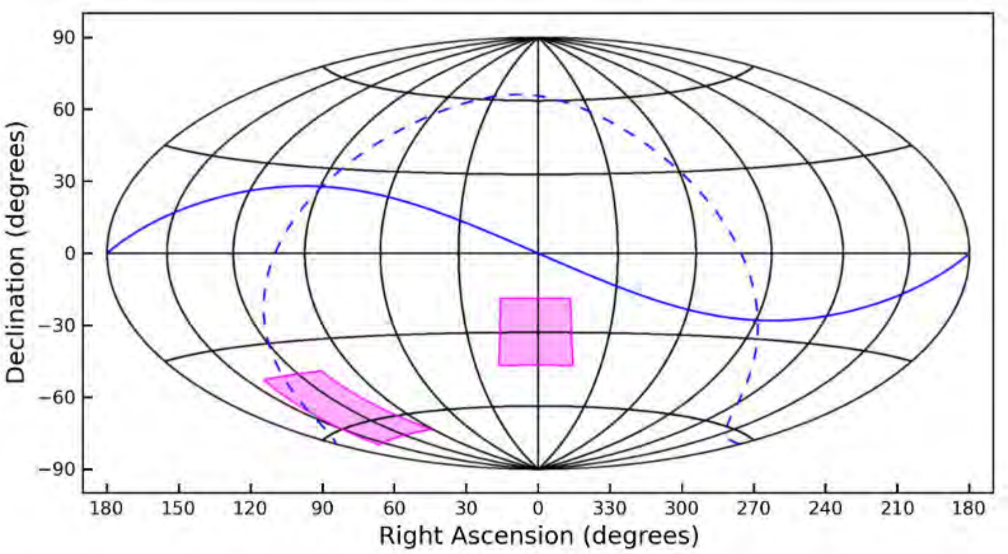

Figure 3.1: The location of the two commissioning fields. The solid blue line is the ecliptic and the dashed blue line represents the Galactic plane.

Two fields were observed right after the KELT-South deployment in 2008 to serve as commissioning data and their locations are shown in Figure 3.1. At the time of observing these two fields the telescope was not fully robotic, requiring an operator to manually open and close the roof and start the script that performed the observing operations. The scripts that would eventually perform the robotic operations were tested and refined during the first commissioning phase. At the end of this first commissioning phase the telescope was taken apart and some parts were upgraded to ensure adequate cooling of the CCD. A second commissioning phase, this time under full robotic operation, was undertaken towards the end of 2009 and the same two fields were used for another set of commissioning data. Data obtained during the first commissioning phase were of very poor quality, partly due to a poor pointing model as well as inadequate cooling of the CCD, and were discarded. The configuration of the telescope also changed considerably after the CCD cooling system upgrade, which meant that any data acquired before the upgrades could not be used in the data reduction pipeline. The pipeline is very sensitive to focus changes and the new configuration of the telescope required the optical system to be refocussed. The weight distribution of the telescope also changed after the upgrade as the new cooling system was substantially heavier than the previous system. The balance of the telescope was redone, the polar alignment was refined and a new pointing model was created before the second commissioning phase was started. The second set of commissioning data was taken with the telescope in the same configuration as the regular survey mode that is still ongoing at

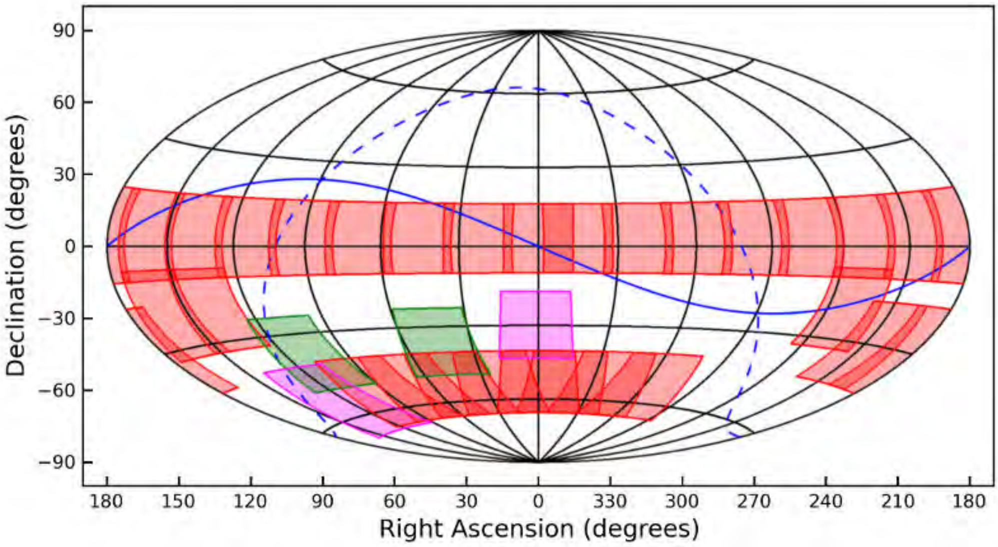

Figure 3.2: The location of the observed fields during the first year of operation. Red fields are the regular observing fields. The magenta fields are the two commissioning field that were still observed, but did not form part of the regular observing program. The green fields are the cluster fields that were added and were only observed twice per night.

present. Any reference to commissioning data in this thesis is to the second set of data obtained from 2009 September to 2010 February.

The first commissioning field was roughly centred on the open cluster Blanco 1 (J2000 $\alpha = 00^h04'07''$, $\delta = -29°50'00''$), and the campaign on that field started 2009 September 16, ended 2009 December 20, and comprises a total of 2123 good quality images from 43 separate nights of the total 95 day baseline. The second field (J2000 $\alpha = 08^h16'00''$, $\delta = -54°00'00''$) encompasses a number of open clusters, including NGC 2516, NGC 2547, and IC2391, and the campaign on that field started 2010 January 4, ended 2010 February 19, and comprises a total of 3041 images from 32 separate nights of the total 46 day baseline. The cadence for the commissioning mode observations was 3 minutes (150 second exposures and 30 second readout time). The data reduction and results of the search for variable stars and transiting exoplanets from the second commissioning field are discussed in Chapter 5.

3.3.2 Survey Fields

In the regular survey mode the telescope observes a number of fields located around the sky throughout the night. The number of fields has changed over the course of the telescope operations with constant removal and addition of fields as the observing strategy is changed and improved. Initially there were 29 fields observed. Figure 3.2 shows the locations of the original fields during the first year of operation. The northern strip of fields are centred at a declination of +3° and were included to enable KELT-South and KELT-North to observe the same parts of the sky, effectively doubling the amount of data obtained. A collaborative

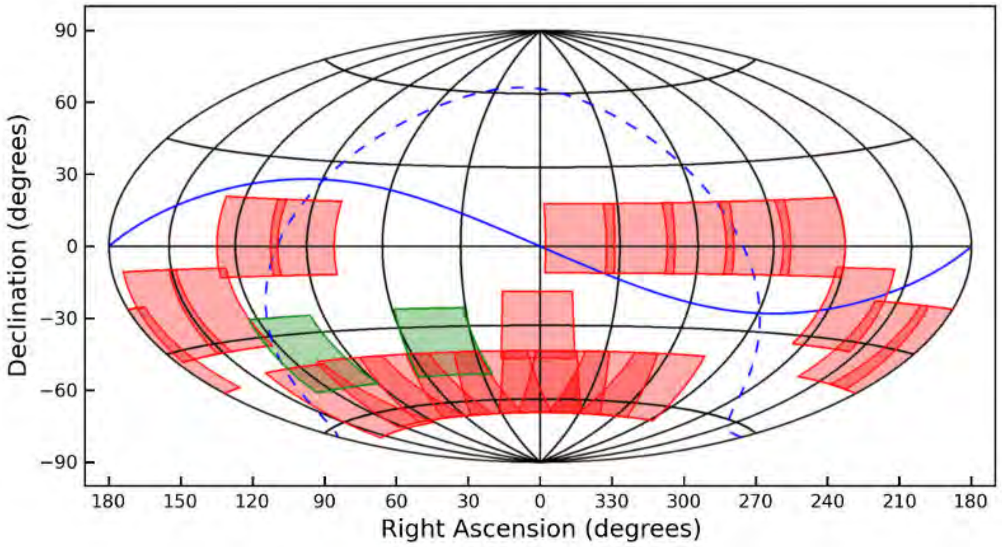

Figure 3.3: The location of the observed fields for the current observing operation of the KELT-South telescope. Note that the two commissioning field have been changed to regular observing fields.

effort between KELT-South and the **M**ulti-object **APO** **R**adial **V**elocity **E**xoplanet **L**arge-area **S**urvey (MARVELS) (Ge et al. 2008), whereby KELT-South would obtain photometric lightcurves of targets that MARVELS observed spectroscopically, was also attempted. The locations of the other fields were chosen through a combination of factors, including the desire to avoid the Galactic plane (due to concerns about crowding and the number of false positives), distance from the ecliptic (to reduce the chances of the Moon getting in the way of observing a field) and others. That process yielded a set of fields located around the mid latitudes of the southern hemisphere, covering ∼45% of the southern sky. During the first year of observations the original commissioning fields were observed only on certain occasions (for testing purposes) and did not form part of the regular survey. The two green coloured fields in Figures 3.2 and 3.3 were added in mid 2011 and were intended for use for stellar science investigations (rotational periods of members of the open clusters, long term variability, etc). Those fields are observed two or three times per night, at most, and are not expected to yield significant data for discovering exoplanets. In late 2011 the original two commissioning fields were added to the observing list to form part of the regular survey campaign.

After every year of observations, the number of images obtained per field is determined and adjustments are made to maximise the observing strategy in order to obtain enough data over the following years to facilitate the discovery of transiting exoplanets in a reasonable time frame. The removal or addition of fields has a very large impact on the current set of fields. Where fields with similar right ascensions will experience more “competition” from newly added fields with similar right ascensions, the removal of fields leads to less competition for observing time and those fields will be observed more often. It thus becomes vitally important to know the exact impact the new field locations will have on the observing strategy. The current set of fields observed by KELT-South (as of June 2013) is shown in Figure 3.3 and the field centres are listed in Table 3.1.

Table 3.1: Table of the locations of the current KELT-South observing fields (as of June 2013).

Field Number	Field type	Right ascension (degrees)	Declination (degrees)
0	Commissioning and Survey	1.05	-30.00
5	Survey	91.95	+3.00
6	Survey	115.05	+3.00
12	Survey	253.05	+3.00
13	Survey	276.00	+3.00
14	Survey	298.95	+3.00
17	Survey	1.05	-53.00
18	Survey	22.95	-53.00
19	Survey	46.05	-53.00
20	Survey	69.00	-53.00
21	Survey	91.95	-53.00
22	Survey	138.00	-20.00
23	Survey	160.95	-20.00
24	Survey	184.05	-30.00
25	Survey	207.00	-30.00
26	Survey	229.95	-20.00
27	Survey	298.95	-53.00
28	Survey	322.05	-53.00
29	Survey	345.00	-53.00
30	Stellar Science	45.00	-36.00
31	Stellar Science	109.95	-37.00
99	Commissioning and Survey	124.00	-54.00

3.4 The Observing Simulator

Toward the end of the first year of regular observing, we needed to know what the impact on the observing strategy would be when we decided to rearrange, drop, or add fields to the observing program. For this purpose I developed a program called “The Observing Simulator”. This VBS program simulated the observing procedure of the KELT-South telescope and produced a large number of outputs that could be used to determine the efficiency. Some assumptions had to be made about the amount of time it takes to slew from one target to another as this is highly dependent on the locations of the particular targets. I used the data from the previous year (2010) of observing and determined average times for slews between targets on the same side of the meridian and I also determined the average time for slews between targets on opposite sides of the meridian. The start and end dates could be specified and the program would read the field locations from an input file. The program would output the number of times a particular field would be observed in the given time frame and also report on any dead time the telescope experienced due to no fields being available to observe (sparse RA coverage in the field location selection, Moon contamination, etc). The program did not simulate bad weather conditions and I simply applied a 30% cut on the number of images to account for the average bad weather conditions in Sutherland throughout a regular year. To test how realistic the 30% cut due to bad weather was, I compared the simulated data with the true data obtained in 2010 and concluded that the same number of images were obtained in both.

A full year of observing could be simulated in about 30 minutes on a standard desktop computer. I ran hundreds of simulations, with multiple field location configurations and this program proved a very useful tool in the planning of the observing strategy for KELT-South. Before any new fields were added or taken away in the subsequent years of operation, the simulation tool was used to gauge the impact. It is as a direct result of this simulator that the northern strip of fields are now observed at a higher priority than the southern fields. I realised that due to their close proximity to the ecliptic, the northern fields were far more likely to be Moon contaminated and not observed as often as a southern field with the same right ascension. So to get as many data points as possible on these fields, when they were available, the strategy was adjusted to image them twice, once before the southern fields and once after the southern fields before the telescope would perform a meridian flip. The number of observations per field is a crucial quantity in the KELT-South operations, as experiences with the KELT-North data reduction and candidate identification procedure indicated that a minimum of ∼3000 data points were required to reliably identify transits in the lightcurves of the target stars. The number of images obtained each year of the telescope operations is listed in Table 4.2 and the effect of removing some fields can clearly be seen on the number of images obtained for the rest of the fields when moving from year to year. At present the southern strip of fields are observed ∼1000 times per year, depending on right ascension and proximity to the ecliptic. The number of fields in the northern strip has changed more dramatically over the observing program and currently there are only 5 active fields, each being observed ∼500 times per year.

From this it is clear that to obtain the ∼3000 minimum good images required per field to search for transit signals requires many years of observing and this is the reason the KELT-South team has only started the identification of possible transiting exoplanets in 2013.

3.5 Scripted Operations

There are a large number of VBS programs that control the KELT-South telescope. These programs are either started at specific times by the Windows XP operating system or are called by other VBS programs. In the following sections all the scripts are discussed and flowcharts of the more complex scripts have been included to make it easier to understand and follow the observing operations of KELT-South. The colours of the blocks are also meaningful, with green blocks indicating the start of the script, the red blocks indicate the end of the script, yellow blocks are operations that the script itself performs, grey blocks are other scripts called by the current script and blue blocks are more complex parts of the script that have their own flowcharts to explain the operations performed in that block. Over the 5 year period I've been involved with the project I have written over 35000 lines of code, of which 15000 are used to run the telescope at present. The rest of the code is either used to simulate the observing program or formed part of scripts that are now old and deprecated. One of the main goals when developing the scripts that control the KELT-South telescope was to make it as modular as possible. This ensured that any script would primarily perform only one task, making the process of finding and removing errors much easier. Certain scripts could be disabled without halting the entire telescope operations. A downside to this kind of modular scripting is that many scripts could be running at the same time and be competing for the resources on the Windows XP operating system, potentially slowing it down or even causing crashes. For this reason, great care was taken to ensure that scripts were as efficient as possible in the execution of the tasks and did not tax the computer system unnecessarily. The processing of images was not done in real time as they were acquired, instead the observing script was allowed to complete before the processing of images (which is highly CPU and memory intensive) started. Another process that runs when no other resources are required is the image compression script. By doing things in this manner, the KELT-South control computer has been highly reliable and not experienced a single crash or data failure in the 5 years of operation.

3.5.1 Startup Script

The STARTUP script is run every time the control computer is rebooted. This script makes sure that DirecTemp is started correctly and able to record the temperature data. The software provided by Qti has a strange "quirk" whereby it doesn't recognise the USB temperature probes upon first start of the program after the computer is rebooted. The DirecTemp program is started by the STARTUP script, allowed to run for 60 seconds, and then closed. DirecTemp is then restarted and the program will correctly connect to the USB temperature probes and start recording temperature data. The STARTUP script is also responsible for resetting the PLC into its default state and ensuring that it is in remote mode that will allow other scripts to send it instructions directly without having to reset it first. Other programs that start up when the control computer is rebooted, but that are started by the operating system itself include, Fling File Transfer, Dimension4, SnapShot Utility and LanSafe. These programs run as services on the operating system and are responsible for monitoring certain devices connected to the control computer or other crucial functions of the telescope operations.

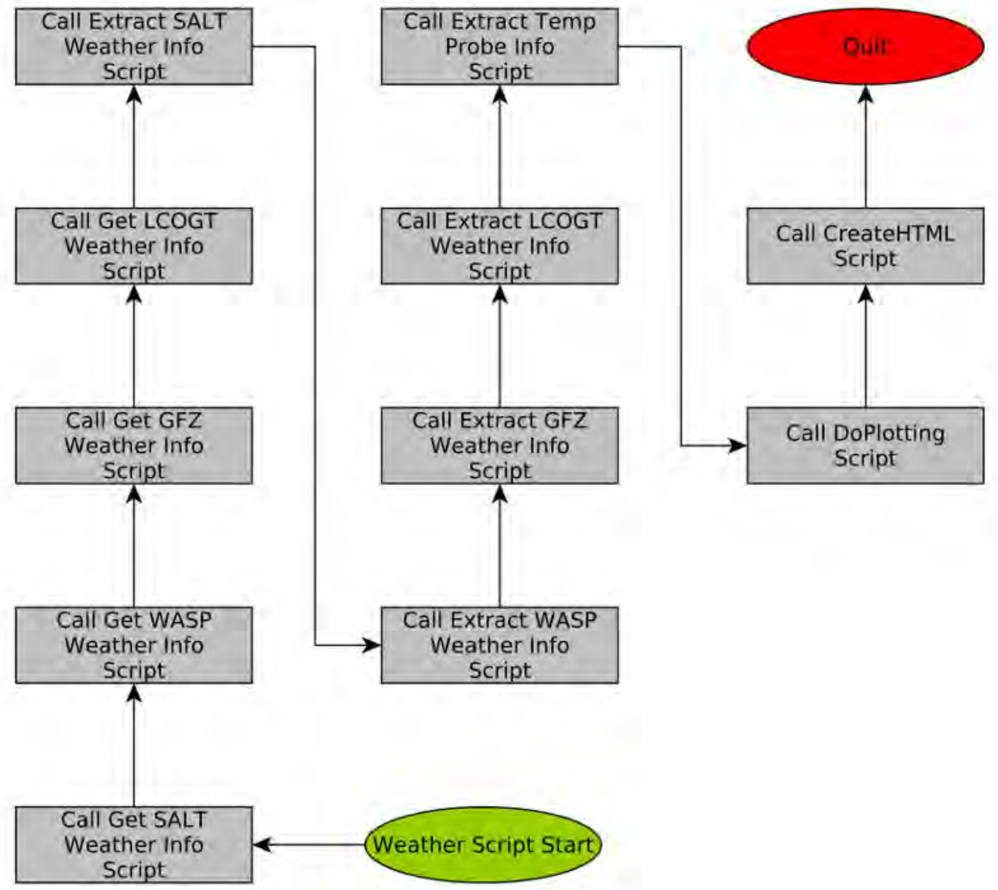

Figure 3.4: Flowchart showing the WEATHER script working procedure.

3.5.2 Weather Script

The Windows Scheduler runs the WEATHER script every five minutes of the day. This script (see Figure 3.4) is responsible for getting weather information from four different weather stations located on the observing plateau at Sutherland. The first weather station belongs to the SAAO and is used by SALT to determine if conditions are favourable for observing. The second weather station is owned and operated by the SuperWASP consortium and is located just outside the SuperWASP-South telescope about 20 m away from the KELT-South telescope. The third is owned by GFZ and forms part of their network of geodynamic observatories that study geological, physical, chemical and biological processes which occur on the surface as well as the interior of the Earth. The LCOGT weather stations located less than 10 m away from the KELT-South enclosure were added in 2013 August. Each weather station collects different information that the operators of those facilities then use to determine whether or not conditions are good for observing. The weather script simply collects the information from the weather stations themselves or websites run by the operators of the weather stations. All the weather stations have a copy of their respective website that is accessible from the local network in Sutherland which means that even if the internet connectivity should fail, the local area network should still function and the weather information should still be available to be collected.

Although it is known that changes in weather (rain) can happen on timescales shorter than five minutes, there are a number of safeguards the KELT-South telescope uses to ensure that the roof does not stay open when it starts raining. Firstly, the roof will close when the relative humidity is over the 90% level and it is highly unlikely that it will start raining below this value. Secondly, the information collected from the cloud monitors is there to ensure that the roof does not stay open when it is cloudy (when rain is most likely to occur). The cloud monitors are pointed directly upward and have a 120° field of view. This ensures that clouds that are not overhead are spotted and the appropriate action can be taken before the clouds are overhead. Finally, the roof motor and PLC are connected to a rain sensor on the outside of the building (see Section 2.3.1) that will close the roof in the event that rain is detected. This action cannot be stopped by user intervention or even the control computer. A “rain trigger flag” on the PLC needs to be reset by the control computer via special instruction to allow the roof to open once it has been closed by the rain sensor trigger. The roof moves from fully open to fully closed in less than 10 seconds and this ensures that the telescope does not get rained on in the unlikely event that it starts raining when the relative humidity is below 90% and it is not cloudy at all. In the 5 years of operation, this system has never failed and the telescope has never had any issue with being left open during a rain storm.

The WEATHER script itself only makes calls to other scripts that actually perform the gathering and extraction of the weather information. Once the information has been collected and extracted, the WEATHER script calls a script that plots the relevant information and produces graphs that are then uploaded to the KELT-South monitoring website*(see Figure 3.5). A standard HTML website is created with the new updated information and uploaded to the KELT-South website.

GetWeather Script

The GETWEATHER script for each individual weather station simply uses a Windows version of the WGET command with two retries and a 20 second wait between retries to download the relevant information page for each weather station from the local area network. The downloaded pages are stored in their raw HTML format and the files are overwritten every time the GETWEATHER script is run.

ExtractWeatherInfo Script

The EXTRACTWEATHERINFO script parses the various downloaded pages and tries to find the relevant information from each page. The information that is extracted includes the current date and time, temperature, dew point temperature (if provided), relative humidity, wind speed, wind direction, rain conditional flag and the level of cloud cover. Not all the weather stations provide the same level of information and the formatting and units for each station are slightly different. For example, only SuperWASP and LCOGT provide information on the cloud cover. The wind speed measurements for SuperWASP and LCOGT are measured in km h^{-1} whereas the wind speeds reported by SALT and GFZ are in m s^{-1}. Once the relevant information is extracted and converted into the same standard set of units, it is written to four separate tab separated text files (one for each weather station) that share a common structure. These files are easily readable and can be stored for archiving purposes. Archived weather information can later be used to determine the effect weather conditions have on the telescope operations and can be very useful in the diagnosis of errors or to explain trends in the reduced lightcurves after the reduction process.

DoPlotting Script

The DOPLOTTING script calls another script that reads the entire tab separated text file for each weather station and splits it into smaller parts containing only the last 24 hours, 3, 7, 14 and 30 days worth of information. It then calls a set of GNUPLOT scripts to produce plots of the outside temperature, the temperature inside the KELT-South enclosure, the temperature inside the climate controlled cabinet, the relative humidity, the difference between external temperature and dew point temperature, wind speed and cloud cover. The plots are saved and copied to the FLING FILE TRANSFER monitoring folder and uploaded to the KELT-South website. This can then be used to determine trends in the weather conditions and the plots can be used to make sure the telescope was not operating when it was not supposed to.

---

*The current status of the KELT-South telescope can be found at the website: http://keltsouth.saao.ac.za

CreateHTMLPage Script

This script reads the last line of the tab separated text files created earlier for each weather station. It then queries the PLC to determine its current state and determines the amount of free space available on the internal hard drive of the control computer as well as the two external drives. It then creates a standard HTML page with the collected information. The final part of this script moves all the relevant files needed to display the website correctly into a folder that is monitored by FLING FILE TRANSFER. When FLING FILE TRANSFER determines that new files are available it automatically connects to the webserver in Cape Town and copies files to the correct place for display on the KELT-South web page. Figure 3.5 shows the KELT-South monitoring web page in full.

KELT-South Monitoring Website

The top half of the web page displays the current status of the telescope, while the bottom half displays information about the images collected from the previous night's observing. The image on the right at the top of the page is the current view of the telescope as taken by the IP camera. This image can be used to make sure the telescope is correctly parked and not in an abnormal position that would indicate some kind of problem. The image on the left is a place holder at present and simply shows what the KELT-South enclosure looks like. In future this image will be replaced by an image taken by another IP camera mounted outside the KELT-South enclosure.

The next part of the web page displays the current weather conditions in Sutherland as collected by the WEATHER script. The green background colours indicate values that are within the observing limits and indicate that conditions are favourable for observing. The table entries with red coloured backgrounds are either out of the observing limits, or the information for the particular weather station is outdated. In this particular case, the weather information from the SuperWASP weather station was more than three days old and thus all values are ignored.

The next two sections simply display the current status of the PLC and the amount of free space available on the control computer and two external hard drives.

Further down on the web page the archived weather information is displayed. Trends in weather patterns can be viewed for the last 24 hours, 3, 7, 14 and 30 days providing a quick and easy way to determine why the telescope has not been taking images, for example. Instead of reading through many log files, one look at the cloud cover graph will show that conditions have not been favourable at all.

The archived image previews and data quality statistics section at the bottom of the page display thumbnails and other image statistics collected from the previous nights observing. Section 3.6 provides full details on what these entries represent and how they were determined.

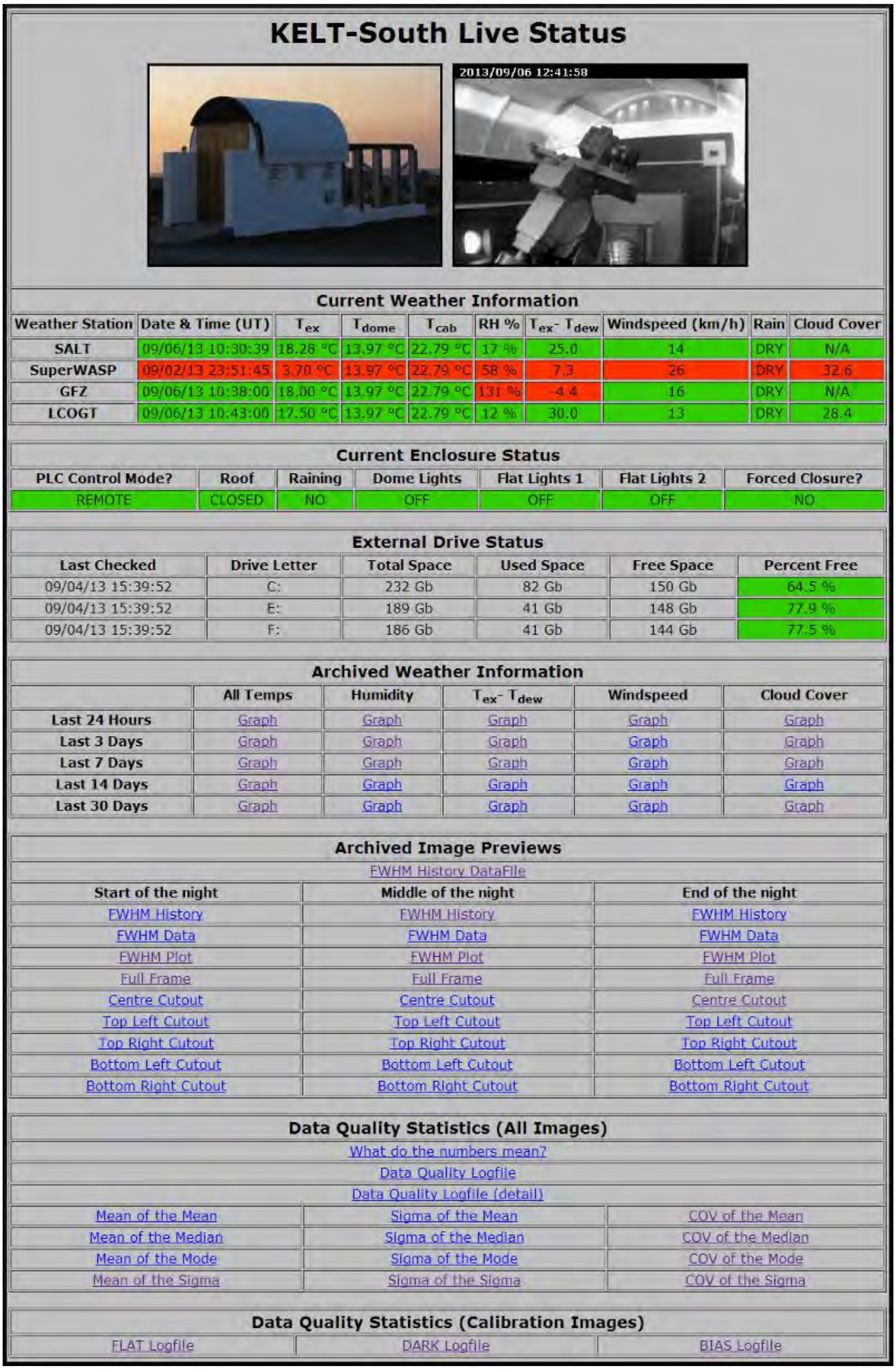

KELT-South Live Status

Current Weather Information

Weather Station	Date & Time (UT)	T_{ex}	T_{dome}	T_{cab}	RH %	T_{ex}- T_{dew}	Windspeed (km/h)	Rain	Cloud Cover
SALT	09/06/13 10:30:39	18.28 °C	13.97 °C	22.79 °C	17 %	25.0	14	DRY	N/A
SuperWASP	09/02/13 23:51:45	3.70 °C	13.97 °C	22.79 °C	58 %	7.3	26	DRY	32.6
GFZ	09/06/13 10:38:00	18.00 °C	13.97 °C	22.79 °C	131 %	-4.4	16	DRY	N/A
LCOGT	09/06/13 10:43:00	17.50 °C	13.97 °C	22.79 °C	12 %	30.0	13	DRY	28.4

Current Enclosure Status

PLC Control Mode?	Roof	Raining	Dome Lights	Flat Lights 1	Flat Lights 2	Forced Closure?
REMOTE	CLOSED	NO	OFF	OFF	OFF	NO

External Drive Status

Last Checked	Drive Letter	Total Space	Used Space	Free Space	Percent Free
09/04/13 15:39:52	C:	232 Gb	82 Gb	150 Gb	64.5 %
09/04/13 15:39:52	E:	189 Gb	41 Gb	148 Gb	77.9 %
09/04/13 15:39:52	F:	186 Gb	41 Gb	144 Gb	77.5 %

Archived Weather Information

	All Temps	Humidity	T_{ex}- T_{dew}	Windspeed	Cloud Cover
Last 24 Hours	Graph	Graph	Graph	Graph	Graph
Last 3 Days	Graph	Graph	Graph	Graph	Graph
Last 7 Days	Graph	Graph	Graph	Graph	Graph
Last 14 Days	Graph	Graph	Graph	Graph	Graph
Last 30 Days	Graph	Graph	Graph	Graph	Graph

Archived Image Previews

FWHM History DataFile

Start of the night	Middle of the night	End of the night
FWHM History	FWHM History	FWHM History
FWHM Data	FWHM Data	FWHM Data
FWHM Plot	FWHM Plot	FWHM Plot
Full Frame	Full Frame	Full Frame
Centre Cutout	Centre Cutout	Centre Cutout
Top Left Cutout	Top Left Cutout	Top Left Cutout
Top Right Cutout	Top Right Cutout	Top Right Cutout
Bottom Left Cutout	Bottom Left Cutout	Bottom Left Cutout
Bottom Right Cutout	Bottom Right Cutout	Bottom Right Cutout

Data Quality Statistics (All Images)

What do the numbers mean?

Data Quality Logfile

Data Quality Logfile (detail)

Mean of the Mean	Sigma of the Mean	COV of the Mean
Mean of the Median	Sigma of the Median	COV of the Median
Mean of the Mode	Sigma of the Mode	COV of the Mode
Mean of the Sigma	Sigma of the Sigma	COV of the Sigma

Data Quality Statistics (Calibration Images)

FLAT Logfile	DARK Logfile	BIAS Logfile

Figure 3.5: The KELT-South monitoring web page. The red coloured background for some table entries indicate that the information is either outside the operating limits we established or the information is old and should be ignored.

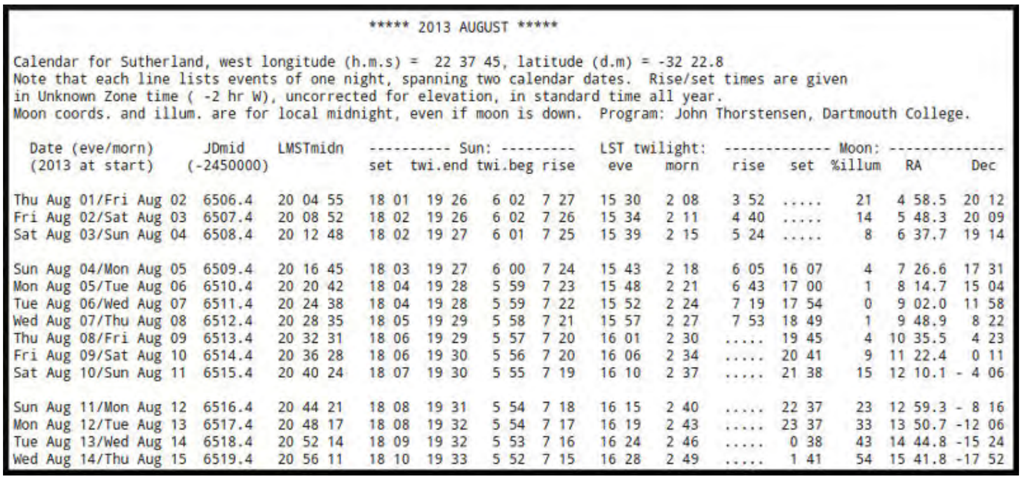

```
                                  ***** 2013 AUGUST *****

Calendar for Sutherland, west longitude (h.m.s) =  22 37 45, latitude (d.m) = -32 22.8
Note that each line lists events of one night, spanning two calendar dates.  Rise/set times are given
in Unknown Zone time ( -2 hr W), uncorrected for elevation, in standard time all year.
Moon coords. and illum. are for local midnight, even if moon is down.  Program: John Thorstensen, Dartmouth College.

  Date (eve/morn)      JDmid    LMSTmidn   ---------- Sun: ---------   LST twilight:   ------------ Moon: -------------
  (2013 at start)    (-2450000)             set  twi.end twi.beg rise    eve    morn    rise   set  %illum   RA      Dec

Thu Aug 01/Fri Aug 02  6506.4   20 04 55   18 01  19 26   6 02  7 27   15 30   2 08    3 52  .....   21   4 58.5  20 12
Fri Aug 02/Sat Aug 03  6507.4   20 08 52   18 02  19 26   6 02  7 26   15 34   2 11    4 40  .....   14   5 48.3  20 09
Sat Aug 03/Sun Aug 04  6508.4   20 12 48   18 02  19 27   6 01  7 25   15 39   2 15    5 24  .....    8   6 37.7  19 14

Sun Aug 04/Mon Aug 05  6509.4   20 16 45   18 03  19 27   6 00  7 24   15 43   2 18    6 05  16 07    4   7 26.6  17 31
Mon Aug 05/Tue Aug 06  6510.4   20 20 42   18 04  19 28   5 59  7 23   15 48   2 21    6 43  17 00    1   8 14.7  15 04
Tue Aug 06/Wed Aug 07  6511.4   20 24 38   18 04  19 28   5 59  7 22   15 52   2 24    7 19  17 54    0   9 02.0  11 58
Wed Aug 07/Thu Aug 08  6512.4   20 28 35   18 05  19 29   5 58  7 21   15 57   2 27    7 53  18 49    1   9 48.9   8 22
Thu Aug 08/Fri Aug 09  6513.4   20 32 31   18 06  19 29   5 57  7 20   16 01   2 30   .....  19 45    4  10 35.5   4 23
Fri Aug 09/Sat Aug 10  6514.4   20 36 28   18 06  19 30   5 56  7 20   16 06   2 34   .....  20 41    9  11 22.4   0 11
Sat Aug 10/Sun Aug 11  6515.4   20 40 24   18 07  19 30   5 55  7 19   16 10   2 37   .....  21 38   15  12 10.1 - 4 06

Sun Aug 11/Mon Aug 12  6516.4   20 44 21   18 08  19 31   5 54  7 18   16 15   2 40   .....  22 37   23  12 59.3 - 8 16
Mon Aug 12/Tue Aug 13  6517.4   20 48 17   18 08  19 32   5 54  7 17   16 19   2 43   .....  23 37   33  13 50.7 -12 06
Tue Aug 13/Wed Aug 14  6518.4   20 52 14   18 09  19 32   5 53  7 16   16 24   2 46   .....   0 38   43  14 44.8 -15 24
Wed Aug 14/Thu Aug 15  6519.4   20 56 11   18 10  19 33   5 52  7 15   16 28   2 49   .....   1 41   54  15 41.8 -17 52
```

Figure 3.6: Snippet of the calendar file produced by SKYCALC.

3.5.3 Read Almanac Script

At 12:00 SAST each day the Windows Scheduler runs the READALMANAC script. This script simply reads a sky calendar file that was created by the Linux version of the SKYCALC* program written by John Thorstensen and Brian Casey. The generated calendar file is specific to Sutherland and contains the Julian Day Number, Local Mean Sidereal Time at midnight SAST, rise and set times of the Sun, start and end times of astronomical twilight, Local Sidereal Time at the end of astronomical twilight, the rise and set times of the Moon, illumination percentage of the Moon and also the right ascension and declination of the Moon at midnight SAST. Figure 3.6 shows a snippet of the calendar file produced by SKYCALC. The script determines the current date using the Windows system clock and reads the corresponding line in the calendar file. All entries are stored in a separate file that only contains one entry per line and this file is overwritten every day when the READALMANAC script is run. This newly created "almanac output" file is then read by the other scripts when required, instead of these scripts having to read the entire calendar file containing hundreds of lines and wasting time searching for the relevant line.

3.5.4 Backup Script

At 14:00 SAST the Windows Scheduler runs a script called DOZIPPING. This script first finds the folder containing the data from the previous night and then uses the FPACK program to compress the data. Each image is compressed individually, allowing other FITS compatible programs to manipulate the files. Once all the data are compressed, the raw images are deleted and the script runs a Windows version of RSYNC and simply copies any changes to the data directory onto the two external hard drives. The script also checks the sizes of the weather data files created by the WEATHER script before closing. If these files are larger

---

*http://www.briancasey.org/artifacts/astro/skycalendar_notes.html than 5MB in size, data older than 30 days are archived and compressed. This ensures that the weather data files used to determine the weather conditions during observing operations are not excessively large. Large files take a long time to read and might slow down the observing procedure unnecessarily.

When the KELT-South telescope was first constructed the internet connection between Sutherland and the rest of the world was not very good. This meant that when the external hard drives reach 90% capacity, they were manually swapped out for a new pair of drives, and the full drives were transported to the SAAO headquarters in Cape Town. One of the drives was shipped to Vanderbilt University in Nashville and the other stayed in Cape Town as a backup copy. When the shipped drive arrived in Nashville, and the data were copied and verified to be uncorrupted, the drive was shipped back to Cape Town. Both drives were then transported back to Sutherland and put back into rotation. The shipping of the drives from Cape Town to Nashville and back sometimes took very long (longer than it took for the drives to reach 90% capacity) and to ensure that there were always two external drives ready for data, a total of 8 external hard drives were purchased. Upgrades to the network connectivity in Sutherland in 2012 now enables the transfer of data directly via the internet from Sutherland to Vanderbilt. The two external hard drives are still used and data copied to them as backup, but they are no longer shipped back and forth.

A different script containing a very similar RSYNC command as described above is run manually to copy the data from Sutherland to Vanderbilt. The reason for not automating this task is that the transfer speed between Sutherland and Vanderbilt is extremely variable depending on a number of factors, including the time of day, the amount of data being moved from Sutherland to Cape Town for other telescopes on the observing plateau and general network congestion levels. We found it best to transfer data over weekends when a speed of 150KB/s can be maintained.

3.5.5 Main Script

At 17:00 SAST every night the Windows Scheduler starts the MAIN script. The MAIN script (see Figure 3.7) is responsible for calling all other scripts at the correct times and making sure that all observations are done correctly. Each event that occurs is timestamped and the event is written to a log file that the script opens before anything else is done. This log file can then be used to see which commands were executed and error tracking is simplified a great deal. The first thing the script does is determine the current time using the Windows system clock. It then reads the almanac output file to find the times of sunset, the end of astronomical twilight and the start of astronomical dawn. It then calculates the difference between the current time and sunset and if this difference is larger than -20 minutes the script is instructed to wait for 5 minutes and check the time difference again. This effectively means that the SKYFLAT script is executed 20 minutes after sunset. The script then waits until the procedure for taking flat field images is complete before starting the OBSERVING script. Once the OBSERVING script has finished the MAIN script closes the log file and quits. This indicates the end of the observing run for that particular night.

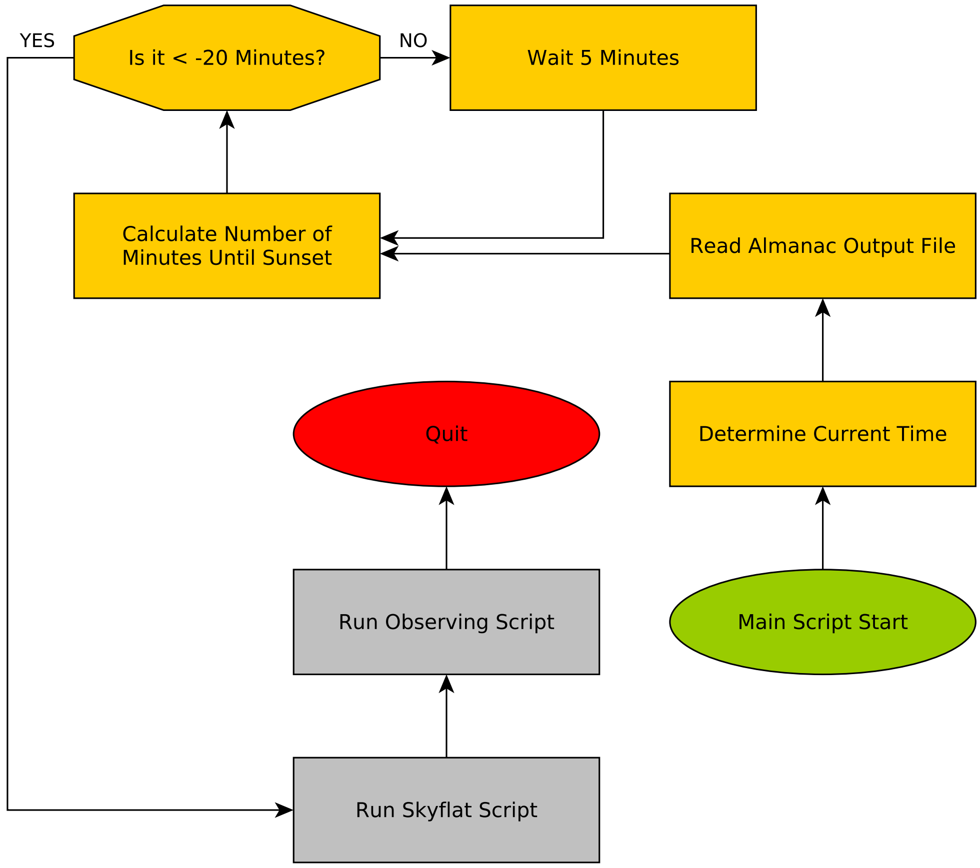

Figure 3.7: Flowchart of the Main script that controls all of the observing operations of the KELT-South telescope.

3.5.6 Skyflat Script

At 20 minutes after sunset the SKYFLAT script is executed. This script (see Figure 3.8) will open its own log file that can be used to do error tracking. Once again each action taken by the script is timestamped and the event is written to the log file. The first thing the script does is connect to the PLC by sending it a wake-up command. It then resets all the flags on the PLC and sets the PLC into remote access mode if not already in that mode. Information is read into memory about the times of sunset and the end of astronomical twilight by reading the almanac output file created specifically for that particular day. The next thing the script does is establish a connection to CCDSOFT which is responsible for camera control. It then sets the CCD temperature to -20°C (this is simply an extra precaution, as the CCD should always be at that temperature), and connects to the software package THESKY6, which is responsible for the pointing of the telescope mount. The script then establishes a connection to the mount allowing it to control the telescope by issuing slew commands. The mount is instructed to slew to its home position which initialises the encoders, allowing the mount

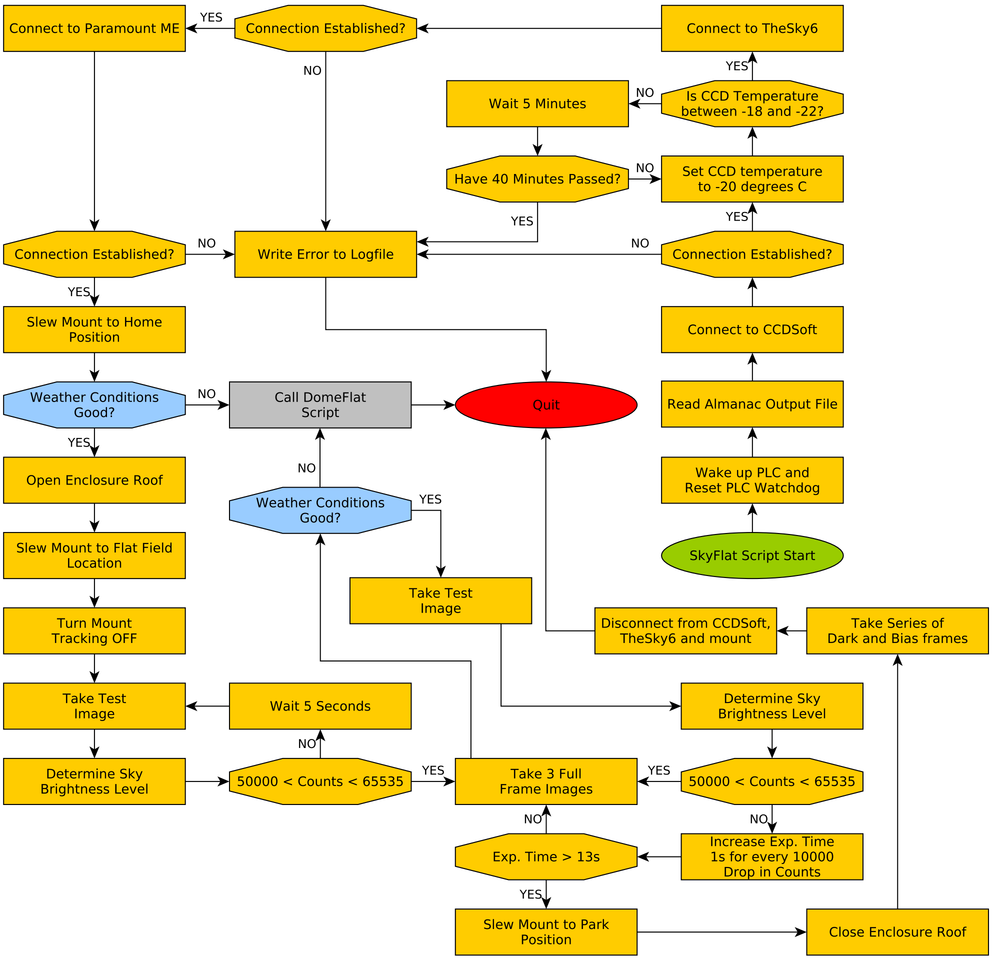

Figure 3.8: Flowchart showing the procedure followed to take the sky flat field images.

to know exactly where it is pointing. At this point the script checks the weather conditions and if weather conditions do not permit observations the SKYFLAT script calls another script that performs the dome flat fielding procedure. If the weather is favourable for observing, the PLC is instructed to open the roof of the enclosure and the mount is instructed to slew to the zenith and the taking of flat field images starts.

At first a test image is taken and the central 256×256 pixel block is read out and analysed to determine the sky brightness (modal pixel value in the central image section). If the pixels are saturated, the telescope waits for 5 seconds and another test images is taken and analysed. This process repeats until the sky brightness in the central 256×256 block is between 50000 and 65535 (ADC limit), with the goal being to acquire the most signal without hitting non-linearity. The telescope then takes three full frame images at 1 second exposures, making small ($\sim 2'$) random adjustments to the telescope position between successive images as well as resetting the PLC watchdog. The weather conditions are checked and another test image is taken and the sky brightness level is determined again. If the sky brightness has decreased, the exposure time is increased by 1 second for every 10000 count drop in brightness, to ensure that all the sky flat field images have roughly the same number of counts. Another three full frame images are taken and the procedure repeated. The evening flat fielding routine stops once the exposure time required to reach 50000 counts in the central image section is greater than 13 seconds. At this point, stars start to appear in the corner of the images and further images can no longer be used for flat fielding (a similar procedure, run in reverse order, is done at dawn to take morning sky flats).

With the flat fielding complete, the roof is closed and the telescope is instructed to move to the park position. At this point a series of 10 dark and 10 bias images are taken, in alternating pairs. The script disconnects from TheSky6, CCDsoft, closes the log file and quits. If an error occurs at any point in the execution of commands, the SKYFLAT script writes the error to the log file and quits.

3.5.7 Domeflat Script

If weather conditions are not favourable for the telescope to perform the normal sky flat procedure, the DOMEFLAT script is called. This script is very similar to the SKYFLAT script in operation with the major difference being that the script will not open the roof. A command to turn on the flat field illumination lights inside the enclosure is issued and the script instructs the mount to point the camera at the flat field screen. There are 4 lights that are evenly spaced around the telescope mount on the walls of the enclosure that provide illumination for the flat field screen. Each light can be individually adjusted for brightness and the current levels were obtained by taking a large number of flat field images and minimising the gradients across the images. A series of 26 dome flat field images are taken in a regularly spaced grid pattern. The exposure time is fixed at 3 seconds for all images taken during the dome flat fielding procedure as the need to change the exposure time is not required since the lights provide a constant source of brightness. The flat field illumination lights are turned off and the telescope is moved to the park position where a series of 10

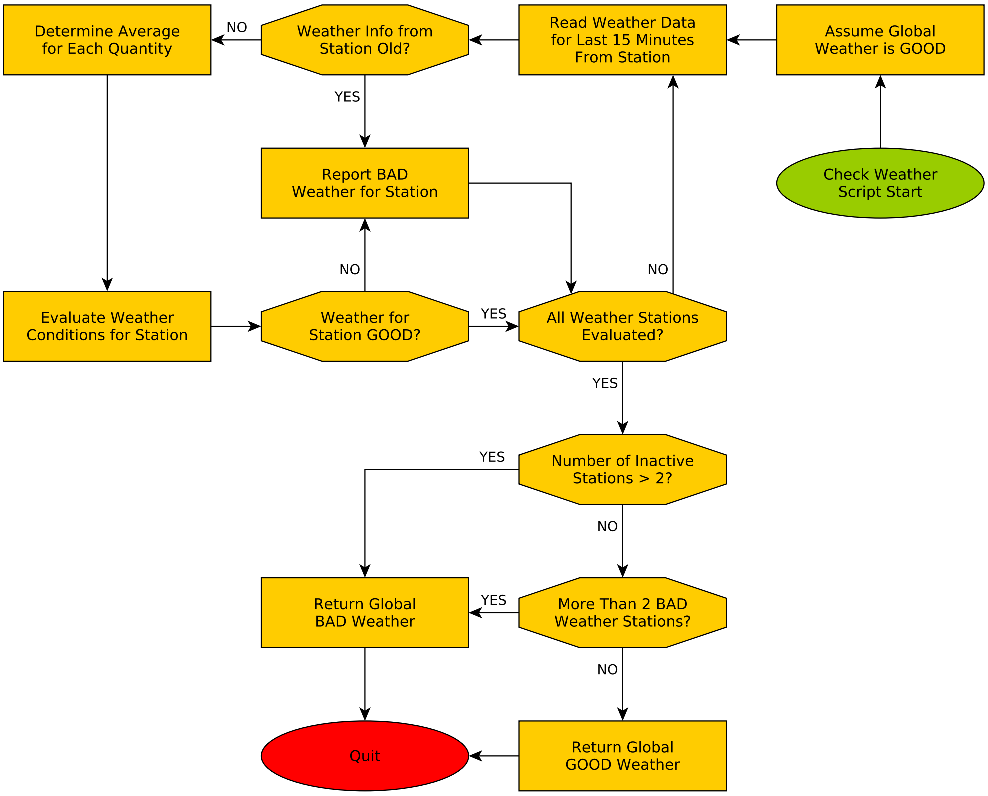

Figure 3.9: Flowchart showing the procedure followed to check if weather conditions are favourable for observing. Information from the weather stations are determined in the order SALT firs then SuperWASP then GFZ and lastly LCOGT.

dark and 10 bias images are taken in alternating pairs. The script disconnects from the software packages and quits. The SKYFLAT script, which called the DOMEFLAT script, will then assume control of the telescope again and realise that regular sky flat field images are no longer required and will also disconnect from the software packages and terminate.

3.5.8 Checkweather Script

During observing operations, the telescope checks that weather conditions are still good enough to continue after every image is taken (See Figure 3.9). To accomplish this the data from the active weather stations are averaged over the last 15 minutes before making a determination of weather conditions. This ensures that a sudden gust of wind or any anomalous behaviour of one weather station does not affect the overall determination of conditions and prevents unnecessary closures of the enclosure roof. The weather information for each station is evaluated according to the criteria set out in Section 3.2 and the global weather condition is considered bad if two or more weather stations report bad weather. If the weather information from one station is older than 30 minutes that weather station is regarded as inactive and the data are disregarded. Weather information from the remaining three weather stations will be used to determine favourable observing conditions. If two or more weather stations are inactive, the script assumes bad weather and halts the observing. It is very rare for two stations to be inactive as the support staff members in Sutherland usually fix them fairly quickly and normal operations are restored. In cases where one specific value for a station is causing that entire station to report bad weather (and the problem is known or reported by the support staff), that value can be ignored by a slight modification of the script. This will allow the script to use all other values it collects from that station and determine favourable conditions based on the other good working values. Figure 3.5 shows an example of this. Here the GFZ weather station is reporting 131% relative humidity. This faulty reading was reported by staff members and the script was modified to ignore this faulty measurement and use the rest of the information from GFZ as normal.

3.5.9 Commissioning Mode Observing Script

As discussed in Section 3.2, in the commissioning mode the telescope operated in a "point and stare" mode and a single field was observed for as long as that field was available. The script (see Figure 3.10) starts by sending a wake up command to the PLC, setting it into remote mode and resetting the watchdog trigger. The current time is determined using the system clock and various camera and telescope properties are reset. These properties include the size of the image to use for observing, the binning of pixels and slew rate of the mount. The almanac output file is read and the time for the end of astronomical twilight and the time for astronomical dawn for the next morning are read into memory. Connections to TheSky6, CCDSoft and the mount are established and a directory using the day, month and year is created to store the expected data for the night. The airmass of the target field is calculated and the number of minutes between the current time and the end of astronomical twilight is determined. The script will wait until both the airmass (M_a) of the target field is less than two and the number of minutes until the end of astronomical twilight is less than zero.

If conditions are not favourable for observing, the script disconnects from the software packages, determines the reason for not observing and quits. In this observing mode a lot of time was lost due to weather conditions being unfavourable at the start of the night, but becoming better later on. The telescope did not take advantage of this "lost" time and in the regular survey mode that followed the commissioning seasons, the telescope was instructed to enter a standby mode in unfavourable weather conditions and keep checking the weather every five minutes until conditions improved and allowed for observing to start, or astronomical dawn had arrived. This small alteration improved the efficiency by taking advantage of previously lost time.

If conditions are determined to be good for observing the PLC watchdog trigger is reset once more and the roof of the enclosure is opened. The mount is initialised by slewing to the home position and tracking is turned on. The telescope then slews to the target field, takes

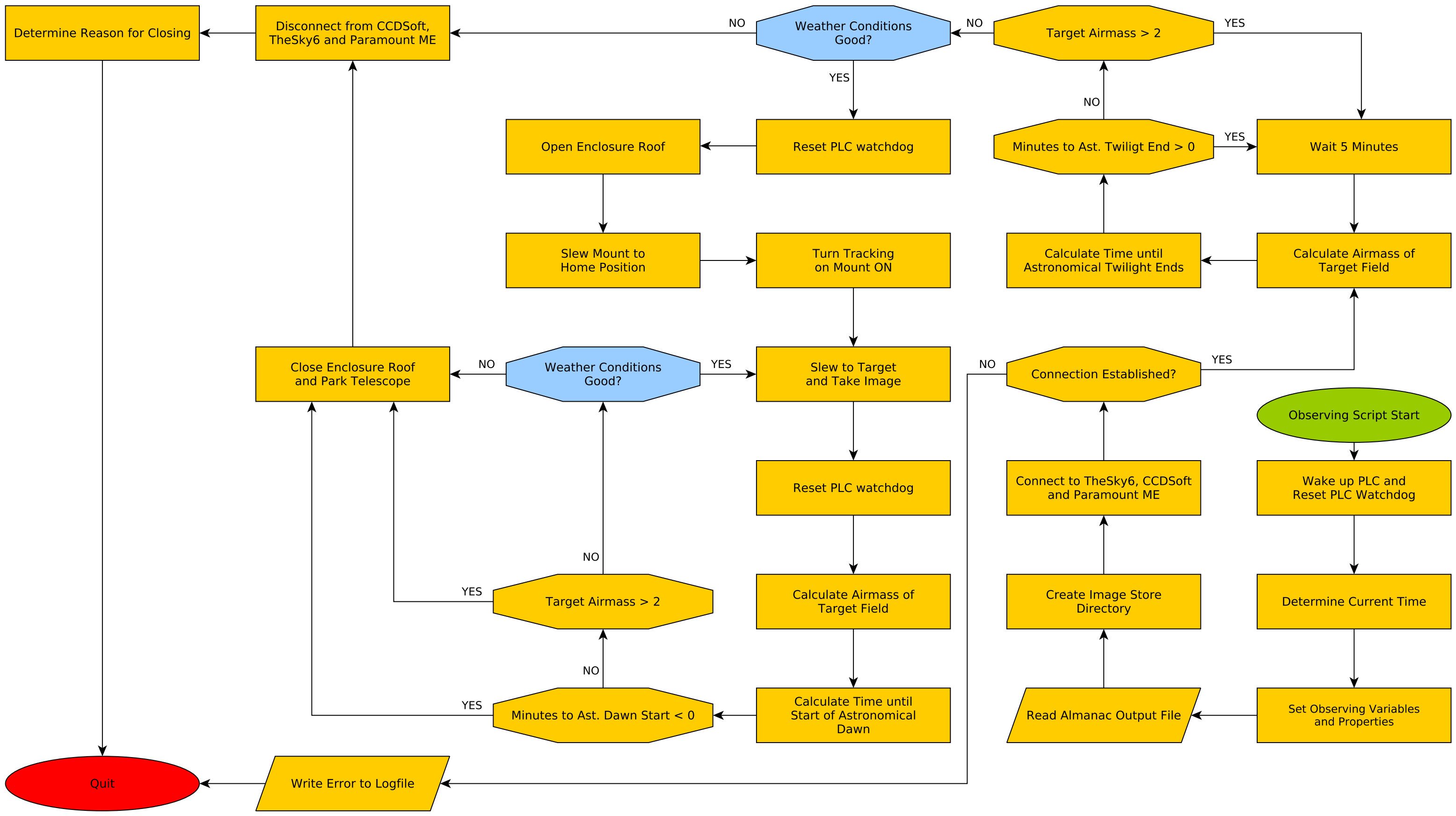

Figure 3.10: Flowchart of the observing procedure during the commissioning phases of the telescope.

an image, resets the watchdog, recalculates the airmass of the target and also determines how long until the start of astronomical dawn. The script resets the PLC watchdog and checks the weather after every image is acquired. If the weather becomes unsuitable the script will halt observations, close the roof and instruct the telescope to park. If $M_a > 2$ or the time until astronomical dawn is less than zero, the roof is closed and the telescope instructed to park. Connections to the software packages are closed and the reason for closing are determined (either bad weather or astronomical dawn was reached). The script writes all relevant information to a log file and the quits, ending observations for the night. In the commission mode flat field images were obtained only in the evening and no sky flats were taken at dawn.

3.5.10 Survey Mode Observing Script

As discussed in Section 3.2, in the survey mode the telescope observes a number of fields across the sky. The script (see Figure 3.11) starts by reading the almanac output file. It then reads two files that contain the right ascension and declination coordinates for the northern and southern strip of fields. A command to reset the PLC watchdog is sent and the PLC set into remote mode. The hour angle and airmass for each field is calculated and the script determines whether or not a field is contaminated by the Moon, meaning the Moon is within 50° of the field centre. The current time is determined and the number of minutes until the end of astronomical twilight is calculated. If this is more than 25 minutes the telescope waits for five minutes and checks again. If it is less than 25 minutes until the end of astronomical twilight the weather conditions are checked.

In unfavourable weather conditions the telescope enters a standby mode, wherein it checks the weather every five minutes until it becomes good for observing or astronomical dawn is reached, at which point the telescope takes a series of 10 dark and 10 bias images in alternating pairs with the telescope in the park position and ends the observing operations.

If weather conditions are favourable, the PLC watchdog is reset and the roof is opened. Various camera and telescope properties are reset to get all the components ready for observing. If the number of minutes until astronomical twilight is larger than zero then the telescope will take images of fields that are east of the meridian only. This procedure was implemented to get extra time on fields that are far enough away from the western horizon at sunset. Large scale gradients in the sky brightness levels across a image taken after sunset cannot be used in the data reduction process, but fields that are far from the location of sunset show no large scale gradients, so it was decided to use the extra time to get a few more images and maximise efficiency. Figure 3.12 shows how the telescope performs the east-only observations.

The hour angle (HA), airmass (M_a) and Moon contamination are calculated for all the fields in the list. If HA < 0, $M_a < 1.5$ and the field is not Moon contaminated, the field is considered available for observing. Images of the available fields are taken in order of increasing right ascension starting with the northernmost declination and moving to the southernmost declination then back to the northernmost. If the script determines that no

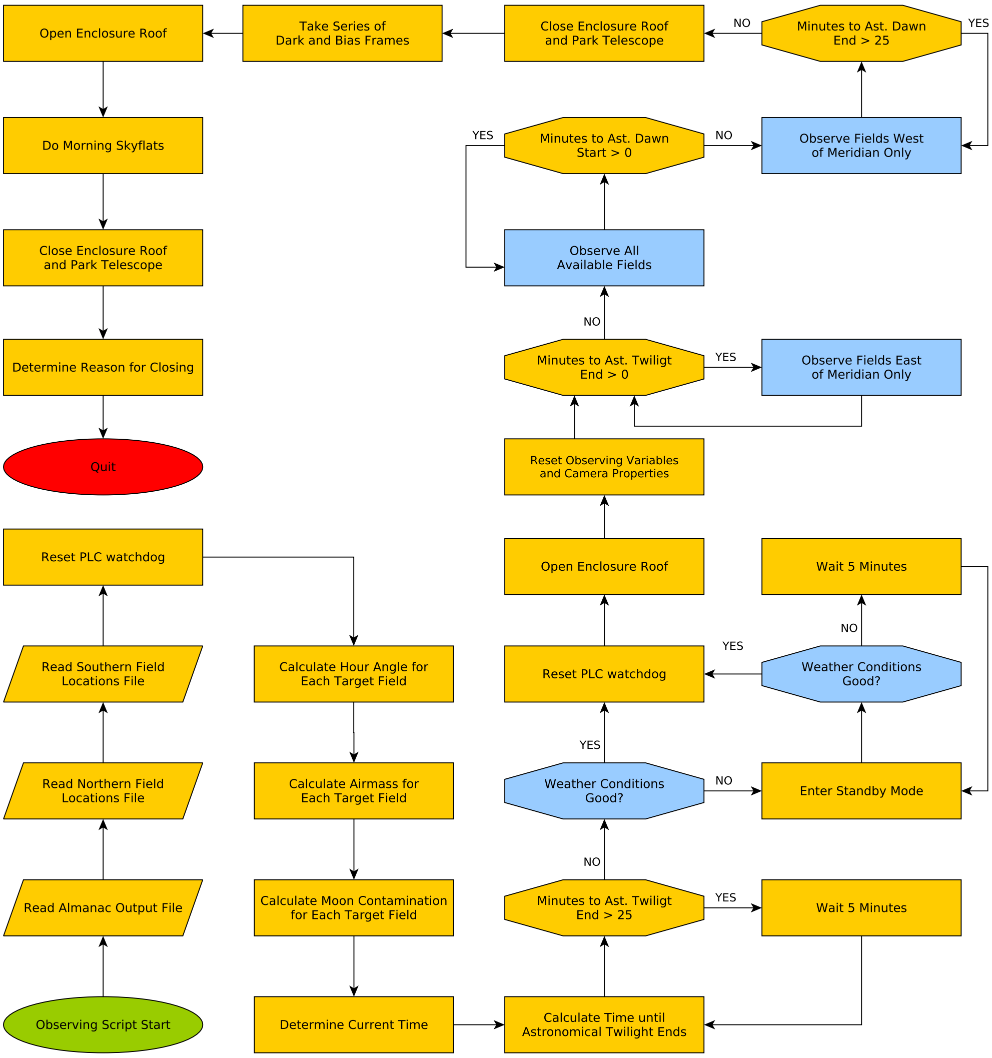

Figure 3.11: Flowchart of the observing procedure during the regular survey mode of the telescope.

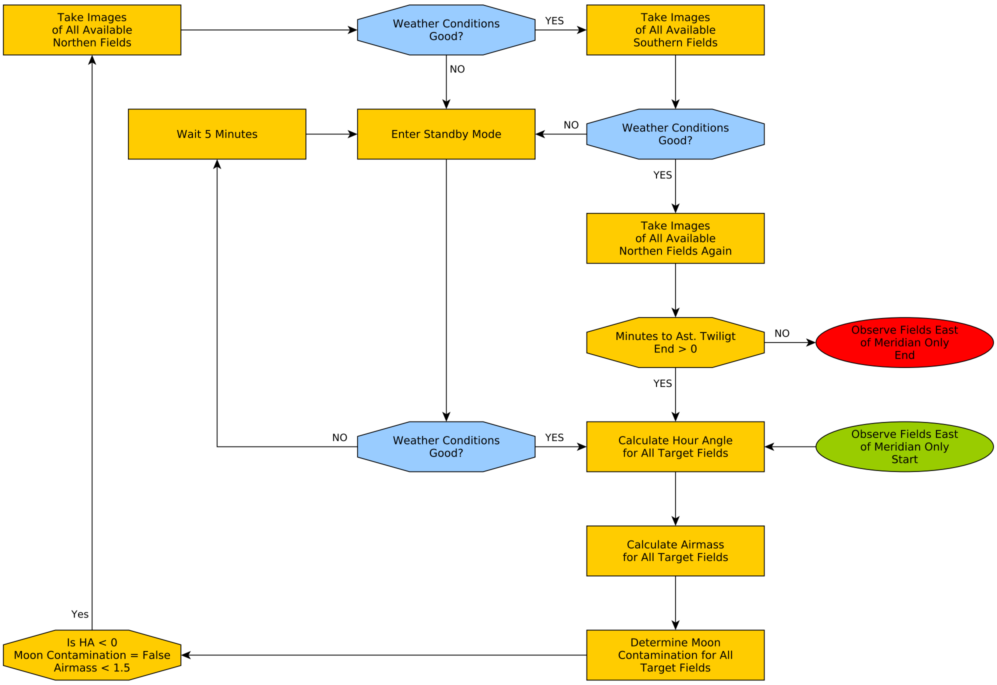

Figure 3.12: Flowchart showing the procedure for taking images of fields east of the meridian only.

fields are available (due to not meeting the requirements) it will halt observing and wait for five minutes while continuously checking the weather as well as the availability of fields. The cycle of taking images east of the meridian only continues until the end of astronomical twilight.

At the end of astronomical twilight the telescope will observe all available fields regardless of their hour angle (fields need to satisfy only the airmass and Moon contamination requirements to qualify for availability). The telescope determines which fields are above 1.5 M_a east of the meridian, and it observes each field in order from northernmost declination to southernmost then going back to the northernmost ones. It then performs a meridian flip, determines which fields are available west of the meridian, and observes those fields in the same manner. As targets set below the airmass limit, new fields become available east of the meridian, and the telescope will tile between available fields for the entire night.

At the start of astronomical dawn the telescope will only observe fields west of the meridian, using a similar procedure as above. At 25 minutes before sunrise, the sky brightness levels become too high for the regular science images and the observations are ended. The roof is closed and a series of 10 dark and 10 bias images are taken. The roof then opens and the morning SKYFLAT procedure is run. At the end of the morning sky flat fielding procedure, the telescope is parked, the roof is closed and connections to software packages are closed. This ends the observing for the night.

3.6 Image Processing Script

One of the more complex scripts is the one used to determine whether or not an image is good enough to be used in the current data reduction pipeline or whether is should be kept separate from the regular science images. In this context a “bad” image is one that is either partially or totally covered in clouds, has a larger than usual FWHM value for stars or has excessively large background count values. Although the telescope should not operate in cloudy or unfavourable weather conditions, the information from the weather stations is not always very accurate. The scripts only collect weather information every five minutes and evaluate the conditions based on the last 15 minutes worth of information, which means that fast moving clouds are sometimes observed in parts of the images. The Boltwood* cloud monitors used by the weather stations are also not very good at reporting high level cirrus clouds, which can produce very bad images especially when the Moon is bright.

Data points that are obtained from bad images cause the final lightcurve of a particular object to have many outliers increasing the overall RMS of the lightcurve artificially. If enough of the outlier data points happened to correlate in time, the final lightcurve could be identified as a possible transit candidate, leading to a false-positive. It thus became very important to find some way of identifying and isolating these bad images, in an automated fashion, before they entered the data reduction pipeline. At present the bad quality images are not deleted as some of them might be used in future versions of the data reduction pipeline for additional data points. Most of the images that are classified as bad at present have cloud cover in only parts of the images and it is envisioned that the data reduction pipeline will be improved to take advantage of the unaffected sections.

The IMAGEANALYSIS script is run at 10:00 SAST every day and is started by the Windows Scheduler. The script first calls the CALIBRATIONANALYSIS script (see Section 3.6.1) and waits until this is complete. The image analysis occurs in six basic steps:

1. Calibration image analysis
2. Rename the image files
3. Do subframing
4. Get statistics from sub-images
5. Classify the image
6. Determine FHWM statistics for 3 images

Each of these steps is described in more detail below, with a complete flowchart of the entire process show in Figure 3.13.

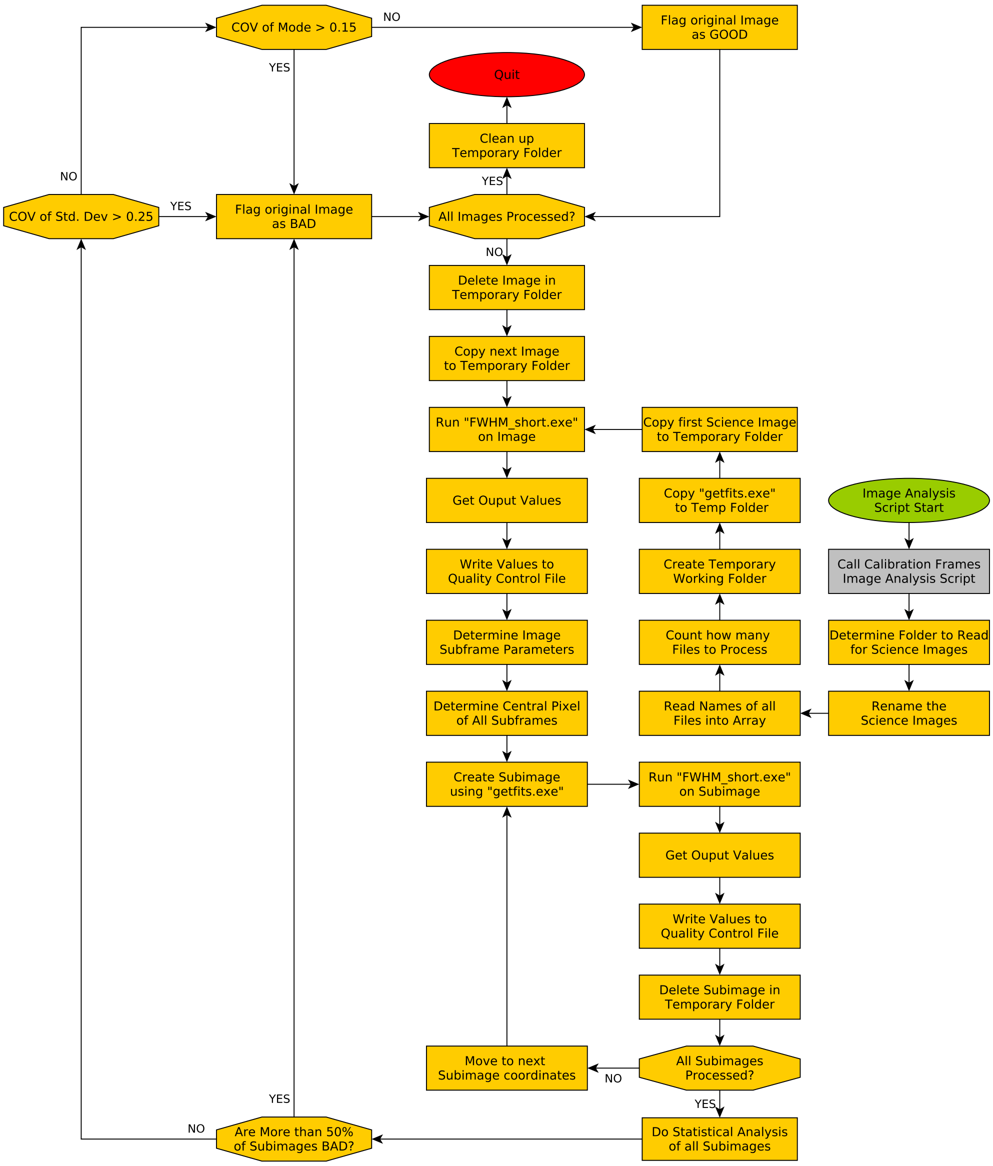

Figure 3.13: Flowchart of the image processing Script.

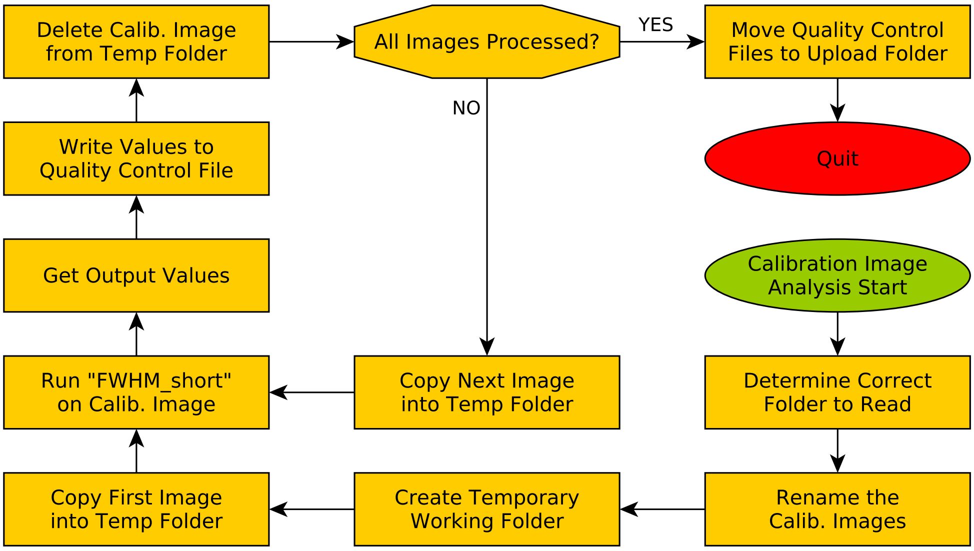

Figure 3.14: Flowchart of the image processing on calibration images.

3.6.1 Calibration Image Analysis Script

The calibration images (flat field, bias and dark) are processed as part of the larger task that does the analysis on all the images taken during the previous night of observation. The CALIBRATIONANALYSIS script (see Figure 3.14) first determines which folder to read and then renames all files in that folder so that they are in a standard format. CCDSoft includes extra information, such as the position of the telescope, the type of image, the right ascension, declination and hour angle of the target, in the names of the files it saves. Since that information is already stored in the headers of the FITS image files, the standard naming provides only the required information to identify the image at a quick glance. This ensures that the bookkeeping of images does not rely on the folder structure on the local hard drive of the control computer, making it easy to transfer files to a single location during data reduction and still know when they were acquired. The first 4 characters indicate the type of image, the next 8 characters are the date of observation and the last 3 characters are the sequential number of that type of image for the particular night (for example: "bias.20130826.002.fits" indicates that this is the second bias image taken on the night starting 26 August 2013). The script creates a temporary working directory in the data folder where all the image processing takes place and this folder is removed at the end of the processing. This ensures that the original data are not destroyed or overwritten as the file to be processed is copied into this temporary folder. A custom C program called FWHM_SHORT then determines the minimum, maximum, mean, standard deviation, median and modal pixel value for the entire image.

The original C program FWHM formed part of the Difference Image Analysis Package

---

[*] http://www.cyanogen.com

(Wozniak 2000) (later modified* by W. Pych) and was used to determine the full-width-at-half-maximum (FWHM) of stars identified on images. A modified version created by R. Pogge was used in the analysis of KELT-North images in 2004/2005. I further modified the FWHM program to only determine the basic statistics of an image instead of identifying point sources and reporting their FWHM value. The FWHM_SHORT program is run from the command line of the Windows XP operating system and the output is redirected to a plain text file. This text file can then be read by a VBS program to extract the required information. There is currently no way to pass information from the FWHM_SHORT directly to the VBS program.

The final step of the script is to delete the current file and copy the next calibration image into the temporary working folder, repeating the process, until all images have been processed. The three plain text output files (one for each type of calibration image) containing all the information are then archived and a copy is moved to the watched folder of FLING FILE TRANSPORT. Once they have been uploaded to the KELT-South monitoring website, they provide a quick and easy way of determining and identifying any problems with the telescope. Unusually high dark or bias counts can be spotted and preventative measure taken to ensure the telescope is operating as it should.

3.6.2 Renaming the Image Files

After the calibration images have been analysed the IMAGEANALYSIS script will start processing the science images. Firstly it determines which folder to do the analysis on and then renames all the files to ensure a standard formatting. The first 9 characters indicated the field number, the next character indicates on which side of the meridian the image was taken, the next 8 characters are the date of the observation and the last 3 characters are the sequential number of that image for the particular night (for example: "survey13s.w.20130826.024.fits" indicates that this is an image for field 13 from KELT-South, the field was west of the meridian and it was the 24^{th} image acquired on the night starting 26 August 2013). After all files are renamed the script determines the number of science images to process and stores the names of the files into an array that can be looped over when the processing begins. Next a temporary working folder is created and all processing takes place in this folder. This ensures that the original data are not touched and cannot be deleted or overwritten by accident as at this point in the KELT-South operations there is only one copy of the raw images (backup of images happens after the processing is complete). The GETFITS program is copied into the temporary working folder and the first science image to be analysed is copied into the same folder.

3.6.3 Do Sub-imaging

To get a global overview of the science image, the FWHM_SHORT program determines the minimum, maximum, mean, standard deviation, median and modal pixel values for the

---

[*] The modified version can be found at: http://ftp.camk.edu.pl/camk/pych/DIAPL_diapl_src.tgz

entire image. The sub-imaging part of the script extracts sections from the original image and determines the same statistical quantities.

The script determines the central pixel coordinate for each sub-image to extract from the original image so that this information can be passed to GETFITS that does the actual extraction. The size of the sub-images and the layout of the grid can be changed in the script. For the script to reliably identify bad images, there needs to be enough sub-images to provide a good statistical sample, but not so many that the process to analyse a single image takes too long to complete. The size of the sub-image is also very important. Smaller sub-images might process faster, but do not sample enough of the original image to provide a good statistical representation of the entire image. Larger sub-images take longer to process and if they are too large, the sub-image edges start to overlap at which point the original image becomes oversampled, leading to a longer processing time than processing the whole image itself. In testing the IMAGEANALYSIS script, 100 sub-images of size 256×256 pixels in a 10×10 grid equally spaced across the original image were found to work best at finding bad images while still completing the process in a reasonable amount of time (currently it takes just over 40s to process one image). The sub-images that are extracted avoid the outer 100 pixels, due to the extreme vignetting. An example of the sizes and locations of the sub-images in relation to the original image can be seen in Figure 3.15.

3.6.4 Get Statistics from Sub-images

The first sub-image is extracted and saved under a temporary file name. The mean, standard deviation, median and modal pixel values are determined for the sub-image and all values recorded in the same quality control file as was created earlier. The script will then delete the current sub-image and move to the next position on the original image and the next sub-image will be extracted and processed. Once all the sub-images have been extracted and processed, the script will do some statistical analysis on all the values stored in the quality control file. A sub-image itself can be classified as bad if the FWHM_SHORT program fails to determine any of the values for that particular sub-image. Some of the reasons a value for the sub-image might not be determined are that the entire sub-image is saturated or obscured by clouds. The following quantities for every sub-image are then determined:

1. Mean pixel value of the sub-image: M_{Si}
2. Standard deviation of pixel value of the sub-image: S_{Si}
3. Median pixel value of the sub-image: E_{Si}
4. Modal pixel value of the sub-image: O_{Si}

where i is the ith sub-image.

Next the following quantities are determined for the entire original image:

1. The number of sub-images: N_S

2. The number of sub-image means determined: N_{SM}
3. The number of sub-image standard deviations determined: N_{SS}
4. The number of sub-image medians determined: N_{SE}
5. The number of sub-image modes determined: N_{SO}
6. The mean of all the sub-image means: μ_M
7. The mean of all the sub-image standard deviations: μ_S
8. The mean of all the sub-image medians: μ_E
9. The mean of all the sub-image modes: μ_O
10. The standard deviation of all the sub-image means: σ_M
11. The standard deviation of all the sub-image standard deviations: σ_S
12. The standard deviation of all the sub-image medians: σ_E
13. The standard deviation of all the sub-image modes: σ_O
14. The coefficient of variation of all the sub-image means: CV_M
15. The coefficient of variation of all the sub-image standard deviations: CV_S
16. The coefficient of variation of all the sub-image medians: CV_E
17. The coefficient of variation of all the sub-image modes: CV_O

where the coefficient of variation (CV) is defined as the ratio of the standard deviation (σ) to the mean (μ) and is a normalized measure of the dispersion around the mean. Based on these 17 values, an image can be classified as good or bad.

3.6.5 Classify the Original Image

In order to use the value determined in the previous section, a large number of good and bad images needed to be compared to one another to find some metric that will show a clear distinction between known good and known bad images. For this purpose, I spent many nights in Sutherland observing when it was unsuitable for regular observing and collected well over 200 images with varying degrees of cloud cover and different Moon illumination fractions. After many images were processed using the methods described above, it was found that there are four parameters that can be used to determine if an image is good or bad. The original image is classified as bad if any of the following conditions are satisfied:

1. $\frac{N_{SS}}{N_S} < 0.5$
2. $\frac{N_{SO}}{N_S} < 0.5$

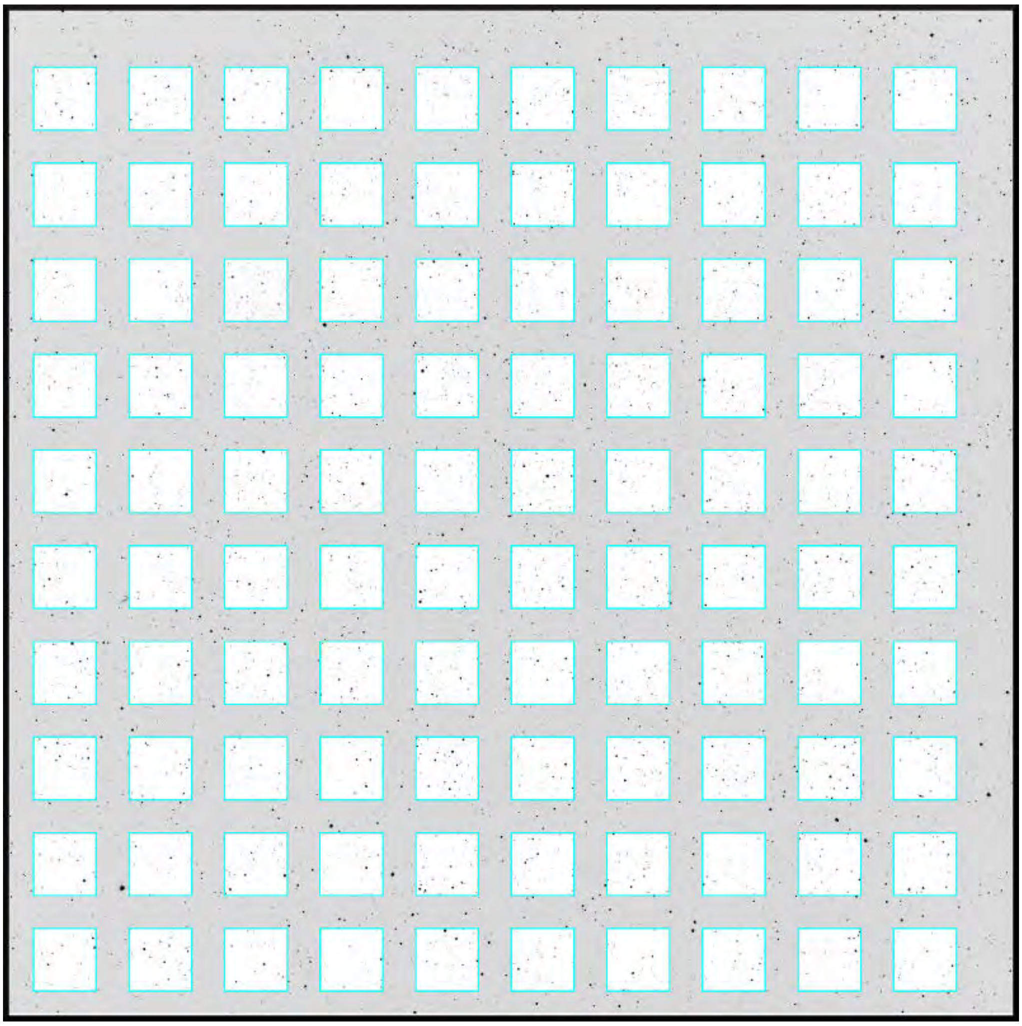

Figure 3.15: An example image showing the size and locations of the sub-images extracted during the image analysis procedure.

3. $CV_S > 0.25$
4. $CV_O > 0.15$

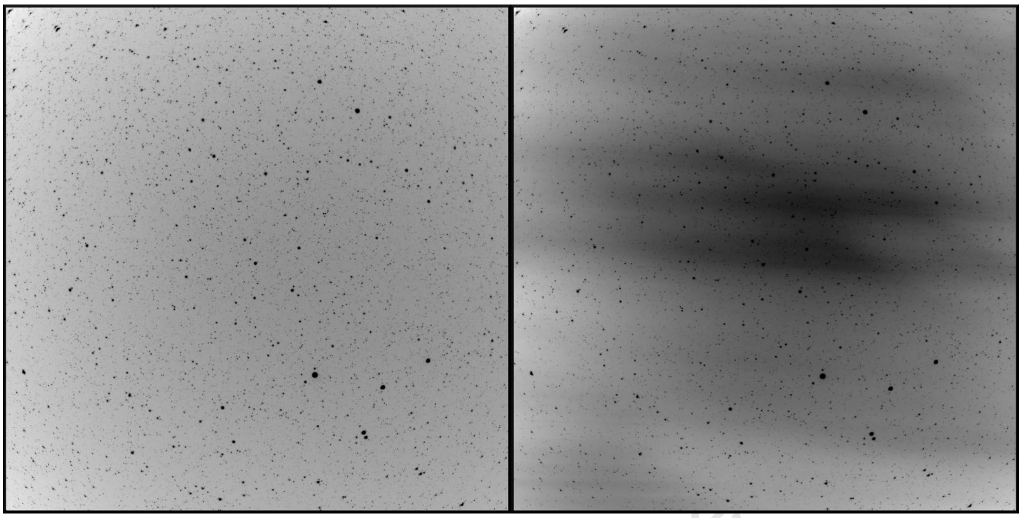

(a) Image with no clouds. (b) Image with clouds.

Figure 3.16: Two images of the same field taken a few hours apart. The image on the left shows no clouds present and the image processing script determined that it was good for data analysis. The image on the right clearly shows the effect clouds can have on an image and the image processing script correctly identified it as a bad image.

Figure 3.16 shows an example of a good image on the left and an image that was identified as bad on the right. The full list of all determined quantities for the images can be seen in Table 3.2.

This process of classifying images does a reasonably good job at finding really bad images, but images with slight gradients are not found using this method. Large scale variations from one side of the image to the other are most easily identified and the image is flagged as bad. Images that pass the classification are further checked by eye before entering the data reduction pipeline, but the current image analysis script has reduced the number of images to visually inspect by ~15%. No flat fielding or bias/dark corrections are done on the images before the images are processed, as it was found that this did not have any influence on the classification of an image.

3.6.6 FWHM for 3 Images

The last part of the IMAGEANALYSIS script determines the FWHM of all identified stars on 3 images and this information can be used to keep track of the stability of the optical components of the telescope. Only the images that passed the quality check are considered for this analysis and the script will obtain the information for images acquired at the beginning,

Table 3.2: Table of the statistical quantities determined for the two images in Figure 3.16.

Statistical Quantity	Good Image Values	Bad Image Values
N_S	100	100
N_{SM}	100	100
N_{SS}	100	100
N_{SE}	100	100
N_{SO}	100	100
μ_M	4483.561	16519.182
μ_S	787.78	908.397
μ_E	4371.583	16444.096
μ_O	4349.227	16260.494
σ_M	494.137	2426.732
σ_S	95.046	275.915
σ_E	477.662	2453.294
σ_O	478.549	2496.502
CV_M	0.11	0.147
CV_S	0.121	0.304
CV_E	0.109	0.149
CV_O	0.11	0.154

middle and end of the night. If no images were good from the previous night, this part of the script simply doesn't run.

The full version of the FWHM program is run on each image and the FWHM for the identified point sources are recorded. A plot of the FWHM distribution is generated using GNUPLOT and the data file and plot are uploaded to the website (an example of the FWHM distribution can be seen in Figure 3.17). A file containing the history of the FWHM's of all the files previously processed is updated, plotted and uploaded to the monitoring website. The history file provides a good archive of the FWHM values of the images over the course of the lifetime of the telescope and can be used to track changes in the focus of the telescope lens (a detailed discussion is presented in Section 4.10.2).

Once the three images have been chosen, the script makes use of IMAGEMAGICK to convert each full 4096×4096 FITS image into a 1024×1024 JPEG image file that is uploaded to the KELT-South monitoring website. Five sub-images for each full image are also extracted, one for the central 128×128 pixels and one for each of the corners of the full image (see Figure 3.18) are also converted into JPEG image files and uploaded to the monitoring website. These images are viewable from the monitoring website and can be used to investigate the shapes of the stars in those images, making the process of identifying irregularities in the telescope performance possible.

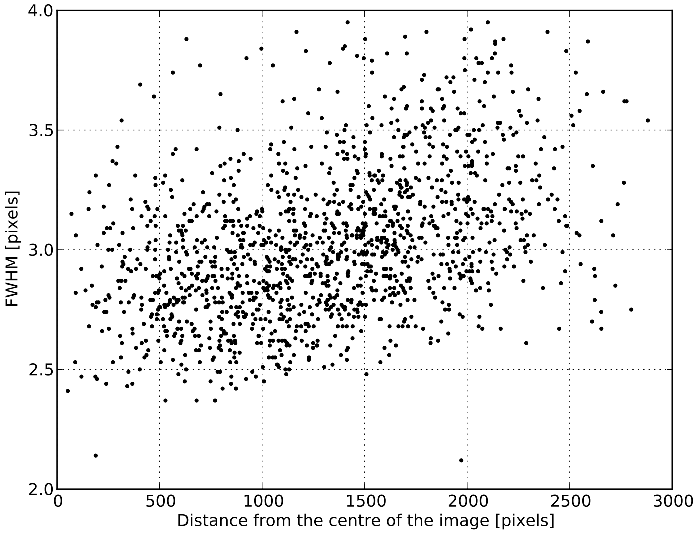

Figure 3.17: Plot of the FWHM distribution for all identified stars for a typical image. Notice the increase in FWHM for stars located further away from the centre of the image. This is simply due to the distorted shapes of the stars towards the edges of the image.

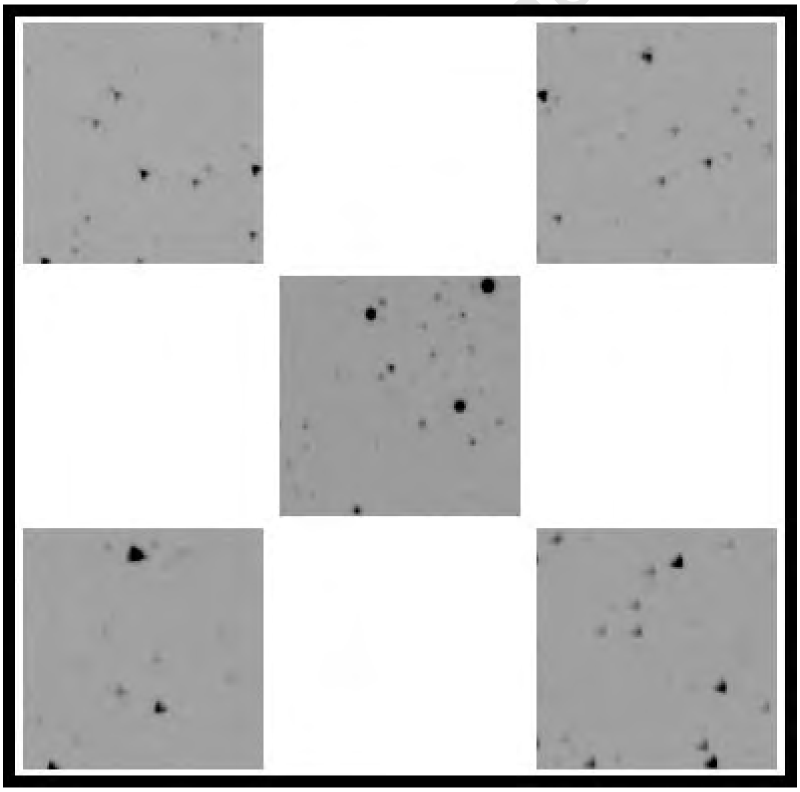

Figure 3.18: Image of the thumbnail previews of the full science image. The placement of each thumbnail represents the location it was extracted from on the full size image.

Chapter 4

Instrument Performance

4.1 Introduction

The previous chapters described the KELT-South hardware, software and control scripts that allows the telescope to perform the robotic observing operations. In this chapter the performance of the various aspects of the telescope will be discussed. I will also show how the hardware specifications provided by the manufacturers of the various components were verified. Over the 5 year operation of the telescope, there have been only two major downtimes. The first was after the first commissioning season when it was found that the two-stage Peltier cooling system could not maintain the CCD at a temperature of -20°C, resulting in a 3 month period with no observations while the upgrades to the cooling system were performed. The second downtime occurred after a lightning strike close to the KELT-South dome damaged the original UPS and transformer. This resulted in a complete loss of power to all the hardware systems of the telescope and replacement parts were only installed a few weeks later.

4.2 Telescope Field of View and Plate Scale

4.2.1 Field of View

The "angle of view" describes the angular extent of a given scene that is imaged by a camera. It is used interchangeably with the more general term field of view (FOV) and for lenses projecting non-spatially-distorted images of distant objects, the effective focal length and the image format dimensions completely define the FOV. The manufacturer of the Mamiya 654 lens used by the KELT-South telescope lists the angle of view at 47°. However, when used in combination with the CCD sensor, the total FOV of the telescope can be calculated as follows:

$$\alpha = 2\arctan\frac{d}{2f} \tag{4.1}$$

where d is the detector size (in either the horizontal or vertical direction) and f is the focal length of the lens. In KELT-South the detector is 36.88×36.88 mm in size and the focal length of the lens is listed as 80 mm. This results in a viewable area for the KELT-South telescope of 25.96°×25.96°.

4.2.2 Plate Scale

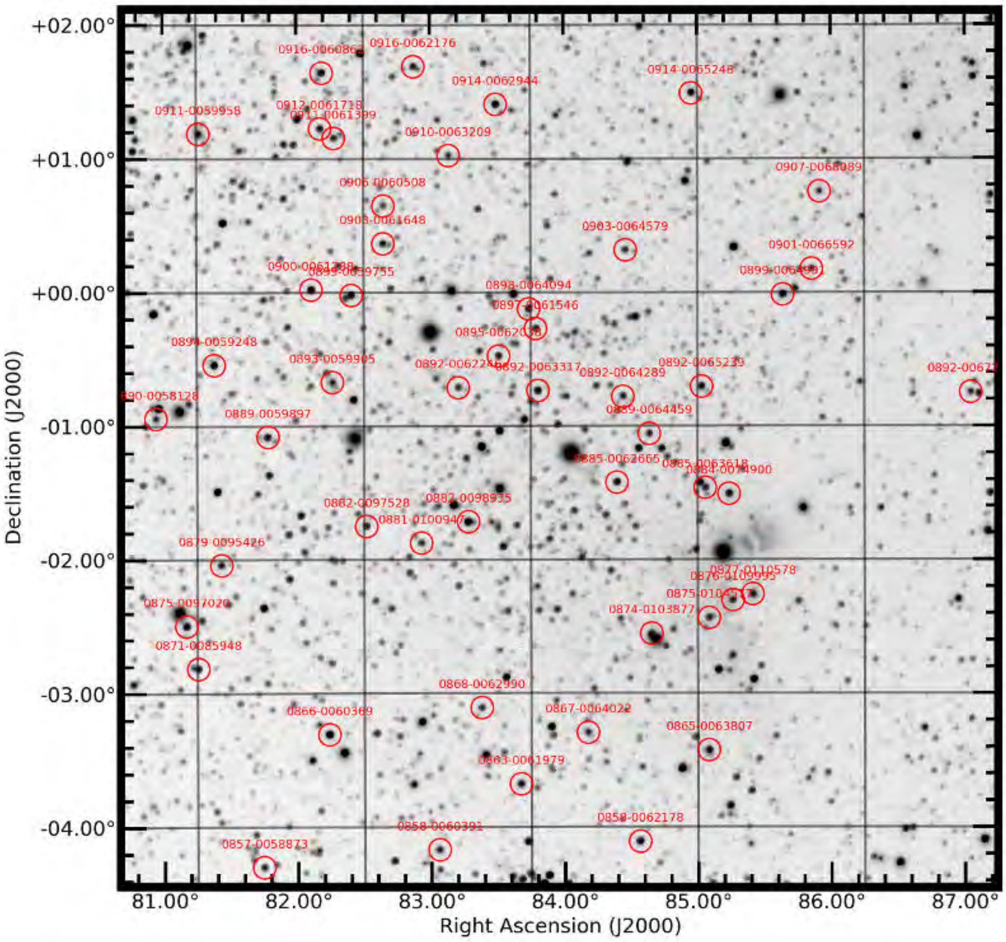

Figure 4.1: Image of known star field showing the stars used to determine the plate scale of the telescope.

The plate scale of the telescope was determined in three different ways. The first method simply uses the FOV of the telescope and the number of pixels on the CCD detector. For KELT-South the FOV is 25.96° and the number of pixels is 4096. The plate scale was determined to be 22.82″ pixel^{-1}.

The second method to determine the plate scale involved the following steps:

- Take an image of a known part of the sky.

Table 4.1: Table of the positions of stars used to determine plate scale. Only the first 10 entries are listed, but all 50 were used to calculate the plate scale.

USNO-B1 Name	X Pos	Y Pos	RA (J2000)	Dec (J2000)
0890-0058128	41.06	545.95	80.942745	-0.945584
0875-0097020	77.11	303.87	81.168242	-2.497848
0871-0085948	91.01	254.08	81.255006	-2.81547
0911-0059958	90.07	878.64	81.26465	1.185595
0894-0059248	108.99	608.67	81.379495	-0.543953
0879-0095426	117.96	375.16	81.429912	-2.040312
0857-0058873	168.07	23.01	81.743814	-4.299139
0889-0059897	171.97	524.94	81.780548	-1.083075
0900-0061288	222.08	696.96	82.107295	0.020334
0912-0061718	232.06	885.07	82.175384	1.22697

- Identify a number of non-saturated stars in the image using the IMSTAR utility (central pixel location for saturated stars is poorly defined).
- Determine the pixel coordinate location of each star.
- Determine the distance in pixels from every star to each of the others and record those values.
- Compare the list of identified stars with an online catalogue to find the celestial coordinates of each one.
- Determine the angular distance from every star to each of the others and record the values.
- Determine the plate scale by dividing the angular distance by the pixel distance.
- Calculate the mean and standard deviation of all the plate scales determined.

Figure 4.1 shows the locations of the stars used to determine the plate scale and Table 4.1 lists the relevant information for all the stars. The pixel separation can be determined by the Pythagoras theorem:

$$D = \sqrt{(x_2 - x_1)^2 + (y_2 - y_1)^2} \tag{4.2}$$

where D is the pixel distance between the two stars on the image, x_1 and x_2 are the X coordinates of the two stars and y_1 and y_2 are the Y coordinates of the two stars. Angular separation was determined as follows:

$$\theta = \tan^{-1}\left(\frac{\sqrt{\cos^2\delta_2 \sin^2(\alpha_2 - \alpha_1) + [\cos\delta_1 \sin\delta_2 - \sin\delta_1 \cos\delta_2 \cos(\alpha_2 - \alpha_1)]^2}}{\sin\delta_1 \sin\delta_2 + \cos\delta_1 \cos\delta_2 \cos(\alpha_2 - \alpha_1)}\right) \tag{4.3}$$

where θ is the angular distance between two of the stars, α_1, α_2, δ_1 and δ_2 are the right ascension and declination of the two stars respectively. The pixel and angular distances for

1225 pairs of stars were determined and the plate scale was determined for each of these pairs. Finally the mean plate scale was determined. Using this method the plate scale was determined to be $23.09\pm0.01''$ pixel^{-1}.

A third method to determine the plate scale was to upload the image to the Astrometry.net website and obtain a coordinate solution for the image shown in Figure 4.1. Astrometry.net is capable of providing coordinate solutions using blind search methods and in the process provides an estimate for the plate scale of the image (see Section 5.2.4 for a detailed description of how this program works). The plate scale estimate from Astrometry.net was $23.11''$ pixel^{-1}.

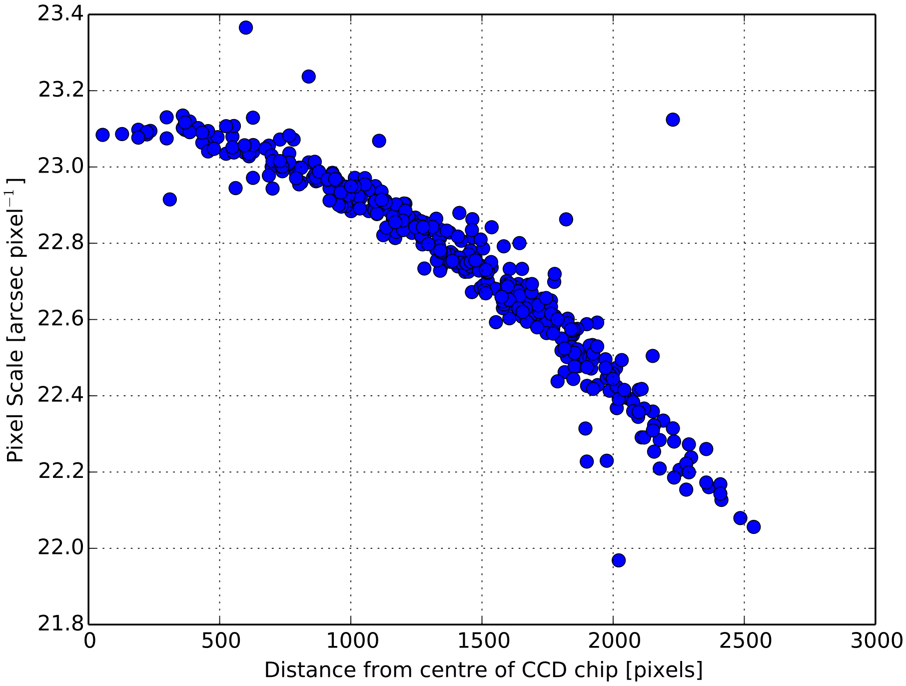

Figure 4.2: Plot of the plate scale as a function of the radial distance from the centre of the CCD chip.

The three values determined above can be seen as a “special” average plate scale. In reality, the plate scale of the telescope will vary with radial distance from the centre of the CCD chip due to the barrel distortion introduced by the wide field of view of the Mamiya lens. To show how the plate scale changes across the FOV, the eastern orientation Target1 reference image (see Section 5.2 for more details) was cut into 400 blocks of 256×256 pixels in size, arranged in a 20×20 grid equally spaced across the entire image (some of the blocks overlap slightly). Each of these blocks was then analysed with Astrometry.net and the plate scale of each block as well as the central pixel coordinate of each block recorded. Figure 4.2 shows how the plate scale changes as a function of radial distance from the centre of the

CCD chip. The plate scale changes from ∼23″ pixel^{-1} in the centre, decreasing to ∼22″ pixel^{-1} in the corners. The average plate scale using this method was 22.73±0.24″ pixel^{-1}. This is not unsurprising as this type of barrel distortion is a well understood phenomenon with wide angle lenses used in photography*.

4.3 CCD Calibration and Performance Verification

4.3.1 CCD Gain

The gain of a CCD is set by the electronics that read out the charges on the chip and is usually expressed in units of electrons per count. This means that a CCD with a gain of 2.5 e^- ADU^{-1} will produce 1 count for every 2.5 recorded electrons. However, electrons cannot be split into fractional parts, which means a gain of 2.5 e^- ADU^{-1} will result in 1 count being registered from 2 electrons 50% of the time, and 1 count being registered from 3 electrons the other 50% of the time (see the discussion on CCD gain by Newberry (1998)). It should be noted that the gain is an average conversion ratio and can only be determined by changing many electrons in many counts. The manufacturer of the CCD can, to some degree, estimate the gain by using the nominal tolerances of the electronic components and this is based on the resistor values used in the gain stage of the CCD readout electronics. However, the actual gain can be vastly different from the estimate as the resistance is subject to component tolerances. The actual gain can only be determined using a gain calibration test.

The gain can be measured by comparing the signal level to the amount of variation in the signal of the CCD, and is a consequence of the relationship between the counts and the electrons being different for the signal and the variance.

The signal in counts and the amount of noise in counts are related to the signal level in electrons and noise level in electrons via the gain as follows (Newberry 1998):

$$S_C = \frac{1}{g} S_E \tag{4.4}$$

$$N_C = \frac{1}{g} N_E \tag{4.5}$$

where S_C and N_C are the source and noise measured in counts, S_E and N_E are the source and noise measured in electrons and g is the gain. Any signal measured from the CCD will also contain a certain amount of noise. This noise comes from various sources and includes the readout noise R_E, photon noise σ_P and any other constant source of noise σ_E. The noise sources can be combined to give a final noise contribution in terms of number of electrons in the following way:

$$N_E^2 = R_E^2 + \sigma_P^2 + \sigma_E^2 \tag{4.6}$$

where the fact that the noise sources are independent of one another is used to add them in

---

*http://photographylife.com/what-is-distortion quadrature. Photon noise obeys Poissonian statistics, which means that the square of the noise is equal to the signal, which leads to:

$$N_E^2 = R_E^2 + S_E + \sigma_E^2 \tag{4.7}$$

and by substituting what we know of how the gain relates the electrons to counts we obtain the following:

$$g^2 N_C^2 = g^2 R_C^2 + g S_C + g^2 \sigma_C^2 \tag{4.8}$$

which can be simplified to relate the noise level in counts to the signal level in counts as follows:

$$N_C^2 = \frac{1}{g} S_C + (\sigma_C^2 + R_C^2) \tag{4.9}$$

From this it can be seen that a plot of S_C versus the N_C^2 should produce a straight line with slope g, if the noise term $(\sigma_C^2 + R_C^2)$ were constant. Figure 4.3 shows that this is not the case for the KELT-South CCD. The noise term, σ_C, is due to the pixel-to-pixel

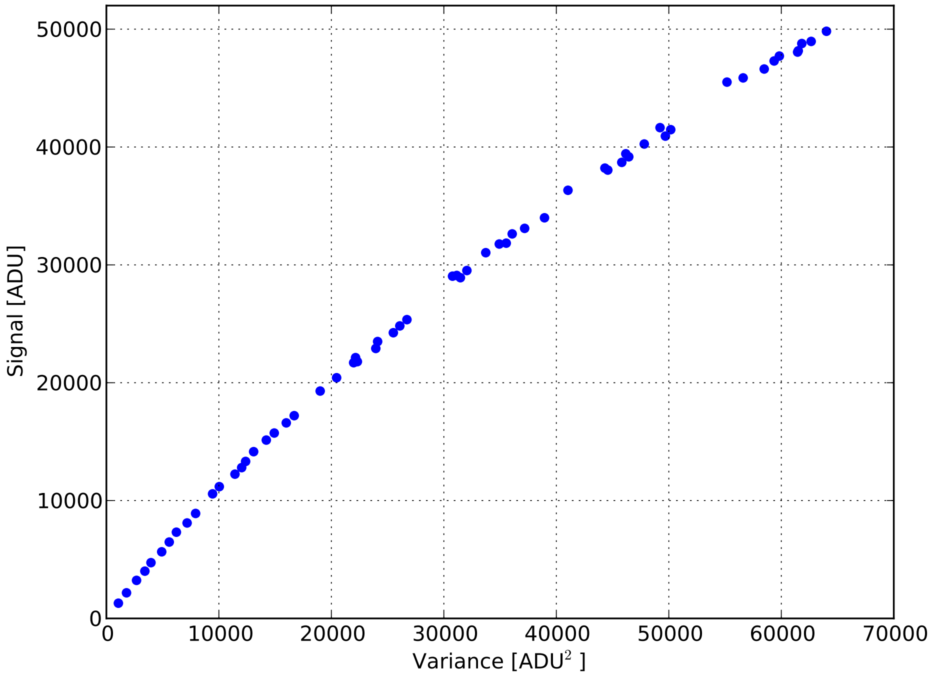

Figure 4.3: Figure showing that the noise added to the signal in the KELT-South CCD is not linear.

variation (also known as the flat field effect) in the sensitivity of the CCD and to correctly determine the gain of the CCD this noise factor needs to be taken into account. The "flat field noise" can be expressed as a constant offset of the signal, $\sigma_C = kS_C$. Substituting this new proportionality into equation 4.9 leads to:

$$N_C^2 = \frac{1}{g} S_C + k S_C + R_C^2 \tag{4.10}$$

and solving the quadratic function for S_C will produce an equation that fully describes the Signal-Variance plot shown in Figure 4.3:

$$S_C = \frac{-1 + \sqrt{1 + 4g^2k^2(N_C^2 - R_C^2)}}{2gk^2} \tag{4.11}$$

The strength of the flat field variation k determines the curvature of plot. This shows that it is impossible to determine the gain from the Signal-Variance plot unless the value of k is known or the determination of the gain is done in such a manner as to avoid the flat field variation. The determination of k can be done numerically, but removing the flat field effect is much easier to implement and only requires that the strategy used to obtain the calibration images be altered slightly. Instead of obtaining calibration images at various exposure times, the revised strategy involves taking pairs of calibration images with the same exposure times and at the same signal level. This process is then repeated with an increased light intensity level received by the CCD and not changing the exposure time. This can be done by altering the amount of light passing into the camera or by varying the light intensity level itself. For KELT-South, the amount of light entering the camera was changed by pointing the camera upwards and stacking pieces of white paper on the lens hood. The more papers that were added, the lower the intensity of light that entered the camera.

To eliminate the flat field effect, the following procedure was followed to determine the gain:

1. Two light images were obtained at the same light intensity level and exposure time.
2. A bias images was also obtained after each light image.
3. The bias level was subtracted from each image.
4. The mean signal level (S_1 and S_2) in the central 128×128 pixels was determined for each image.
5. The ratio $R = S_1/S_2$ was calculated and image 2 was multiplied by this ratio to correct for any variation in the signal levels of the two images (which should be minimal due to the fact that they were both obtained at the same exposure time and light intensity level).
6. The images were subtracted from one another to remove the flat field effects present in both images.
7. The standard deviation in counts was determined for the subtracted image in the same central pixel region as used earlier.

8. The variance was determined and divided by 2 to correct for the fact that the variance is doubled when subtracting similar images from one another.
9. The signal level and variance was recorded.
10. The steps were repeated, changing the light intensity level until the central pixel region was almost saturated.

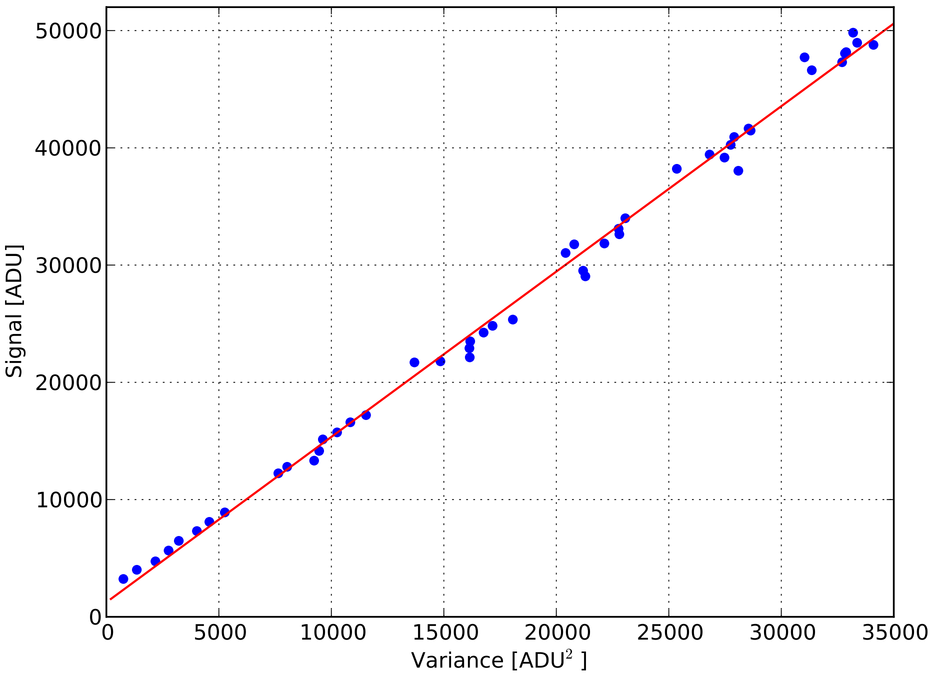

Figure 4.4: Figure showing the improved Signal-Variance plot that can be used to determine the gain of the CCD used by the KELT-South telescope. The red line indicates the best fit straight line to the datapoints.

A Signal-Variance plot can now be made and Figure 4.4 shows the result. The data now follow a straight line and the slope of the straight line was determined to be 1.41 e^- ADU^{-1} which corresponds very well with the claim by Apogee Instruments that the gain of the CCD is 1.4 e^- ADU^{-1}.

4.3.2 Read Noise

The readout noise of the CCD can be calculated by making use of two bias images and the gain value calculated in the previous section. The bias images were subtracted from one another and the standard deviation was determined for the same central pixel region as used earlier. This was then divided by $\sqrt{2}$ to obtain the readout noise in units of counts. Multiplied by the gain determined earlier provides the readout noise of the CCD in electrons.

The read noise for 48 pairs of bias images were taken and the mean was determined to be 7.2 counts, which means that the read noise is $\sim 10\ e^-$. This agrees very well with the quoted read noise of $\sim 9\ e^-$ provided by the manufacturer.

4.3.3 Dark Current

After the calibration images were obtained for the gain calculation, the telescope was instructed to obtain 60 pairs of dark and bias images. These images were obtained with the telescope in the park position and exposure times were the same as for the calibration images. The dark current for each image was determined by subtracting the mean pixel count value for each bias frame (the central 128×128 pixels) from every dark frame, dividing by the exposure time and multiplying by the gain. The median dark current was determined to be 0.105 e^- pixel^{-1} s^{-1}. The laboratory testing performed by Apogee Instruments lists the dark current as $< 1.4\ e^-$ pixel^{-1} s^{-1}.

4.3.4 CCD Linearity Response

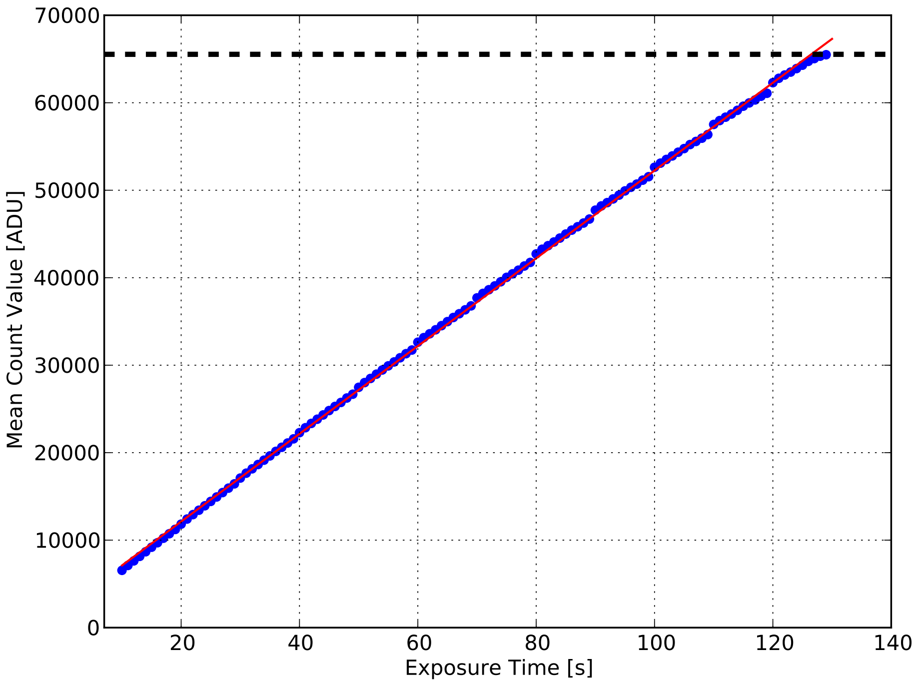

Figure 4.5: Figure showing the linearity response of the KELT-South CCD. The thick black dashed line indicates the saturation level of the CCD at 65535. The red line is the best fit straight line to the datapoints and shows that the CCD is almost perfectly linear. There is a slight deviation from linearity at very high counts.

Figure 4.5 shows the results of the CCD linearity response. Flat field calibration images were obtained with increasing exposure times until the central 128×128 pixels reached the saturation level of 65535 counts. The mean count value for each image was recorded as well as the exposure time and then plotted. The CCD has an almost perfect linear response, deviating slightly from linear only at very high counts. The results of this test did not take the dark current contribution into account, as the exposure times were short enough to minimize the impact the dark current would have on the final results. Dark current increases with exposure time, but at 130 second exposure the contribution is ∼9 counts, which is less than ∼0.0001% of the total counts at the saturation level. The KODAK KAF-1603 CCD can have exposure times from as short as 30 milliseconds to 183 minutes (in 2.56 microsecond increments), which means that each exposure has an accuracy of ∼3 microseconds*. This level of time accuracy is far better than the required accuracy for transiting exoplanet searches, where a typical accuracy of minutes is usually obtained. The slight deviation from a straight line in Figure 4.5 is therefore not due to any incorrect calibration of the exposure time.

4.3.5 CCD Temperature Stability

Apogee Instruments quoted the temperature stability of the CCD at ±0.1°C. From the calibration frames obtained and used in the previous sections it was determined that the CCD temperature is in actual fact -21.55±0.71°C, even though the control scripts instruct the CCD to maintain a temperature of -20°C. This indicates that the manufacturer greatly underestimated the temperature stability. However, the dark current (which increases with increasing temperature) is extremely low at these temperatures and has no influence on the operations of the KELT-South CCD.

4.3.6 Vignetting

Relative to other hardware designs, vignetting is not a big problem for KELT-South due to the medium format camera lens. The lens is designed to illuminate a patch of film much larger than the physical size of the KELT-South CCD, which greatly reduces the amplitude of vignetting. Even with the reduced vignetting due to the CCD detector being much smaller than the medium-format image size, there is a decrease in flux measured from the centre of the image to the edges of ∼28% and from the centre of the image to the corners of ∼45%. Figure 4.6 shows a master flat field image and clearly shows the vignetting effect. The decreased flux levels were determined by extracting 100 pixels in a 10×10 grid from the corners and edges of the flat field image, calculating the mean counts in each block and comparing the number of counts with a similar extracted block from the middle of the image.

The typical pointing precision (see Section 4.11.2) is relatively good over the course of an entire observing season and the vignetting does not cause any problems. Generally the stars don't move around in areas where their flux measurements change rapidly due to vignetting

---

[*] http://www.opticstar.com/Run/Astronomy/Astro-Imagers-Apogee.asp?p=0_10_0_10_515

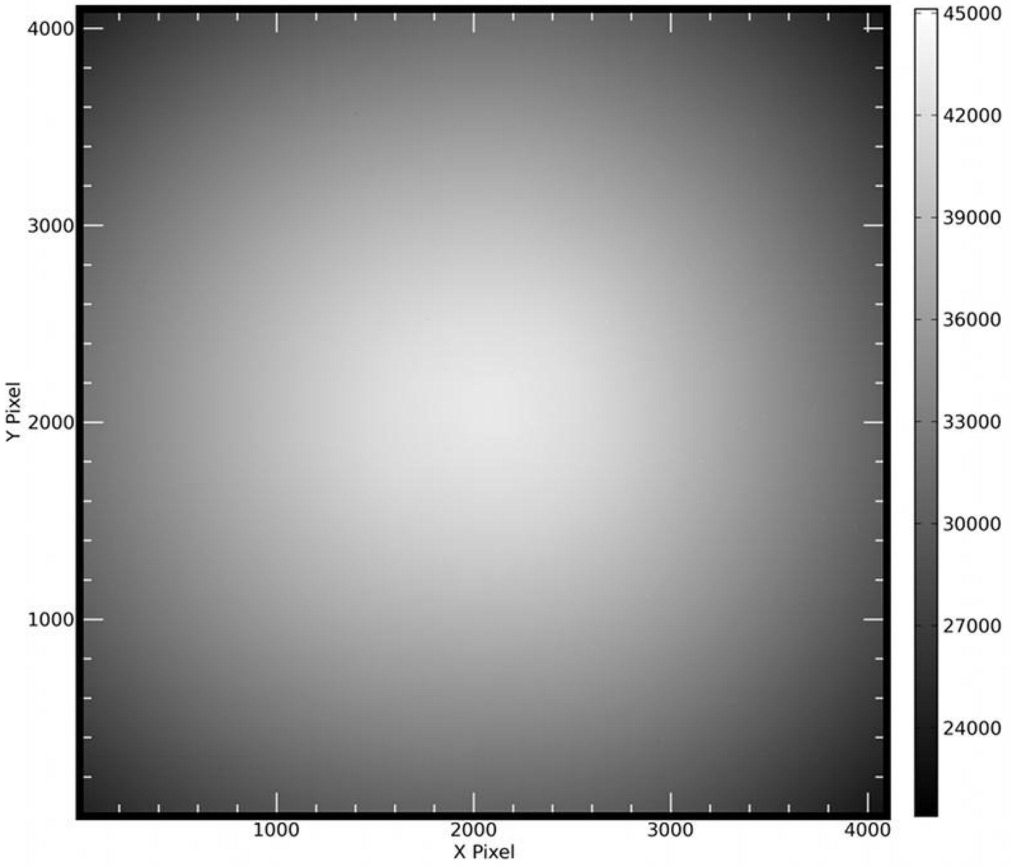

Figure 4.6: Master flat field image showing moderate vignetting.

and slow changes in brightness do not pose a problem for ISIS and the image subtraction data reduction pipeline (discussed in more detail in Section 5.2.3). A larger problem is the pixel-to-pixel sensitivity variation where the spatial scale is comparable to the PSF size. This problem is discussed in Section 4.4

4.4 Flat Fielding and Scattered Light

An ideal CCD detector will generate electrons in direct proportion to the number of photons that were incident on it. However, things like pixel-to-pixel variation in response to photons and vignetting will interfere with this ideal behaviour. One of the ways to correct for most of these problems is flat field correction.

Flat fielding is required for two reasons. Firstly, the effect due to vignetting needs to be removed (see Section 4.3.6). Secondly, the pixel-to-pixel variation needs to be taken into account. Each pixel in the CCD detector has a slightly different gain and the response of each pixel to the same amount of flux will be slightly different. A pure flat field is meant to preserve this difference in sensitivities and by dividing all science images by the flat field image, the changes due to the decrease of flux caused by vignetting and the pixel-to-pixel variation are removed. Three types of flat field images are obtained with KELT-South; dome flats, a night sky "super" flat and twilight flats.

Dome flats are obtained (usually in bad weather conditions), by pointing the telescope at the flat field screen that is bolted to the underside of the roll off roof in the KELT-South dome. The main benefit to dome flats is that the flux levels can be adjusted to get counts at ∼90% of the full well capacity (just before CCD non-linearity starts). For KELT-South, the dome flat field screen is illuminated by 4 lamps that are mounted to the walls of the KELT-South building, making the telescope the centre of the square. Some of the considerations when installing the dome flat field screen were the reflective nature of the screen, the perpendicularity of the screen with respect to the optical axis of the telescope, the size of the panel and the even illumination of the screen. The 4 lamps that surround the telescope can be independently switched on or off and the brightness levels can be controlled from inside the dome. By making small adjustments to the lamps during the commissioning phase of the telescope a relatively even illumination of the flat field screen was achieved. The main problem with the dome flat field images we obtain is that the exposure times are very short to prevent the CCD from saturating. In normal procedures, the flat field images should be obtained with exposure times that are relatively close to the exposure times used for science images, but this cannot be done with KELT-South as the CCD saturates with exposure times as short as 5 seconds (at which point vignetting effects due to the shutter are noticeable) even with the lowest illumination setting of the 4 flat field lamps.

The night sky super flat is constructed by a median combination of many thousands of science images. The raw science images have a non-flat background and this information can be used to create a flat field image. A median combination of many thousands of science images removes the contribution of the stars (the positions of the stars do not fall on the same pixels every time) but preserves the background sky. This night sky super flat in general does not have enough background flux to get to the desired ∼90% of the CCD full well capacity.

At present, the KELT-South data reduction pipeline does not use the dome or night sky super flat field images. These images are only used to check large scale changes in pixel-to-pixel variation of the CCD. If these flat field images indicate a change in the pixel-to-pixel response, the creation of a new master twilight flat field image is initiated.

For the twilight sky flats, images of the twilight sky are usually taken a few minutes after sunset and a few minutes before sunrise. The flat fielding of a very large field of view telescope like KELT-South is an extremely difficult procedure. The basic problem is that since the field of view is so wide (26×26 degrees), we are unable to get a true flat field with perfect illumination across the entire field. Taking images of the twilight sky with the telescope pointed straight up is the usual procedure for obtaining flat field images, but with the German equatorial mount, pointing directly at the zenith is not possible. Instead we point the telescope to a few degrees either side of the meridian, but with the extremely wide field of view of the KELT-South telescope, the twilight sky is not uniform across the entire image. Twilight flats are taken with the telescope in the eastern orientation after sunset and dawn flats are taken with the telescope in the western orientation. To obtain a “master flat” for KELT-South, many hundreds of twilight sky flat field images are inspected by eye and then stacked into a single image. The exact requirements for a flat field image to be included in the set that make the final master flat is the main focus of an upcoming paper (Siverd 2014), but the main features are that they should contain no clouds and star trails in the outer edges should not be present. This one master flat field image is then used for all science images. This is unusual as most other exoplanet survey telescopes will use a flat field image that varies from day to day. KELT-South is able to use this one master flat field image for all science image calibration by having a fairly small lens, operating out of focus and getting semi-regular cleaning. The CCD chip used by the KELT-South telescope is very stable and the creation of a master flat field image has only been done twice in the four years of the regular survey. With these procedures, KELT-South is able to achieve a master flat field image that has a RMS scatter of ∼0.002, which is below the 5-10 mmag depth of a typical Hot Jupiter transiting exoplanet.

Scattered light does not contribute significantly to the overall noise of the KELT-South telescope. The large pixel scale and high sky brightness levels are the dominant source of noise when making measurements of fainter stars. The KELT-South telescope does suffer from internal reflections in the lens when fields are very close to the Moon, which is why a specific routine was built into the observing script to avoid any field that is within 50° of the Moon (see Section 3.5.10). To show that no scattered light is present in the KELT-South system, a sequence of twilight flat images were median combined (images acquired just after sunset) and divided by the master flat. The resulting image was then divided by the median value of the pixel counts. Figure 4.7 shows that the only contribution left after this procedure is the sky gradient and no other light contributions are present in the image.

4.5 Sources of Noise

There are a number of factors that contribute to the overall noise in a lightcurve when making observations using a telescope like KELT-South. In general, noise can be divided into two main categories; random uncorrelated (white) noise and time correlated (red) noise. This noise can make the detection of transiting exoplanet signals very difficult by either obscuring the real transit signal (white and red noise) or by creating false signals (red noise) that lead to a false positive detection (Pont et al. 2006). Noise in the lightcurves is especially problematic for small aperture telescopes such as KELT-South and the combination of white and red noise (pink noise) cannot be ignored and tends to be the dominant source of noise in the observations of bright stars. The different sources of each type of noise are discussed below.

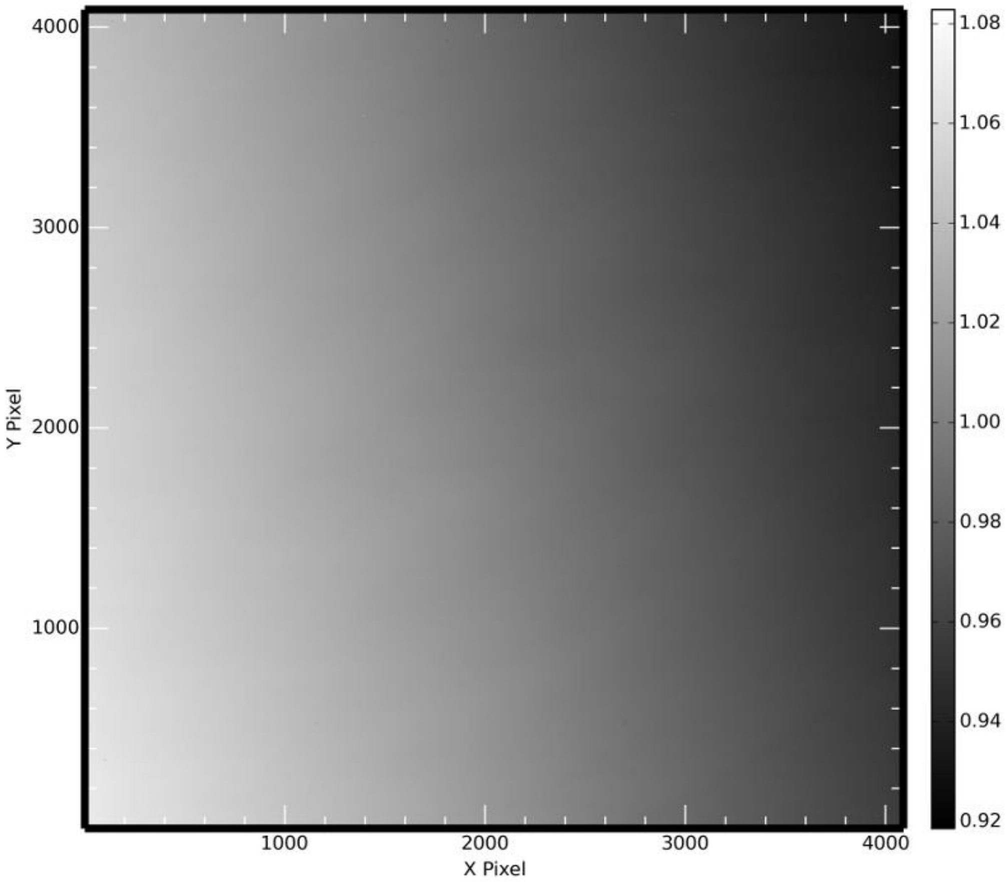

Figure 4.7: Figure of the remaining light contribution after a sequence of twilight flat field images were divided by the master flat field image and normalized. The only residual present is the sky gradient and no other sources of contamination are present.

4.5.1 White Noise

White noise comes from the fact that the signals that are measured at the telescope originate from the random arrival times of photons at the telescope. This type of noise is completely random and follows a Poisson distribution. To improve the chances of detecting a transit like event in the presence of white noise, more photons need to be collected. White noise arises from a number of sources discussed below:

1. *Dark Current Noise*

Dark current arises from thermal energy within the silicon lattice that make up the CCD chip. Given enough thermal energy, some electrons are liberated from the lattice over time and this liberation is independent of the light falling on the detector. These liberated electrons are then captured by the potential wells of the CCD and are counted as signal. The number of liberated electrons fluctuates and this statistical fluctuation is known as dark current noise. The dark current of the KELT-South CCD was calculated in Section 4.3.3, and in general can be expressed as:

$$\sigma_d = \sqrt{D n_p t} \tag{4.12}$$

where σ_d is the dark current noise, D is the dark current, n_p is the number of pixels and t is the exposure time. Dark current in the CCD is sensitive to the temperature and can be minimized to the point where it becomes negligible if the the CCD is cooled to a suitable degree, which is why the KELT-South CCD operates at -20° C.

2. *Read Noise*

Read noise is the amount of noise generated by the electronics of the CCD as the charge in the pixels is transferred to the camera. It is a combination of all the noise generated by the system components responsible for the conversion of the charge in each pixel into an ADU signal. Read noise is added to each pixel as it is read out and is applied uniformly across the CCD as the data is read out, it does not depend on the exposure time. The read noise of the KELT-South CCD was calculated in Section 4.3.2 and is expressed as:

$$\sigma_R = \sqrt{R^2 n_p} \tag{4.13}$$

where σ_R is the total read noise, R is the read noise per pixel and n_p is the number of pixels. In most modern CCD's, the components are manufactured to minimise the amount of read noise and can be ignored in most applications, unless the target of the observation is very faint.

3. *Photon Noise of the Star*

The star produces photons in a random Poisson process, so that there are random variations in the number of photons which strike the CCD chip in any fixed time interval. The size of these random variations is simply the square root of the number of produced electrons:

$$\sigma_{ph} = \sqrt{N_s} = \sqrt{F_s t} \tag{4.14}$$

where σ_{ph} is the photon noise, N_s is the number of photons detected, F_s is the flux (measured in e^- s^{-1}) of the star and t is the exposure time.

4. *Sky Background Noise*

When an aperture is placed around a star in an image, the signal we detect will contain contributions from the electrons produced by the photons of the star, electrons knocked free by thermal motions, electrons introduced during the read out process and electrons produced by photons from the "background" sky in the aperture around the star. The amount of background light can be measured by examining the pixel values in a region near the target object, and then subtracting the average value. However, just as the number of photons from a star varies randomly, following a Poisson distribution, so does the number of photons from the background sky. At most astronomical observatories, the sky brightness is generally celestial in origin (zodiacal light, scattered moonlight in the atmosphere). The noise due to this random variation is:

$$\sigma_{sky} = \sqrt{N_{sky}} = \sqrt{F_{bs} n_p t} \tag{4.15}$$

where σ_{sky} is the background sky noise, N_{sky} is the number of photons detected from the background sky, F_{bs} is the flux of the background sky, n_p is the number of pixels in an annulus around the target star and t is the exposure time.

4.5.2 Red Noise

One of the major problems for transiting exoplanet detection using small aperture ground based telescopes is the presence of time correlated red noise (Pont et al. 2006, Smith et al. 2006), also called systematic noise. Red noise can reduce the signal-to-noise ratio of real transit signals in the lightcurves of stars and can also lead to the detection of more false positives by creating features in lightcurves that look like transiting exoplanets. Red noise is caused by a number of physical sources which include temperature dependent optical system changes, air mass effects, local weather conditions, flat fielding errors, telescope tracking errors, and many other sources. One of the most common ways to characterise the amount of red noise in the system is to use an autocorrelation function. In this function, the similarity between observations as a function of the time lag between them is computed. By doing this it is possible to find noise that is produced by repeating patterns in the data itself. An analysis and characterization of the red noise in the KELT-South Target1 commissioning dataset is performed in Section 5.2.9.

4.5.3 Scintillation Noise

One of the major factors that determines the limiting precision of ground based photometric observations is stellar scintillation and is a large contribution to the error in measurements of the magnitudes of really bright stars. Scintillation occurs due to the turbulent nature of the atmosphere of the earth and can be determined by (Young 1967):

$$\sigma_s = \left(\frac{S_0 X^{\frac{3}{2}}}{\sqrt{2T_{exp}} D^{\frac{2}{3}}} \right) e^{-\frac{h}{h_0}} \tag{4.16}$$

where σ_s is the scintillation noise, S_0 is a measure of the intensity of the scintillation, X is the airmass, T_{exp} is the exposure time, D is the diameter of the telescope, h is the altitude of the observatory and h_0 is the scale height of the atmosphere. Using values of $S_0 = 0.09$ (Young 1967), $X = 1.5$, $T_{exp} = 150$ s, $D = 4.2$ cm, $h = 2$ km and $h_0 = 8$ km, the value of $\sigma_s = 0.0029$ or ∼3 mmag. In Section 5.2.9 the total noise of the KELT-South telescope is discussed and from that analysis it is found that the scintillation noise is a large fraction of the overall noise for the KELT-South telescope.

4.6 Total Noise

The various sources of noise can be combined to form a single expression for the total level of noise in the data. Using equation [12] from Newberry (1991):

$$\sigma_t = \sqrt{\sigma_r^2 + \sigma_s^2 + \frac{1}{gF_s} + n_* \left(1 + \frac{1}{n_s}\right)\left(\frac{F_{bs}}{F_s}\right)^2} \tag{4.17}$$

where σ_t is the total noise, σ_r^2 is the red noise, g is the gain of the CCD, F_s is the flux from the target star, F_{bs} is the flux in the background annulus, and n_s and n_* are the number of pixels in the sky background annulus and stellar aperture, respectively. This equation can be used to determine the level of σ_r and F_{bs} by fitting to F_s and σ_t for a large number of lightcurves. In Section 5.2.8 the RMS (which is a measure of the total noise) of the Target1 commissioning dataset lightcurves is discussed and Figure 5.10 is plotted with a number of theoretical total noise curves with different estimates for the sky background flux levels.

4.7 Geometric Distortion

For the 80 mm Mamiya lens used by KELT-South, the effective pixel scale decreases from 23.1″ near the centre of the image to 22.6″ (∼2% decrease) near the edges and 22.1″ (∼4% decrease) in the extreme corners of the image. This is consistent with the typical pincushion distortion of ∼2% for most wide angle lenses used in photography. Figure 4.8 shows a contour plot of constant effective pixel scale and shows that the contour lines are roughly circular, with the centre of the distortion being almost perfectly aligned with the intersection of the optical axis of the lens and the CCD. The most noticeable effect of the optical distortion is that pixels project onto smaller effective areas on the sky as one moves from the centre of the image toward the corners and makes the sky appear to decrease in flux. As one goes radially outward from the centre of the image, the decreasing pixel area on the sky and the vignetting (discussed in Section 4.3.6) both contribute to a decrease in the measured flux per pixel. Another consequence of this distortion is that the shapes of stars in the centre and corners of the image will be completely different and is discussed in Section 4.8.

4.8 PSF Shape

For an optical system similar to KELT-South, it is not unexpected to find that the image PSF varies systematically as a function of position from the centre of the CCD chip. As discussed before, the lens optics are the main contributor to the PSF shape and the PSF is insensitive to atmospheric seeing variations. Near the centre of the CCD chip, the PSF

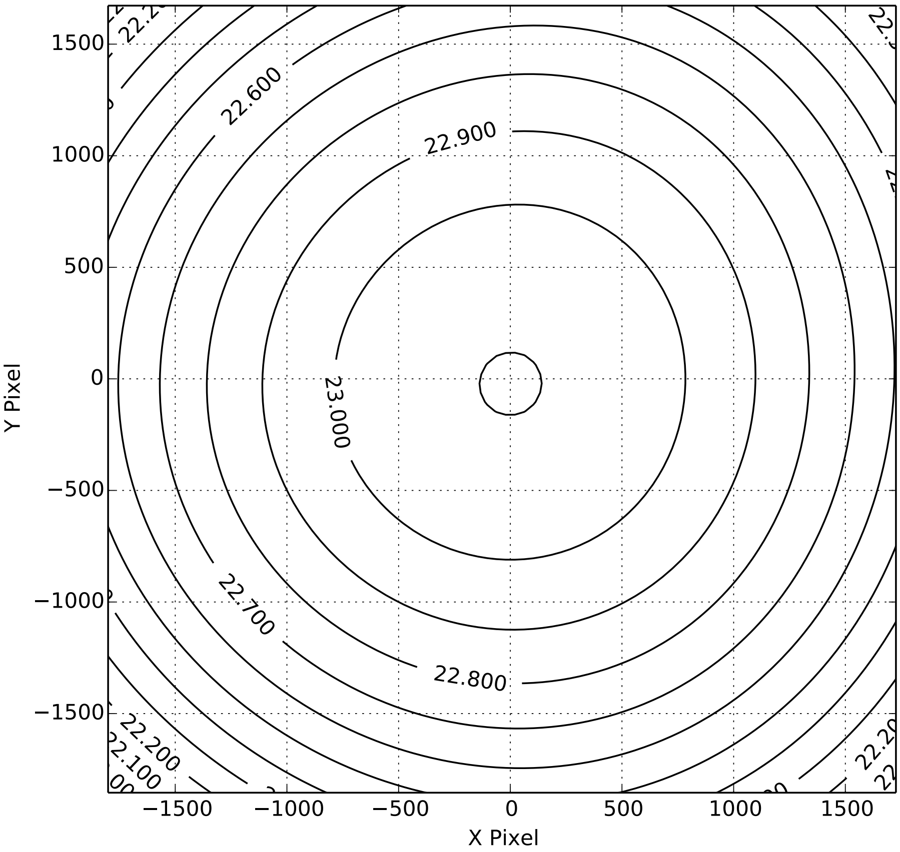

Figure 4.8: Contour plot of the effective pixel scale of the KELT-South telescope. The curves are of constant effective pixel scale and it is clear that there exists significant distortion from the centre of the optical field towards the edges. The contour lines are plotted relative to the central pixel coordinate.

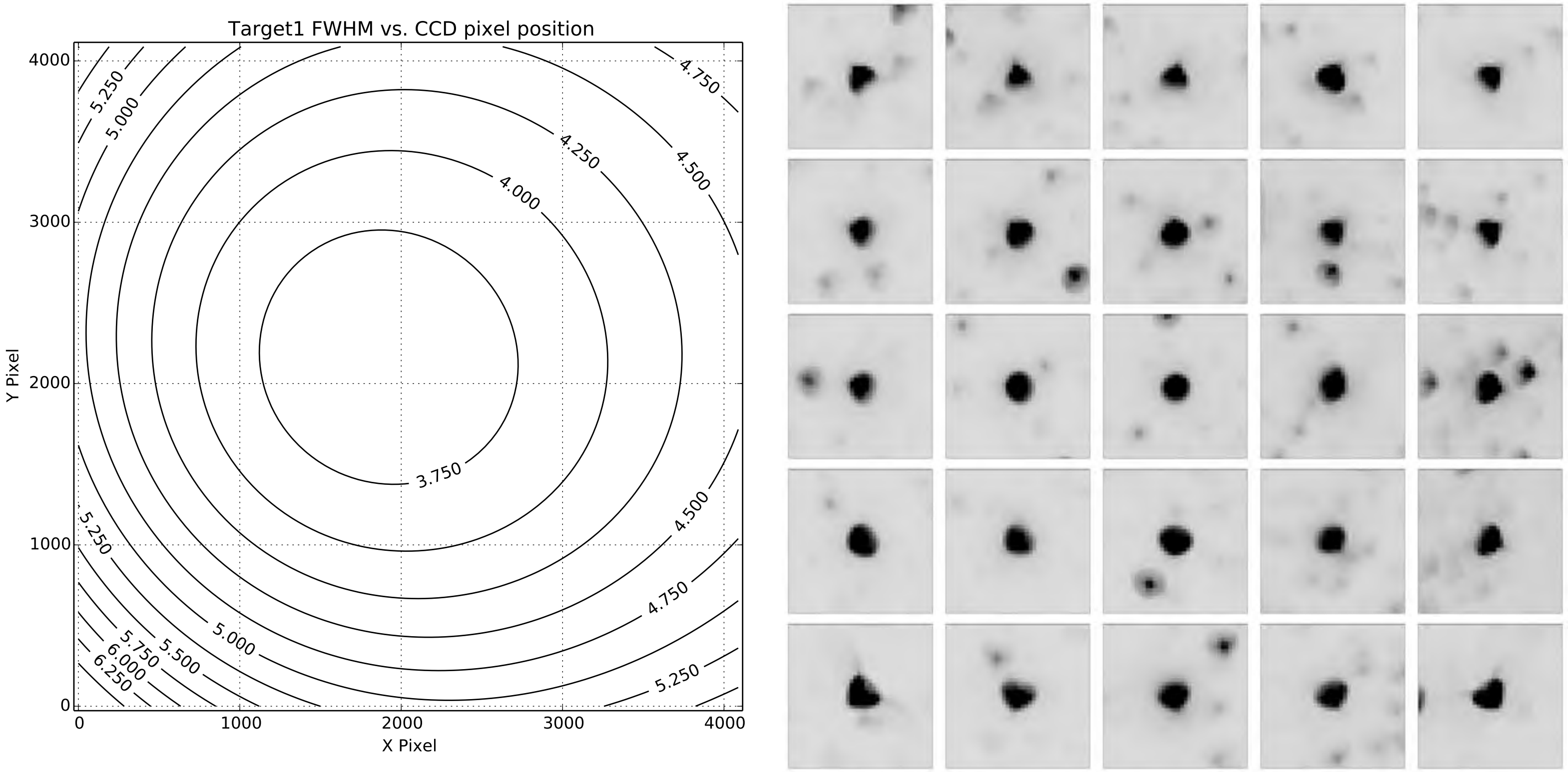

(a) (b)

Figure 4.9: Figure 4.9a shows a contour plot that shows how the FWHM value of the PSF changes across the CCD chip. The plot is made for the reference image of the commissioning data discussed in Chapter 5. The contour labels are in pixels. Figure 4.9b shows image stamps of bright, non-saturated, fairly isolated stars located in the respective regions of the Target1 commissioning field. It is clear from this image how the PSF is distorted at the edges and sides of the image and fairly circular in the middle of the CCD.

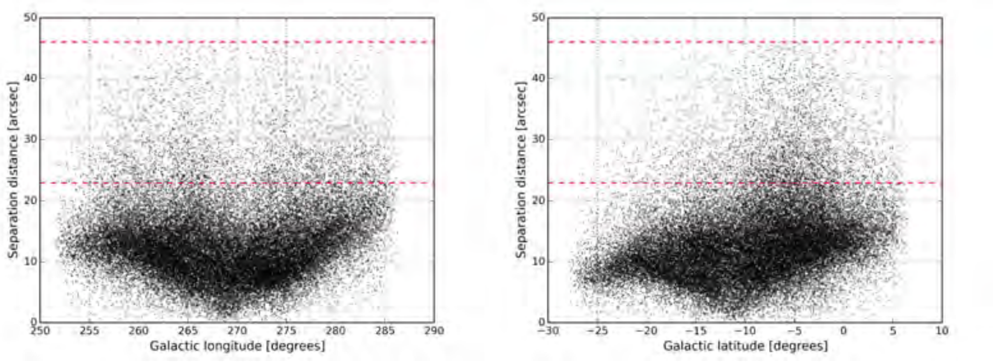

(a) (b)

Figure 4.10: Figure 4.10a shows the separation distance between identified KELT-South stars and the same stars in the Tycho-2 catalogue as a function of Galactic Longitude. Figure 4.10b shows the separation distance between identified KELT-South stars and the same stars in the Tycho-2 catalogue as a function of Galactic Latitude. It is clear from both figures that most of the positions of stars are good to within 1 pixel. The two dashed red lines indicate the separation at 23 and 46 arcsec, which correspond to 1 and 2 pixels respectively.

shape is roughly circular and is generally close to a FWHM value of 3.5 to 3.75 pixels. The FWHM is determined from a fit of a two dimensional Gaussian function to the PSF. As the locations of the stars approach the corners and edges, the PSF shape is becomes more triangular shapes and the FWHM values increase to between 5 and 7 pixels. It can also been seen from Figure 4.9a that the bottom left corner shows a sharper increase in FWHM values than the top right corner. Figure 4.9b shows how the PSF changes from the centre of the CCD to the corners and edges. This change in PSF contributes to the large scatter in RMS magnitude at a fixed stellar magnitude (see the discussion in Section 5.2.8 for more details), but it does not add any complications to the data reduction and image subtraction process (see Section 5.2.2).

It is suspected that the cause of this effect is due to the CCD being slightly misaligned with respect to the optical axis of the lens assembly. Because the lens designs are a product of Mamiya and proprietary, there is no way to determine how much the detector is tilted or even the origin of the tilt. This effect could be due to how the Apogee CCD chip is mounted inside the camera, or it could be due to the adapter bracket used to combine the lens and camera housing together. The stability of the PSF is described in Section 4.10.2.

4.9 Defocussing and Blending Effects

The KELT-South telescope operates slightly defocussed, with the minimum FWHM in the centre of the field being ∼3 pixels. This is done to prevent under sampling of the images. When the regular survey started in 2010 March, the commissioning data had not been reduced yet. Initially the locations of the fields to be observed in the regular survey (see Section 3.3) were selected on the basis that stellar crowding would reduce the accuracy with which we were able to determine the centroid of a particular star. This is the reason the Galactic plane was avoided. The second commissioning field was selected, which included a large fraction of the Galactic plane, to test new routines introduced in the data reduction pipeline that would enable the identification of bright stars in crowded fields and accurately determine their positions. After the reduction of the commissioning data, it was found that stellar crowding does not impact our ability to accurately determine the positions of the bright stars which are the main targets for our transiting exoplanet search. The separation distance between the star we identified and the positions of stars in the Tycho-2 catalogue (a more complete discussion is given in Section 5.2.5) are shown in Figure 4.10. The separation distance for most of the KELT-South stars is well below the 1 pixel level and there is a slight dependence on the Galactic latitude, but this is still well below the 1 pixel level. The main contribution to the error of accurate positions is due to an imperfect astrometric solution of the reference image provided by ASTROMETRY.NET (Section 5.2.6 discusses the astrometric solution procedure during the data reduction pipeline). Figure 4.11 shows that the errors in position are more dependent on pixel position on the CCD chip than position in the sky with respect to the Galactic plane.

The main problem is that crowded stellar fields (especially those close to the Galactic plane) contain many stars per area sampled and with the KELT-South pixel scale of 23″ pixel^{-1}, many of the stars will be blended together into a single aperture. This makes the determination of which star is undergoing the eclipsing event slight more difficult. However, the issue of blending was never factored into the original selection of the field locations as the follow-up network of KELT-South collaborators have larger telescopes and are able to provide higher angular resolution observations than the KELT-South telescope. This enables them to separate most of the stars of interest and determine the exact location of the star that is actually undergoing the transit event. In most cases the transiting event is a blended eclipsing binary, as is seen with the photometric follow-up data provided by the collaborators discussed in Section 5.6.2. All promising KELT-South exoplanet candidates are first subject to a centroid shift image analysis procedure where a number of median combined out-of-transit images are subtracted from a set of median combined in-transit images. This procedure will remove all the non-variable stars from the subtracted image and changes in the position of peak brightness of the target system could indicate that an eclipsing binary system is blended with the target star (see the discussion in Section 1.3.3 and Figure 1.3). If the candidates pass this test, they are sent for photometric follow-up observations to confirm that the target star is the actual star that shows the eclipsing event, before applying for time on larger telescopes for spectroscopic follow-up observations.

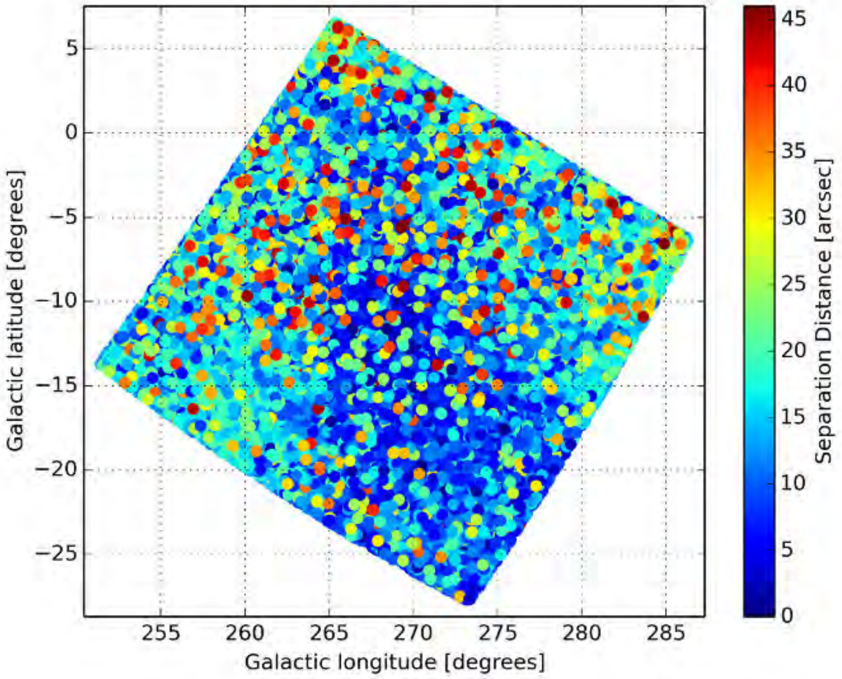

Figure 4.11: Separation distance versus Galactic Coordinates of matched KELT-South and Tycho-2 stars. The colour bar indicates the degree of separation and it can be seen that although there is a slight dependence on Galactic Latitude, the main contribution to the error is positions of the KELT-South stars is toward the edges of the CCD chip. This is most probably due to an imperfect astrometric solution of the reference image provided by ASTROMETRY.NET and can be solved by adding an additional polynomial term to the solution provided.

4.10 Observing Performance

4.10.1 Number of Fields Observed

As discussed earlier the number of fields that the KELT-South telescope observes is evaluated and changed on an almost yearly basis. To find the most efficient and optimal locations for new observing fields or the impact of removing certain fields, the “Observing Simulator” (discussed in Section 3.4) is used extensively. Table 4.2 lists the number of fields observed by year since the regular survey mode of operation started in 2010 February. Data from 2013 was not included in the table as the field locations and numbering system were changed completely in 2013 June. From the table it is clear that 2011 was the most productive in terms of number of images collected throughout the year, due to a number of the northern fields being removed from the observing program at the end of 2010, and an exceptionally good year for observing in terms of weather conditions. A further reduction in the number of northern fields occurred at the end of 2011 but poorer weather conditions than the previous year, as well as downtime due to power failures, resulted in fewer images obtained in 2012 than in 2011. The few images acquired for the northern fields at the end of 2012 also initiated the need to observe the northern fields at higher priority than the southern fields, effectively doubling the number of images that could be obtained in 2013.

Table 4.2: Table of the number of images for every year of the KELT-South operations to date[1].

Field Name	2010	2011	2012	Field Name	2010	2011	2012
North_Field_1	304	0	0	South_Field_17	653	2875	1704
North_Field_2	471	1	0	South_Field_18	771	2876	1595
North_Field_3	402	29	0	South_Field_19	813	2569	1515
North_Field_4	277	116	0	South_Field_20	793	2262	1557
North_Field_5	250	353	413	South_Field_21	728	2101	1708
North_Field_6	298	921	1165	South_Field_22	636	1645	1594
North_Field_7	379	234	0	South_Field_23	632	1429	1727
North_Field_8	407	165	0	South_Field_24	874	1396	2273
North_Field_9	494	888	0	South_Field_25	1118	1362	2532
North_Field_10	589	735	0	South_Field_26	1252	1185	2219
North_Field_11	812	817	0	South_Field_27	1444	2048	1955
North_Field_12	967	962	504	South_Field_28	1157	2514	1878
North_Field_13	774	735	389	South_Field_29	1367	2998	1943
North_Field_14	636	613	544	South_Field_30	0	240	258
North_Field_15	624	455	0	South_Field_99	0	0	252
North_Field_16	542	0	0	South_Field_0	0	1681	1250
Total	8226	7024	3015		12238	29181	25960

NOTES

[1] Data from the 2013 season not included in the table due to a change in field locations and numbering system in 2013 June.

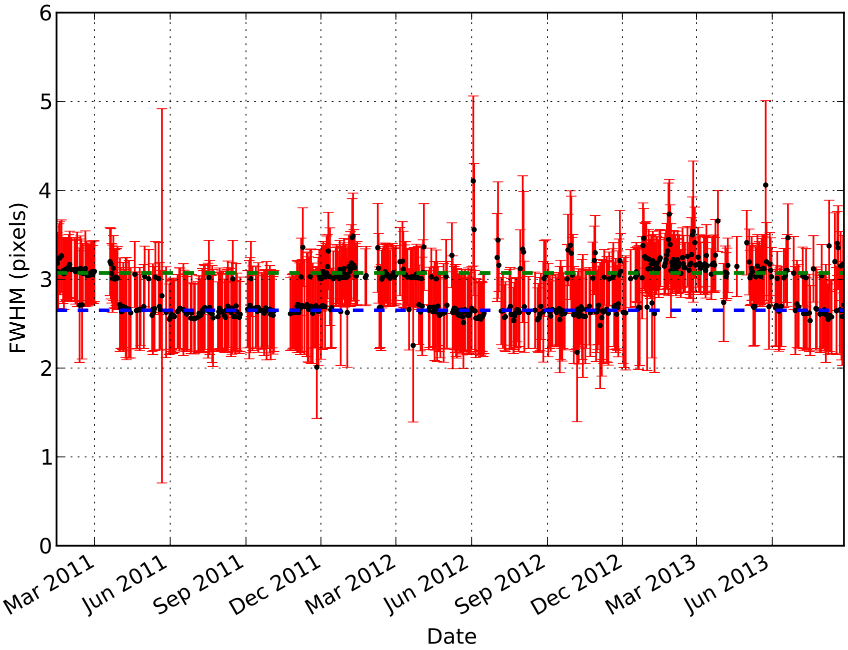

Figure 4.12: Plot of the median FWHM value for all identified stars on the image obtained in the middle of the night since the implementation of the image analysis script after removal of 3σ outlier datapoints. The higher median FWHM values during summer time is clearly visible (indicated with the green dashed line), where the FWHM is ∼3 pixels. In winter the median FWHM is ∼2.7 pixels (indicated with the blue dashed line).

4.10.2 Image Stability

A plot of one of the history files can bee seen in Figure 4.12, where the 3σ outlier datapoints have been removed. These outliers are in general images that are affected by cirrus clouds that increase the FWHM values for all stars. One interesting feature to note is how the FWHM values of the stars change periodically with season. In the summer months the measured FWHM is slightly larger at ∼3.0 pixels than in the winter months at ∼2.7 pixels. At present the cause of this is being investigated, with the most plausible explanation being that the different glass elements in the lens used by KELT-South are temperature sensitive resulting in the distances between them varying. During colder weather conditions the lens elements are closer together by a couple of mm and the focus of the telescope is slightly better and the FWHM values are slightly smaller. It is also clear from the data that it is not a gradual increase in FWHM values from one season to the next but a discrete “jump” between these two values. This indicates that the lens reaches some “critical” temperature above which the lens elements reposition themselves and below this temperature the lens elements are in their normal positions. Another possible cause is the metal bracket that holds the lens and camera system together. This bracket might also be expanding during the hot weather in the summer months and increasing the distance between the lens and CCD, causing the telescope to be slightly out of focus. Or it might be a combination of the two effects working together to produce the periodic change in FWHM values.

Seeing conditions don't affect the FWHM values of stars on our images, as the pixel scale is much larger than the atmospheric seeing variation, making it impossible for this to be the contributing factor. Background sky levels are higher during full Moon and this results in a slight decrease in the measured FWHM of the stars as the "wings" of the PSF shapes are lost in the background. But the periodic change in FWHM would then be seen on a monthly basis and not on a seasonal basis.

However, the small change in FWHM value does not affect our ability to perform data analysis and no attempt is made to refocus the telescope during the summer months. Refocussing of the telescope has to be done manually and this is a very time consuming process and we felt it best to leave the system as is and not attempt to make any drastic changes.

4.11 Polar Alignment

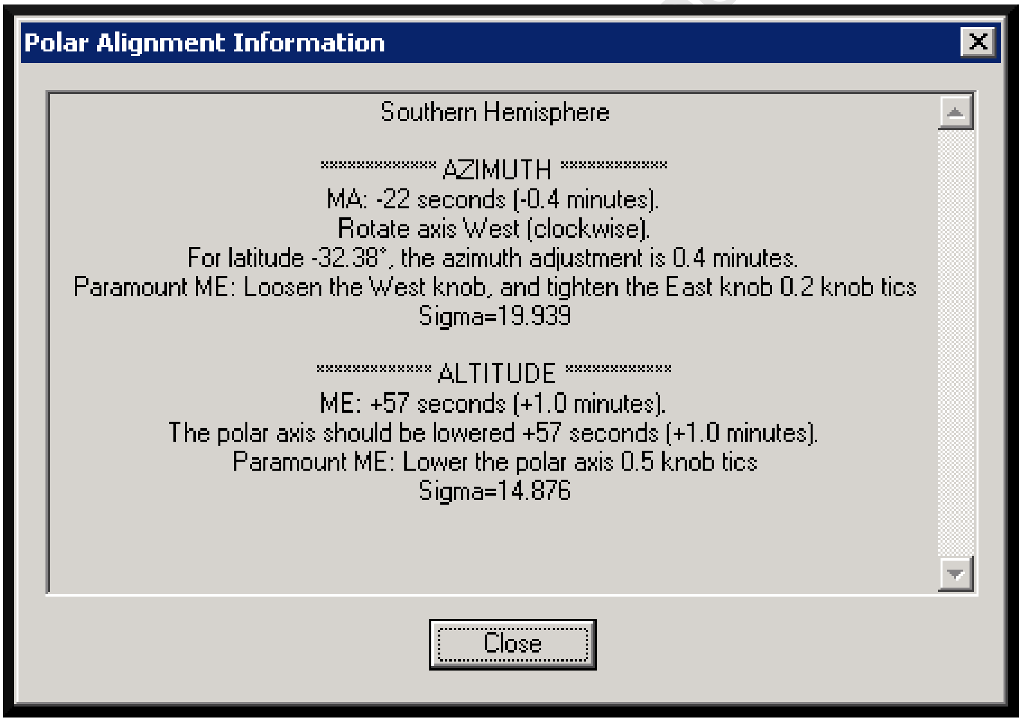

Southern Hemisphere

************* AZIMUTH *************
MA: -22 seconds (-0.4 minutes).
Rotate axis West (clockwise).
For latitude -32.38°, the azimuth adjustment is 0.4 minutes.
Paramount ME: Loosen the West knob, and tighten the East knob 0.2 knob tics
Sigma=19.939

************* ALTITUDE *************
ME: +57 seconds (+1.0 minutes).
The polar axis should be lowered +57 seconds (+1.0 minutes).
Paramount ME: Lower the polar axis 0.5 knob tics
Sigma=14.876

Figure 4.13: Polar misalignment information of the KELT-South telescope produced by TPoint.

The first goal after setting up the KELT-South telescope was to make sure the telescope pointed toward the south celestial pole. A rough alignment was achieved using the adjustable base plate and elevation screws provided on the Paramount ME. A polar alignment mapping run was done using the methods outlines in the TPoint software manual. This process involved mapping a couple of points across the sky and then using the TPoint software to determine the extent of the polar misalignment. Adjustments to the mount were made as suggested by TPoint and the polar alignment mapping run was done again. This was repeated until KELT-South was almost perfectly polar aligned. Once a good alignment was established the pointing model could be created. Every time any changes are made to the hardware components of the telescope, the polar alignment and pointing model need to be recreated as the weight distribution of the telescope is now different and the mathematical model that compensates for errors will no longer be valid.

4.11.1 Pointing Model

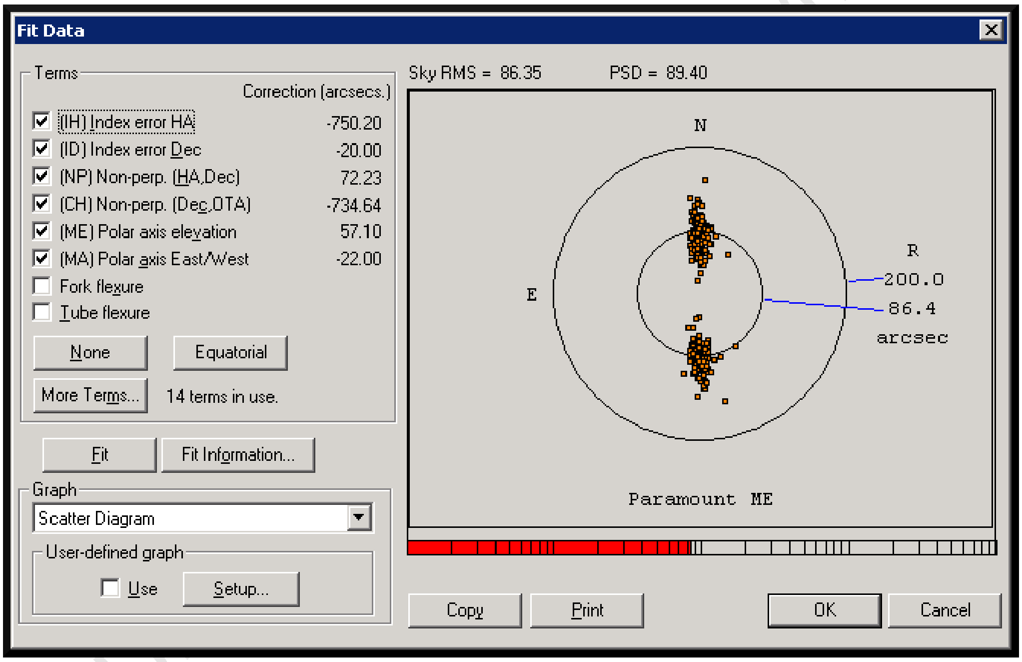

Sky RMS = 86.35 PSD = 89.40

Terms	Correction (arcsecs.)
☑ (IH) Index error HA	-750.20
☑ (ID) Index error Dec	-20.00
☑ (NP) Non-perp. (HA,Dec)	72.23
☑ (CH) Non-perp. (Dec,OTA)	-734.64
☑ (ME) Polar axis elevation	57.10
☑ (MA) Polar axis East/West	-22.00
☐ Fork flexure	
☐ Tube flexure	

14 terms in use.

Graph: Scatter Diagram

☐ Use

Figure 4.14: Scatter diagram of the pointing error of the KELT-South telescope.

Once the polar alignment of the telescope is complete, a pointing model can be created. A pointing model is a collection of mathematical formulae (each one describing a particular error in pointing) that act together to improve the performance of the telescope. The new pointing of the telescope system can be evaluated by the root mean squared (RMS) of the pointing errors. The current TPoint pointing model contains well over 200 mapped points, enough to provide polar misalignment information and adequate to produce RMS pointing errors as small as 86″ (see figure 4.14). Although this might seem large, it represents an error of less than ∼4 pixels on the CCD. The telescope alignment information from TPoint gives the azimuth misalignment as 22″ and the altitude misalignment as 54″. Although these numbers seem quite large, they only represent 1 pixel in azimuth and 2.5 pixels in altitude which is much less than the size of the CCD. Future visits to the telescope will add more points to the pointing model and increase the pointing accuracy even further.

4.11.2 Mount Tracking and Acquisition Accuracy

At present we do not employ any kind of periodic error correction. According to the Paramount ME manual, the worm / gear drive train has a very small periodic error of $7''$ peak to peak or less. This is much less than the $23''$ pixel scale for the KELT-South telescope, which means that any error in the tracking of the telescope due to the gears will be extremely difficult to detect in regular observing operation.

To determine the tracking error, the centre of a particular observing field was monitored over the course of an entire observing season in 2011. A plot of the difference between the real central coordinate (the coordinate that the telescope was instructed to slew to) and the observed central coordinate (where the telescope was actually pointing) is shown in Figures 4.15 and 4.16. On these plots the intended central coordinate is indicated by the zero position, and the data are plotted relative to that position. The error in pointing in right ascension is -0.124 ± 3.044 pixels and the error in pointing in declination is -0.085 ± 5.087 pixels when the telescope is in the eastern orientation. With the telescope in the western orientation the error in pointing in right ascension is -0.977 ± 1.349 pixels and the error in pointing in declination is $+4.083\pm5.847$ pixels. This represents an error in pointing of less than 1% across the entire field of view of the telescope for an entire season. From the plots it is clear that the current pointing model is good for the telescope in the eastern orientation, but the error and scatter is much larger when the telescope is in the western orientation. Fixing this slight difference would require the addition of more points to the pointing model on the western side of the meridian and future visits to the telescope will make these adjustments. It should also be noted that this is for a single field in regular observing operations, which means that between each successive point in the plot, the telescope observed any number of other fields that were available as well.

However, this level of tracking and pointing accuracy was not always the case. Before the current pointing model, the telescope performed relatively poorly when tracking a single field for an entire observing run. An example of the poor tracking and acquisition accuracy experienced during the commissioning phase of the telescope in 2009 can be seen in Figures 5.12 and 5.13 and is discussed in Section 5.2.10.

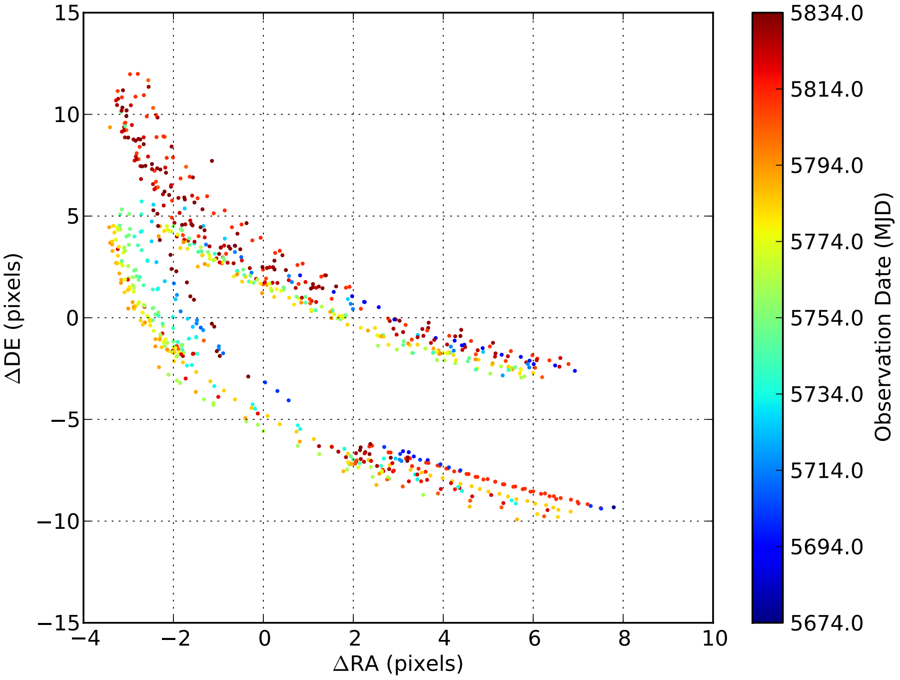

Figure 4.15: This plot shows the central RA and Dec of a particular field taken for an entire observing season in 2011 with the telescope in the eastern orientation. The error in pointing in right ascension is -0.124±3.044 pixels and the error in pointing in declination is -0.085±5.087 pixels when the telescope is in the eastern orientation. This might seem large given the pixel scale of $23''$ pixel^{-1}, but this represents an error of less than 1% across the entire field of view over an entire season of observing.

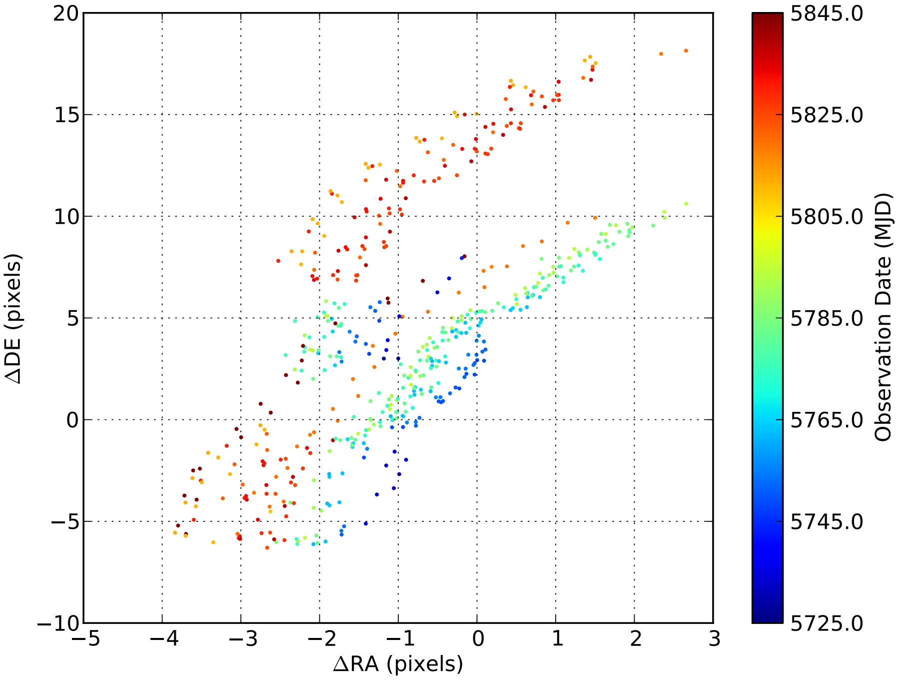

Figure 4.16: This plot shows the central RA and Dec of a particular field taken for an entire observing season in 2011 with the telescope in the western orientation. The error in pointing in right ascension is -0.977±1.349 and the error in pointing in declination is 4.083±5.847 pixels when the telescope is in the western orientation. Similar to the plot above, this represents an error in pointing of $< 1\%$.

Chapter 5

KELT-South Commissioning Data

5.1 Introduction

The previous chapters provided a good overview of the KELT-South construction, deployment and operations. In this chapter I will report on the result I obtained on the search for variable stars and transiting exoplanets in the second of the commissioning datasets we acquired with the telescope after the construction. Most of this chapter is written in first person plural because the work has been prepared to be published and is the result of collaborations with faculty members at other institutions. I was responsible for the data acquisition and the transfer of the data from Sutherland to Vanderbilt University and all of the data analysis work in this chapter was done by me, with the only exceptions being the data reduction (Sections 5.2.2 and 5.2.3) and the astrometry of the reference images (Section 5.2.4).

5.2 Commissioning Datasets

The KELT-South telescope obtained two datasets during the engineering and calibration phase of the construction and deployment. The first dataset was obtained from 2009 August to 2009 December and was toward the Blanco 1 open cluster with the centre of the observed field located at J2000 $\alpha = 00^h04'07''$, $\delta = -29°50'00''$. The analysis of that dataset resulted in a determination of the age of that cluster using two different gyrochronology methods (Cargile et al. 2014). Here we report the results of the second dataset obtained during the commissioning phase of the telescope.

5.2.1 Target1 Observations

The second commissioning campaign was centred on a field located at J2000 $\alpha = 08^h16'00''$, $\delta = -54°00'00''$. We chose that particular field for three reasons. Firstly we wanted a field at a declination that would allow us to test the limits of the observing procedure and be a suitable test-bed for the full KELT-South survey campaign that would start in 2010 March. Secondly we wanted the field to contain a fairly large fraction of the Galactic Plane. This would allow us to test new routines in the data reduction pipeline that would improve our ability to extract lightcurves for stars in extremely crowded areas. The third reason for choosing that field was that it contained a fairly large number of open clusters. If any variable stars were found in these clusters, they could be used to determine the age of the clusters using gyrochronology (Skumanich 1972, Kawaler 1989, Barnes 2003; 2007). Open clusters in the field of view included IC2391, NGC 2547, NGC 2516, Pismis 4, Ruprecht 6, Trumpler 10, and ESO 165-19. Internally we called this field Target1 (T1).

Observations of T1 were carried out every clear night from 2010 January 4 to 2010 February 19 giving a total baseline of 46 days. The observational cadence was $\sim$3 minutes with 150 second exposures and 30 second readout time. We observed the field continuously as long as the centre of the field was above 2 airmasses. Observing the field in this manner resulted in about 100 images per night on average. At the end of every night the images were run through the image analysis routine (discussed in Section 3.6) to eliminate bad images. A total of 3041 images obtained on 32 nights were determined to be good enough for data analysis.

5.2.2 Data Reduction

KELT-South shares a data reduction pipeline with the KELT-North telescope. Both telescopes use similar optics, with the only difference between the telescopes being the detector and minor differences in the observing procedures. It is thus easy to use the same pipeline and reduction procedures for both telescopes with minor changes to accommodate these differences. KELT-South uses a slightly updated version of the pipeline, with new routines that are able to identify more individual stars in extremely crowded regions. The detrending of lightcurves (discussed below) is also done differently in the KELT-South pipeline. Additional information is available in Siverd et al. (2012) and Pepper et al. (2012). When constructing a data reduction pipeline, there are generally three options; aperture photometry, PSF fitting photometry and image subtraction. Although aperture photometry and PSF photometry have been in use for an extended period of time and both of these reduction techniques are very well tested, KELT-South uses an image reduction technique, first proposed by Tomaney & Crotts (1996), for data analysis. Image subtraction has been shown to work much better than aperture/PSF photometry at finding variable stars and transiting exoplanets in extremely crowded fields like globular clusters (Olech et al. 1999, Hartman et al. 2008, McCormac et al. 2014) and open clusters (Hartman et al. 2004, Howell et al. 2005, Montalto et al. 2007). Image subtraction is also much better at accounting for the rapid change in PSF shape seen in the corners of the KELT-South images (see Section 4.8 and does not require isolated stars to create a convolution kernel to convolve the reference image. The KELT-South telescope has an extreme field of view, differing PSF shapes, and large pixel scale (almost always operating in the "crowded" regime), which necessitated the choice of an image subtraction data reduction pipeline over the other options.

5.2.3 Pipeline Overview

The KELT project makes use of a heavily modified ISIS* difference-image-analysis package (Alard & Lupton 1998, Alard 2000, Hartman et al. 2004) to achieve high-precision relative photometry. Raw data images are dark-subtracted and flat-fielded. A "master" dark image is acquired for each observing night by median combination of the dark images taken at the start and end of every night. A "master" flat field image is used for all science images, which was constructed using hundreds of twilight sky flats, each of which was individually bias-subtracted, scaled-dark-subtracted, and additionally gradient-corrected prior to combination. Light curves for individual objects are then constructed using the heavily modified ISIS image-subtraction pipeline. Image subtraction is highly computer intensive. To improve performance the ISIS scripts were modified to facilitate distributed image reduction across many computers in parallel. Other elements of the ISIS package were also modified or replaced with faster alternatives. For example, the standard ISIS source-identification routines are ill equipped to deal with the nature and ubiquity of the aberrations in KELT-South images and the "extract" utility was replaced with the SExtractor program (Bertin & Arnouts 1996). More details of these modifications can be found online.† Each observational image is examined for pointing scatter and a suitable high-quality image is selected to serve as an astrometric reference. All the other images are then registered (aligned) to this image. Shifts in x and y positions of the individual images are caused by incorrect pointing of the telescope or slight drifts due to a incorrect pointing model. Once all the images are registered, the highest quality images are combined to assemble a so-called "master" reference image. The highest quality images used to construct the master reference image are typically (a) acquired at low air mass, (b) have low sky background flux, (c) have lower full width at half-maximum (FWHM), and (d) exhibit high stellar flux. These highest quality images are then median combined and the result is a maximally high signal-to-noise ratio image that we use to define positions and fluxes of all objects identified for extraction.

The reference image is convolved using a series of Gaussian functions to match the object shapes and fluxes for each individual image, and the convolved reference is then subtracted from that image. By first matching object shapes in this fashion, we ensure that any residual flux has the same shape (PSF) as the original image. The residual flux from the subtracted image is then measured using PSF-weighted aperture photometry and added to the median flux of the object identified on the reference image. Median fluxes are obtained from the reference image using the stand-alone DAOPHOT II (Stetson 1987; 1990, Stetson et al.

---

[*] See http://www2.iap.fr/users/alard/package.html

[†] http://astro.phy.vanderbilt.edu/~siverdrj/soft/is3/index.html

1990). This allows us to assemble light curves for each individual object. Light curves are generated over the total baseline of the observations, rather than in separate time segments such as per night or per week.

5.2.4 Lightcurve Combination and Astrometry

The meridian flip of the telescope causes images taken west of the meridian to be rotated by 180 degrees when compared to images taken east of the meridian. It is thus necessary to treat images taken on either side of the meridian as completely separate observations. The PSF's (see Section 4.8) of stars in the corners of the field of view are not exactly the same in each orientation and different reference images were created to account for the non symmetrical nature of the distortions. Other factors like flat fielding errors and detector defects also contribute to images obtained in either orientation being slightly different. The data reduction pipeline produces three versions of a lightcurve for each identified object in each orientation. The first is the raw flux converted lightcurve. The second is a lightcurve with the 3 highest and 3 lowest data points removed eliminating extreme outliers. The third lightcurve is a 3σ clipped lightcurve that removes all outlier data points. These lightcurves are called LCS1, LCS2 and LCS3 respectively. Finally we use the Trend Filtering Algorithm (TFA) (Kovács et al. 2005) to remove common systematics in the lightcurves. We use the closest 225 neighbouring stars as an input template to detrend the lightcurve for each star. This detrended lightcurve is called the TFA3 lightcurve. We thus have a final total of four lightcurves for each object in each orientation. The data reduction pipeline produced 89480 lightcurves for the eastern orientation and 104854 lightcurves for the western orientation. The large difference in number between the two orientations is due to the fact that the pointing of the telescope was not very good at the time of observations. The western reference image is offset from the eastern reference image by about 1 degree and resulted in more of the Galactic Plane being visible. This "extra" portion of the sky resulted in more stars being visible in the western reference image. We use the ASTROMETRY.NET package (Lang et al. 2010) to find astrometric solutions for each of our reference images (east and west reference image separately). The ASTROMETRY.NET performs astrometric image calibrations without any prior input aside from the data in the image pixels themselves. The calibration information that ASTROMETRY.NET provides includes image pointing, orientation, plate scale and full coordinate solutions. The software works by first identifying and cataloguing the positions of the brightest stars visible on the frame. Next it uses subsets of 4 stars called "quads" to generate a geometric hash code that describes how the positions of each star in the quad is related to the others. The benefit of generating hashes in this manner is that the final vectors are invariant to translation, rotation and scaling. The system is also resilient to small errors in the relative positions of the input stars as these will introduce very small errors in the code vector. Next it compares the geometric hash with a database of indexed hashes, pre-generated by the ASTROMETRY.NET group, from the USNO-B1, 2MASS and GALAX (Galaxy Evolution Explorer) catalogues. Once a few suitable matches, or hypotheses, are found the most likely hypothesis is selected using a Bayesian decision process. The team

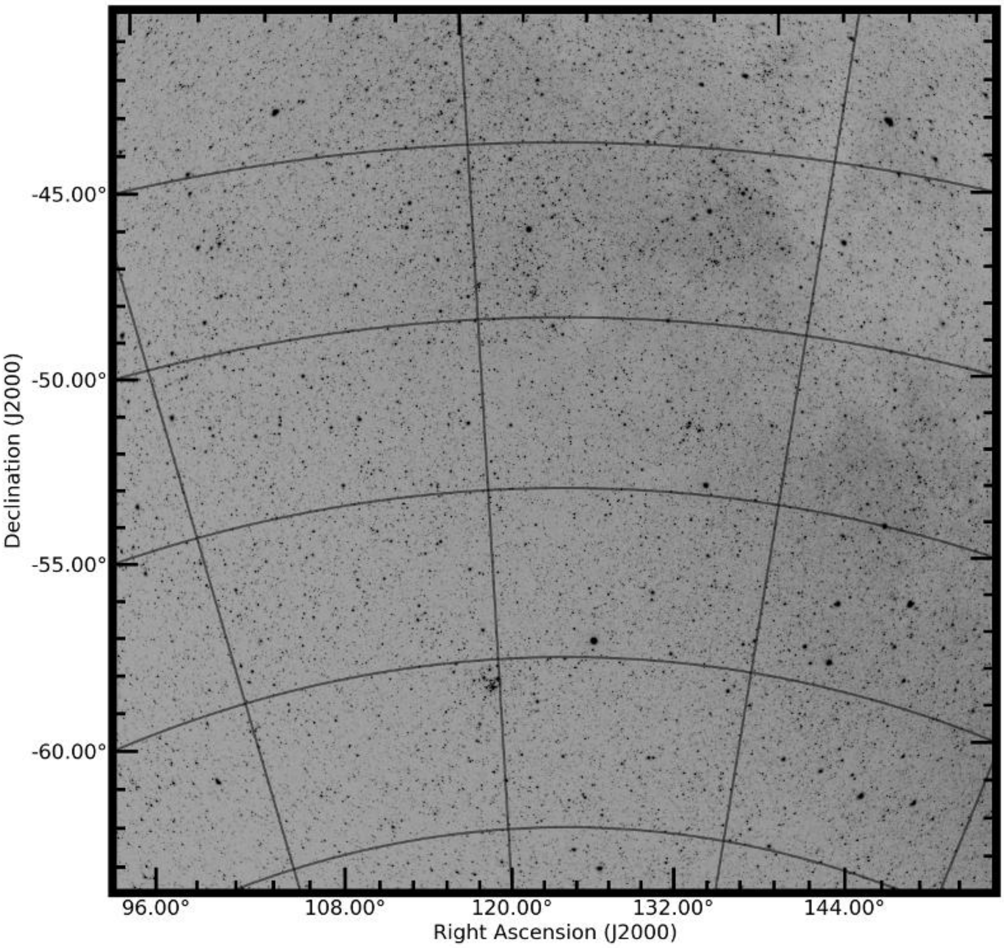

Figure 5.1: The Target1 field with coordinate grid overlay. North is up and East is to the right. (This image is the eastern orientation reference image.)

elected to err on the side of caution and the program will fail to produce a result rather than return a false positive. In testing a success rate of 100% for solving "blind" images taken from the Sloan Digital Sky Survey was obtained (See Lang et al. (2010) for a complete discussion on the ASTROMETRY.NET software).

Both of the T1 reference images were solved and the World Coordinate Solutions (WCS) were included in the FITS file headers. The T1 field with the coordinate grid overlayed on the eastern reference image can be seen in Figure 5.1. Notice the extreme distortion visible in the image. This is purely a consequence of the large field of view of the KELT-South telescope.

To get a combined lightcurve for each star, KELT-South objects from the western reference image were matched to KELT-South objects from the eastern reference image if the sky projected distance between them was less than 76 arcsec (∼3.5 pixels). We chose this distance as it produced the least amount of double matches (a star in the eastern reference image was matched to 2 or more stars in the western reference image), while still producing a relatively large fraction of correctly matched stars. If more than one match was found for a star in the eastern reference image, we selected the closest one from the western reference image as the matching object. Matching was done using the TOPCAT (Taylor 2005) database software. This software was specifically designed to deal with the large datasets produced by the astronomical community and has various functions built into the program to deal with common astronomical tasks. The final list contained 78297 objects. To obtain a single lightcurve for each object the eastern and western median subtracted lightcurves were combined and the average magnitude was used as the final KELT-South instrumental magnitude. For a final coordinate for each object we simply took the average of the eastern and western right ascension and declination. At the end of the data reduction process, we thus have a final total of 12 lightcurves for each object identified (4 versions of the eastern lightcurve, 4 versions of the western lightcurve and 4 versions of the combined lightcurve).

5.2.5 Matching to Known Sources

We match our dataset to 2 known catalogues. We first matched our KELT-South objects with the Tycho-2 catalogue (Høg et al. 2000), as this catalogue contains almost all bright stars with a V magnitude less than 12. There are 75051 objects in the Tycho-2 Catalogue within the field of view of T1. We found that 47314 objects from the Tycho-2 catalogue matched KELT-South objects, using a search radius of 46 arcsec (∼2 pixels). If more than one Tycho-2 star was found to be a match to one KELT-South object, we selected the closest Tycho-2 object as the corresponding match. A histogram of the matching can be seen in Figure 5.2. Many of the KELT-South sources are too faint to be included in the Tycho-2 catalogue which is complete to 99% at V = 11 and 95% complete at V = 11.5. Seeing as the target magnitude for exoplanet candidates for KELT-South is $8 < V < 11$ we wanted to determine how many of the known bright stars we were able to extract during the data reduction process. In the Tycho-2 Catalogue there are 25877 objects in the target magnitude range and we managed to match 21695 of them to KELT-South objects. This represents a matching success of ∼84%. Most of the objects we were not able to match are located along the edges of the KELT-South reference images and are distorted in shape and position. This makes the task of finding their correct position very difficult. Next we matched the KELT-South objects with known sources in the Two Micron All Sky Survey (2MASS) catalogue (Skrutskie et al. 2006). We followed a similar procedure as above, matching 2MASS objects to our KELT-South objects using a search radius of 46 arcsec (∼2 pixels). We managed to find 2MASS counterparts to all but 2 of the 78297 KELT-South objects. The 2 objects we could not match were visually inspected and it was found that both are extremely bright objects, where both were saturated in the KELT-South reference images. As well as the saturation effect, both objects were far away from the centre of the image and extremely distorted in shape. This made the centroid detection very difficult and the positions listed after the data reduction procedure were clearly in error.

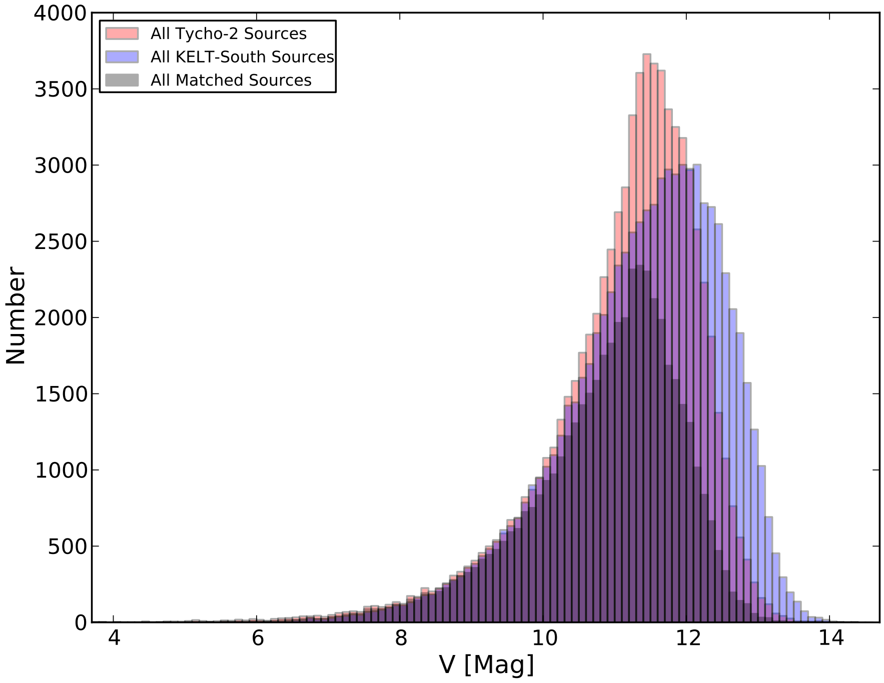

Figure 5.2: Histogram of the Tycho-2 and KELT-South object matches. All sources in the Tycho-2 catalogue are plotted in red and the KELT-South sources are plotted in blue. The matched sources are overplotted in grey and it is clear from the histogram that almost all the Tycho-2 sources with $8 < V < 11$ have corresponding KELT-South matches.

5.2.6 Astrometric Precision

To determine the overall astrometric precision, we compared the coordinates of all the KELT-South objects with their matches from the Tycho-2 catalogue (see section 5.2.5). We found the median offset between our coordinates and Tycho-2 coordinates to be 13.4981 arcsec (just over half a pixel) with a standard deviation of 6.9163 arcsec (see Figure 5.3). The offset in coordinates compares well with similar coordinate solutions done by Pepper et al. (2012), when one considers that about half of the reference image contains part of the Galactic Plane where extreme stellar crowding reduces the centroid accuracy we can achieve.

Proper motion of the stars was considered as a possible cause for the large variation seen in Figure 5.3. Figure 5.4 shows a plot of the radial distance from the centre of the CCD chip on the y-axis, the reduced proper motion on the x-axis and the KELT-South objects coloured by the separation distance. The plot clearly shows that the separation distance is mainly dependent on the radial distance from the CCD centre and no dependence on proper motion is seen. This comes as no surprise as the reduced proper motions of most stars in the Tycho-2 catalogue is $\sim 10^{-2}$ arcsec year^{-1} and the difference between the epoch of positions is only 9 years, which means that most stars would have moved by less than 0.1 arcsec (equivalent to 0.004 of a pixel).

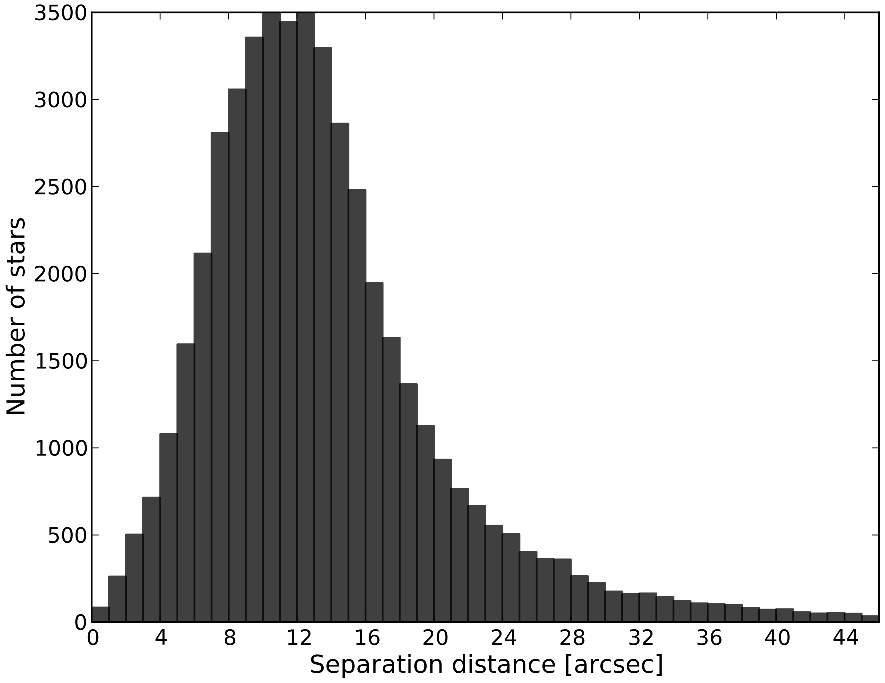

Figure 5.3: Histogram of the separation distance between the Tycho-2 coordinates and the KELT-South coordinates for known sources.

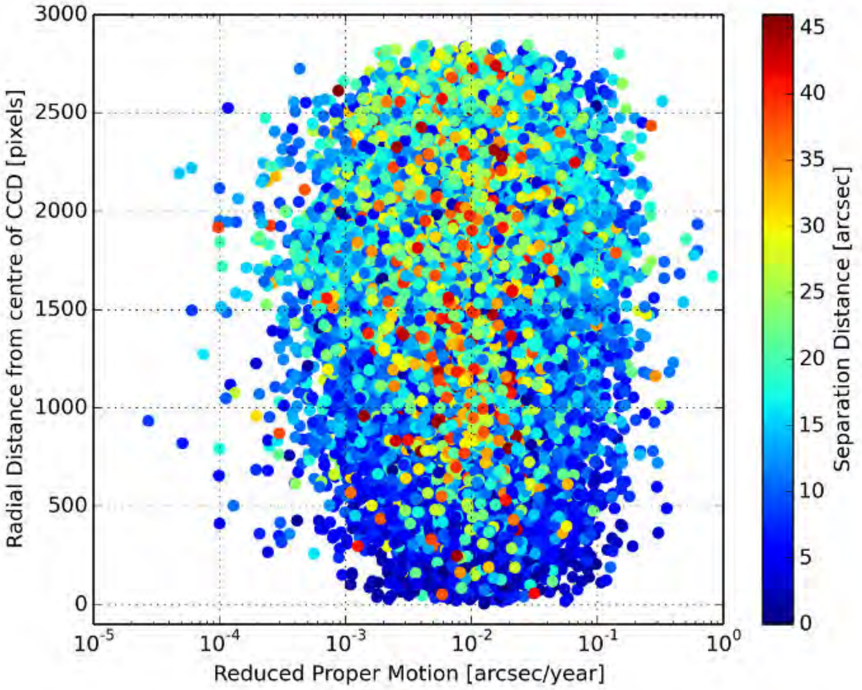

Figure 5.4: Plot of the radial distance from the centre of the CCD chip as a function of the reduced proper motion of all the matched KELT-South and Tycho-2 sources. The colour of the different points indicates their separation distance with red points being the largest and blue points the smallest separation distance.

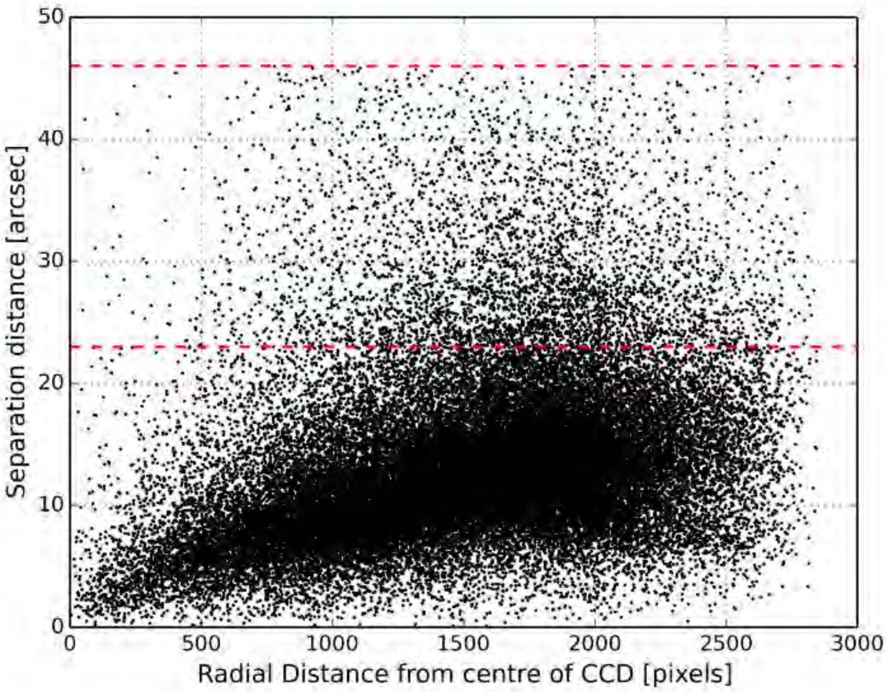

Figure 5.5: Plot of the separation distance as a function of the radial distance from the centre of the CCD chip. The two dashed red lines indicate the separation at 23 and 46 arcsec, which correspond to 1 and 2 pixels respectively.

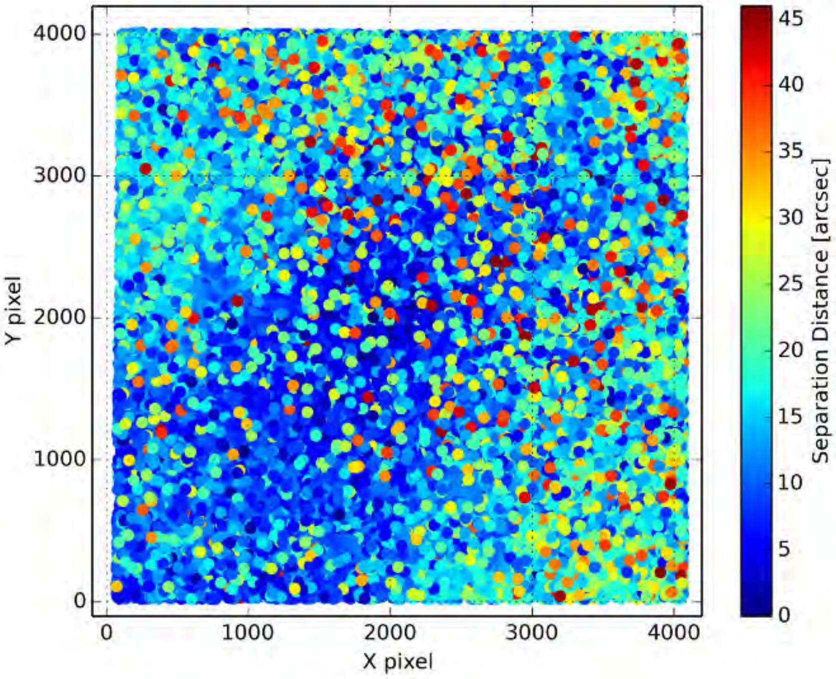

Figure 5.6: Plot of the separation distance as a function of the physical pixel position of the objects.

To further investigate the reason for the offset in coordinates between the KELT-South objects and the Tycho-2 coordinates, the separation distance was plotted as a function of the radial distance from the centre of the CCD chip. From the plot shown in Figure 5.5 it can be seen that there is a slight dependence of separation distance with radial distance from the centre of the CCD chip, with only ∼9% of the matching objects having a separation distance larger than 1 pixel. A plot of the separation distance as a function of physical pixel position can be seen in Figure 5.6. This shows that the slight increase in separation distance is not mainly due to stellar crowding in the Galactic Plane, but rather increases toward the top and toward the right of the CCD chip. This is most probably due to an improper astrometric solution provided by ASTROMETRY.NET and could be improved by allowing ASTROMETRY.NET to fit additional polynomial terms when solving the reference image. Seeing as this step is performed before the data reduction process and the entire data reduction takes many weeks to complete, the extra time required to reprocess all the lightcurves was not considered necessary, as more than 90% of the KELT-South objects were matched to the Tycho-2 objects by less than 1 pixel and the extra time and effort to correct for this tiny error would not be justified.

5.2.7 Photometric Calibration

We do not attempt to get highly precise absolute photometry for the sources we detect with KELT-South, but rely on highly precise relative photometry. KELT-South has a very broad filter, equivalent to a wide R band, and while the components are similar to KELT-North, the conversion from KELT-South instrumental magnitude to standard magnitudes is different. We converted the KELT-South instrumental magnitude to standard magnitudes by comparing a set of non-saturated KELT-South stars (across the entire field of view, which would include any off-axis colour terms) with the Johnson V magnitude for the stars listed in the Tycho-2 catalogue. Figure 5.7 shows the plot of the magnitude calibration. The Johnson V magnitude was obtained by converting from the Tycho-2 V_T magnitude using the procedure set out in the catalogue description. We find that KELT-South instrumental magnitude corresponds to V as follows:

$$V = R_K - 2.093(\pm 0.002) \tag{5.1}$$

We also compared the same non-saturated KELT-South stars to R magnitude for stars listed in the NOMAD (R magnitudes listed in the NOMAD catalogue are from different sources, including the UCAC2 and USNOB1 catalogues; Most of the R magnitudes are from the USNOB1 catalogue, but for stars not in that catalogue the R magnitudes are taken from the UCAC2 catalogue and UCAC2 R magnitudes are non-standard and are between Johnson V and Johnson R. The R magnitudes in the USNOB1 catalogue are converted from the non-standard photographic systems O, E, J, F, N). Figure 5.8 shows the plot of the magnitude calibration. We find that KELT-South instrumental magnitude corresponds to

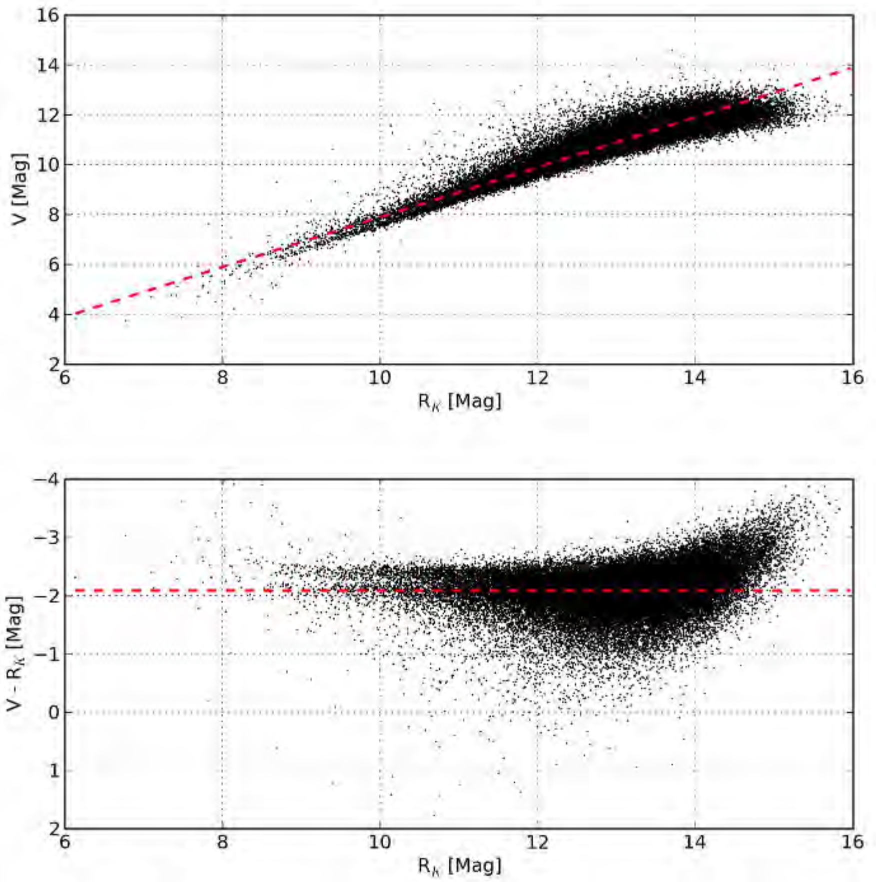

Figure 5.7: Comparison of the Tycho-2 V magnitude and the KELT-South instrumental magnitude.

R as follows:

$$R = R_K - 2.499(\pm 0.003) \tag{5.2}$$

5.2.8 Relative Photometry

As discussed in Section 5.2.3, KELT-South uses a difference-image-analysis pipeline to derive relative photometry for all the sources we detect. The most common way to show the photometric precision we are able to achieve is by plotting the magnitude Root-Mean-Squared (RMS) values as a function of magnitude. We show in Figure 5.9 the RMS plot of the commissioning field with a horizontal line at 1%. This line generally represents the photometric precision that is required to find Hot-Jupiter type transiting exoplanets as the depth of the

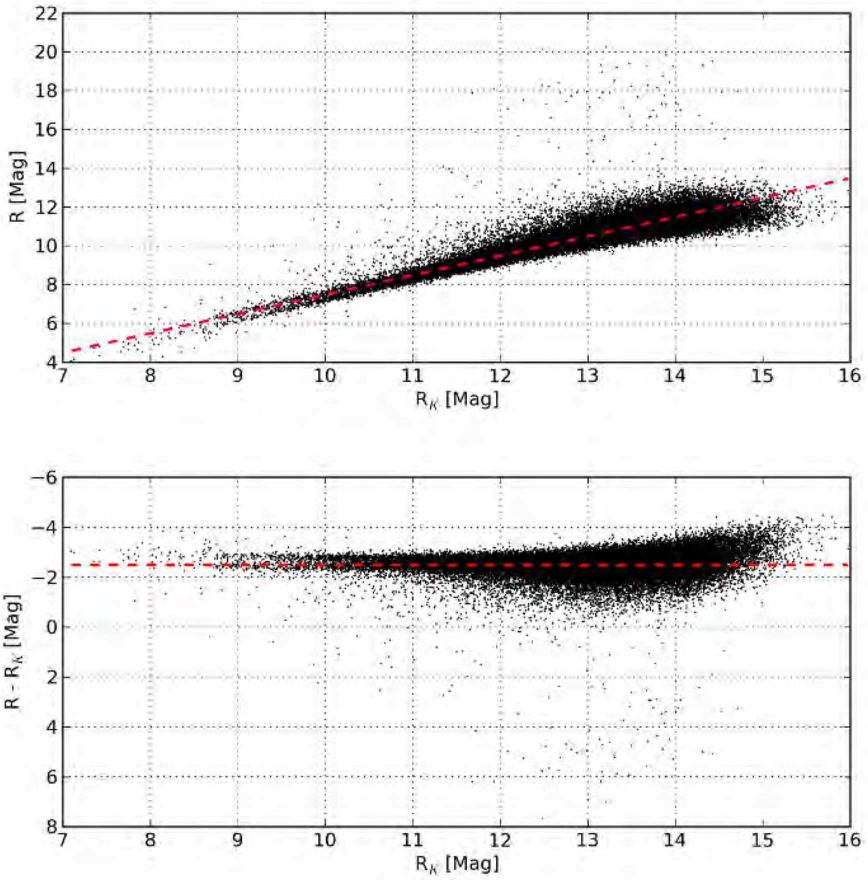

Figure 5.8: Comparison of the NOMAD R magnitude and the KELT-South instrumental magnitude.

transit for these systems is usually of order 1% or less. Figure 5.9 shows that we have 22059 with better than 1% RMS, of which 19653 are in the range $8 < V < 11$. These lightcurves are the best candidates to use in the search for exoplanets. The slow upward trend in the plot shows the photon-noise limitation of the KELT-South system whereas the upturn at the bright end of the plot indicates the onset of non-linearity and saturation effects. Outlier points are for stars with higher than normal magnitude rms and are generally variable stars. Although the data used to construct Figure 5.9 relies on a different cadence than the regular survey campaign, the results demonstrate the typical precision we are able to achieve. In the regular survey mode of the telescope, the cadence is between 8 and 15 minutes compared to 3 minutes for the commissioning data.

Figure 5.10 shows a detailed RMS plot incorporating light curves from the stars in the central 1024 × 1024 pixel section of the CCD chip. In Section 4.8 the shape and size of the

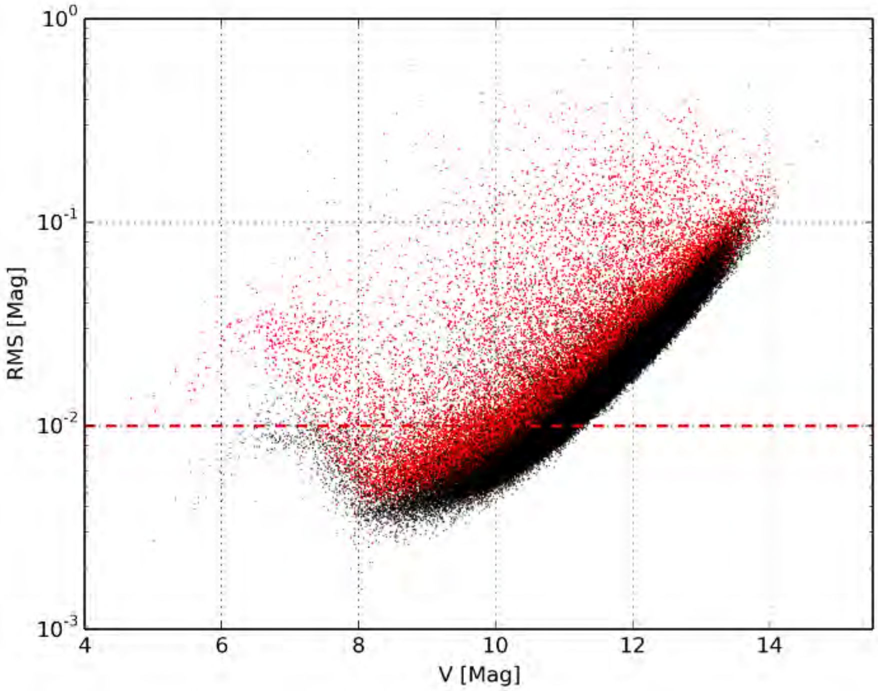

Figure 5.9: The RMS of the lightcurves as a function of V magnitude. The red points show the RMS of the lightcurves before TFA was applied and 13742 lightcurves were below the 1% RMS level. After the application of TFA a total of 22059 are below the 1% RMS level of which a total of 19653 lightcurves in the magnitude range $8 < V < 11$.

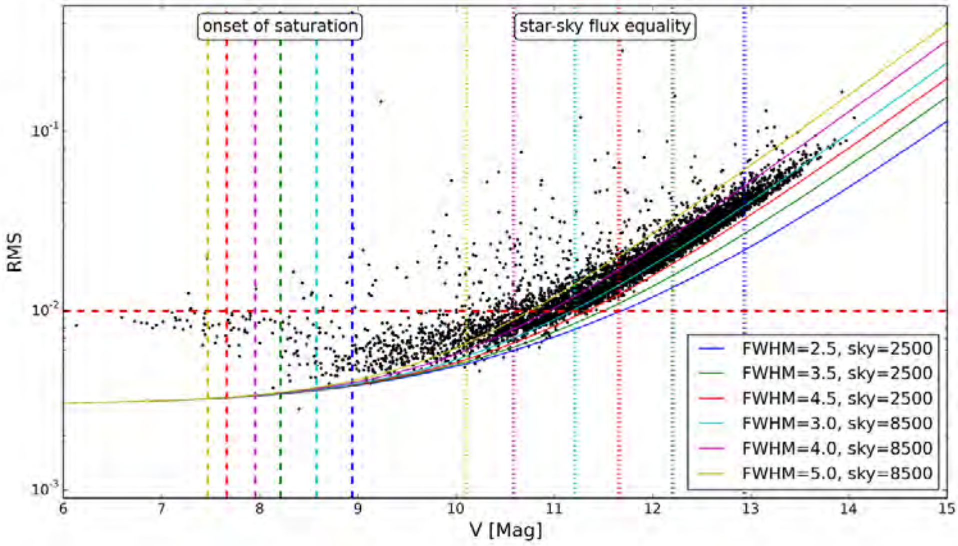

Figure 5.10: The RMS of the lightcurves as a function of V magnitude for the central portion of the T1 commissioning field. This plot has fewer stars, but displays the performance of the KELT-South telescope in greater detail. The horizontal dashed red line represents the 1% RMS limit. The solid curves indicate theoretical photon-noise limits. The dashed and dotted vertical lines indicate the onset of ADU saturation in the brightest pixels and the magnitudes where the star and background sky contribute equal amounts of flux in a PSF, respectively. The theoretical photon noise curves all include an assumed systematic noise floor of 3.0 mmag.

PSF was discussed and shown to vary from the centre to the edge of the detector. Scattered light from Moon illumination can increase the background sky level significantly. Figure 5.10 shows the curves of the theoretical photon noise under different assumptions of PSF size and sky background levels. These assumptions lead to different magnitudes at which the sky background and the star in a PSF contribute equal amounts of flux. The points at which ADU saturation occurs are also shown (assuming a Gaussian shaped PSF). From the figure it is clear that these two thresholds vary across the field and are dependent on the Moon illumination (i.e. time dependent). This makes it impossible to define a single value for either threshold. It can also be seen that at the centre of the field, well behaved stars have background-star flux equality at V$\sim$11.2 and ADU saturation starts at V$\sim$8.5. Although most stars with $7 < \mathrm{V} < 9$ start experiencing saturation, the RMS levels are still below the 1% level.

5.2.9 Red Noise

In order to characterize the level of red noise in the T1 data, the autocorrelation function was computed for a number of low RMS stars (within a certain magnitude range) on an intra-night timescale. We plot the combined autocorrelation function for a number of stars in each magnitude bin indicated in the sub-plots of Figure 5.11. We also show the limiting RMS values for each plot and the number of stars used to compute the combined autocorrelation function. As seen from the plots, there is no correlated noise on the timescales of 3 minutes up to the duration of 8 hours (number of hours in a single night of observation). The noise floor included in RMS plot in Figure 5.10 is most probably due to some small amount of red noise, but at 3.0 mmag this is below the expected 5-10 mmag depth of a typical Hot Jupiter transiting exoplanet. The combination of the low noise floor and the lack of red noise in the autocorrelation functions indicate that our ability to detect transits of Hot Jupiter planets should not be compromised by large amounts of red noise.

5.2.10 Mount Tracking

At the time of T1 commissioning observations, the KELT-South telescope was not properly polar aligned and did not have a good pointing model (the pointing model contained points only mapped on the eastern side of the meridian). To illustrate the amount of drift during the night we have included Figures 5.12 and 5.13 that show the central coordinate of the T1 field over the course of a single night as well as the intra-night drift. The data are coloured by observation data and the amount of drift within one night can clearly be seen. Although all observations are roughly symmetric around the real central coordinate (the coordinate that the telescope was instructed to slew to), the scatter in where the telescope was actually pointing is very large. The error in pointing in right ascension is 0.000±9.913 pixels and the error in pointing in declination is 0.000±5.517 pixels when the telescope is in the eastern orientation. With the telescope in the western orientation the error in pointing in right ascension is 0.000±9.640 pixels and the error in pointing in declination is 0.000±15.567

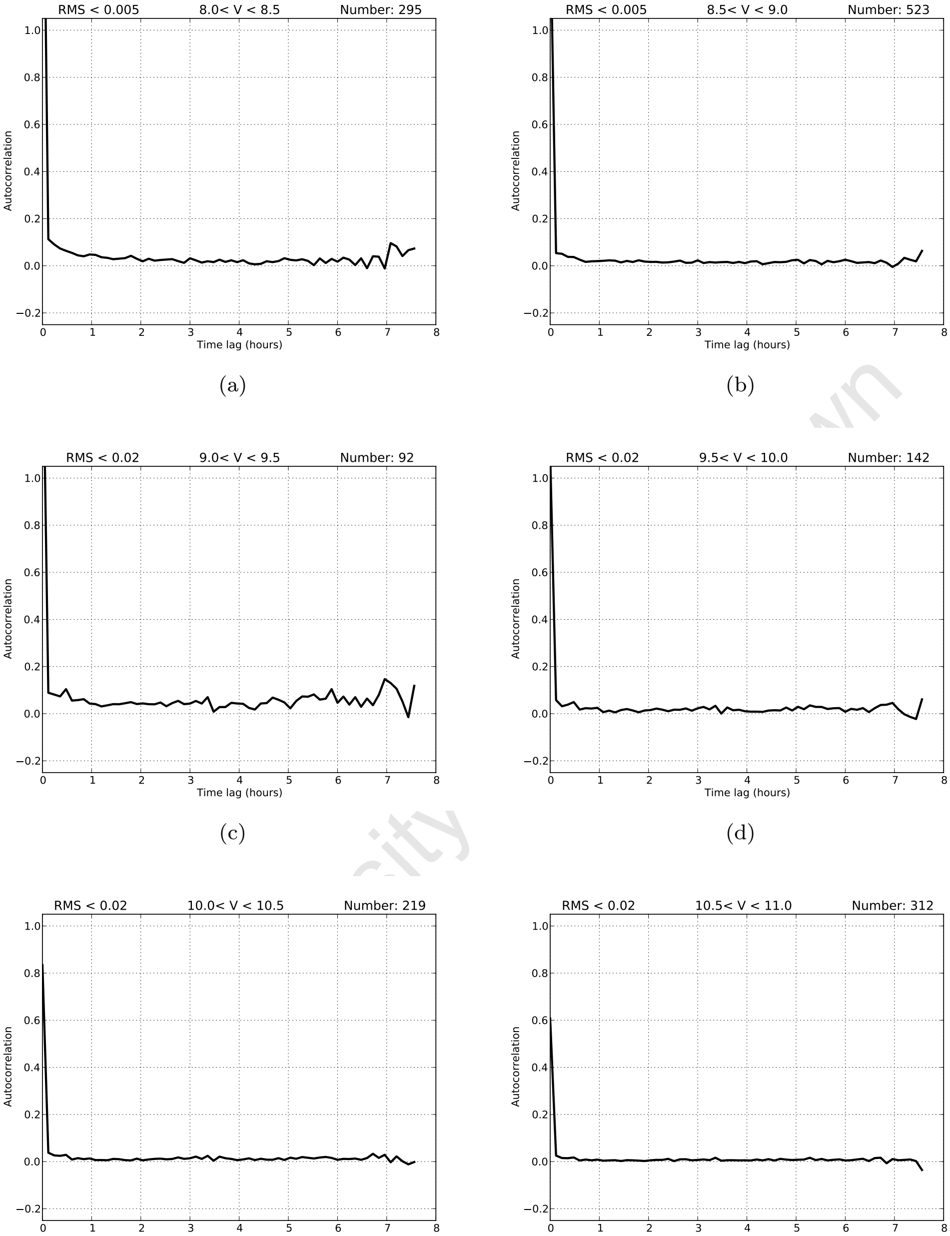

(a) (b)

(c) (d)

(e) (f)

Figure 5.11: Combined autocorrelation function for low RMS stars in the KELT-South Target1 commissioning data. No significant signals are seen in any of the plots on timescales of 2-3 hours (the typical transit duration of a Hot Jupiter transiting exoplanet).

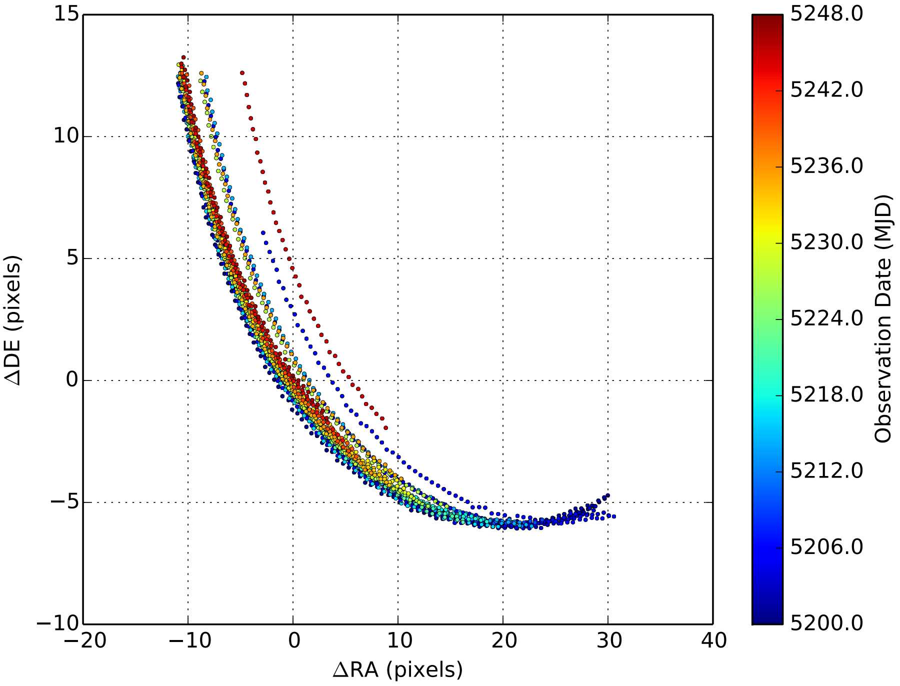

Figure 5.12: This plot shows the central RA and Dec of the Target1 field with the telescope in the eastern orientation. The error in pointing is roughly symmetric around the real central coordinate, with a scatter of 9.913 pixels in RA and 5.517 pixels in Dec.

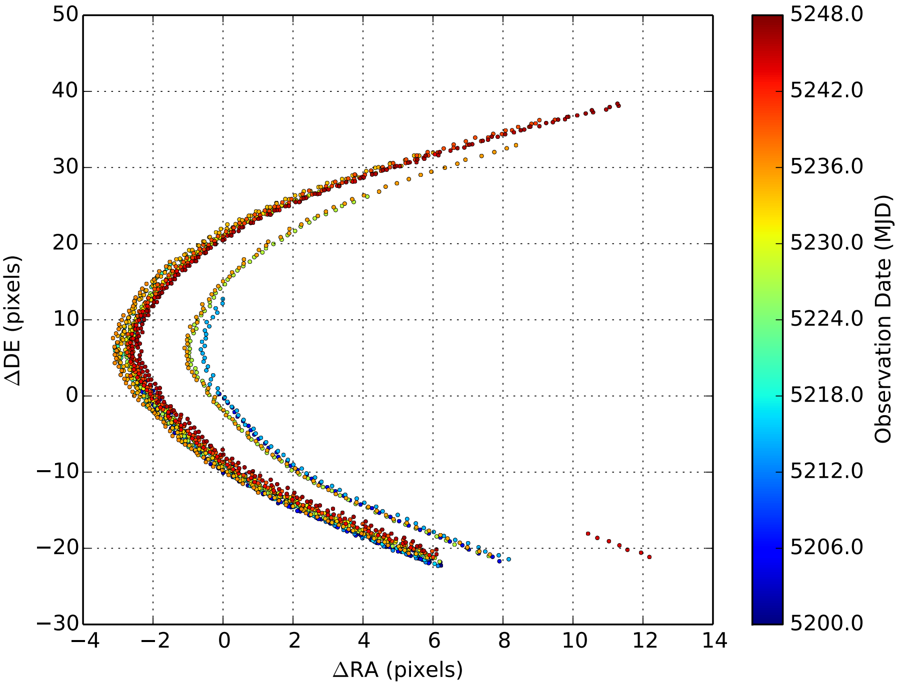

Figure 5.13: This plot shows the central RA and Dec of the Target1 field with the telescope in the western orientation. The error in pointing is roughly symmetric around the real central coordinate, with a scatter of 9.640 pixels in RA and 15.567 pixels in Dec.

pixels. This is very poor accuracy considering that the telescope did not point to any other locations during this observing season and simply tracked the T1 field the entire time it was visible.

5.3 Variable Star Selection

Any survey that searches for planetary transits will also yield data that could be used to find variable stars. We used three methods to search for variable stars and at the end we compiled a combined catalogue of all the variables found by the different techniques. The three methods were used to identify possible periodic variables from our time series observations:

1. General periodic variables were identified using the analysis of variance (AoV) periodogram (Schwarzenberg-Czerny 1989, Devor 2005).
2. Sinusoidal periodic variables were identified by using the Lomb-Scargle (L-S) (Lomb 1976, Scargle 1982, Press & Rybicki 1989, Press et al. 1992) algorithm.
3. Eclipsing systems were identified using the Box-Least-Squares (BLS) (Kovács et al. 2002) algorithm.

We used the VARTOOLS package developed by Hartman et al. (2008) to perform the search for variable stars. After the identification of possible variable stars we performed a period search using the Fast χ^2 (Fχ^2) (Palmer 2009) algorithm on all the lightcurves to confirm the periodicities found by either AoV, L-S or BLS. We also made extensive use of the Stetson J statistic (Stetson 1996) in combination with the statistics produced by the AoV, L-S and BLS search algorithms to make a final decision on whether or not an object should be included in the catalogue of variable objects. Possible transiting exoplanets were identified as a subset of the eclipsing systems with the selection criteria being slightly more strict. All searches for periodic variables were performed on the de-trended lightcurves. The closest 225 stars were used as input templates to de-trend against. Although it is known that methods like TFA distort the signal of large amplitude variables (Kovács et al. 2005, Kim et al. 2009), the signals of very small amplitude variables cannot be recovered when using the non de-trended lightcurves for our dataset. A reconstructive mode of TFA is available, but we did not implement this feature as this mode of TFA is much more computationally intensive and requires significantly more computer processing time. Once a periodic signal was identified in a de-trended lightcurve, we used the non de-trended one to confirm the variability. All plots of lightcurves presented below are the non de-trended lightcurves (LCS2 versions) unless otherwise specified.

5.3.1 Analysis of Variance Search

We searched for variables with period between 0.013 and 15.5 days using AoV with phase binning. The shortest period we searched for was ∼6 times the observational cadence of 3

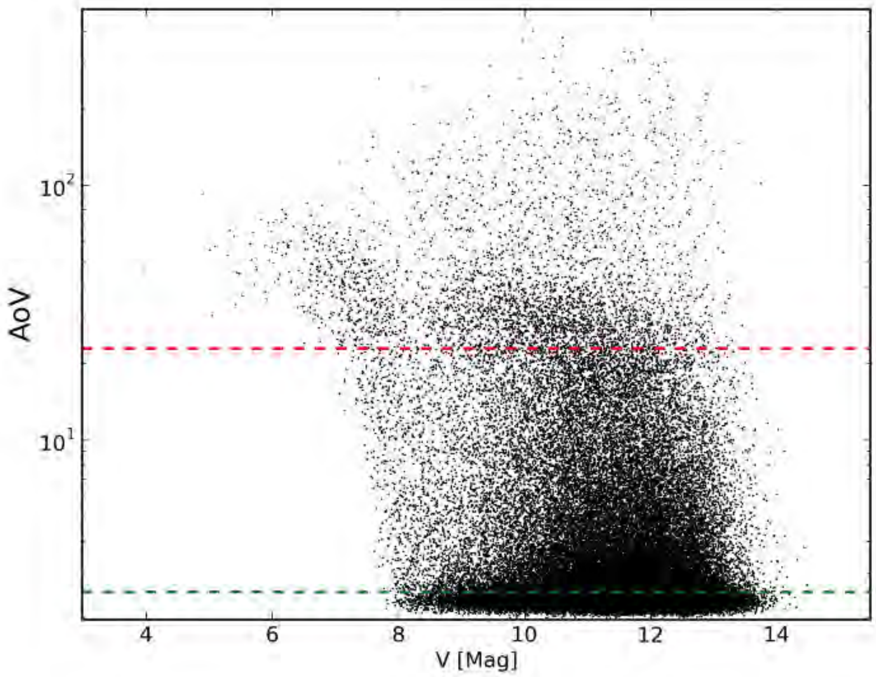

Figure 5.14: The AoV statistic of the lightcurves as a function of V magnitude. The dashed green line indicates the median AoV value and the dashed red line indicates the variable selection threshold. Any lightcurve with AoV $> 1.75\sigma$ is considered to be variable (see the text for the reason for this selection threshold).

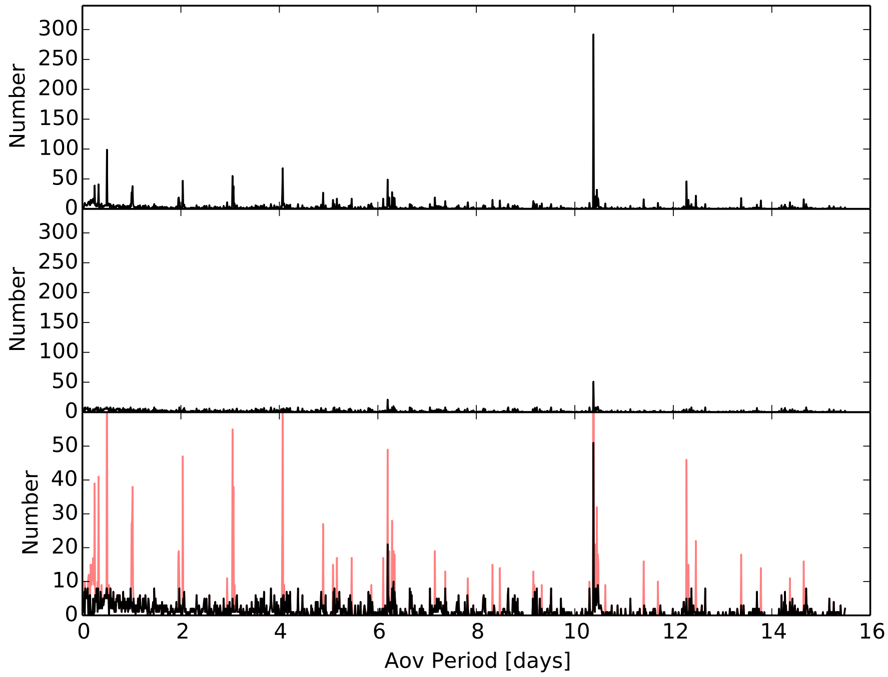

Figure 5.15: Histogram of the AoV periods. The top panel shows the histogram before the removal of the bad periods, while the middle panel shows the histogram after the bad period removal. The top and middle panel are plotted on the same vertical scale to better illustrate the effect of the bad period removal. The bottom panel is a zoomed in view to show the details of the period distribution after the removal of the bad period. The red lines show the locations of the original period distribution.

minutes and the longest period was roughly one third the entire baseline of the observations. This meant that even at the longest possible period found, the target system would show at least 3 full cycles increasing the likelihood of correctly identifying the period. The VARTOOLS package allows one to specify two parameters for searching for periodicity called “sub-sample” and “finetune”. The sub-sample parameter is used to perform the initial coarse search for periods and the finetune parameter is used to refine the peak periods identified. Both parameters are divided by the total baseline of the observation. We used a value of 0.5 for the sub-sample parameter and 0.1 for the finetune parameter, effectively giving a coarse search frequency of 0.01 d^{-1} and a fine search frequency of 0.002 d^{-1}. The top 10 highest peaks in the periodogram were output and the lightcurve was whitened at each peak period before searching for the next highest peak in the periodogram. The VARTOOLS package also outputs the negative natural logarithm of the formal false-alarm-probability (FAP) for each peak, which is calculated from the value of the AoV statistic using the Horne & Baliunas (1986) estimate for the bandwidth penalty. The FAP for each peak in the periodogram is given by:

$$FAP(z) = 1 - (1 - e^{-z})^M \tag{5.3}$$

where z is the peak value in the periodogram and M is the number of independent frequencies sampled. The value of M is approximated by:

$$M \approx N_0 \left(\frac{P_M}{P_N}\right) \tag{5.4}$$

where P_M is the maximum frequency searched and P_N is the Nyquist frequency.

The Figure 5.14 shows the AoV statistic as a function of V magnitude for all the lightcurves. We selected a lightcurve as variable if AoV $>$ 1.75 times the standard deviation; which selected 3481 candidate variables. We chose the value of 1.75σ as the cut-off limit because it selected a relatively large number of possible variables that could be checked by eye, while keeping the number of non-variables to a minimum. Most of the lightcurves below this value showed no sign of variability (with quick inspection by eye), while most of the lightcurves above this value showed clear signs of variability (a threshold value of 1σ selected far too many non-variable stars, while the 2σ threshold did not select many variables that showed clear signs of variability by visual inspection). Searches for variable stars in large datasets usually select a fixed value for the AoV statistic, or a stepped cut-off limit (Hartman et al. 2011a; 2008) when selecting candidate variable stars. We chose to use the data itself to identify the cut-off limit by choosing the “outlier” datapoints as possible variables. By using this method we expect to find most of the variable stars, while keeping the number of non-variables to a minimum (seeing as all the lightcurves need to be checked by eye, which is a very time consuming process). We are in the process of working on an automated classification system using machine learning (see Section 6.2.2) to identify and classify the variable lightcurves in the future, which would save a lot of time by eliminating the need for humans to inspect every lightcurve.

A histogram of the period distribution of the possible variable stars identified using the

AoV statistic revealed that many objects had similar periods (see top panel of Figure 5.15). The histogram spans the range of the periods we search for variability and the size of the bins was 0.01 day. Most of the false periodicities are caused by the 1 sidereal day alias of the observations. One particular period of 10.37750098 days was identified in over 250 lightcurves and can be seen as the large spike in the histogram. This false periodicity was caused by the gaps in the dataset due to weather. Bad weather at roughly every 11 days resulted in the dataset being broken up into four and a half sets. This could also indicate that we did not remove all the systematics from the lightcurve with the TFA implementation. A larger set of templates (instead of the closest 225 stars) might need to be used to correctly remove trends in the data.

To remove all the false periods we applied 3 rounds of 3σ clipping to the histogram. A lightcurve in one of the 3σ outlier bins was removed unless the AoV statistic and the Stetson J statistic for that lightcurve was 3 times larger than the median absolute deviation (MAD) of all the variable candidate lightcurves. This ensured that we did not remove strong variable candidates even though they shared similar periods to other lightcurves. The final set of 2028 lightcurves were inspected by eye to remove any false variables that made all the cuts. A total of 1230 were rejected leaving a final total of 798 variables that we included in the final variable candidate catalogue.

5.3.2 Lomb-Scargle Search

The lightcurves were searched for sinusoidal periodicity with period between 0.005 and 23 days. The shortest period we searched for was ∼2 times the observational cadence and was selected in order for us to discover the shortest known pulsating stars. The longest period searched for was half the total baseline length of the observations. We used a sub-sample value of 0.1 which meant that periods were refined at a resolution frequency of 0.002 d^{-1}.The top 5 peaks of each lightcurve were recorded and the lightcurve was whitened at each peak period before searching for the next highest peak in the periodogram. Figure 5.16 shows the Lomb-Scargle signal-to-noise ratio (SNR) of the most dominant frequency as a function of V magnitude. The Lomb-Scargle SNR value is an indication as to how well the signal is distinguishable from the background noise in the lightcurve of the star. We selected a lightcurve as a potential variable object if the L-S SNR $>$ 1.75 times the standard deviation (using a similar argument for this threshold value as discussed in the AoV search section). This selected 3976 possible variable stars. We followed a similar procedure as described in Section 5.3.1 to remove bad periods due to systematics and aliasing. Most of the bad periods are aliases of 1 sidereal day. We do not see the same 10.37750098 day false period in the L-S period distribution as seen in the AoV period distribution and we think this is simply due to the fact that the resolution of the L-S method is limited by the relatively broad profile of a sinusoid. Figure 5.17 shows the histogram of the period distribution before and after the removal of the bad periods. The final set of possible variables contained 990 objects which were all inspected by eye to remove spurious detections that made it through the reduction process, but were clearly not true variables. Once all the spurious detections were

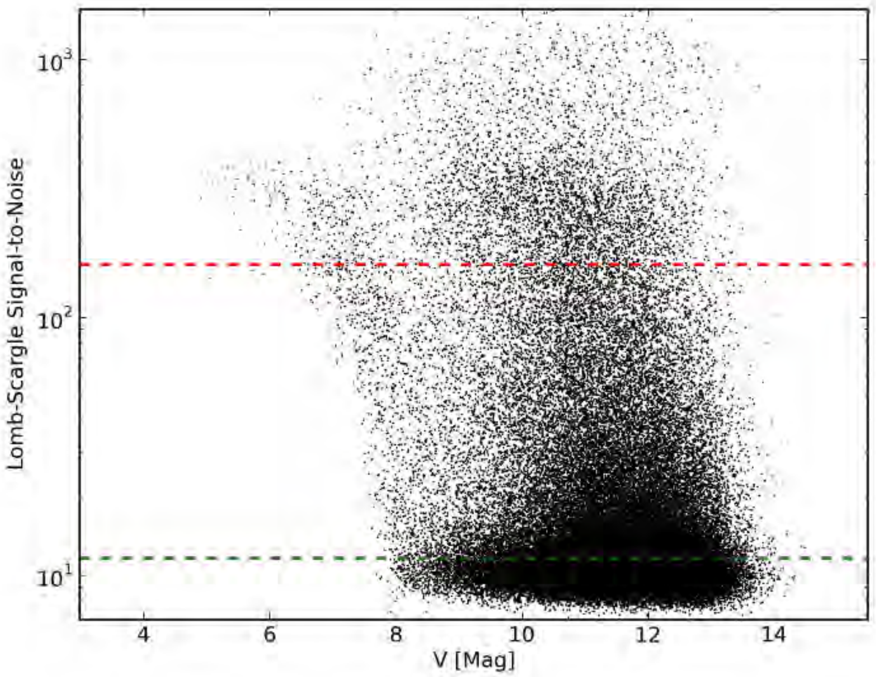

Figure 5.16: The Lomb-Scargle signal-to-noise (SNR) ratio of the lightcurves as a function of V magnitude. The dashed green line indicates the median and the dashed red line indicates the variable selection threshold. Any lightcurve with SNR $> 1.75\sigma$ is considered to be variable (see the text for the reason for this selection threshold).

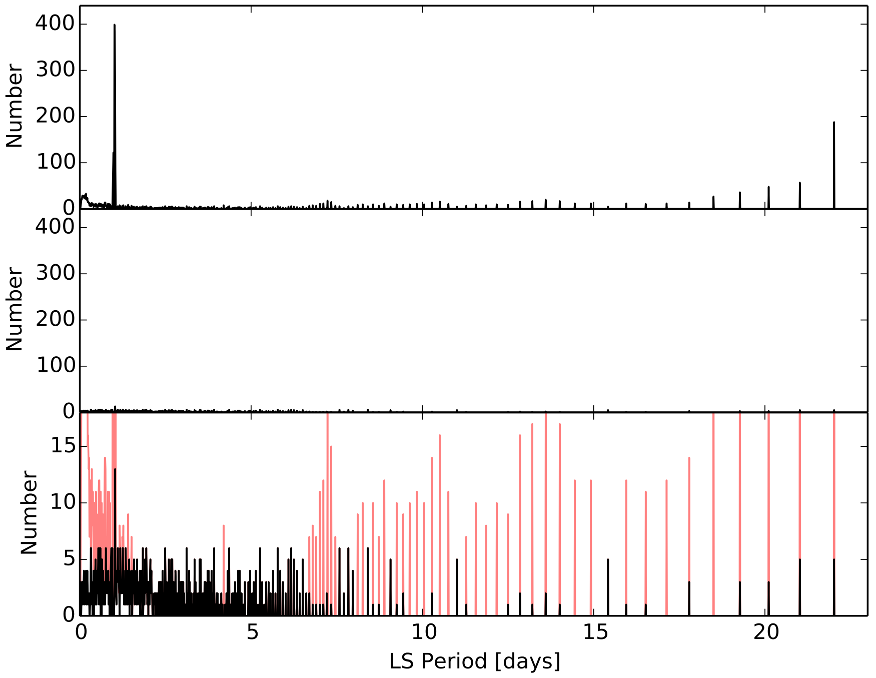

Figure 5.17: Same as figure 5.15, but this time for the Lomb-Scargle periods.

eliminated, we were left with 596 possible sinusoidal variables that we included in the final catalogue of variable candidates.

5.3.3 Box-Least-Squares Search

The BLS algorithm searches for top-hat like features in the lightcurves by cycling through periods, phases, and duration of the top-hat feature and selecting the one with the highest significance. The advantage of searching for a predefined shape rather than a method that fits trigonometric functions to the lightcurve is efficiency and speed (Grziwa et al. 2012, Enoch et al. 2012). We searched for eclipsing variables in our data set with periods between 0.5 and 5 days with 20000 trial frequencies. We restricted the search to a maximum period of 5 days because the detection efficiency becomes very small for longer periods (Enoch et al. 2012) and only one transiting exoplanet is known to have a period less than 0.5 days. Even though many known eclipsing binary systems have periods < 0.5 days, the primary purpose for using the BLS algorithm was to find transiting exoplanets (future versions of the identification process using machine learning techniques will search for periods shorted than 0.5 days and periods much longer than 5 days). The lightcurves were divided into 200 bins and we searched for eclipses where the fraction of the orbit in transit was between 1% and 15%. Figure 5.18 shows a plot of the BLS Signal-to-Pink-Noise (SPN) as a function of V magnitude. The SPN value is defined by Hartman et al. (2008) as follows:

$$SPN = \sqrt{\frac{\delta^2}{\sigma_w^2/n_t + \sigma_r^2/N_t}} \tag{5.5}$$

where δ is the depth of the eclipse, n_t is the number of points in the eclipse, N_t is the number of distinct eclipses sampled, σ_w is the white noise, and σ_r is the red noise at the timescale of the eclipse. The SPN value is a method to assess the significance level of a detected transit. In the implementation of the BLS search algorithm by Hartman et al. (2008), the best BLS model is subtracted from the lightcurve and σ_w is set equal to the standard deviation of the residual. The residual lightcurve is then binned in time with bin size equal to the duration of the eclipse. The value of σ_r is then set equal to the standard deviation of this binned residual lightcurve.

We selected a lightcurve as variable if BLS SPN > 4.75 times the standard deviation (following a similar reasoning as for the AoV and L-S thresholds). This selected 3521 candidate eclipsing systems. We followed the same procedure to remove false periodicities due to systematics and aliasing as described in Section 5.3.1. Figure 5.19 shows the BLS period histogram before and after the bad period removal. The final list contained 1896 lightcurves that were all examined by eye to remove spurious detections. At the end of this procedure we were left with 873 eclipsing systems that were included in the final catalogue of variable candidates.

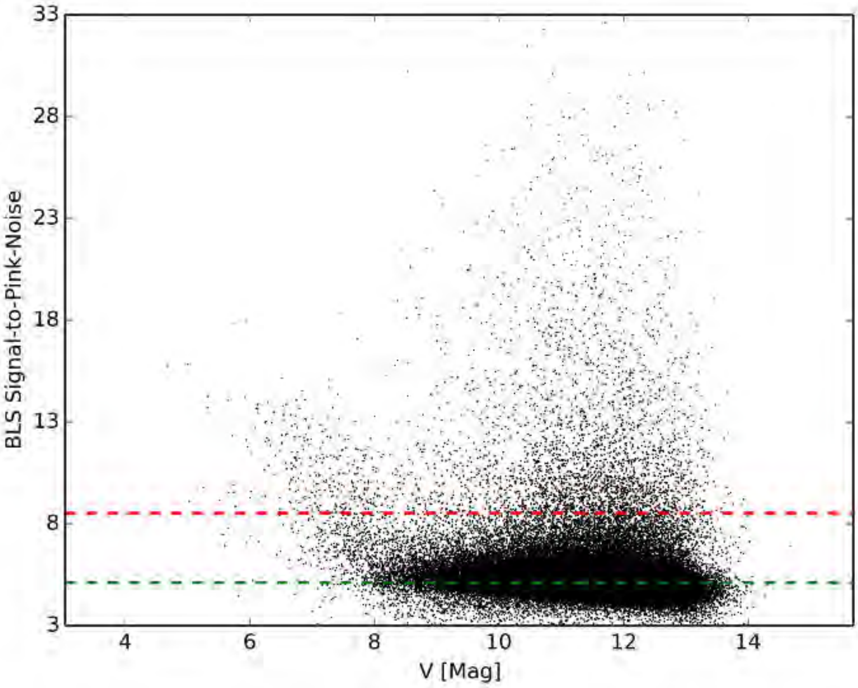

Figure 5.18: BLS Signal-to-Pink-Noise as a function of V magnitude. The dashed green line indicates the median and the dashed red line indicates the variable selection threshold. Any lightcurve with Signal-to-Pink-Noise $> 4.75\sigma$ is considered to be variable (see the text for the reason for this selection threshold).

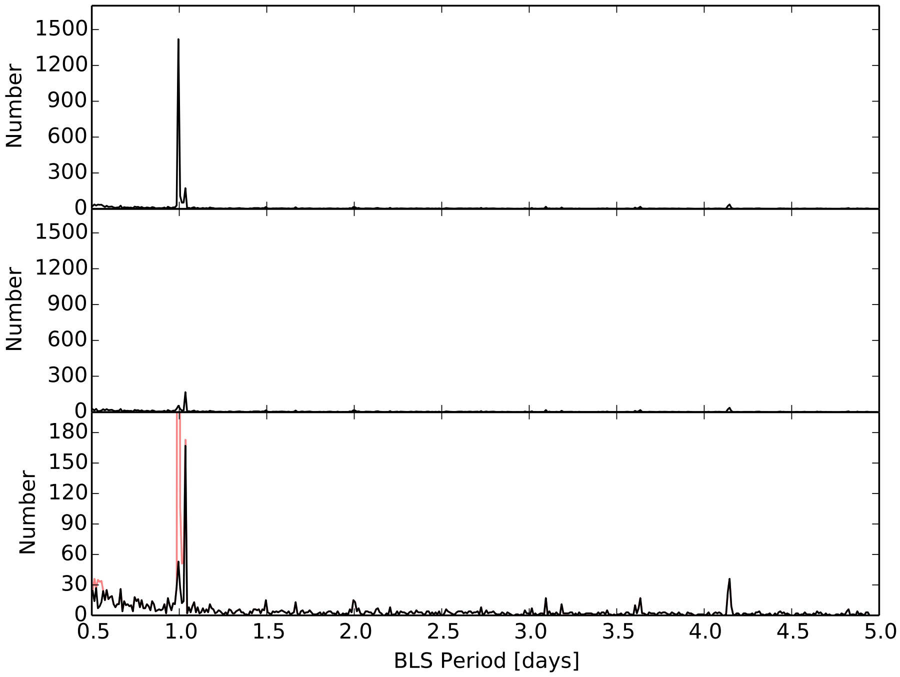

Figure 5.19: Same as figure 5.15, but this time for the BLS periods.

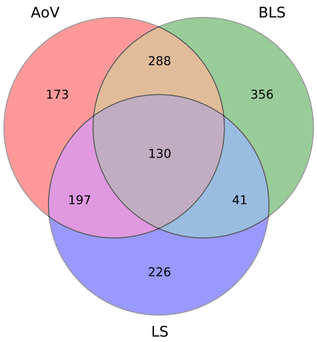

Figure 5.20: Venn diagram of the numbers of variable stars identified by each method.

Table 5.1: Table of the numbers of variable stars identified by each method.

AoV	L-S	BLS	Total
✓	✓	✓	130
✓	✓	✕	197
✓	✕	✓	288
✕	✓	✓	41
✓	✕	✕	173
✕	✓	✕	226
✕	✕	✓	356

5.4 Combined Variability Catalogue

We created a combined catalogue, the KELT-South Variability Catalogue (KSVC). This catalogue contains 1473 variable candidate objects and was done combining the candidates identified by the methods described above. We also performed a blending check to eliminate variable candidates that showed variability in their lightcurves that were clearly due to proximity to true variables. This procedure removed 29 blended sources from the final list. We also removed 33 possible exoplanet candidates from the list and included these objects in the list of possible transit candidates (see section 5.6). These were identified by the depth of the eclipse being less than 5 mmag.

The final catalogue of variable star candidates contained 1411 objects. Of these objects 130 were identified by all three methods. 197 objects were detected by AoV and L-S but not by BLS, 288 were detected by AoV and BLS but not by L-S, and 41 were detected by L-S and BLS but not by AoV. 173 objects were found by AoV only, 226 objects were found by L-S only, and 356 objects were found by BLS only. See Table 5.1 as well as Figure 5.20 for a summary.

5.4.1 Matching to Known Variable Sources

The American Association of Variable Star Observers (AAVSO) (Watson et al. 2013) catalogue contains a total of 282000 variable stars of which 2882 are within the T1 field of view. The AAVSO catalogue contains stars known or suspected to be variable and lists all stars that have an entry in the AAVSO International Variable Star Index (VSX).* The catalogue consisted initially of the General Catalogue of Variable Stars (GCVS) (Samus et al. 2009) and the New Catalogue of Suspected Variables (NSV) (Kukarkin et al. 1995, Kazarovets et al. 1998) and was then supplemented with a large number of variable star catalogues, as well as individual variable star discoveries or variables found in the literature.

---

*http://www.aavso.org/vsx

The magnitudes of most of the variable stars in the AAVSO catalogue are listed in Johnson V, with others listed in either Johnson U, B, R, or I[*], Johnson infra-red J or K, Hipparcos magnitude *Hp*, photographic magnitude *pg*, Sloan *u'* or *r'*, or white (clear) *w*.

The range of magnitudes for the variable candidates we found using the methods described above is $7 \leq \mathrm{V} \leq 14$. Out of the known 2882 known variables, 2560 are within that range. We matched this list of 2560 objects to the closest KELT-South lightcurve within a search radius of $46''$ and found that 1716 of these stars have a KELT-South counterparts. Of the 844 known variables for which we do not have KELT-South lightcurves, most are either saturated in the KELT-South images, blended with saturated stars or are too faint for the pipeline to identify a star at that particular location on the image. For a small number there is no KELT-South object identified at that location, suggesting that the positions, proper motions, or magnitudes could be reported incorrectly for these objects. Of the 1716 known variables with KELT-South counterparts, 559 have periods less than 23 days (the maximum period we searched for periodic variables using the L-S search algorithm).

We then compared the list of 1411 possible KELT-South variable stars to the 559 known variables with periods less than 23 days and found 393 matches. Of the 166 known variables we did not identify as variable stars with our procedures, 45 have periods longer than 15.5 days (longest period searched for with AoV). These variables would only have been detected by the L-S routine if they showed sinusoidal variability, which most did not as they are listed as "MISC" type variables in the AAVSO Catalogue (4 are listed as eclipsing binary systems and would not have been found by the L-S routine). This leaves 121 sources which are not found using the routines described earlier. An investigation of these 121 sources revealed that 17 stars were saturated or blended with saturated sources in the KELT-South images, 23 were rejected due to the phase coverage available in the KELT-South lightcurves not being good enough to confirm the variability, 14 sources showed variability but the amplitude of variability could only be extracted once the outlier data points were removed (large RMS scatter reduced the detectability of the variations), 25 lightcurves showed no sign of variability at the period given in the AAVSO catalogue, 14 were removed by the aliasing removal procedure because they had periods very close to known aliases (and the amplitude of variability was not significant enough to distinguish it as a true variable above the other sources), 10 sources had different periods identified by LS and AoV than the ones listed by AAVSO and 4 sources were correctly identified as variable but were wrongly discarded when they were visually inspected. We found that the last 14 sources showed clear signs of variability and should have been included in the KELT-South catalogue of variable objects, but were rejected during the alias removal procedure as all of them have very similar periods of ∼0.43 days. All of these showed signs of sinusoidal variability with low amplitudes and are most probably δ-Scuti or Beta Cephei type variables. This pile-up of true variables, with very strong indicators of variability, at roughly the same period "confused" the alias

---

[*] The original Johnson system consists of the UBV filters whose calibration was intimately tied to the photoelectric detectors in use at the time. The system has since been extended to the red with optical RI and near-infrared JHK filters (Bessell 2005). The definitions of these filters are not always independent of the detectors involved and can vary slightly from observatory to observatory.

removal procedure, resulting in all of them being removed from the final list of variable star candidates. Additional verification of periodicity, before removal will be implemented in future version of the variable star identifier (see Section 6.2.1 for more details).

183 of the 1716 stars in the AAVSO catalogue with KELT-South counterparts are listed without periods. We found 18 of those stars in the KELT-South variability catalogue and the periods we found are listed in Table 5.2.

5.4.2 Classification of Variables

The possible variable stars were assigned a variability type using a simplified version of the classification scheme of the GCVS. The identification was based only on the photometric lightcurve obtained with the KELT-South telescope through a visual inspection. The classification of a lightcurve into one of the three categories (pulsating variable, contact eclipsing binary or detached eclipsing binary) was based on the shape, amplitude and period of the brightness variability alone. Where a star could not be classified as either a contact or detached eclipsing binary, but clear variability was visible, it was assigned as a pulsating star. The following classes could be identified:

1. *Detached eclipsing binaries:* Lightcurves with clear eclipses that showed very little or no variability outside of the eclipses was classified in this class. These lightcurves are most probably Algol-type binaries of which β Per is the prototype.

2. *Contact eclipsing binaries:* Lightcurves with eclipses the showed different depths and clear ellipsoidal variation were put into this class. The prototypical example for this class is β Lyr. This class of variable star also contains W Ursae Majoris type variables.

3. *Pulsating star:* All other lightcurves that showed clear variability was placed into this category. This category contains many types of variables that could be sub-classified by more rigorous analysis. This group contains RR Lyrae, Cepheids, γ Doradus, δ Scuti type variables and variables that showed variations in brightness due to stellar rotation, magnetic variability, or ellipsoidal variations.

It is possible that many variables are not identified correctly using this simplified classification scheme and are placed into the wrong class. Without any additional follow-up observations either through photometric observations in multiple filters or spectroscopic follow-up observations, it is very difficult to determine the exact nature of all the variables.

5.4.3 KELT-South Variability Catalogue (KSVC)

We list the properties of all the variable stars we found in Table 5.3. We list only the first 20 stars here to show the form and content. The full machine-readable table can be found online*. In total, 240 contact eclipsing binaries, 391 detached eclipsing binaries and 780 pulsating variables were identified. For each star in the catalogue we list the KELT-South

---

*Catalogue of possible variable stars: http://keltsouth.saao.ac.za/KS_Var_Cat/KS_VarCat_Final.fits

Table 5.2: Variable Stars in AAVSO Catalogue with no periods listed. The KELT-South period is listed.

AAVSO Name	KELT-South ID	2MASS ID	RA (J2000)	Dec. (J2000)	K-S instr. magnitude	Approx. V magnitude	Period (days)
V0393 Car	KST1C00641	07590267-6135009	119.7612	-61.5836	9.784	7.691	0.1413
NSV 17732	KST1C00693	08042986-4245291	121.1258	-42.7586	9.819	7.727	0.4946
NSV 17431	KST1C00899	07182710-5721067	109.6129	-57.3519	10.076	7.983	0.5704
V0367 Pup	KST1C00998	07235992-4407470	111.0083	-44.1350	10.139	8.046	20.763
NSV 18243	KST1C01034	09392747-6315182	144.8642	-63.2550	10.095	8.002	4.1512
V0388 Car	KST1C01256	07215144-5546159	110.4643	-55.7711	10.332	8.239	2.9586
NSV 17861	KST1C01420	08195793-4740481	124.9912	-47.6800	10.402	8.309	0.8627
HD 72675	KST1C01857	08322318-4547008	128.0975	-45.7852	10.572	8.479	0.0566
V0383 Car	KST1C01928	06590403-5830533	104.7668	-58.5148	10.714	8.621	0.1122
NSV 17904	KST1C01963	08293744-4405523	127.4075	-44.0994	10.630	8.538	1.1332
NSV 17450	KST1C02280	07221926-4920334	110.5837	-49.3442	10.849	8.756	1.1925
V0343 Pup	KST1C02736	07320760-4656327	113.0317	-46.9424	10.983	8.891	0.4754
NSV 17697	KST1C04255	07585154-5600495	119.7146	-56.0139	11.302	9.210	0.1231
NSV 17610	KST1C05765	07463841-6143542	116.6600	-61.7317	11.585	9.492	1.8409
NSV 4517	KST1C08180	09305578-5125057	142.7261	-51.4211	11.879	9.786	1.1400
NSV 18252	KST1C09946	09411184-5349355	145.3054	-53.8324	11.991	9.898	5.8992
NSV 17925	KST1C17996	08340971-4933262	128.5421	-49.5600	12.648	10.555	2.3250
V0378 Vel	KST1C18422	08444729-4558554	131.1970	-45.9821	12.590	10.497	6.2233

ID number, the coordinates in right ascension and declination (J2000.0), the KELT-South instrumental magnitude, the approximate V magnitude, the period in days, the type of variable based on our classification, the 2MASS ID and the AAVSO name. We also plot some example lightcurves in Figures 5.21, 5.22 and 5.23.

5.4.4 Variable Catalogue Characterisation

The 1018 suspected new variable we have found in using the KELT-South telescope will increase the number of variables listed in the AAVSO catalogue (282000 as of 2013 October) by 0.3%. If we only consider the number of known variables within the Target1 field (2882 in the AAVSO catalogue), that number rises dramatically to 35.3%. Of the total 78297 stars in the T1 field for which we have lightcurves, the fraction of new variables is 1.3%. This compares very well with similar exoplanet and other photoelectric variability surveys which ranges from 0.1% (OGLE-III) to 2.3% (ASAS-2) for regular surveys. The search for variability in field K and M dwarf stars by Hartman et al. (2011a) has a detection yield significantly higher (5.6%) than the other surveys listed, as this type of targeted search excludes giant stars which generally have variability periods that are much longer than the typical timescale of the survey. In Table 5.4 we list the survey name, the number of stars observed $N_\star$, the number of new variables found in that sample N_v, the fraction of new variables to number of stars observed F_v and the visual magnitude range of the survey. We further investigate the KSVC by examining the magnitude and period range in the following sections.

Magnitude Range

We compared the KSVC to the AAVSO catalogue to investigate the magnitude distribution of the variable stars in each catalogue. We limited the AAVSO catalogue to only the stars for which there is a V magnitude listed, which selects 2475 known variables within the T1 field. 365 variables have magnitudes listed in other filters. The histogram in Figure 5.24 shows that for the magnitude range 8 < V < 11, the KSVC contains roughly 70% as many variable stars as the AAVSO catalogue. There is a steady decrease in the number of variables toward fainter magnitudes where the precision in the lightcurves of the KELT-South survey decreases.

In Figure 5.25 we show the magnitude distribution of the various classes of variables in the KSVC. The pulsating star class shows a relatively Gaussian shaped distribution across the magnitude range with a peak at ∼10.5 V magnitude. The eclipsing binary distributions both have a similar shape, but the peaks for the eclipsing binaries is at ∼11.5 V magnitude. This indicates that as long as the eclipse depths are relatively large (larger than the RMS of the KELT-South lightcurve at that magnitude), we are able to identify eclipsing systems to fainter magnitudes than the pulsating variables with low amplitude pulsations. Beyond V = 12 for all the classes, the number of variables decreases sharply and no new variables are found beyond V = 14.

Table 5.3: Table of KELT-South Combined Catalogue of Variable Stars (we only show the first 20 entries; the full machine-readable table can be found online).

KELT-South ID	RA (J2000)	Dec. (J2000)	K-S instr. magnitude	Approx. V magnitude	Period (days)	KELT-South Class.	2MASS ID	AAVSO Name
KST1C00387	113.1894	-53.5551	9.492	7.399	0.9804	EB Contact	07324613-5333190	...
KST1C01357	136.5983	-59.2074	10.343	8.250	3.2011	EB Contact	09062241-5912231	NSV 18137
KST1C01519	123.7075	-42.0362	10.374	8.281	3.5528	EB Contact	08144979-4202215	QR Pup
KST1C01823	114.8455	-43.9727	10.625	8.532	0.8581	EB Contact	07392297-4358297	...
KST1C02055	114.1039	-61.8756	10.729	8.636	5.1365	EB Contact	07362523-6152258	V0455 Car
KST1C02457	133.1245	-48.4905	10.803	8.710	1.7296	EB Contact	08522942-4829299	HIP 43579
KST1C02435	114.9759	-49.4248	10.870	8.777	0.8454	EB Contact	07395429-4925310	ASAS J073955-4925.6
KST1C03042	111.8944	-40.9407	11.055	8.962	0.8877	EB Contact	07273433-4056203	...
KST1C03318	118.4949	-45.6419	11.108	9.015	1.1030	EB Contact	07535904-4538357	...
KST1C03307	108.3375	-55.5717	11.178	9.085	0.3472	EB Contact	07132177-5534164	...
KST1C03505	130.0786	-64.8399	11.201	9.108	1.5808	EB Contact	08401799-6450168	...
KST1C03828	124.4164	-41.7050	11.225	9.132	1.1263	EB Contact	08173982-4142278	AU Pup
KST1C03636	107.3452	-57.4979	11.240	9.147	0.9024	EB Contact	07092358-5729469	ASAS J070922-5729.8
KST1C04011	136.3268	-56.0352	11.249	9.156	1.4497	EB Contact	09051737-5602068	...
KST1C04608	142.0100	-54.5697	11.321	9.228	1.8810	EB Contact	09280311-5434036	...
KST1C04484	121.8906	-55.3279	11.326	9.233	0.9676	EB Contact	08073395-5519370	V0608 Car
KST1C04554	114.6796	-43.5920	11.402	9.309	1.5580	EB Contact	07384353-4335409	HIP 37222
KST1C05052	108.7078	-59.2690	11.520	9.427	0.4723	EB Contact	07145062-5916042	V0604 Car
KST1C06457	143.8221	-54.0884	11.580	9.487	0.5870	EB Contact	09351751-5405198	...
KST1C07897	125.0722	-43.8794	11.854	9.761	1.6177	EB Contact	08201698-4352513	AY Vel

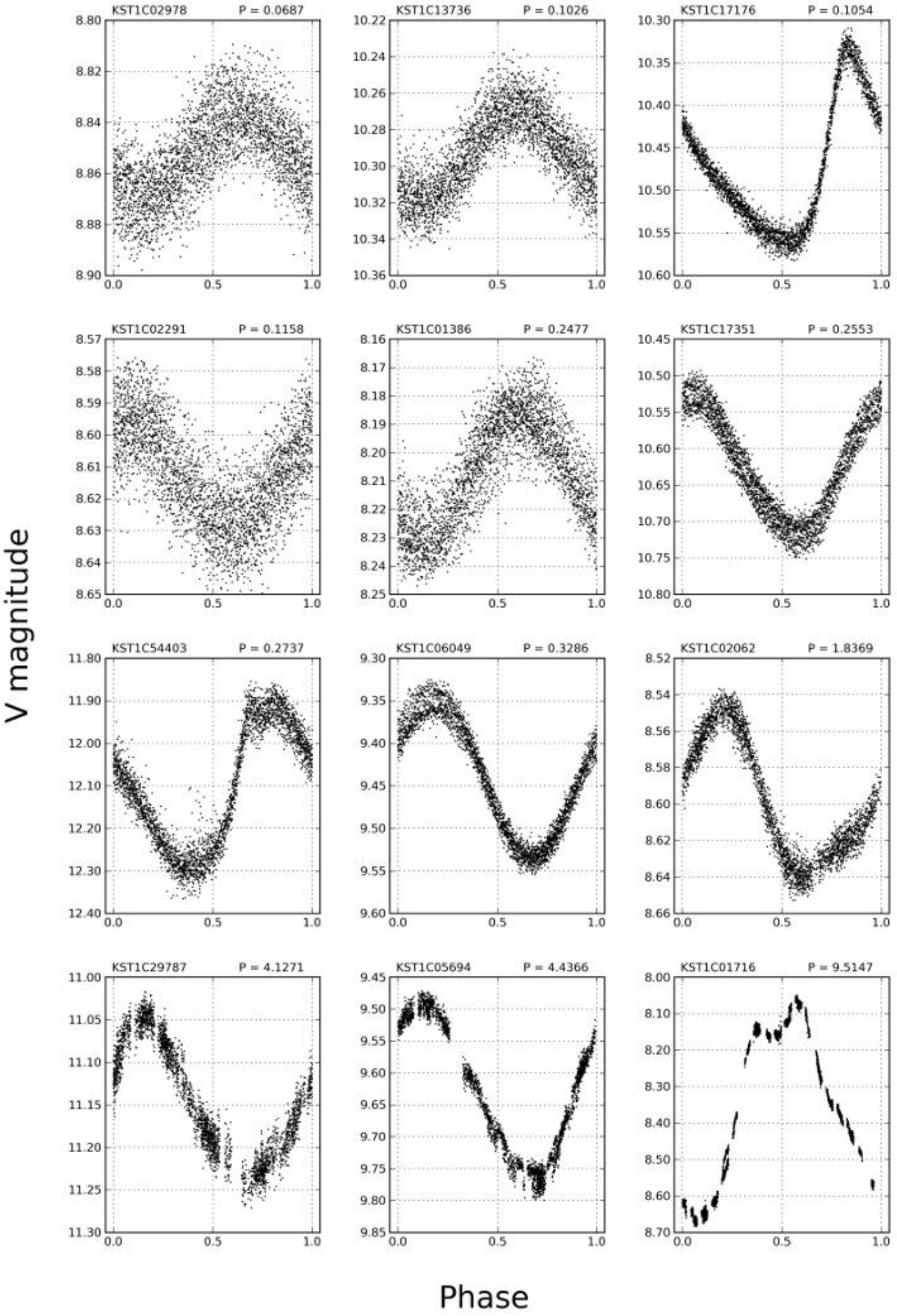

Figure 5.21: Example lightcurves of pulsating stars identified by KELT-South, for period range 0.0 < P < 10.0 days

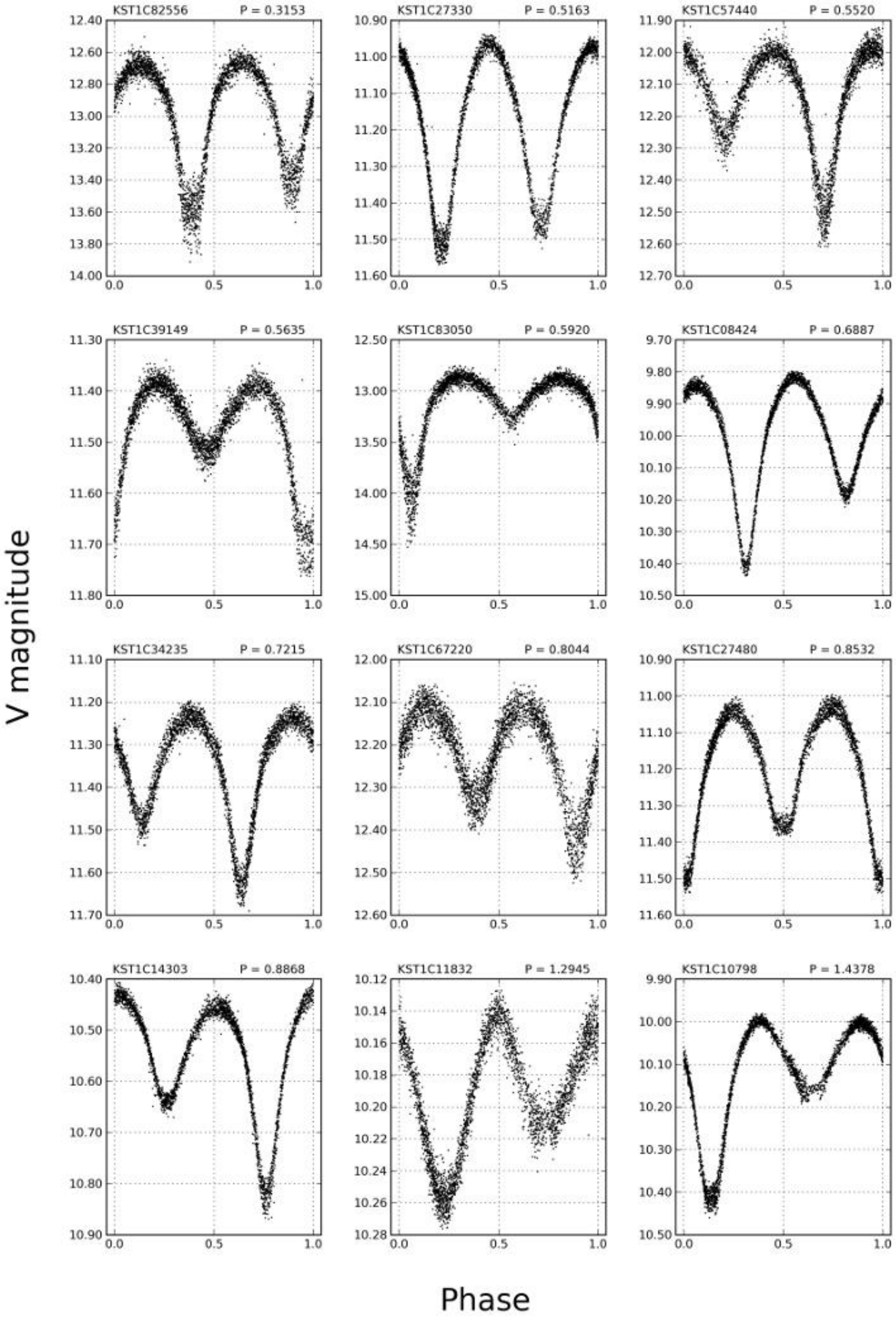

Figure 5.22: Example lightcurves of contact eclipsing systems identified by KELT-South, for period range $0.0 < P < 1.5$ days

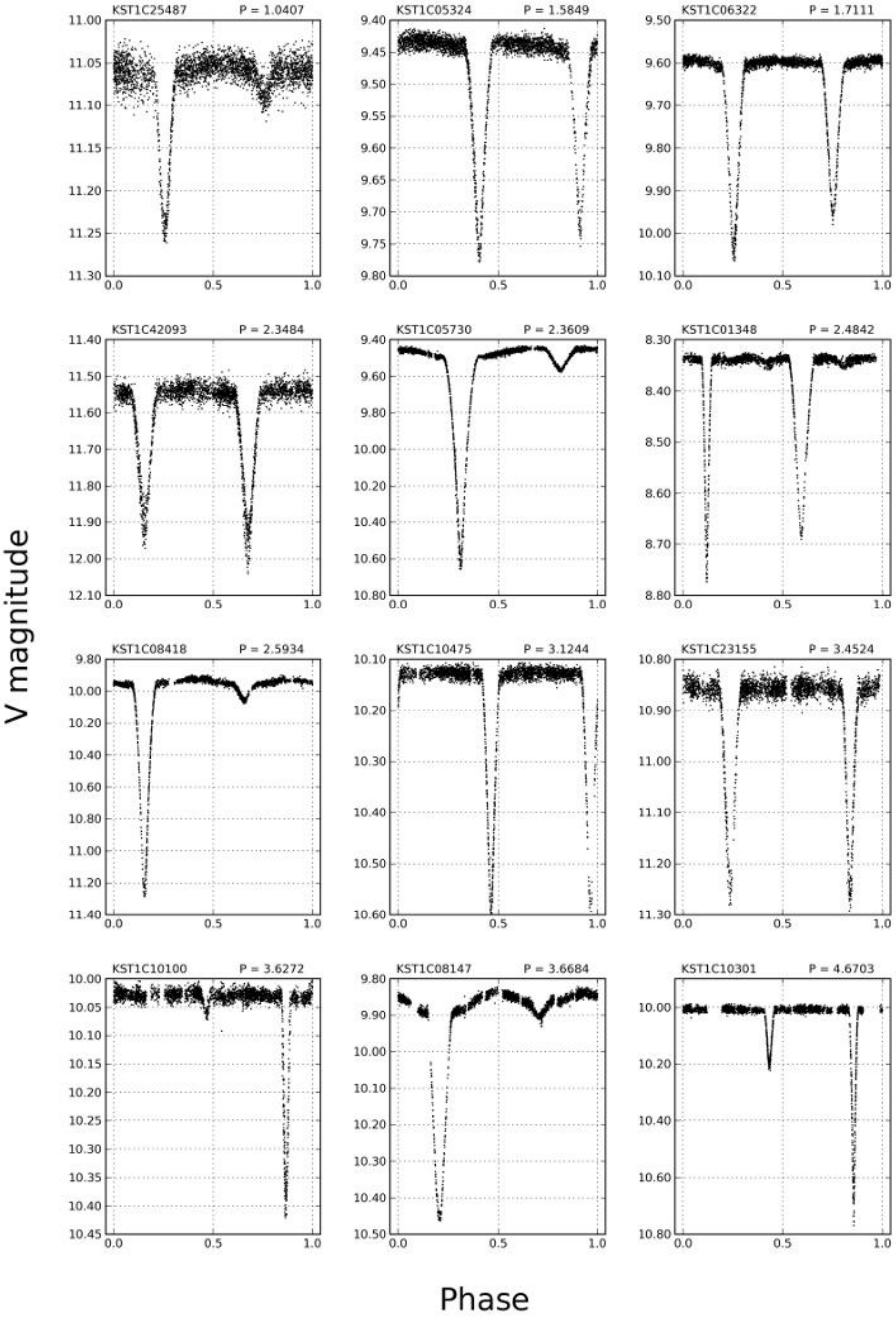

Figure 5.23: Example lightcurves of detached eclipsing systems identified by KELT-South, for period range 1.0 < P < 5.0 days

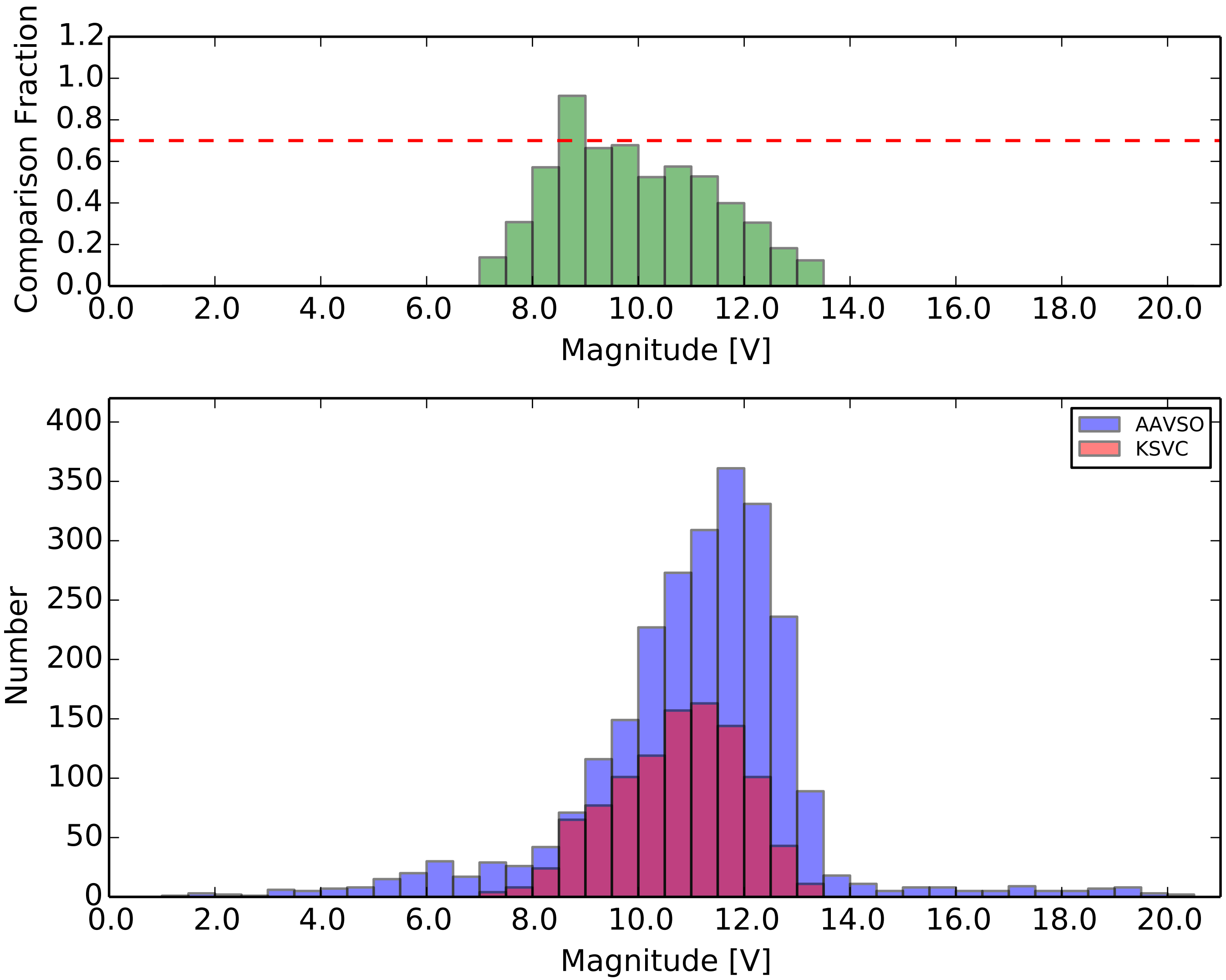

Figure 5.24: Histogram of the V magnitude distribution of the KELT-South Variability Catalogue compared to the V magnitudes of the variables stars in the AAVSO catalogue. The top panel shows the KSVC as a fraction of the number of variables stars in the AAVSO catalogue. The horizontal dashed red line is plotted at 70% , which indicates that we have significantly less variable stars within the same 0.25 magnitude bins than the number of variable stars in the AAVSO catalogue. The bottom panel is a histogram of the number of variables stars found in the KSVC and AAVSO catalogues.

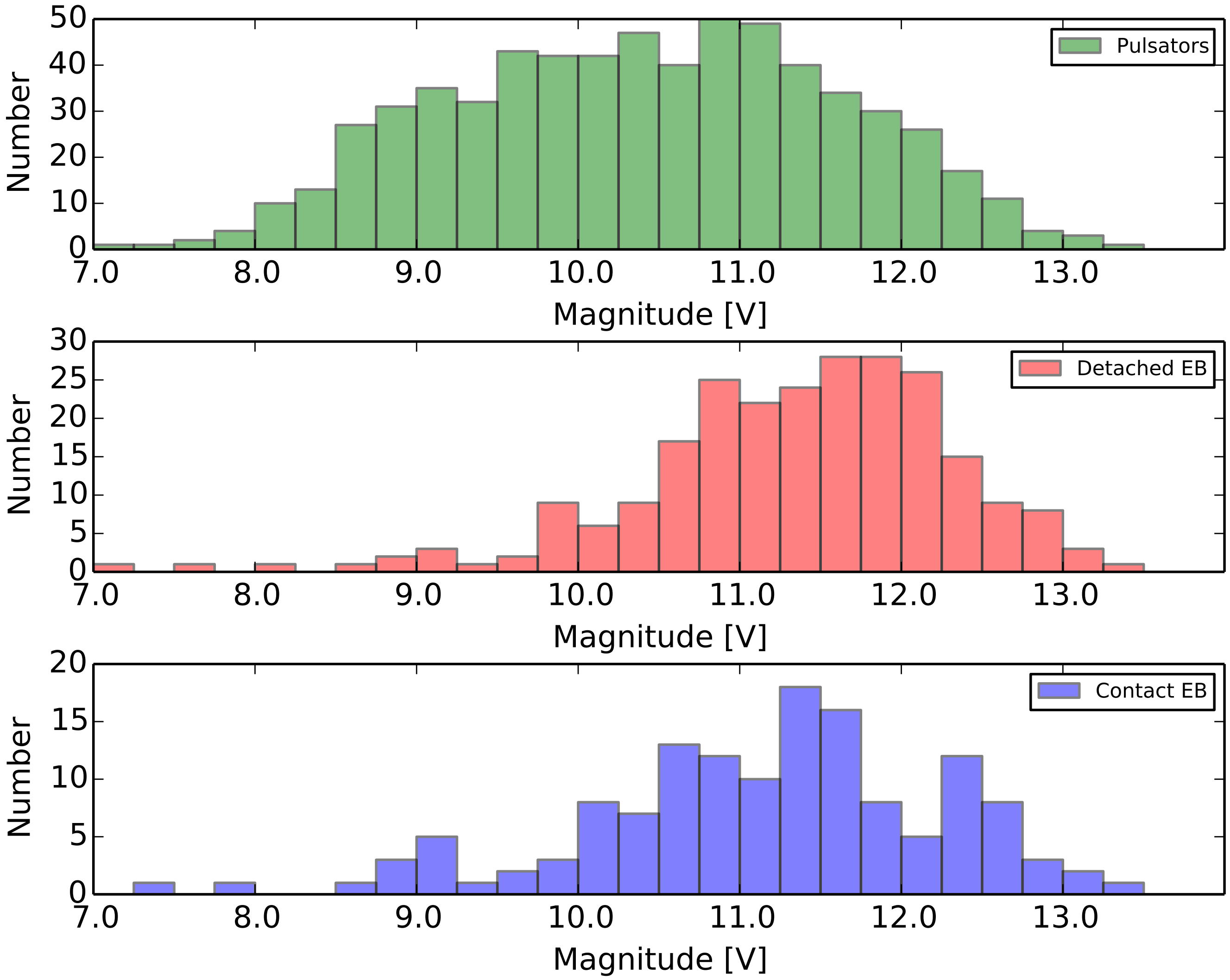

Figure 5.25: Histogram of the V magnitude distribution for each class of variable in the KELT-South Variability Catalogue.

Table 5.4: Comparison of KELT-South variable star detection yield against other surveys.

Survey Name	$N_\star$	N_v	F_v	Mag [V]	References
KELT-South (T1)	78297	1018	0.0130	7-14	This work
BEST II	209070	2406	0.0115	11-17	Fruth et al. (2013)
UNSW	87000	659	0.0076	8-14	Christiansen et al. (2008)
HATNet[a]	27560	1530	0.0555	10-16	Hartman et al. (2011a)
ASAS-2	140000	3170	0.0226	8-13	Pojmanski (2000)
ASAS-3	1.7×10^7	50099	0.0029	8-14	Paczyński et al. (2006)
OGLE-III	2×10^8	193000	0.0010	12-20	Soszyński et al. (2008; 2011)

NOTES
[a] This study selected only field K and M dwarf stars in the HATNet survey dataset to search for variability.

Period Range

The cadence of observations of a photometric survey like KELT-South will have a significant impact on the types and periods of variables found. For the T1 field, with a cadence of ∼3 minutes and a total baseline of observation of ∼46 days, it is reasonable to assume that the detection efficiency will be biased toward shorter periods, especially considering that the BLS search algorithm was instructed to only report a detection of periodicity for periods between 0.5 and 5 days. We plot a histogram of the period distribution for each of the three classes of variables stars we identified in Figure 5.26. We limit the plot to a maximum period of 10 days, as only 36 (∼3%) of all the potential variables in the KSVC have periods longer than 10 days. The contact binaries we identified have a peak period between 0.25 and 0.75 days, which agrees with previous studies of variable stars in other surveys (Pietrukowicz et al. 2013, Fruth et al. 2013). There are also a number of contact eclipsing binaries we identified with period longer than 2 days, which are most probably misidentified and should be included in the pulsating variable category. However, contact eclipsing binaries with periods longer that 10 days were identified in the OGLE data (Rucinski 1998, Rucinski & Maceroni 2001) and further investigation into the true nature of these objects is required. We also find very few contact binaries with periods shorten than 0.5 days, but this is entirely due to the BLS search parameters we used. A large fraction of the pulsating variables with periods < 0.5 days might also be contact eclipsing binaries, but without any additional follow-up data on these objects it is very difficult to determine their true nature by visual inspection of the phase folded lightcurves alone.

5.5 Target1 Transiting Exoplanet Expectations

At present the frequency of Jupiter type planets that orbit solar type stars in the neighbourhood of our Sun is a very active research field. Studies by Bayliss & Sackett (2011) provide frequency rates from less than 1.5 (with orbital periods between 1 and 3 days) per thousand dwarf stars to a frequency rate of $1.5^{+4.1}_{-1.1}$ (with orbital periods between 3 and 5 days) per thousand dwarf stars from the SuperLupus Survey. Results from the Kepler

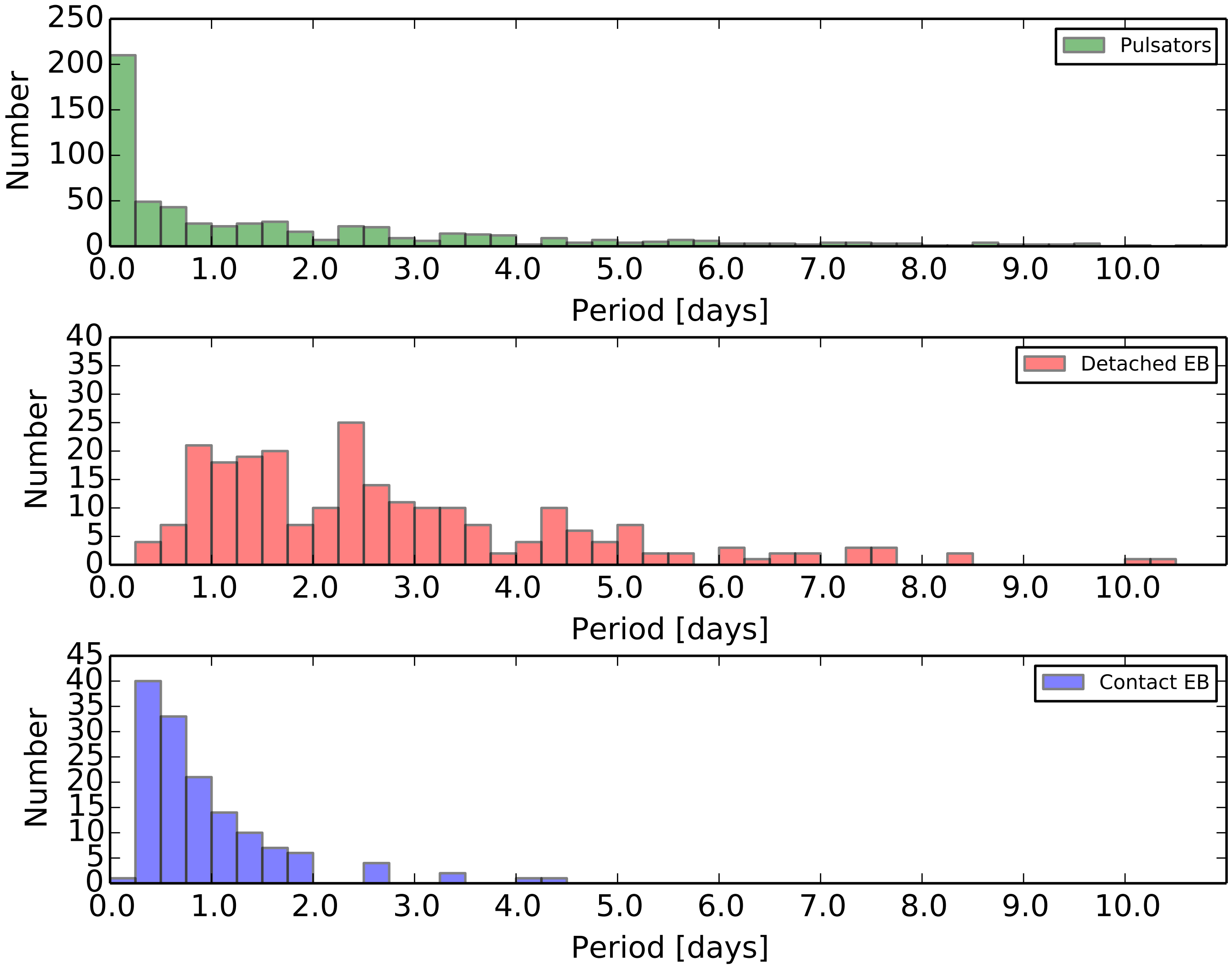

Figure 5.26: Histogram of the period distribution of the KELT-South Variability Catalogue.

spacecraft report frequency rates of 4 ± 1 (with orbital periods less than 10 days) for stars with magnitude $K_p < 15$ (Howard et al. 2012b). The frequency of Hot-Jupiters using the OGLE-III data is $1.4^{+1.5}_{-0.8}$ per thousand stars for periods between 1 and 3 days, and $3.1^{+4.2}_{-1.8}$ per thousand stars for periods between 3 and 5 days (Gould et al. 2006). These numbers are quite different from the occurrence rates of hot Jupiters around solar type stars from RV surveys. The RV surveys typically have frequency rates of ∼10 per thousand stars (Marcy et al. 2005, Cumming et al. 2008, Mayor et al. 2011, Wright et al. 2012). The large differences in the frequency rates found by the two different methods are usually attributed to the fact that the RV surveys typically target higher metallicity stars which are known to have a higher likelihood of planet occurrence (Gonzalez 1998, Gonzalez et al. 2001, Santos et al. 2001; 2003; 2004, Fischer & Valenti 2005, Sousa et al. 2008, Neves et al. 2009, Johnson et al. 2010, Sousa et al. 2011, Adibekyan et al. 2012b).

If we assume an average frequency rate from the transiting exoplanet surveys, we can expect ∼2 Hot-Jupiter planets per thousand stars with orbital periods less than 5 days around solar type stars in the solar neighbourhood.

If we limit the T1 dataset to a sample that includes stars with 8 < V < 11 and RMS levels < 1% (see Section 5.2.8 for details of this selection cut), we simply need to determine the number of solar type stars within those parameters and multiple it by the fraction of expected Hot-Jupiters with orbital periods less than 5 days to find out how many transiting exoplanets we expect to find in the T1 dataset.

To exclude giant stars from our dataset, we make use of the reduced proper motion (H_J) diagram (Gould & Morgan 2003), using the same procedure outline in Siverd et al. (2012). The reduced proper motion is calculated using the information from the 2MASS catalogue as follows:

$$H_J = J + 5 \log \mu \tag{5.6}$$

where μ is defined as the proper motion of the star given by:

$$\mu^2 = {\mu^2}_\delta + {\mu^2}_\alpha \cdot cos^2\delta \tag{5.7}$$

where μ_δ is the proper motion in declination, μ_α is the proper motion in right ascension and δ is the declination of the star. Following the prescription of Collier Cameron et al. (2007), we determine the star to be a giant if it fails to satisfy:

$$H_J > -141.25(J-H)^4 + 473.18(J-H)^3 - 583.6(J-H)^2 + 313.42(J-H) - 43.0 \tag{5.8}$$

where J and H are taken from the 2MASS catalogue.

From section 5.2.8 we have 22059 stars below the 1% RMS level with magnitude 8 < V < 11. Applying the reduced proper motion selection, we obtain 7621 putative dwarf and sub-giant stars in the T1 dataset. Using the average frequency rate of 2 Hot-Jupiter planets and if we then assume that 10% of those are transiting exoplanets, we expect to find ∼1.5 Hot-Jupiter transiting exoplanets in our dataset.

5.6 Transit Search

The KELT-South telescope was built to find bright transiting exoplanets. The primary purpose of the commissioning data set was to refine and improve the data reduction pipeline and variable star selection procedures. It was still useful to search for possible planetary candidates, since there is always the possibility of a discovery (discussed in Section 5.5). From the catalogue of possible eclipsing systems we selected systems where the depth of the transit was less than 0.05 magnitudes and the number of transits was 2 or more. This selected 498 objects. We also included the 33 objects we identified during the variable star selection procedure. The final list of 531 objects were all examined by eye to find the most likely planetary candidates. A number of steps were taken when visually inspecting the remaining lightcurves to ensure that the ones sent for photometric follow-up observations were not astrophysical false positives (see Section 1.3.3). The following steps were taken:

- 1. *An exoplanet-like transit shape.* Most exoplanet transits produce lightcurve with relatively flat bottom features and are relatively U-shaped. Eclipsing binary produce lightcurves with eclipses that look much more V-shaped.
- 2. *Secondary eclipse shape.* Blended or grazing eclipsing binary systems can produce relatively shallow eclipses that look like transiting exoplanet transits. We check for this by doubling the period for each lightcurve that looked like an exoplanet transit and checked that the shape of the transit looks similar. In the cases of eclipsing binary systems this would generally not be the case as the two components are generally different in size and temperature.
- 3. *Reasonable transit duration.* For most transiting exoplanets, the full duration of the transit is ∼10% of the orbital period. If we found the candidate to have a transit duration longer than 20% of the orbital period it was not considered to be an exoplanet.
- 4. *Bad period aliases.* The BLS algorithm suffers from aliasing effects originating from nearly periodic sampling. In Section 5.3.3 we discussed the procedure to remove spurious and bad periods, but not all of the affected lightcurves were removed using the automated routines. Systematic effects at aliases of 1/2 and 1/3 of the sidereal day were still present and all lightcurves with these periods were removed.
- 5. *Even phase coverage.* In some cases, the BLS algorithm found transit features in the lightcurves that were clearly due to gaps or bad phase coverage in the folded lightcurves. Lightcurves were rejected if the number of points in transit was less than 2% of the total number of data points.
- 6. *Out of transit (OOT) variability.* Some of the candidate exoplanet lightcurves displayed significant out of transit variability. Some of these had multiple frequencies of variation which were clearly seen in the BLS periodogram. We subtracted the highest peak frequency from the lightcurve and checked that the "transit" feature survived the subtraction. If it did not, or the depth was affected in a large manner

(reducing by half), the candidate was rejected as the transit was most probably due to some combination of pulsation frequencies.

- 7. *Ellipsoidal variation.* Eclipsing binary systems with short orbital periods and where the secondary component of the eclipsing system has a relative large mass, deformation of the secondary can cause ellipsoidal variation in the lightcurve at phase 0.25 and 0.75. This type of variability usually indicates that these systems are eclipsing binaries and not planetary in nature (Drake 2003, Sirko & Paczyński 2003). Lightcurves that displayed significant ellipsoidal variation were discarded as exoplanet candidates.

- 8. *Blending.* Each of the candidates that passed the previous selection criteria were then subjected to a blending analysis. The nearest neighbours in a search radius of $345''$ ($\sim$15 pixel) radius to each candidate transiting exoplanet was found. If a brighter neighbour had a similar period to the one for the transiting exoplanet candidate, the lightcurve for the neighbour was visually inpected to make sure that it was not an eclipsing binary system that "contaminated" the candidate lightcurve.

These selection criteria were the only ones applied, as the the full vetting of candidates by an automated system was not constructed yet (Section 6.4 describes the normal procedures followed for exoplanet candidate vetting used in the regular survey campaign). As this type of visual inspection is somewhat subjective, the 498 candidate lightcurves were checked on more than one occasion, in some cases separated by weeks. Borderline cases where discussed among various members of the KELT-South team and only included in the final list if they were agreed upon by at least 3 members. From the list of 498 possibly transiting exoplanet candidates we identified 8 objects that we considered the best candidates and scheduled them for follow-up photometric observations.

5.6.1 Target1 Transiting Exoplanet Candidates

The lightcurves of the final set of 8 possible planetary candidates are shown in Figures 5.28, 5.29, 5.30 and 5.31. All of the candidates show periodic eclipsing events with a depth of less than 5%. The periods we find for these objects are generally accurate to better than 20 seconds, and since the observations were taken more than 3 years ago the determination of the ephemerides is only accurate to within 2 hours. It is thus important to keep this in mind when scheduling the follow-up observations.

A slightly modified version of ExoFAST (Eastman et al. 2013) was used to determine the system parameters. We modified ExoFAST to fit only the photometric data obtained with KELT-South and we fixed the impact parameter b to 0, the eccentricity e to 0 and the inclination i to 90°. As input for ExoFAST, we provided the detrended KELT-South lightcurve, the BLS determined period, the time of mid-transit (as determined by BLS) and the effective temperature of the star (found by doing a quick match of position to information in various catalogues). ExoFAST performs a Markov Chain Monte Carlo (MCMC) analysis of the entire system, including constraints on the mass and radius of the host star by using

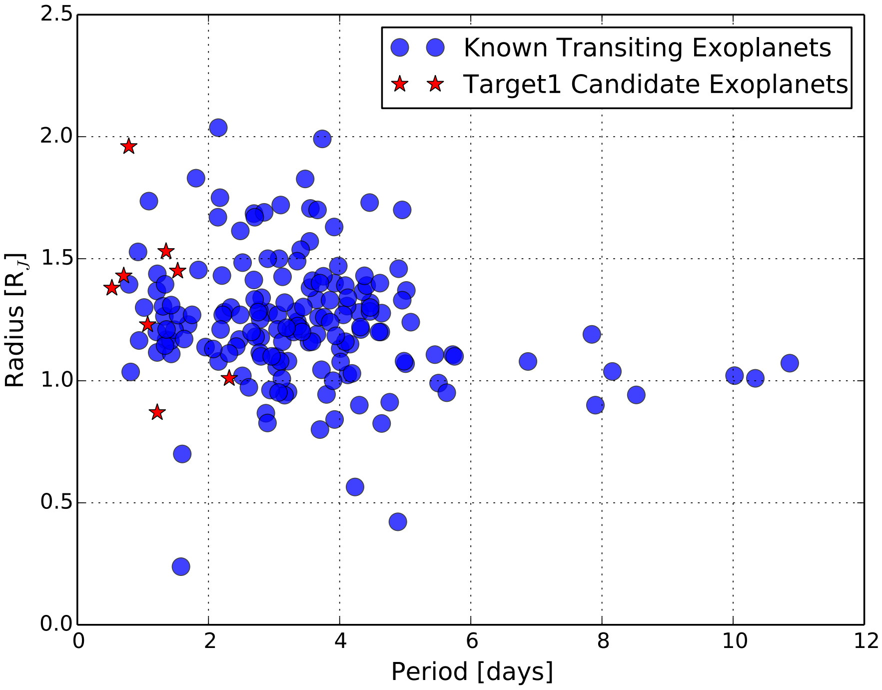

Figure 5.27: Plot of the radius and period of the Target1 exoplanet candidates compared to the known transiting exoplanets discovered by other ground based surveys.

the empirical relations in Torres (2010). The output parameters for the properties of the star are very unconstrained with large errors, which is to be expected with no spectroscopic data to help determine these parameters more accurately.

We list the properties of the candidates obtained from the KELT-South information in Table 5.5. We also list the properties of the candidate transiting exoplanets as obtained from the ExoFAST modelling in Table 5.6 and 5.7. We also plot the radius and period in Figure 5.27 of the T1 candidate exoplanets with the known transiting exoplanets discovered by other ground based surveys to show how they compare. It can be seen from the plot that all the T1 candidate transiting exoplanets have relatively short periods when compared to the known periods of transiting exoplanets discovered from the ground. This is not surprising as the BLS search algorithm was instructed to search for periodicities of up to 5 days, with at least 2 full eclipse events seen in the lightcurves (essentially limiting the search to 2.5 days). The detection efficiency with a dataset as short as 46 days only allows very short period transiting planets to be found.

5.6.2 Photometric Follow-up

In the KELT-South team we have a number of amateur astronomers (part of the AAVSO collaboration) that are able to provide photometric follow up observations. These collabora-

Table 5.5: Properties of the KELT-South Transiting Exoplanet Candidates.

USNOB1 ID	KELT-South ID	RA (J2000)	Dec. (J2000)	K-S instr. magnitude	Approx. V magnitude	Period (days)
254686882	KST1C01169	126.6428	−43.9552	10.294	8.162	1.5309
212945333	KST1C02704	106.4013	−48.8379	11.027	8.925	1.2186
83140005	KST1C16887	143.9148	−63.3503	12.599	10.562	1.3533
257744029	KST1C27428	135.8486	−43.5406	13.037	11.018	0.5267
202594473	KST1C29678	139.1608	−50.1403	13.145	11.131	0.7849
92169458	KST1C30204	147.9669	−62.3985	13.146	11.132	2.3154
241797521	KST1C33585	131.2381	−45.5310	13.271	11.262	1.0721
135698059	KST1C39934	134.8976	−57.4123	13.515	11.516	0.7079

tors have higher angular resolution than the KELT-South telescope and are able to observe the candidate transiting exoplanet systems in multiple colours. The collaborators also help constrain other import parameters such as the depth in different filters (ensuring that the eclipse is due to a planetary companion) and the time of the eclipse (which improves the accuracy of the ephemerides). This allows us to exclude many types of false positives (discussed in Section 1.3.3) before we schedule them for observations on bigger telescopes for spectroscopic observations. 5 of the 8 candidates were identified as possible exoplanet candidates 2 years after the initial KELT-South observations. These targets were identified by simply ordering the BLS output data by the signal-to-pink-noise statistic and visually inspecting the top 1000 lightcurves. This was not a very sophisticated search and many possible candidates were not identified. This served as a first attempt at exoplanet identification and allowed us to test the capabilities of the follow-up collaborators. We were able to get observations for two candidates from our collaborators and these are discussed below. The 6 remaining candidates were put on hold until a more sophisticated data reduction and candidate identification process could be implemented in 2014 January. If these remaining 6 candidates were identified again in the more rigorous analysis, they would have a stronger case to be scheduled for further follow-up observations.

5.6.3 Candidate KST1C33585

The first candidate to be observed was KST1C33585 on 2012 January 15. This candidates was observed by Ivan Curtis using his 11″ Celestron telescope from Adelaide, Australia*. To illustrate the reason we do photometric follow-up before spectroscopic follow-up, we include the finding chart used by Curtis in the KST1C33585 observations and compare it to the same region of the sky as observed by KELT-South in Figure 5.32. Here we can clearly see the effect of having a pixel scale of 23″ per pixel. Many of the sources identified by Curtis in the finding chart are blended together in the KELT-South image. The marked stars C8, C4, C7, T, T1, T2, T3, T4 and T5 were all investigated and it was found that T4 showed a deep eclipse (see Figure 5.33). This type of false positive is not uncommon for follow-up observations (Seager & Mallén-Ornelas 2003, Poleski et al. 2010).

---

*http://brucegary.net/WDE/Observers/Curtis/Curtis.htm

Table 5.6: Table of the ExoFAST determined parameters of Target1 exoplanet candidates.

Parameter	Units	KST1C01169	KST1C02704	KST1C16887	KST1C27428
Stellar Parameters:					
M_*	Mass ($M_\odot$)	$1.83^{+1.2}_{-0.61}$	$1.41^{+0.71}_{-0.57}$	$0.99^{+0.37}_{-0.22}$	$1.83^{+1.3}_{-0.65}$
R_*	Radius ($R_\odot$)	$1.95^{+0.35}_{-0.27}$	$0.89^{+0.14}_{-0.16}$	$1.27^{+0.14}_{-0.11}$	$1.28^{+0.24}_{-0.19}$
L_*	Luminosity ($L_\odot$)	$15.5^{+6.1}_{-4.2}$	$1.07^{+0.37}_{-0.35}$	$0.67^{+0.18}_{-0.13}$	$10.6^{+4.4}_{-3.0}$
ρ_*	Density (cgs)	$0.358^{+0.052}_{-0.047}$	$2.90^{+0.47}_{-0.40}$	$0.693^{+0.043}_{-0.042}$	$1.22^{+0.25}_{-0.15}$
$\log(g_*)$	Surface gravity (cgs)	$4.132^{+0.076}_{-0.079}$	$4.692^{+0.070}_{-0.071}$	$4.230^{+0.047}_{-0.037}$	$4.490^{+0.088}_{-0.079}$
$T_{\rm eff}$	Effective temperature (K)	8197^{+94}_{-96}	6236^{+100}_{-99}	4642^{+97}_{-100}	9210 ± 100
[Fe/H]	Metallicity	$-0.2^{+2.5}_{-2.0}$	$1.0^{+1.9}_{-2.5}$	$1.2^{+1.6}_{-1.2}$	$-0.4^{+2.5}_{-2.1}$
Planetary Parameters:					
P	Period (days)	$1.53028^{+0.00032}_{-0.00027}$	$1.218670^{+0.000081}_{-0.000086}$	1.35316 ± 0.00011	$0.526833^{+0.000052}_{-0.000046}$
a	Semi-major axis (AU)	$0.0318^{+0.0057}_{-0.0040}$	$0.0250^{+0.0036}_{-0.0040}$	$0.0238^{+0.0027}_{-0.0019}$	$0.0156^{+0.0030}_{-0.0021}$
R_P	Radius (R_J)	$1.45^{+0.26}_{-0.20}$	$0.87^{+0.13}_{-0.15}$	$1.53^{+0.18}_{-0.12}$	$1.38^{+0.26}_{-0.20}$
T_{eq}	Equilibrium Temperature (K)	3081^{+82}_{-77}	1784 ± 50	1629 ± 37	4020^{+100}_{-130}
$\langle F \rangle$	Incident flux (10^9 erg s^{-1} cm^{-2})	$20.4^{+2.3}_{-2.0}$	$2.30^{+0.27}_{-0.25}$	$1.60^{+0.15}_{-0.14}$	$59.5^{+6.2}_{-7.3}$
Transit Parameters:					
T_C	Time of transit ($\mathrm{BJD_{TDB}}$- 2450000)	$6840.19^{+0.34}_{-0.28}$	6838.71 ± 0.11	6838.90 ± 0.13	$6839.53^{+0.16}_{-0.14}$
R_P/R_*	Radius of planet in stellar radii	$0.0767^{+0.0013}_{-0.0014}$	$0.1010^{+0.0024}_{-0.0025}$	$0.1246^{+0.0019}_{-0.0018}$	$0.1109^{+0.0027}_{-0.0029}$
a/R_*	Semi-major axis in stellar radii	3.54 ± 0.16	$6.11^{+0.31}_{-0.29}$	$4.062^{+0.082}_{-0.084}$	$2.62^{+0.17}_{-0.11}$
i	Inclination (degrees)	90.0	90.0	90.0	90.0
b	Impact Parameter	0.0	0.0	0.0	0.0
δ	Transit depth	$0.00588^{+0.00020}_{-0.00021}$	0.01020 ± 0.00049	$0.01552^{+0.00048}_{-0.00045}$	$0.01230^{+0.00061}_{-0.00063}$
T_{FWHM}	FWHM duration (days)	$0.1396^{+0.0069}_{-0.0063}$	$0.0638^{+0.0033}_{-0.0031}$	$0.1072^{+0.0023}_{-0.0022}$	$0.0659^{+0.0030}_{-0.0042}$
τ	Ingress/egress duration (days)	$0.01101^{+0.00049}_{-0.00048}$	0.00651 ± 0.00027	0.01365 ± 0.00029	$0.00767^{+0.00036}_{-0.00045}$
T_{14}	Total duration (days)	$0.1506^{+0.0074}_{-0.0067}$	$0.0703^{+0.0035}_{-0.0034}$	$0.1209^{+0.0026}_{-0.0024}$	$0.0736^{+0.0033}_{-0.0046}$
u_1	linear limb-darkening coefficient	$0.240^{+0.039}_{-0.015}$	$0.337^{+0.028}_{-0.077}$	$0.645^{+0.033}_{-0.053}$	$0.213^{+0.015}_{-0.022}$
u_2	quadratic limb-darkening coefficient	$0.295^{+0.037}_{-0.036}$	$0.3134^{+0.0076}_{-0.0084}$	$0.115^{+0.023}_{-0.022}$	$0.2746^{+0.037}_{-0.0100}$

NOTES

[1] No radial velocity follow-up data available to determine these values.

Table 5.7: Table of the ExoFAST determined parameters of Target1 exoplanet candidates (continued).

Parameter	Units	KST1C29678	KST1C30204	KST1C33585	KST1C39934
Stellar Parameters:					
M_*	Mass ($M_\odot$)	$1.60^{+0.70}_{-0.48}$	$0.66^{+0.36}_{-0.23}$	$0.83^{+0.37}_{-0.24}$	$1.85^{+1.1}_{-0.67}$
R_*	Radius ($R_\odot$)	$1.61^{+0.22}_{-0.20}$	$1.30^{+0.25}_{-0.22}$	$1.34^{+0.20}_{-0.19}$	$1.40^{+0.25}_{-0.20}$
L_*	Luminosity ($L_\odot$)	$3.28^{+1.0}_{-0.79}$	$0.55^{+0.25}_{-0.17}$	$0.66^{+0.24}_{-0.18}$	$10.1^{+3.9}_{-2.7}$
ρ_*	Density (cgs)	0.548 ± 0.051	$0.418^{+0.098}_{-0.074}$	$0.497^{+0.099}_{-0.086}$	$0.96^{+0.11}_{-0.10}$
$\log(g_*)$	Surface gravity (cgs)	$4.230^{+0.057}_{-0.053}$	$4.026^{+0.079}_{-0.067}$	$4.107^{+0.066}_{-0.063}$	$4.414^{+0.077}_{-0.071}$
$T_{\rm eff}$	Effective temperature (K)	6133^{+100}_{-98}	4355^{+100}_{-96}	4500 ± 100	8719^{+98}_{-100}
[Fe/H]	Metallicity	1.4 ± 1.8	$-0.6^{+2.1}_{-2.0}$	$0.3^{+1.8}_{-1.7}$	$-0.1^{+2.3}_{-2.1}$
Planetary Parameters:					
P	Period (days)	$0.784852^{+0.000066}_{-0.000061}$	$2.31634^{+0.00079}_{-0.00091}$	1.07231 ± 0.00029	$0.707580^{+0.000064}_{-0.000066}$
a	Semi-major axis (AU)	$0.0195^{+0.0025}_{-0.0022}$	$0.0299^{+0.0046}_{-0.0039}$	$0.0193^{+0.0025}_{-0.0021}$	$0.0191^{+0.0032}_{-0.0026}$
R_P	Radius (R_J)	$1.96^{+0.26}_{-0.23}$	$1.01^{+0.18}_{-0.15}$	$1.23^{+0.18}_{-0.16}$	$1.43^{+0.25}_{-0.21}$
T_{eq}	Equilibrium Temperature (K)	2684^{+60}_{-59}	1388 ± 57	1803^{+68}_{-64}	3595^{+79}_{-78}
$\langle F \rangle$	Incident flux (10^9 erg s^{-1} cm^{-2})	$11.8^{+1.1}_{-1.0}$	$0.84^{+0.15}_{-0.13}$	$2.40^{+0.38}_{-0.32}$	$37.9^{+3.4}_{-3.2}$
Transit Parameters:					
T_C	Time of transit (BJD_{TDB}- 2450000)	$6840.35^{+0.14}_{-0.12}$	$6839.49^{+0.55}_{-0.64}$	$6840.69^{+0.43}_{-0.44}$	6839.56 ± 0.15
R_P/R_*	Radius of planet in stellar radii	0.1255 ± 0.0025	$0.0802^{+0.0044}_{-0.0045}$	$0.0952^{+0.0039}_{-0.0040}$	$0.1051^{+0.0033}_{-0.0034}$
a/R_*	Semi-major axis in stellar radii	$2.613^{+0.079}_{-0.084}$	$4.91^{+0.36}_{-0.31}$	3.11 ± 0.19	2.94 ± 0.11
i	Inclination (degrees)	90.0	90.0	90.0	90.0
b	Impact Parameter	0.0	0.0	0.0	0.0
δ	Transit depth	$0.01574^{+0.00064}_{-0.00062}$	$0.00643^{+0.00073}_{-0.00070}$	$0.00906^{+0.00076}_{-0.00074}$	$0.01105^{+0.00070}_{-0.00071}$
T_{FWHM}	FWHM duration (days)	$0.0983^{+0.0035}_{-0.0031}$	0.151 ± 0.010	$0.1117^{+0.0077}_{-0.0068}$	$0.0782^{+0.0032}_{-0.0029}$
τ	Ingress/egress duration (days)	$0.01300^{+0.00047}_{-0.00044}$	$0.01230^{+0.00086}_{-0.00093}$	$0.01104^{+0.00067}_{-0.00066}$	$0.00857^{+0.00039}_{-0.00040}$
T_{14}	Total duration (days)	$0.1112^{+0.0039}_{-0.0034}$	0.163 ± 0.011	$0.1227^{+0.0082}_{-0.0073}$	$0.0868^{+0.0035}_{-0.0032}$
u_1	linear limb-darkening coefficient	$0.351^{+0.025}_{-0.063}$	$0.60^{+0.13}_{-0.41}$	$0.646^{+0.059}_{-0.17}$	$0.228^{+0.022}_{-0.020}$
u_2	quadratic limb-darkening coefficient	$0.3097^{+0.0093}_{-0.0089}$	$0.128^{+0.29}_{-0.084}$	$0.107^{+0.12}_{-0.036}$	$0.283^{+0.039}_{-0.020}$

NOTES

[1] No radial velocity follow-up data available to determine these values.

The eclipsing system was identified as 0444-0143060 in the USNOB1 catalogue and 0444-0145964 in the NOMAD catalogue. From the NOMAD catalogue the B-V magnitude was calculated to be 0.19 which in turn provided an effective temperature for the star of ∼7800K using the relations found in Torres (2010) (assuming the star is on the main sequence) and an estimated radius for the star of $\sim 1.62 R_\odot$. Equation 1.10 was used to estimate the radius of the object that produced the eclipse depth seen in Figure 5.33. Even though the bottom of the eclipse was not seen in the lightcurve, an estimated depth of 0.2 magnitudes was used and the calculated radius of the eclipsing object was determined to be $6.76 R_J$ or $0.7 R_\odot$, which is far too large to be a planet (the largest known radius for a transiting exoplanet is $\sim 2 R_J$).

5.6.4 Candidate KST1C27428

The second candidate, KST1C27428, was observed on 2012 January 16 by TG Tan using a 12″ Meade LX200GPS telescope from Perth, Australia*. The target system was observed through a Rc filter with 120s integration times. We show the finding chart and KELT-South comparison in Figure 5.34. This candidate turned out to be a nearby eclipsing binary system blended with the brighter KELT-South target. The lightcurve of the stars marked S1 and S2 in the finding chart are plotted in Figure 5.35 and show that star S2 is the eclipsing system. The system was identified to be 0464-0148069 in the USNOB1 catalogue and 0464-0154515 in the NOMAD catalogue. From the NOMAD catalogue the B-V magnitude was calculated to be 0.598 which in turn provided an effective temperature for the star of ∼5900K and an estimated radius of $\sim 1.05 R_\odot$. The depth of the transit was determined to be ∼0.175 magnitude. Using equation 1.10 provided an estimated radius for the transiting object to be $4.1 R_J$ or $0.42 R_\odot$, again too large to be a planet.

---

[*] http://brucegary.net/WDE/Observers/Tan/Tan.htm

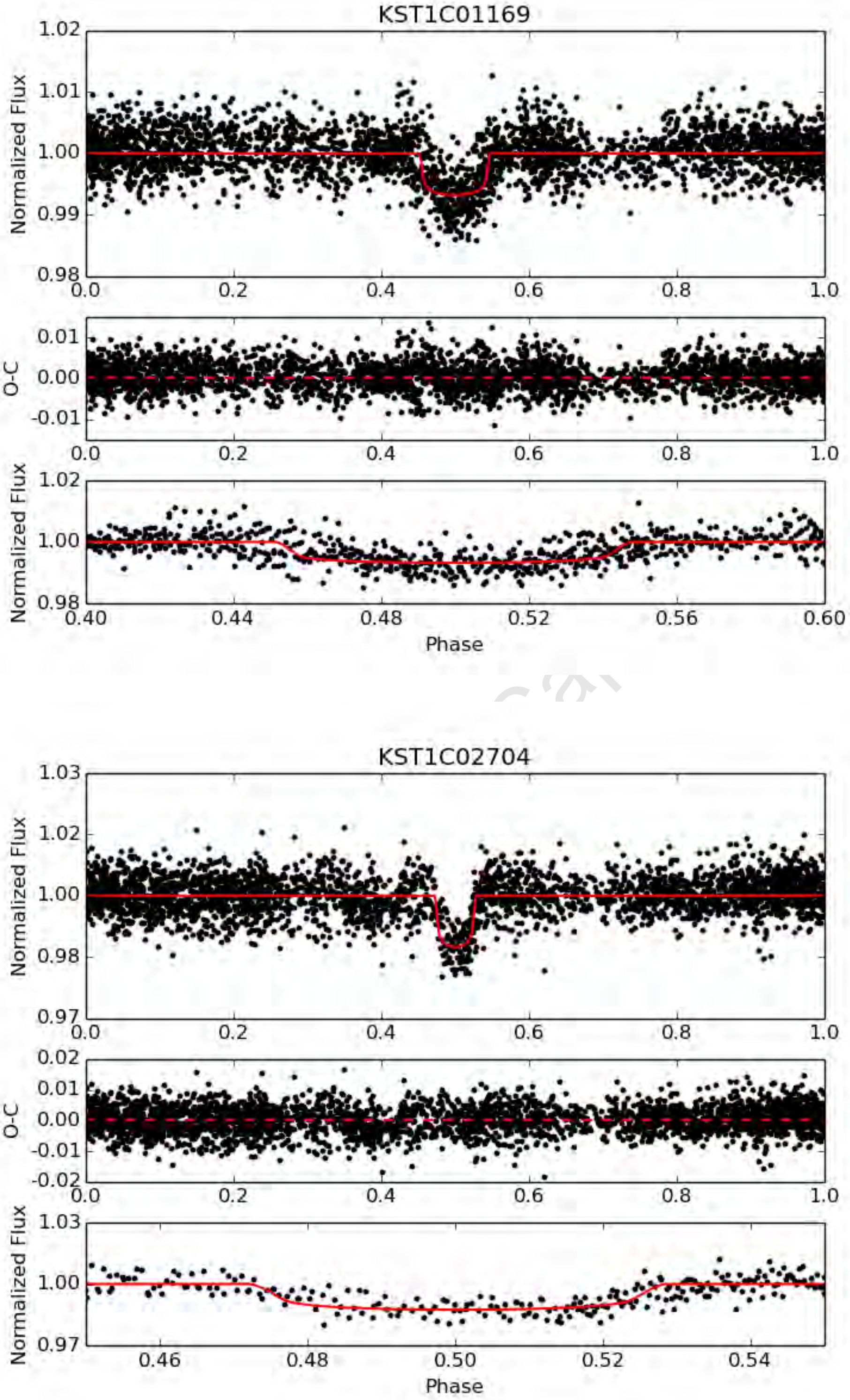

Figure 5.28: KELT-South lightcurve of exoplanet candidate KST1C01169 and KST1C02704. *Top panel:* The phase folded KELT-South lightcurve with the best fit transit model as calculated by ExoFAST. *Middle panel:* Residuals of the best fit model. *Bottom panel:* Zoomed in view of the transit along with the model.

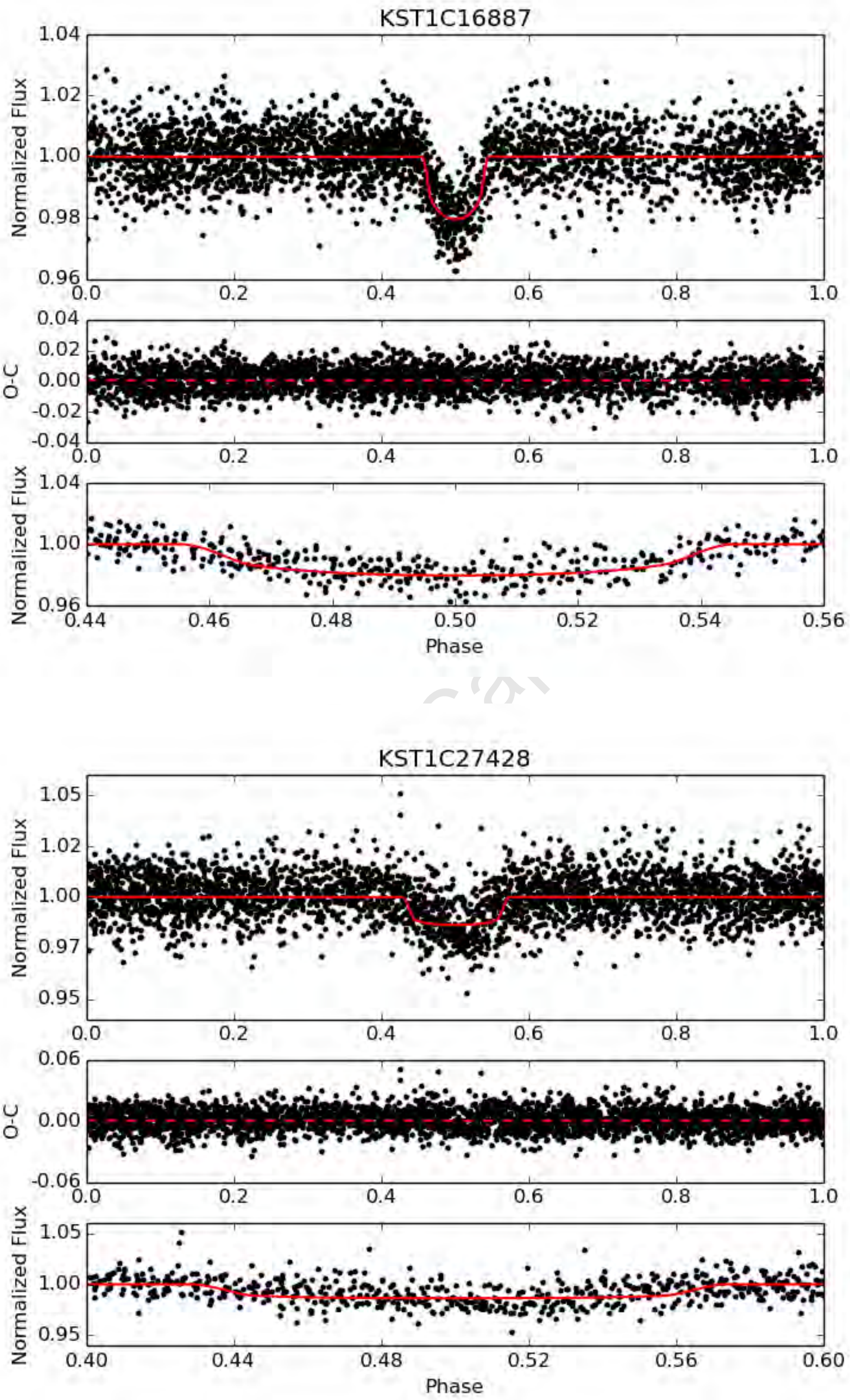

Figure 5.29: KELT-South lightcurve of exoplanet candidate KST1C16887 and KST1C27428. *Top panel:* The phase folded KELT-South lightcurve with the best fit transit model as calculated by ExoFAST. *Middle panel:* Residuals of the best fit model. *Bottom panel:* Zoomed in view of the transit along with the model.

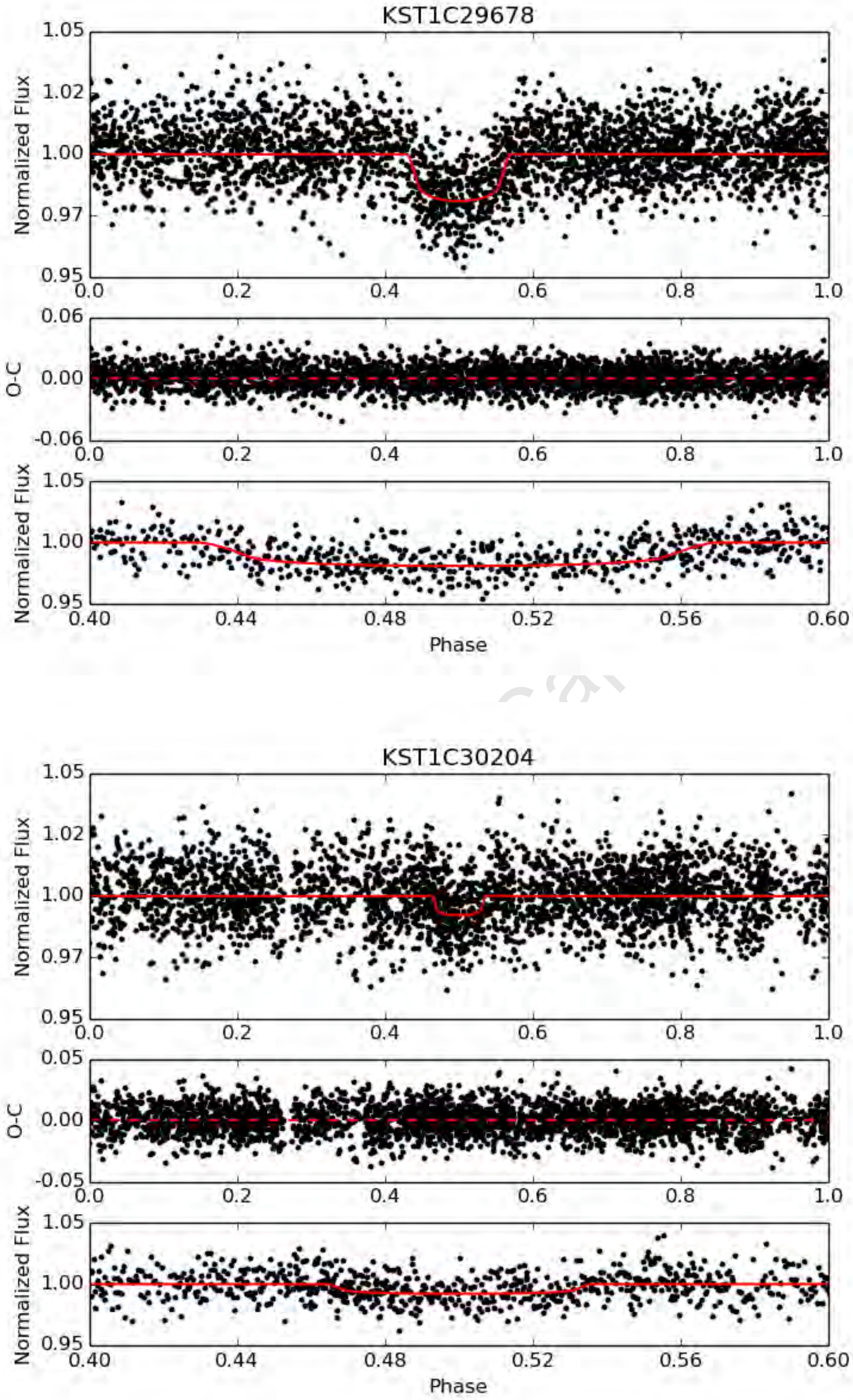

Figure 5.30: KELT-South lightcurve of exoplanet candidate KST1C29678 and KST1C30204. *Top panel:* The phase folded KELT-South lightcurve with the best fit transit model as calculated by ExoFAST. *Middle panel:* Residuals of the best fit model. *Bottom panel:* Zoomed in view of the transit along with the model.

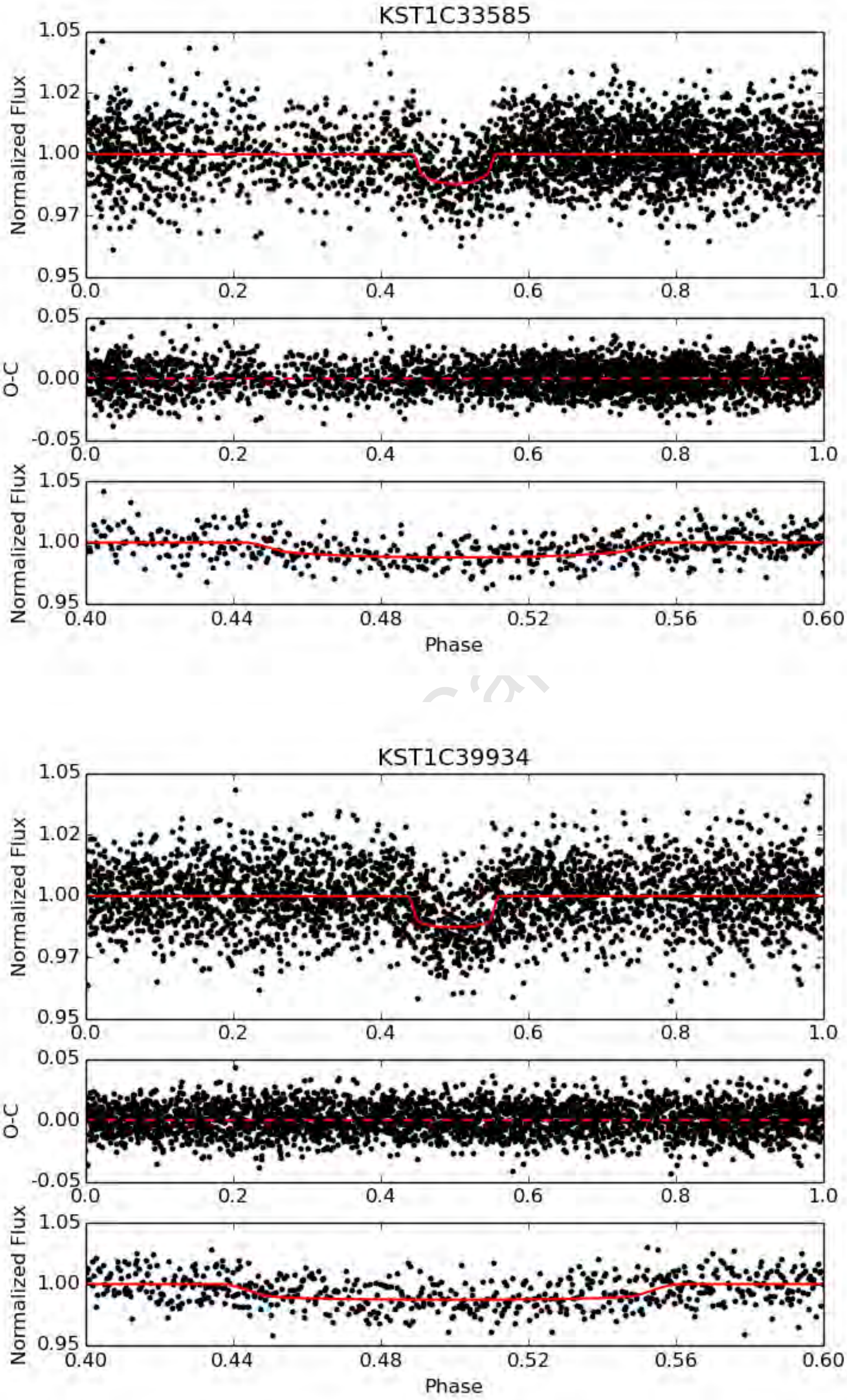

Figure 5.31: KELT-South lightcurve of exoplanet candidate KST1C33585 and KST1C39934. *Top panel:* The phase folded KELT-South lightcurve with the best fit transit model as calculated by ExoFAST. *Middle panel:* Residuals of the best fit model. *Bottom panel:* Zoomed in view of the transit along with the model.

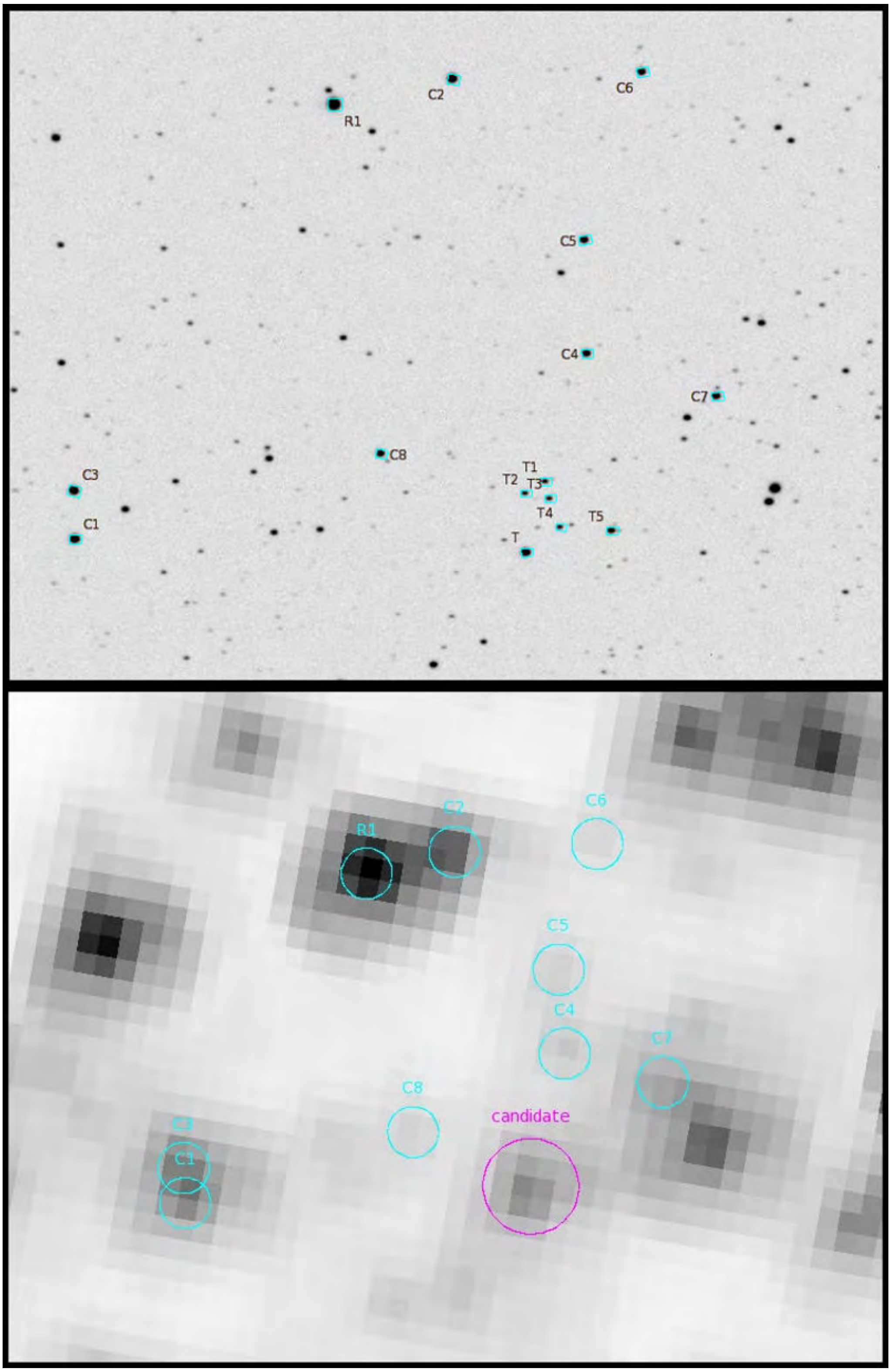

Figure 5.32: The finding chart used by Ivan Curtis for the KST1C33585 observations at the top and the same region from the KELT-South reference image on the bottom.

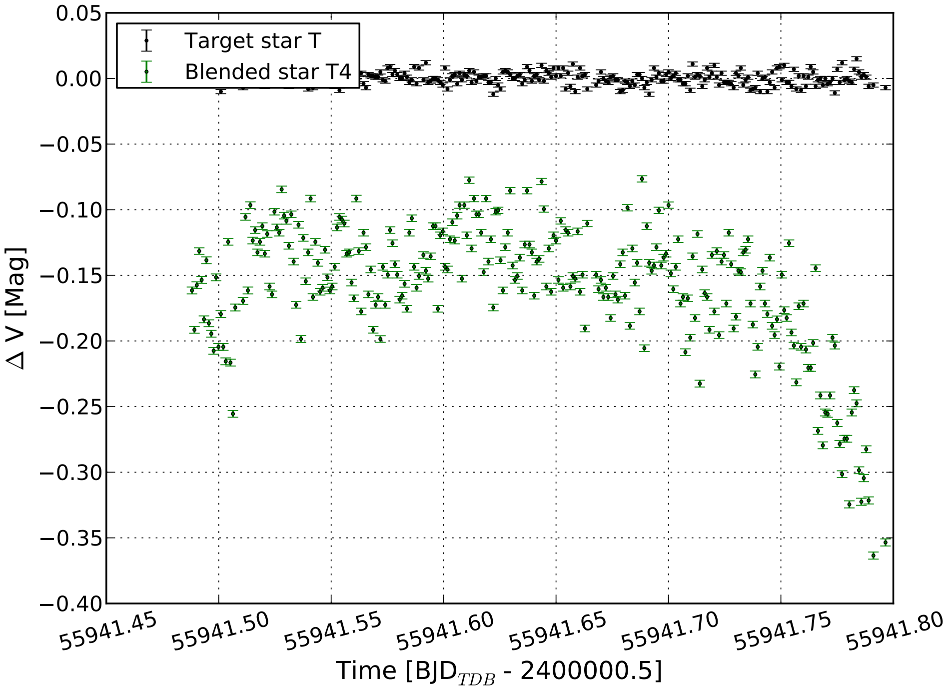

Figure 5.33: Lightcurve produced from the follow-up photometry data for the exoplanet candidate KST1C33585. The lightcurves for the two stars marked T and T4 in figure 5.32 are plotted, clearly showing the eclipsing binary nature of T4. The data are offset from one another to make the eclipse shape more clear.

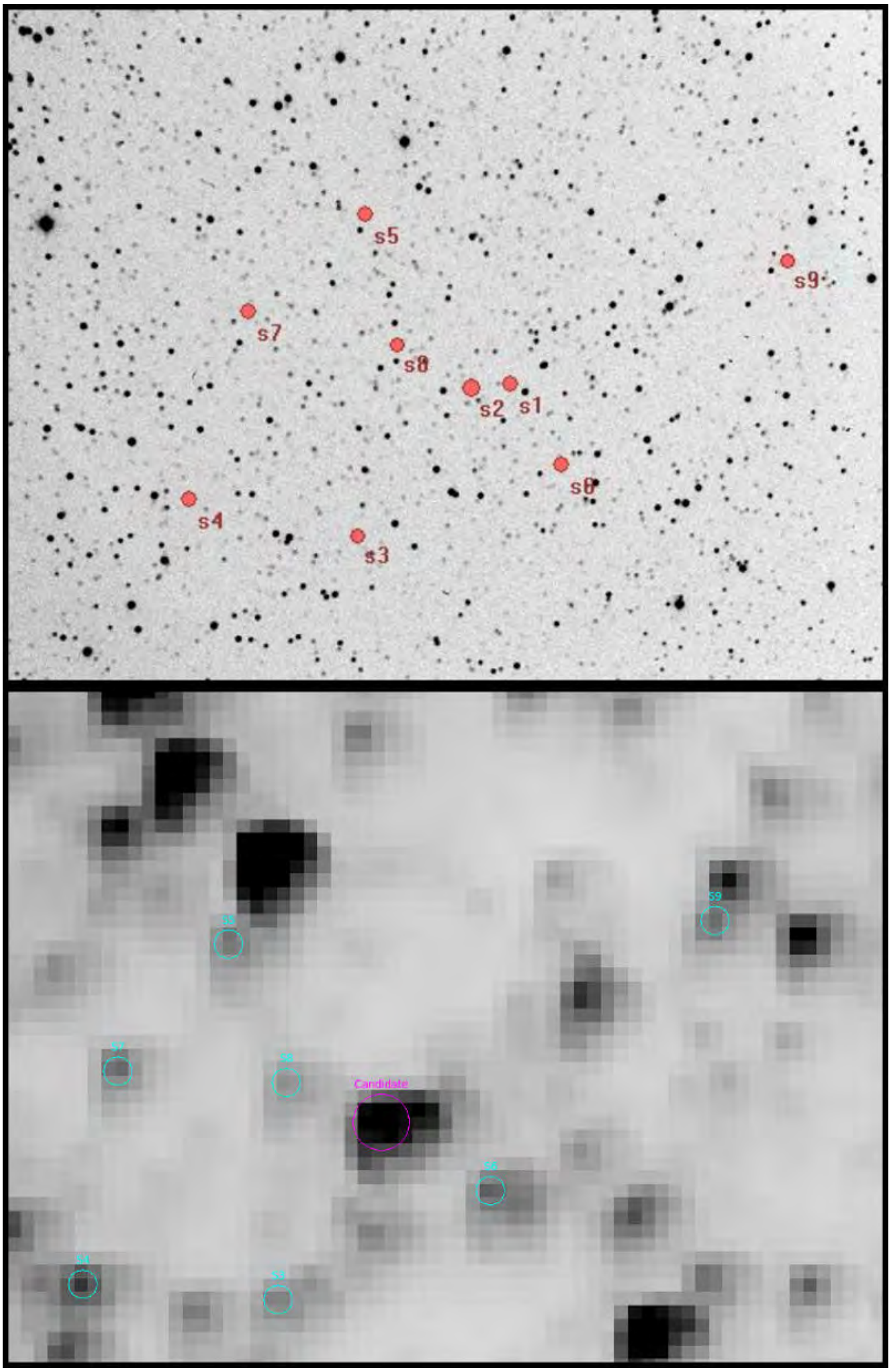

Figure 5.34: The finding chart used for the KST1C27428 observations done by TG Tan at the top and the same region from the KELT-South reference image on the bottom.

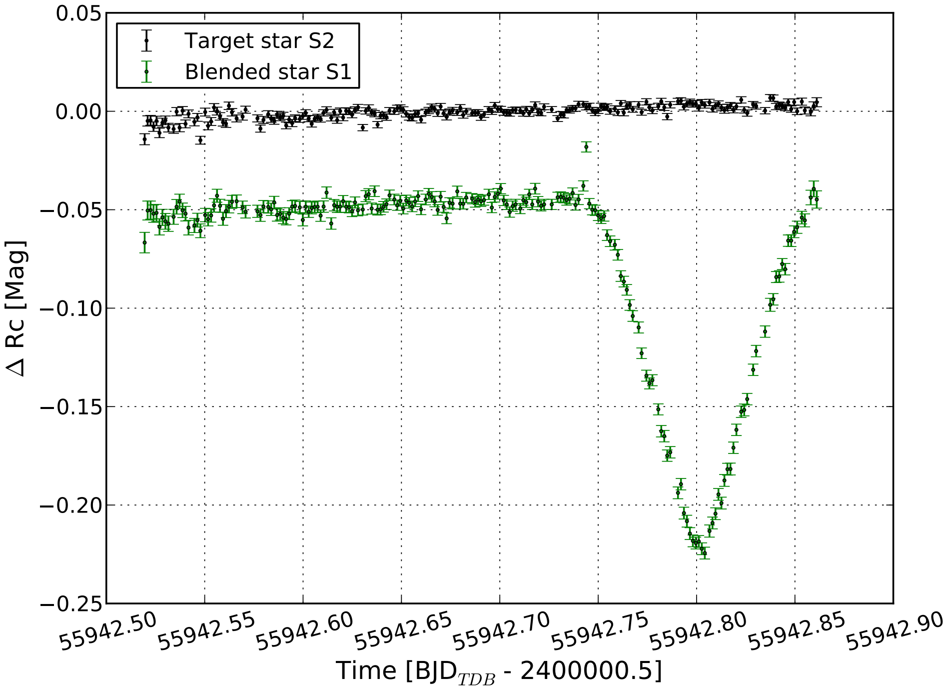

Figure 5.35: Lightcurve produced from the follow-up photometry data for the exoplanet candidate KST1C27428. The lightcurve for the two stars marked S1 and S2 in Figure 5.34 are plotted, clearly showing the eclipsing binary nature of S2. The data are offset from one another to make the eclipse shape more clear.

Chapter 6

Future Work and Conclusions

6.1 Introduction

In the previous chapters the KELT-South telescope was described and the results of the search for variable stars and transiting exoplanets from one of the first commissioning datasets were reported. In this chapter I will discuss some improvements to the procedures to identify the variable stars I have planned for the future and present an interesting eclipsing system identified in the KELT-North dataset. Although this system was identified using the northern twin of KELT-South, it demonstrates the ancillary science that can only be achieved with a telescope system like KELT that observes the same parts of the sky for many years. I will also highlight some additional science we are working on using the data currently available from KELT-South as well as report on the first results obtained in the discovery of bright transiting exoplanets from the regular survey data. I will conclude with a short outlook for the future of the entire KELT-South project.

6.2 Future Work

6.2.1 Improvements to Variable Star Identification

The selection criteria for variable star identification is not optimum at present. Although the procedures select a large number of variable objects with relative ease, the identification of true variables is a very time consuming process, requiring many hours of by eye vetting and confirmation of true variability. The alias removal procedure I developed also removes many true variables if enough of them share a similar period and all have strong indicators of variability from the statistics output by the search algorithms. To avoid this problem in future, a test can be implemented that keeps a lightcurve as a variable candidate if all three methods (AoV, L-S and BLS) find variability at the same period (at present, each method operates independently and implementing such a test would drastically increase the likelihood of retaining true variables). However, this type of stringent selection would exclude variables such as detached eclipsing binaries, which are more likely to be found by BLS than any other search algorithm. To optimize the identification of the variable stars, one would need to inject artificial variability into lightcurves and do a full recovery simulation. This would allow for the fine tuning of the parameters and increase the likelihood of identifying true variables.

Many of the lightcurves also showed false variability at exactly the same period, indicating some systematic that caused this. In the current version of the selection program, only this period for each of the affected lightcurves is used for evaluation. In future versions, the second highest peak (which we calculate as part of the initial search for variability) will then replace this false period and should help to identify true variables that were not included in the list of candidates due to systematics.

6.2.2 Automated Discovery and Selection of Variable Stars

Although many variable stars were correctly identified in the KELT-South commissioning dataset, the classification of these lightcurves was all done by eye. With the KELT-South survey in full operation and many thousands of new variables found, the time taken to inspect each one by eye and then classify it, is becoming far too long. Recent developments in computer learning and neural net based classification of lightcurves is one aspect we would like to implement in the KELT-South operations. I am working with the authors of a recent paper (Paegert et al. 2014) specifically dealing with this issue, to identify and classify the variable stars in the KELT-South dataset. The authors of that paper claim to be able to find 98% of the eclipsing binary systems (with a false alarm rate of 2%) in the ASAS lightcurves and they achieve similar retrieval rates for other variable stars, including RR Lyrae, Mira, and δ-Scuti type variables. Although the sub-classification of the eclipsing binaries remains a problem, the high retrieval rates is encouraging. With future developments of the automated classification system, the authors hope to be able to classify many variables stars into the correct sub-classes.

6.2.3 Short Period Variable Stars

In the second commissioning dataset, I identified two very short period variable stars with periods of ~21 and ~26 minutes. Both are early A type stars and we are in the process of trying to determine whether these stars are Ap, Am or regular δ-Scuti type variables, by spectroscopic follow-up observations to determine the metal abundances using low resolution spectrographs on 2m class telescopes. If found to be members of the Ap class, they might show other short-timescale, millimagnitude photometric variations and variations in radial velocities of spectral lines, making them members of the rapidly oscillating Ap (roAp) class of stars. These stars lie at the bottom of the δ-Scuti instability strip, on the main sequence and there are currently ~40 known roAp stars. The pulsation periods of these oscillators lie between 5 and 24 minutes. The high-overtone acoustic pulsation modes of these stars allow for asteroseismological studies to determine their atmospheric and internal structure.

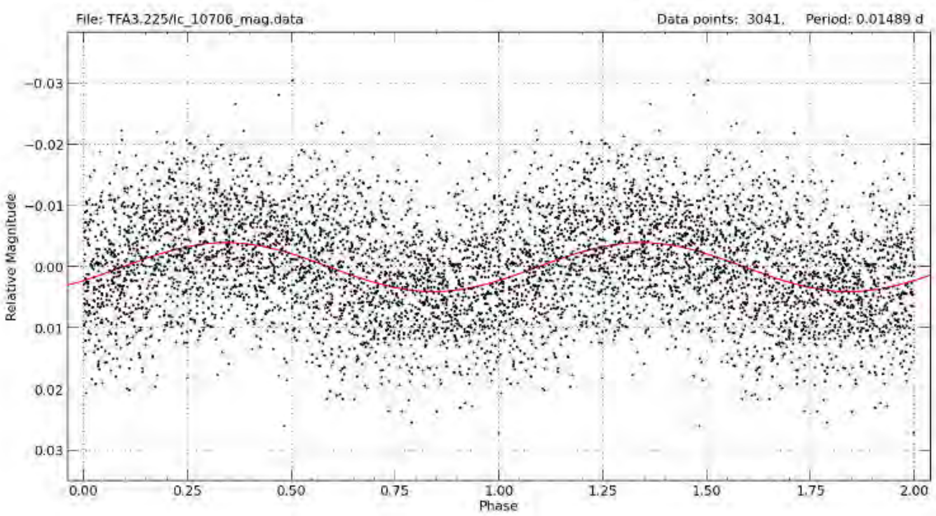

Figure 6.1: The lightcurve of one of the possible roAp variable stars found in the second commissioning dataset from the KELT-South telescope. The solid red line is the best fit sinusoidal model to the pulsations observed in the data.

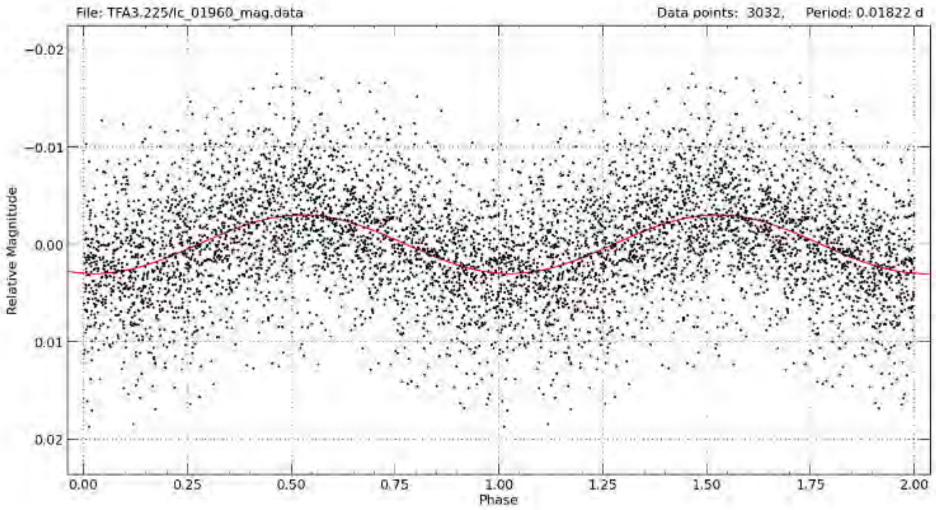

Figure 6.2: The lightcurve of one of the possible roAp variable stars found in the second commissioning dataset from the KELT-South telescope. The solid red line is the best fit sinusoidal model to the pulsations observed in the data.

A recent paper by Alentiev et al. (2012) describes the longest period roAp star found to date, with a pulsation period of 23.6 minutes. This makes our discovery even more exciting, if the 26 minute period found in one of the stars is confirmed. I am working with Dr. Thebe Medupe, at North West University in South Africa, on identifying the exact frequency of pulsation of the stars and possible multi-periodic pulsation modes using KELT-South data, as well as follow-up data from other telescopes at the SAAO observing site in Sutherland. We are also planning a systematic search for short period pulsating stars in all of the future KELT-South datasets.

6.2.4 Citizen Science Project

With any wide field survey similar to KELT-South, the number of variable stars outnumbers the transiting exoplanet candidates by orders of magnitude. Once the variable stars have been identified using similar methods described in this thesis, most exoplanet survey teams have no further use for those targets and the data are never looked at again, rigorously classified or published in papers. With large citizen science projects like Planet Hunters* (part of the larger Zooniverse Project†) showing real promise in getting members of the public to interact with data obtained by professional astronomers and helping to discover new and interesting science, I thought about getting a project started where Zooniverse volunteers help classify the variable stars. Many exoplanet survey teams at present use sophisticated algorithms or neural networks to help them classify variable stars with mixed success (Blomme et al. 2011). Humans are extremely good at pattern recognition and getting volunteers to decide whether or not a lightcurve (phase folded on a particular period) looks similar to a known class of variable star could reduce the need for expensive networks of computers.

6.2.5 Rotation Age of Open Clusters

The first commissioning dataset collected by KELT-South was obtained from 2009 August to 2009 December and was roughly centred on the Blanco 1 open cluster with the centre of the observed field located at J2000 $\alpha = 00^h04'07''$, $\delta = -29°50'00''$. The KELT-South team report for the first time the rotation periods for 33 members of Blanco 1, with spectral types ranging from late-A to mid-K and periods ranging from less than a day to eight days. By using two different gyrochronolgy methods the age of the cluster was determined and the rotation-age agrees with independently determined cluster ages based on the lithium depletion boundary technique (Cargile et al. 2014).

The second commissioning dataset (discussed in Chapter 5) contains the open cluster IC 2391, which is well suited to a similar age determination technique. I am working with the authors of that paper to identify possible cluster members in the KELT-South dataset and extract rotational periods if available. This work will allow us to verify the age of the IC

---

* http://www.planethunters.org

† https://www.zooniverse.org

2391 cluster as reported by Stauffer et al. (1997) and Barrado y Navascués et al. (2004).

6.2.6 Stellar Astrophysics

A recent paper by Rodriguez et al. (2013) used the KELT-North data to show that the circumstellar disk of the classical T Tauri star RW Aurigae A was tidally disrupted by the close passing of its stellar companion RW Auriga B. This disruption stripped away part of the disk, leaving a truncated disk and produced an "arm" feature that occulted RW Auriga A from late 2010 to early 2011 causing a dimming of ∼2 magnitudes with a duration of ∼180 days. With supporting data from SuperWASP and AAVSO the authors determined that the tidally disrupted arm has a thickness of 0.27 AU, a maximum linear velocity of 2.58 km s^{-1} and is separated from RW Auriga A by 180 AU. They conclude by suggesting that the data shows only the leading edge of the tidally disrupted arm occulting the star and that future dimming of the star is possible as the rest of the arm moves across the face of the star as seen along our line of sight. Observations of this kind provide insight into proto-planetary environments around binary stars which has implications for the formation and evolution of exoplanets.

I am working with the authors of that paper to identify similar "giant" eclipse events in the KELT-South dataset and further our understanding of planetary formation in binary systems.

6.3 Conclusions

6.3.1 Results from Commissioning Data

We extracted lightcurves for 78297 objects from the second commissioning dataset obtained with the KELT-South telescope. 22059 of those lightcurves have RMS levels < 1% and are the best candidates to search for transiting exoplanets. With this dataset, I was able to identify eight strong exoplanet candidates. The purpose of the data was not to find transiting exoplanets, but to refine the data reduction and analysis procedures and test new methods for finding variable stars. Of the eight strong exoplanet candidates, six are still marked as promising candidates requiring follow-up observations to determine their exact nature. Two of the candidates were determined to be fainter background eclipsing binary systems that were blended with brighter targets in the KELT-South aperture.

I also showed that we are able to recover ∼70% (393 out of 559) of the known variable stars from the AAVSO catalogue, with only ∼10% (14 out of 121) of the known variable stars we did not find being rejected due to the specific selection methods we use to identify variable objects in the KELT-South dataset. The rest were either saturated, showed no variability at the quoted periods, had periods longer than most of the search routines or had periods different to the ones listed in the catalogue. I also found periods for 18 objects in the AAVSO catalogue that do not have periods listed.

Table 6.1: KELT-South BLS selection criteria for candidate exoplanet lightcurves.

BLS Statistic	Selection Criteria
Signal detection efficiency	SDE > 7.0
Signal to pink-noise	SPN > 7.0
Fraction from one night	$\mathrm{F}_{1n} < 0.8$
Transit depth	$\delta < 0.05$
χ^2 ratio	$\frac{\Delta\chi^2}{\Delta\chi^2_-} > 1.5$
Duty cycle	q < 0.1

In the search for variable stars, 1018 new variable candidates were identified with a range in magnitude of $7.0 < \mathrm{V} < 13.7$ and periods between 20 minutes and 10 days.

6.4 Current Status and Preliminary Results from Main Survey

At the time of writing this thesis, KELT-South has been collecting data in the regular survey mode for almost 4 years. A total of ∼100000 images have been acquired in this mode and the preliminary reduction of the first two fields started in 2013 July. By 2013 October the first few promising transiting exoplanet candidates were identified and scheduled for follow-up observations. The selection of possible transiting exoplanet candidates involves a number of steps, which I briefly describe here (more details available in the discovery paper of KELT-1b Siverd et al. (2012)). Firstly, all identified point sources on the reference image for each field are matched to Tycho-2 sources, which simultaneously provides proper motions and *JHK* apparent magnitudes. Next, the giant stars are identified and excluded using a reduced proper motion diagram (Gould & Morgan 2003) following the procedure outlined by Collier Cameron et al. (2007). The lightcurves of the remaining dwarf stars are then searched for transit like features using the BLS algorithm and selection cuts are performed on six of the statistics output by the VARTOOLS implementation of the BLS algorithm. We perform selection cuts on: signal detection efficiency SDE (Kovács et al. 2002), signal to pink-noise SPN (Hartman et al. 2008), the fraction of transit points from one night F_{1n} , depth δ, the ratio of the best transit model to the best inverse transit model $\Delta\chi^2/\Delta\chi^2_-$ (Burke et al. 2006), and the fraction of the orbit spent in transit or duty cycle q (see Table 6.1). Restrictions on the effective temperature and inferred host star density are also imposed. A further requirement that the inferred stellar density, calculated from the BLS transit fits to the KELT-South lightcurves, and the calculated stellar density, using the $J - K$ colours, be within 1.0 dex of one another removes additional giant stars and possible blended stars (Seager & Mallén-Ornelas 2003). Lightcurves that pass all these tests are then subjected to further LS and AoV analysis. Results of these tests, all the BLS, LS and AoV statistics, calculated quantities and other information gathered from online catalogues are then collected into a website where members of the KELT-South team can use the information to vote on the true nature of the candidate. Votes are divided into categories for probable planet, eclipsing binary, sinusoidal variations, spurious detections, blended stars, or other. All candidates with at least one vote for being a possible planet are discussed among the group and passed along for follow-up photometry or spectroscopic characterisation depending on the confidence level of the group on the particular candidate. In most cases we first request photometric follow-up observations to confirm the time and duration of the eclipsing event before requesting time on larger telescopes for spectroscopic follow-up observations.

From the first observing field 26 candidates were identified and scheduled for follow-up observations, of which 19 are still active in the schedule and seven have been retired as false positives. One of the seven retired candidates was retired before any follow-up observations were taken as a re-examination of the KELT-South lightcurve showed clear signs of a secondary eclipse indicating an eclipsing binary system. One of the expired candidates was previously identified by the SuperWASP team as a possible exoplanet and forwarded to their collaborators for spectroscopic follow-up observations. These observations confirmed it to be an eclipsing binary system and when the same target was independently discovered and forwarded by the KELT-South team to the same collaborators, the object was immediately recognised and eliminated as a potential transiting exoplanet. Two were identified as double lined spectroscopic binaries and the final three were determined to be stellar eclipsing systems with RV semi-amplitudes ranging from 26.5 to 37.7 km s^{-1}. Figures 6.3, 6.4, 6.5, 6.6, 6.7 and 6.8 show the KELT-South lightcurves and radial velocity follow-up data for the three targets that were observed with the Australian National University (ANU) 2.3 m telescope using the Wide Field Spectrograph (WiFeS); Dopita et al. 2007). Below, I summarise the result of the spectroscopic follow-up campaign on these three systems:

6.4.1 Candidate KS27C009001

Observations of this target showed that it is an eclipsing binary system with $T_{eff} = 6440$ K, surface gravity log $g = 4.1$, metallicity [Fe/H] = 0.0 and radial velocity semi-amplitude variations of 31 km s^{-1} at twice the photometric period determined by KELT-South observations.

6.4.2 Candidate KS27C030187

Observations of this target showed that it is an eclipsing binary system with $T_{eff} = 6260$ K, surface gravity log $g = 4.4$, metallicity [Fe/H] = -0.5 and radial velocity semi-amplitude variations of 27 km s^{-1}.

6.4.3 Candidate KS27C034885

Observations of this target showed that it is an eclipsing binary system with $T_{eff} = 6330$ K, surface gravity log $g = 4.3$, metallicity [Fe/H] = -0.5 and radial velocity semi-amplitude

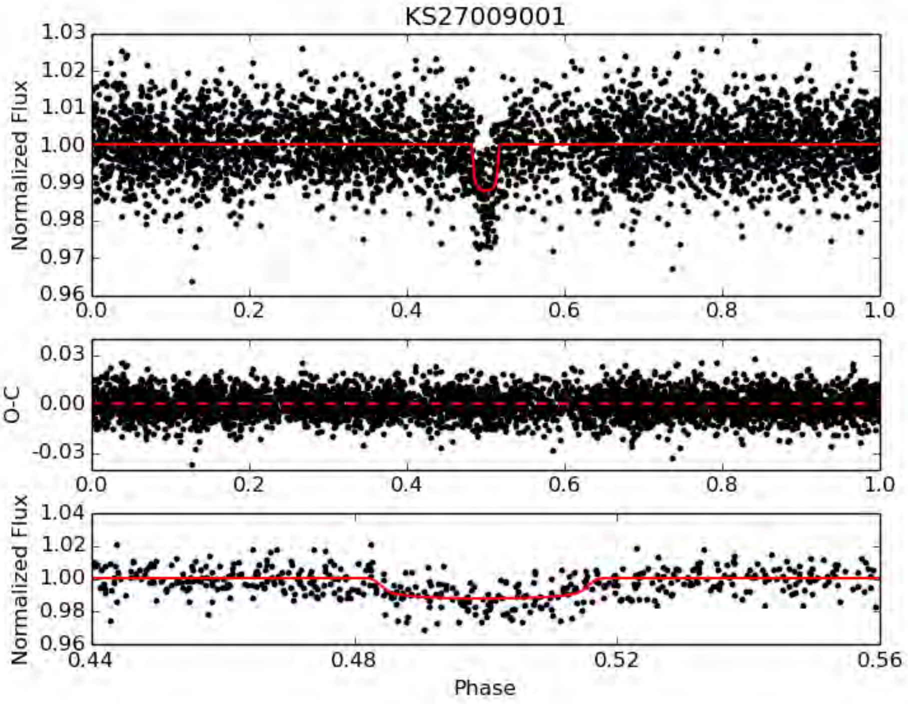

Figure 6.3: KELT-South lightcurve of the exoplanet candidate KS27C009001. *Top:* The phase folded KELT-South lightcurve with the best fit transit model as calculated by ExoFAST. *Middle:* Residuals of the best fit model. *Bottom:* Zoomed in view of the transit along with the model.

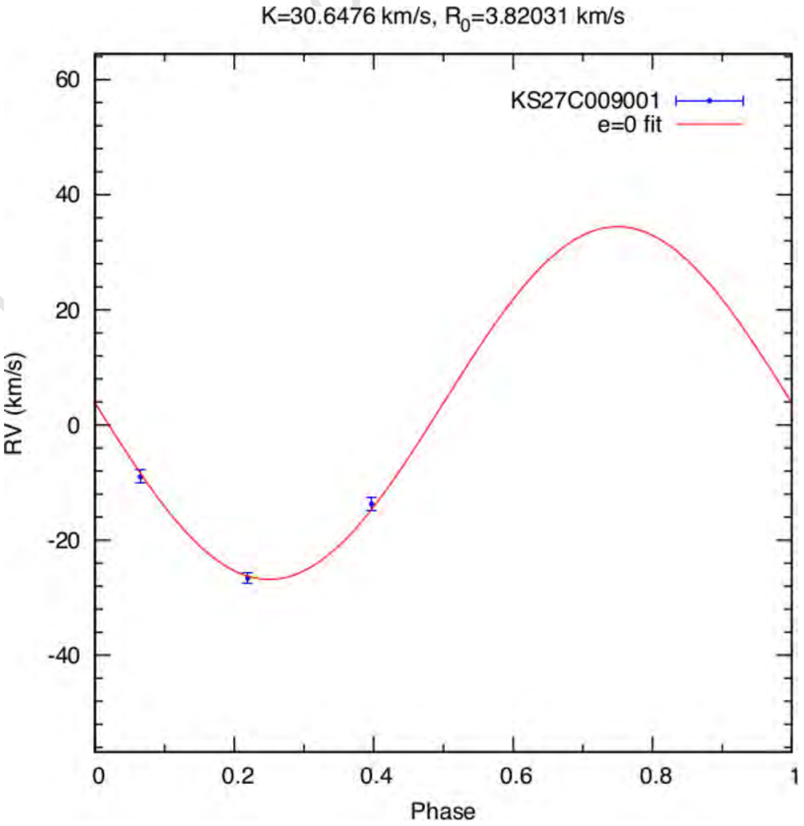

Figure 6.4: Radial velocity follow up observations of the exoplanet candidate KS27C009001. The solid red line is the best fit to the datapoints, forced to a circular orbit.

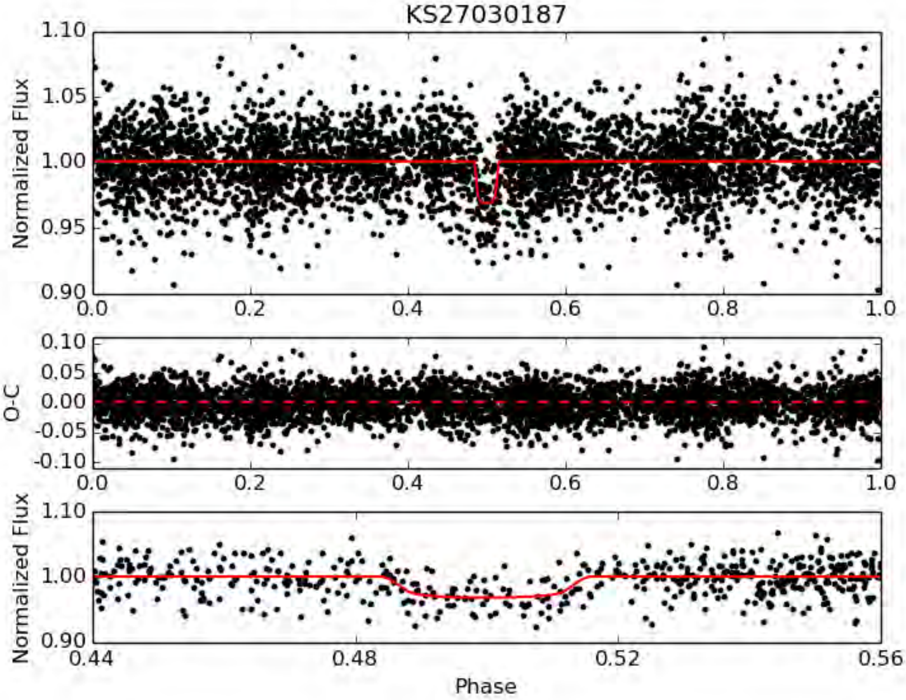

Figure 6.5: KELT-South lightcurve of the exoplanet candidate KS27C030187. *Top:* The phase folded KELT-South lightcurve with the best fit transit model as calculated by ExoFAST. *Middle:* Residuals of the best fit model. *Bottom:* Zoomed in view of the transit along with the model.

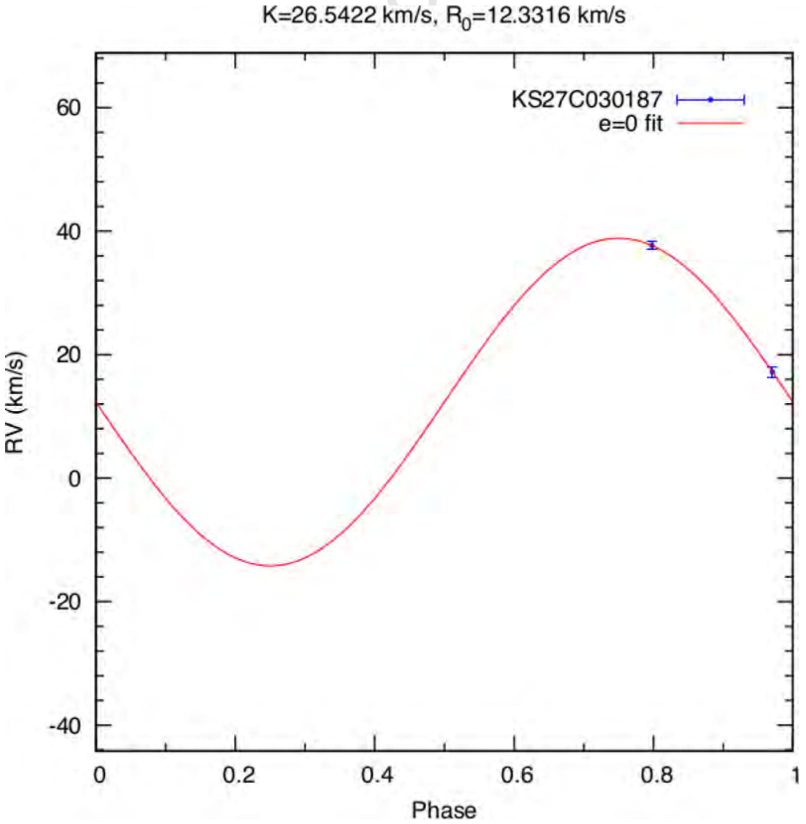

Figure 6.6: Radial velocity follow up observations of the exoplanet candidate KS27C030187. The solid red line is the best fit to the datapoints, forced to a circular orbit.

variations of 38 km s^{-1}. Data from the second regular observing field was reduced and nine possible exoplanet candidates were identified. One was again identified as a previous SuperWASP target that turned out to be an eclipsing binary and was not observed at all, while another was determined to be a double lined spectroscopic binary system. There are thus seven active candidates from the second field still in need of follow-up observations.

6.5 Future of Ground Based Transit Surveys

The search for transiting exoplanets is going to change in the very near future with the introduction of space based all-sky surveys. These planned space missions have very similar design characteristics as the current ground based surveys in that they will observe bright stars, observe almost all of the sky and will discover short period exoplanets. With the failure of two reaction wheels of the Kepler spacecraft in 2013, the spacecraft cannot reliably point to the same field it had done before. Instead, the new mission (called K2) is limited to pointing at fields close to the ecliptic and is capable of pointing at a single field for ∼75 days at a time (Howell et al. 2014). More of the sky will be observed by Kepler than before, but at a slightly worse precision. However, this will still allow it to detect transiting exoplanets and with the new open data policy many more researchers will have access to the data sooner and the discovery rate of transiting exoplanets is likely to increase significantly. Although most of the planets detected with K2 will still be too faint for regular RV surveys to confirm the masses of the planets, other methods can be employed to validate the planetary nature of the objects.

The TESS mission, with a scheduled launch in 2017, will alter the transiting exoplanet discovery research area a great deal. The space based telescope will survey the entire sky over the course of two years, observing a single field for about a month before moving on to the next field. Stars with magnitude $4 < \mathrm{I} < 12$ are the main targets and this makes them bright enough for full characterisation with RV telescopes. The TESS team aim to have reliable photometry for ∼500000 stars and the mission is expected to find many Sub-Neptune ($R_\mathrm{P} < 3.0R_\oplus$), Super-Earth ($R_\mathrm{P} < 2.0R_\oplus$) and Earth like ($R_\mathrm{P} \approx 1.0R_\oplus$)planets. TESS will also find short period exoplanets due to the 30 days of observing time per field, with most of the predicted exoplanet discoveries having periods less than 10 days.

The PLATO spacecraft is scheduled for launch in 2024 and will be a 6 year long mission, with fields being observed for up to 3 years and ∼50% of the sky being observed. Because of its relatively small aperture, the PLATO spacecraft will also observe bright targets that ground based RV telescopes will be able to follow-up. One of the major goals of the PLATO spacecraft is to determine the frequency of small rocky planets in orbits that place them in the habitable zone of their parent stars.

Ground based transiting exoplanet surveys will need to adapt if they want to compete with the new space based missions of the near future. Different areas of the transiting exoplanet parameter space will need to be explored and focused on. The discovery of transiting exoplanets around M dwarf stars (which are intrinsically fainter than F and G main sequence

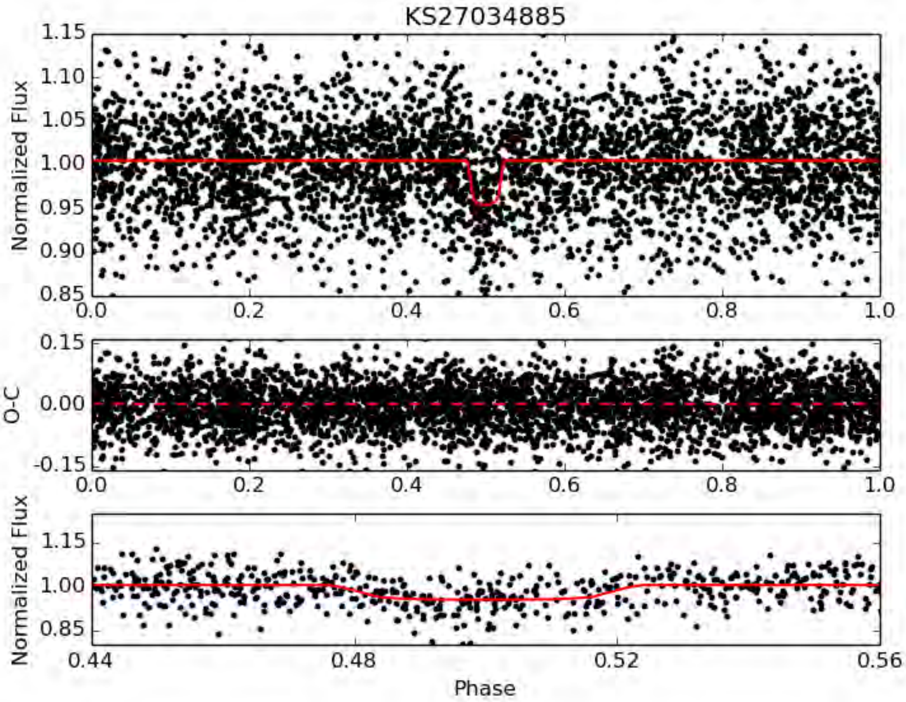

Figure 6.7: KELT-South lightcurve of the exoplanet candidate KS27C034885. *Top:* The phase folded KELT-South lightcurve with the best fit transit model as calculated by ExoFAST. *Middle:* Residuals of the best fit model. *Bottom:* Zoomed in view of the transit along with the model.

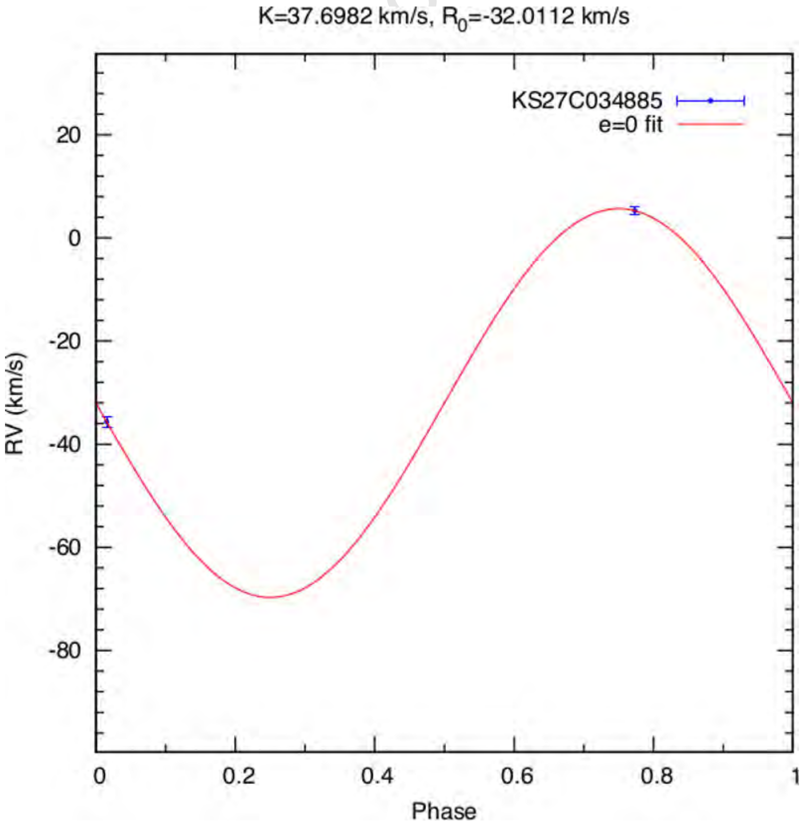

Figure 6.8: Radial velocity follow up observations of the exoplanet candidate KS27C034885. The solid red line is the best fit to the datapoints, forced to a circular orbit.

stars) is beyond most of the space based telescopes. Using slightly larger telescopes than the small aperture space based telescopes will enable the ground based surveys to determine the frequency of planets around smaller stars (Irwin et al. 2014).

Another area of parameter space that ground based surveys might be able to explore is the long period transiting exoplanets. Most of the space missions (except for PLATO) have relatively short times spent on the fields they observe. Ground based surveys from Antarctica will be able to stay on a single field for a much longer period of time and will be able to find planets with longer periods. Networks of telescopes, evenly spaced across the surface of the Earth in longitude, could also explore longer periods to find transiting exoplanets. Projects like the current HATSouth (Bakos et al. 2013) and the future Qatar Exoplanet Survey (Alsubai et al. 2013) have telescopes situated at roughly even spacings in longitude across the globe and will be able to monitor stars almost continuously for 24 hours. This enables those searches to find smaller planets than the regular surveys that only have a telescope at a single location. Future projects like **N**ext **G**eneration **T**ransit **S**earch (NGTS) are being developed to specifically search for Neptune sized planets (Wheatley et al. 2013) by using slightly larger telescopes than the current 4-10 cm class instruments of transiting exoplanet surveys.

Other specialised searches of transiting exoplanets in clusters of stars is also an area that could be explored from the ground as the space based telescopes do not target these systems. Planets around eclipsing binaries (Konacki 2014) and other types of exotic stars (white dwarfs, central stars in planetary nebulae) are also open for exploration and are not the main targets of space based missions.

The deployment of specialized adaptive optics systems on the current 5-10 m class telescopes (Graham et al. 2007, Beuzit et al. 2007, Macintosh et al. 2008, Murakami et al. 2010, McBride et al. 2011, Dekany et al. 2013) and the very large (30+ m) telescopes of the future will enable these telescopes to image Earth-like planets and detect RV variations much smaller than current technology allows. This will enable these telescopes to find the smallest planets and confirm planets around fainter stars than the current limit of $V \approx 13$. With adaptive optics systems it is also possible to get spectroscopic data on the self luminous planet itself, without relying on the light of the parent stars to filter through the atmosphere of the planet to determine the atmospheric composition.

With the launch and operations of the space based telescopes, the need for exoplanet characterisation will increase significantly and the requirements for very sensitive RV instruments will necessitate the construction of new telescopes dedicated to RV follow-up observations of candidate exoplanets.

6.6 Future of the KELT-South Project

KELT-South was designed and built to find new transiting, gas giant planets visible primarily from the southern hemisphere. Most of the survey fields (and by extension possible exoplanet targets) are accessible from the northern hemisphere as long as those telescopes are situated relatively close to the equator. After two seasons of commissioning, the regular observing program started early in 2010 with the telescope using the software and code I developed. The number of data points required to search for transiting exoplanets in the KELT-South data was achieved in middle 2013 and the results from the preliminary data reduction and analysis of the first two datasets has shown that the transit like features seen in the KELT-South data are real (albeit eclipsing binary systems) and should serve as encouragement that the first exoplanet discovery isn't far away.

Spectroscopic follow-up observations of all possible transit detections could be done with SALT using the newly (2013 October) installed high resolution spectrograph (HRS). If the detection is confirmed, a more detailed study (aided by the brightness of the targets) of the transiting system might reveal information about the chemical composition of the upper atmosphere of the planet. Eclipse timing variations using the high speed photometric capabilities of SALT might also reveal other smaller planets present in the system in question.

The data reduction of the main survey data with the aim of finding bright transiting exoplanets started in January 2014 and although no new transiting exoplanets have been discovered by KELT-South to date, we have been able to independently "rediscover" known transiting exoplanets from the SuperWASP survey. Most of these planets are outside our target magnitude range of $8 < V < 11$ and greatly encourages the KELT-South team that in the near future we will be able to discover a planet of our own. In Appendix A I show the KELT-South lightcurves of the known transiting exoplanets and compare the published system parameters for the transiting exoplanets to the parameters we obtain using the KELT-South lightcurves alone.

KELT-South will continue to operate for the foreseeable future with the intention of discovering the brightest transiting exoplanets in the southern hemisphere.

Appendix A

Appendix

A.1 Known Exoplanets in KELT-South Main Survey

From 2014 January the KELT-South team has performed data reduction and analysis of a number of fields that contain known transiting exoplanets. Below is a short discussion of the known exoplanets in those fields. I also include a table (Table A.1) showing the known exoplanets and the various reasons for not finding them in the KELT-South datasets. I followed the same procedure to determine the system parameters as described in Section 5.6.1. For each of the known exoplanets (WASP-4b, WASP-18b, WASP-25b, WASP-38b, WASP-41b, WASP-62b, WASP-95b, WASP-97b, WASP-99b, and WASP-117b) we are able to identify with the KELT-South, I compare the system parameters we obtained using ExoFAST modelling of the KELT-South lightcurves with the published values from the literature. I also include the KELT-South lightcurves and best fitting ExoFAST model in the accompanying figures.

Many of the known exoplanets that are within fields that we have observed with KELT-South are too faint to be included in the Tycho-2 catalogue. Due to the matching of our stars to the Tycho-2 catalogue in the data reduction pipeline, many of the known transiting exoplanets don't appear on our candidate lists. We are working on matching to other catalogues that are more complete up to V $\approx$ 13, which should enable us to find more candidate transiting exoplanets that could have been missed due to their faintness. One of the known planets, WASP-15b, orbits a star that is considered to be a giant star and was excluded due to the RPM cut we employ to remove giant stars from our sample. The remaining known exoplanets failed to meet one or more of the selection criteria described in Section 6.4, which indicates that either we did not have enough phase coverage of the transit event or we simply did not have enough data to reliably detect the transiting event.

Table A.1: Table of the known transiting exoplanets in the regular KELT-South survey fields.

Exoplanet Name	Found by KELT-South?	Magnitude [V]	Reason for not in KELT-South?
WASP-4b	Yes	12.60	-
WASP-18b	Yes	9.30	-
WASP-25b	Yes	11.90	-
WASP-38b	Yes	9.39	-
WASP-41b	Yes	11.60	-
WASP-62b	Yes	10.30	-
WASP-95b	Yes	10.10	-
WASP-97b	Yes	10.57	-
WASP-99b	Yes	9.50	-
WASP-117b	Yes	10.15	-
HATS-1b	No	12.05	Not in Tycho-2 catalogue.
HATS-2b	No	13.62	Not in Tycho-2 catalogue.
WASP-5b	No	12.30	Not in Tycho-2 catalogue.
WASP-23b	No	12.70	Not in Tycho-2 catalogue.
WASP-31b	No	11.66	Not in Tycho-2 catalogue.
WASP-36b	No	12.70	Not in Tycho-2 catalogue.
WASP-42b	No	12.57	Not in Tycho-2 catalogue.
WASP-43b	No	12.40	Not in Tycho-2 catalogue.
WASP-46b	No	12.90	Not in Tycho-2 catalogue.
WASP-96b	No	12.20	Not in Tycho-2 catalogue.
WASP-103b	No	12.10	Not in Tycho-2 catalogue.
WASP-15b	No	10.70	Did not pass RPM cut.
WASP-55b	No	11.80	Did not pass BLS SDE > 7.0
WASP-16b	No	11.30	Did not pass BLS SDE > 7.0
WASP-73b	No	10.50	Did not pass BLS SDE > 7.0
WASP-88b	No	11.40	Did not pass BLS SDE > 7.0
WASP-17b	No	11.59	Did not pass $\Delta\chi^2 > 1.5$
WASP-25b	No	11.90	Did not pass $\Delta\chi^2 > 1.5$
WASP-29b	No	11.30	Did not pass $\Delta\chi^2 > 1.5$
WASP-34b	No	10.40	Did not pass $\Delta\chi^2 > 1.5$

This page is intentionally left blank to make the tables and lightcurves that follow easier to read by placing the table of properties and the lightcurves on opposite sides of the page.

Table A.2: Table of the ExoFAST determined parameters of WASP-4b compared to the published parameters from Wilson et al. (2008).

Parameter	Units	ExoFAST Value	Published Value
M_*	Mass ($M_\odot$)	$0.95^{+0.53}_{-0.36}$	$0.8997^{+0.077}_{-0.072}$
R_*	Radius ($R_\odot$).......................	$0.92^{+0.22}_{-0.21}$	$0.9370^{+0.04}_{-0.03}$
$\log(g_*)$ ...	Surface gravity (cgs)...............	$4.47^{+0.19}_{-0.12}$	$4.45^{+0.016}_{-0.029}$
[Fe/H] ...	Metallicity	$-0.1^{+2.1}_{-2.3}$	
$T_{\rm eff}$	Effective temperature (K)	5494^{+100}_{-97}	5500 ± 150
P	Period (days)......................	$1.338239^{+0.000023}_{-0.000015}$	$1.3382282^{+0.000003}_{-0.000003}$
a.........	Semi-major axis (AU)	$0.0233^{+0.0037}_{-0.0035}$	$0.0230^{+0.001}_{-0.001}$
R_P	Radius (R_J)	$1.33^{+0.29}_{-0.26}$	$1.416^{+0.068}_{-0.043}$
T_{eq}	Equilibrium Temperature (K)	1680^{+110}_{-180}	1761^{+24}_{-9}
T_C	Time of transit	$6903.211^{+0.015}_{-0.011}$	$4365.91464^{+0.00025}_{-0.00023}$
i	Inclination (degrees)...............	90.0 (adopted)[1]	$88.59^{+1.36}_{-1.50}$
b	Impact Parameter	0.0 (adopted)[1]	$0.13^{+0.13}_{-0.12}$
δ	Transit depth......................	$0.0224^{+0.0036}_{-0.0031}$	$0.0241^{+0.0005}_{-0.0002}$
T_{14}	Total duration (days)..............	$0.092^{+0.011}_{-0.018}$	$0.0928^{+0.0009}_{-0.0007}$
u_1	linear limb-darkening coefficient ...	$0.410^{+0.085}_{-0.17}$	
u_2	quadratic limb-darkening coefficient	$0.257^{+0.086}_{-0.036}$	

NOTES

1 No spectroscopic follow-up data available for KELT-South team members to better constrain the stellar parameter values, which leads to the large errors in their determined properties.

2 The ExoFAST determined "Time of transit" is listed in $\rm MBJD_{TDB}$, while the SuperWASP times are listed in MHJD.

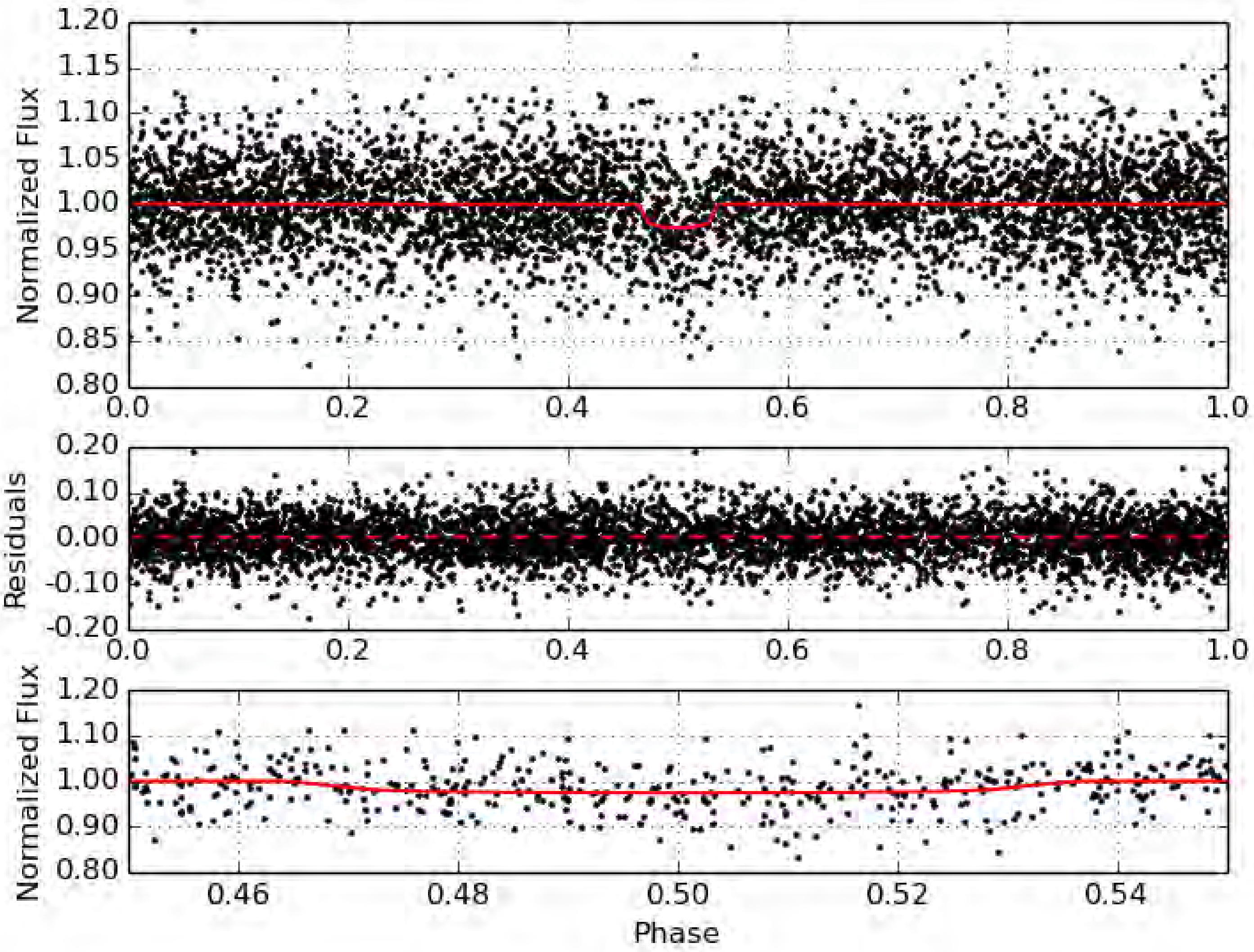

Figure A.1: KELT-South lightcurve of the exoplanet WASP-4b. *Top:* The phase folded KELT-South lightcurve with the best fit transit model as calculated by ExoFAST. *Middle:* Residuals of the best fit model. *Bottom:* Zoomed in view of the transit along with the model.

Table A.3: Table of the ExoFAST determined parameters of WASP-18b compared to the published parameters from Hellier et al. (2009).

Parameter	Units	ExoFAST Value	Published Value
M_*	Mass ($M_\odot$)	$1.12^{+0.68}_{-0.38}$	1.25 ± 0.13
R_*	Radius ($R_\odot$)	$1.13^{+0.20}_{-0.15}$	$1.216^{+0.067}_{-0.054}$
$\log(g_*)$	Surface gravity (cgs)	$4.383^{+0.064}_{-0.062}$	$4.367^{+0.028}_{-0.042}$
[Fe/H]	Metallicity	$-0.4^{+2.2}_{-2.1}$	0.00 ± 0.09
$T_{\rm eff}$	Effective temperature (K)	6403^{+100}_{-99}	6400 ± 100
P	Period (days)	0.9414528 ± 0.0000018	$0.94145299 \pm 0.00000087$
a	Semi-major axis (AU)	$0.0195^{+0.0033}_{-0.0025}$	0.02026 ± 0.00068
R_P	Radius (R_J)	$0.97^{+0.17}_{-0.13}$	$1.106^{+0.072}_{-0.054}$
T_{eq}	Equilibrium Temperature (K)	2349^{+44}_{-43}	2384^{+58}_{-30}
T_C	Time of transit	6912.1497 ± 0.0017	4221.48163 ± 0.00038
i	Inclination (degrees)	90.0 (adopted)[1]	86.0 ± 2.5
b	Impact Parameter	0.0 (adopted)[1]	0.25 ± 0.15
δ	Transit depth	0.00781 ± 0.00030	0.00875 ± 0.00021
T_{14}	Total duration (days)	$0.0891^{+0.0019}_{-0.0018}$	0.08932 ± 0.00068
u_1	linear limb-darkening coefficient	$0.2679^{+0.051}_{-0.0050}$	
u_2	quadratic limb-darkening coefficient	$0.3146^{+0.020}_{-0.0084}$	

NOTES

1 No spectroscopic follow-up data available for KELT-South team members to better constrain the stellar parameter values, which leads to the large errors in their determined properties.

2 The ExoFAST determined "Time of transit" is listed in $\mathrm{MBJD_{TDB}}$, while the SuperWASP times are listed in MHJD.

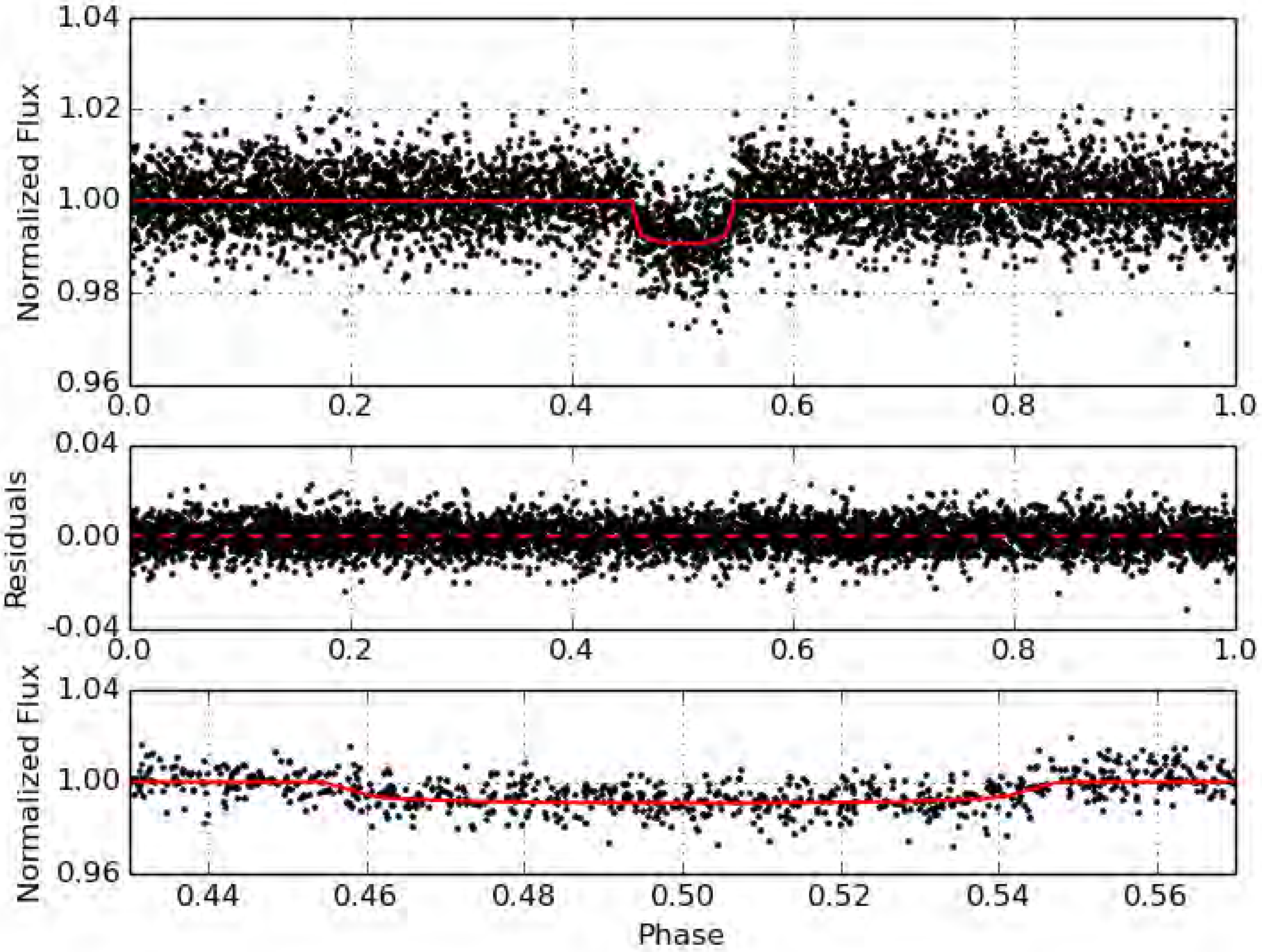

Figure A.2: KELT-South lightcurve of the exoplanet WASP-18b. *Top:* The phase folded KELT-South lightcurve with the best fit transit model as calculated by ExoFAST. *Middle:* Residuals of the best fit model. *Bottom:* Zoomed in view of the transit along with the model.

Table A.4: Table of the ExoFAST determined parameters of WASP-25b compared to the published parameters from Enoch et al. (2011).

Parameter	Units	ExoFAST Value	Published Value
M_*	Mass ($M_\odot$)	$0.98^{+0.59}_{-0.37}$	1.00 ± 0.03
R_*	Radius ($R_\odot$)	$1.01^{+0.22}_{-0.18}$	0.92 ± 0.04
$\log(g_*)$ ...	Surface gravity (cgs)	$4.423^{+0.099}_{-0.096}$	4.51 ± 0.03
[Fe/H] ...	Metallicity	-0.2 ± 2.3	-0.07 ± 0.10
$T_{\rm eff}$	Effective temperature (K)	5752^{+98}_{-100}	5703 ± 100
P	Period (days)	$3.76474^{+0.00011}_{-0.00010}$	3.764825 ± 0.000005
a	Semi-major axis (AU)	$0.0471^{+0.0080}_{-0.0068}$	0.0473 ± 0.0004
R_P	Radius (R_J)	$1.17^{+0.25}_{-0.21}$	$1.22^{+0.06}_{-0.05}$
T_{eq}	Equilibrium Temperature (K)	1283^{+66}_{-63}	1212 ± 35
T_C	Time of transit	$6829.852^{+0.023}_{-0.017}$	5274.99649 ± 0.00017
i	Inclination (degrees)	90.0 (adopted)^1	88.0 ± 0.5
b	Impact Parameter	0.0 (adopted)^1	$0.38^{+0.06}_{-0.07}$
δ	Transit depth	$0.0143^{+0.0018}_{-0.0019}$	0.0187 ± 0.0002
T_{14}	Total duration (days)	$0.134^{+0.013}_{-0.012}$	0.116 ± 0.001
u_1	linear limb-darkening coefficient ...	$0.346^{+0.096}_{-0.092}$	
u_2	quadratic limb-darkening coefficient	$0.290^{+0.039}_{-0.034}$	

NOTES

1 No spectroscopic follow-up data available for KELT-South team members to better constrain the stellar parameter values, which leads to the large errors in their determined properties.

2 The ExoFAST determined "Time of transit" is listed in $\mathrm{MBJD_{TDB}}$, while the SuperWASP times are listed in MHJD.

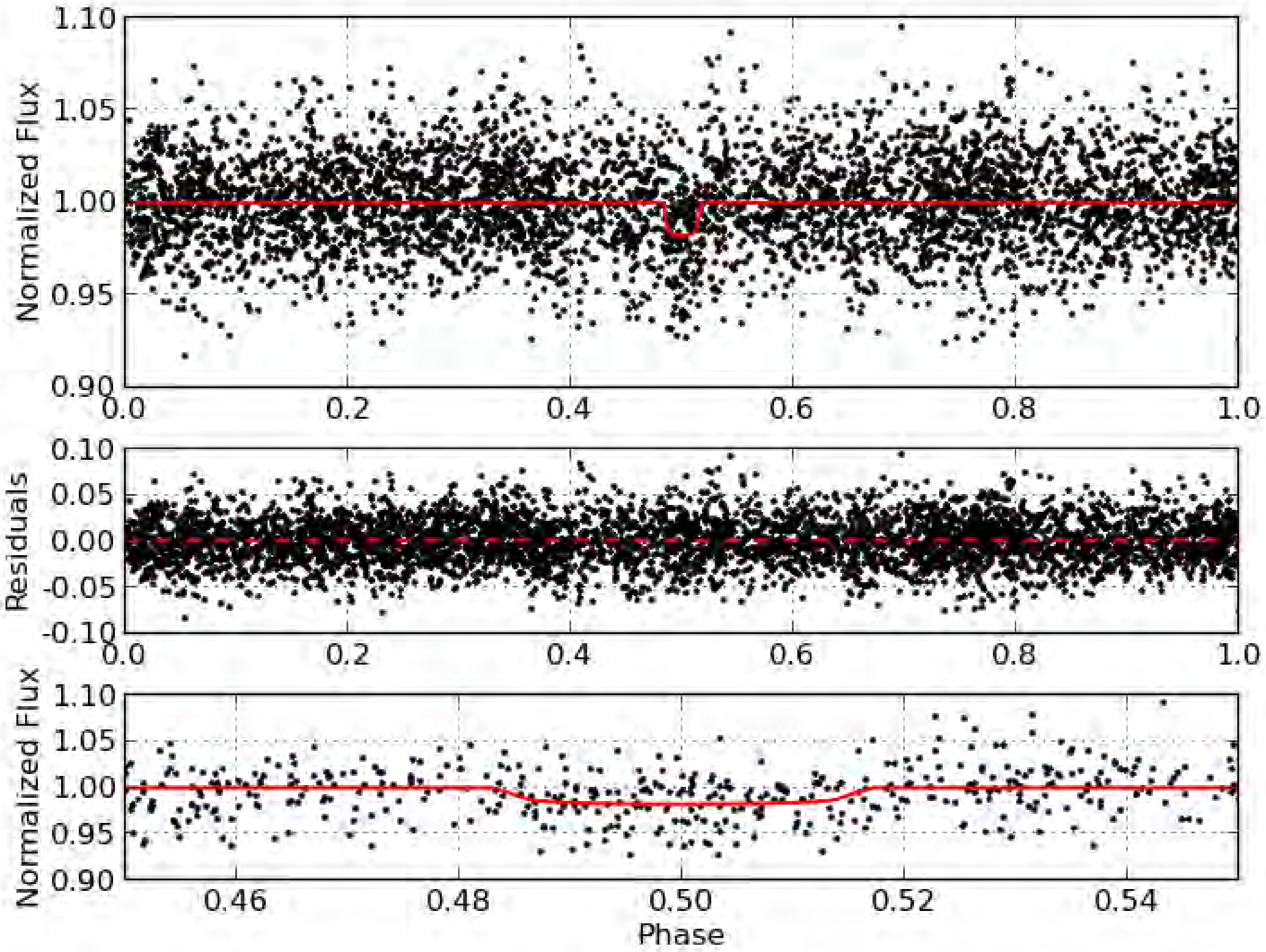

Figure A.3: KELT-South lightcurve of the exoplanet WASP-25b. *Top:* The phase folded KELT-South lightcurve with the best fit transit model as calculated by ExoFAST. *Middle:* Residuals of the best fit model. *Bottom:* Zoomed in view of the transit along with the model.

Table A.5: Table of the ExoFAST determined parameters of WASP-38b compared to the published parameters from Barros et al. (2011).

Parameter	Units	ExoFAST Value	Published Value
M_*	Mass ($M_\odot$)	$1.21^{+0.69}_{-0.45}$	1.203 ± 0.036
R_*	Radius ($R_\odot$)	$1.30^{+0.26}_{-0.22}$	$1.331^{+0.030}_{-0.025}$
$\log(g_*)$	Surface gravity (cgs)	$4.294^{+0.089}_{-0.085}$	$4.250^{+0.012}_{-0.013}$
[Fe/H]	Metallicity	0.1 ± 2.2	-0.12 ± 0.07
$T_{\rm eff}$	Effective temperature (K)	6148 ± 100	6150 ± 80
P	Period (days)	6.87181 ± 0.00021	$6.871815^{+0.000045}_{-0.000042}$
a	Semi-major axis (AU)	$0.075^{+0.012}_{-0.011}$	$0.075222^{+0.00074}_{-0.00075}$
R_P	Radius (R_J)	$1.05^{+0.20}_{-0.18}$	$1.094^{+0.029}_{-0.028}$
T_{eq}	Equilibrium Temperature (K)	1230^{+53}_{-50}	1292 ± 33
T_C	Time of transit	$6840.860^{+0.014}_{-0.017}$	5335.9205 ± 0.00074
i	Inclination (degrees)	90.0 (adopted)[1]	$89.69^{+0.30}_{-0.25}$
b	Impact Parameter	0.0 (adopted)[1]	$0.066^{+0.093}_{-0.046}$
δ	Transit depth	$0.00681^{+0.00079}_{-0.00075}$	0.00712 ± 0.00018
T_{14}	Total duration (days)	$0.190^{+0.015}_{-0.013}$	$0.1942^{+0.0018}_{-0.0019}$
u_1	linear limb-darkening coefficient	$0.310^{+0.055}_{-0.043}$	
u_2	quadratic limb-darkening coefficient	$0.3104^{+0.0072}_{-0.0060}$	

NOTES

1 No spectroscopic follow-up data available for KELT-South team members to better constrain the stellar parameter values, which leads to the large errors in their determined properties.

2 The ExoFAST determined "Time of transit" is listed in $\mathrm{MBJD_{TDB}}$, while the SuperWASP times are listed in MHJD.

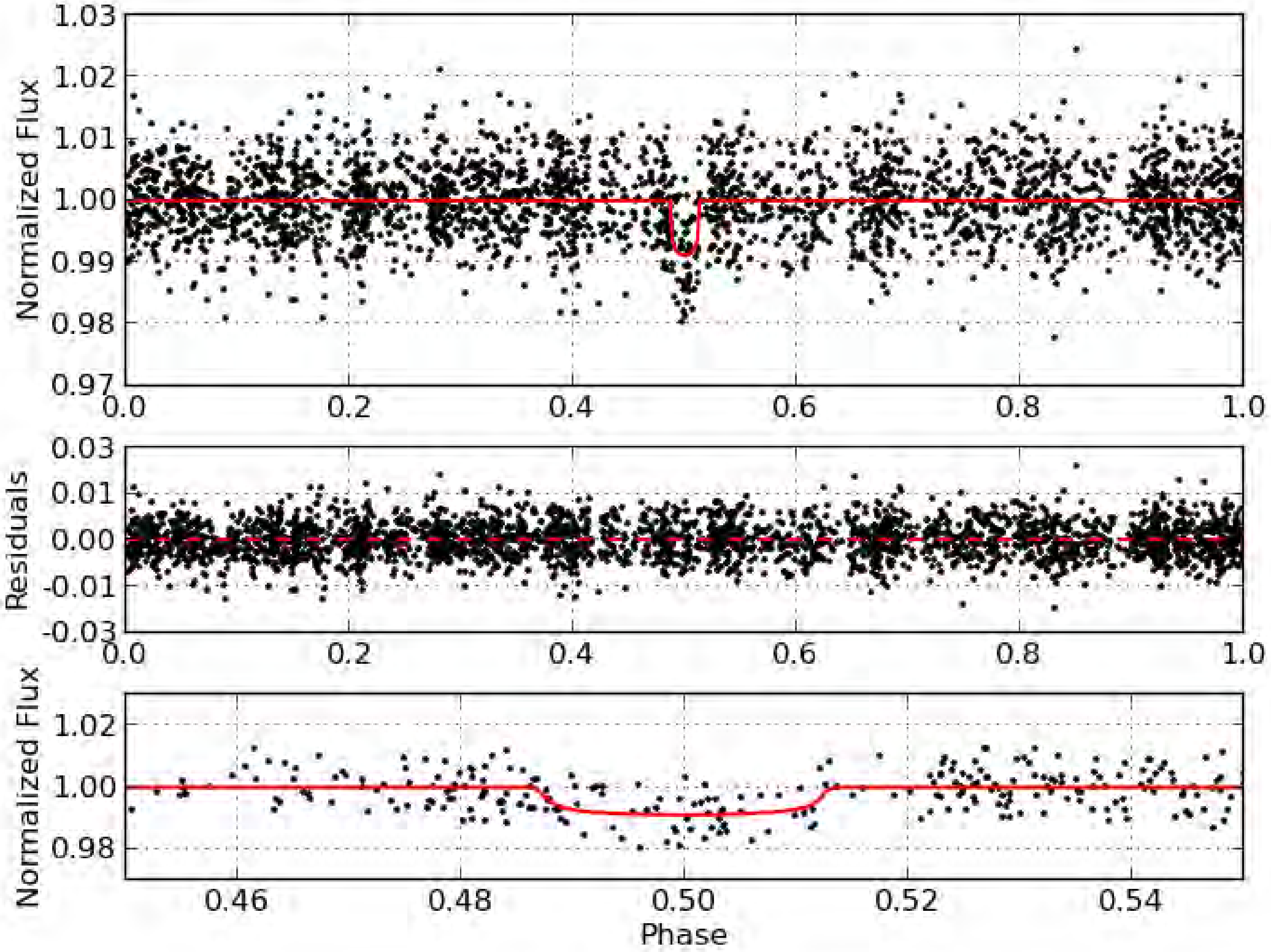

Figure A.4: KELT-South lightcurve of the exoplanet WASP-38b. *Top:* The phase folded KELT-South lightcurve with the best fit transit model as calculated by ExoFAST. *Middle:* Residuals of the best fit model. *Bottom:* Zoomed in view of the transit along with the model.

Table A.6: Table of the ExoFAST determined parameters of WASP-41b compared to the published parameters from Maxted et al. (2011).

Parameter	Units	ExoFAST Value	Published Value
M_*	Mass ($M_\odot$)	$0.89^{+0.53}_{-0.34}$	0.93 ± 0.03
R_*	Radius ($R_\odot$)	$0.82^{+0.16}_{-0.15}$	0.90 ± 0.05
$\log(g_*)$ ...	Surface gravity (cgs)	$4.556^{+0.088}_{-0.082}$	4.4 ± 0.2
[Fe/H] ...	Metallicity	$-0.2^{+2.2}_{-2.3}$	-0.08 ± 0.09
$T_{\rm eff}$	Effective temperature (K)	5445^{+100}_{-98}	5450 ± 150
P	Period (days)	$3.052388^{+0.000031}_{-0.000028}$	3.052401 ± 0.000004
a	Semi-major axis (AU)	$0.0396^{+0.0066}_{-0.0059}$	0.0402 ± 0.0005
R_P	Radius (R_J)	$1.01^{+0.19}_{-0.17}$	1.20 ± 0.06
T_{eq}	Equilibrium Temperature (K)	1196^{+51}_{-52}	1230 ± 50
T_C	Time of transit	$6845.2350^{+0.010}_{-0.0088}$	5343.463 ± 0.001
i	Inclination (degrees)	90.0 (adopted)[1]	87.7 ± 0.08
b	Impact Parameter	0.0 (adopted)[1]	$0.40^{+0.015}_{-0.011}$
δ	Transit depth	0.0159 ± 0.0014	0.0186 ± 0.0004
T_{14}	Total duration (days)	$0.1059^{+0.0079}_{-0.0078}$	0.108 ± 0.002
u_1	linear limb-darkening coefficient ...	$0.408^{+0.096}_{-0.17}$	
u_2	quadratic limb-darkening coefficient	$0.258^{+0.092}_{-0.044}$	

NOTES

1 No spectroscopic follow-up data available for KELT-South team members to better constrain the stellar parameter values, which leads to the large errors in their determined properties.

2 The ExoFAST determined "Time of transit" is listed in $\mathrm{MBJD_{TDB}}$, while the SuperWASP times are listed in MHJD.

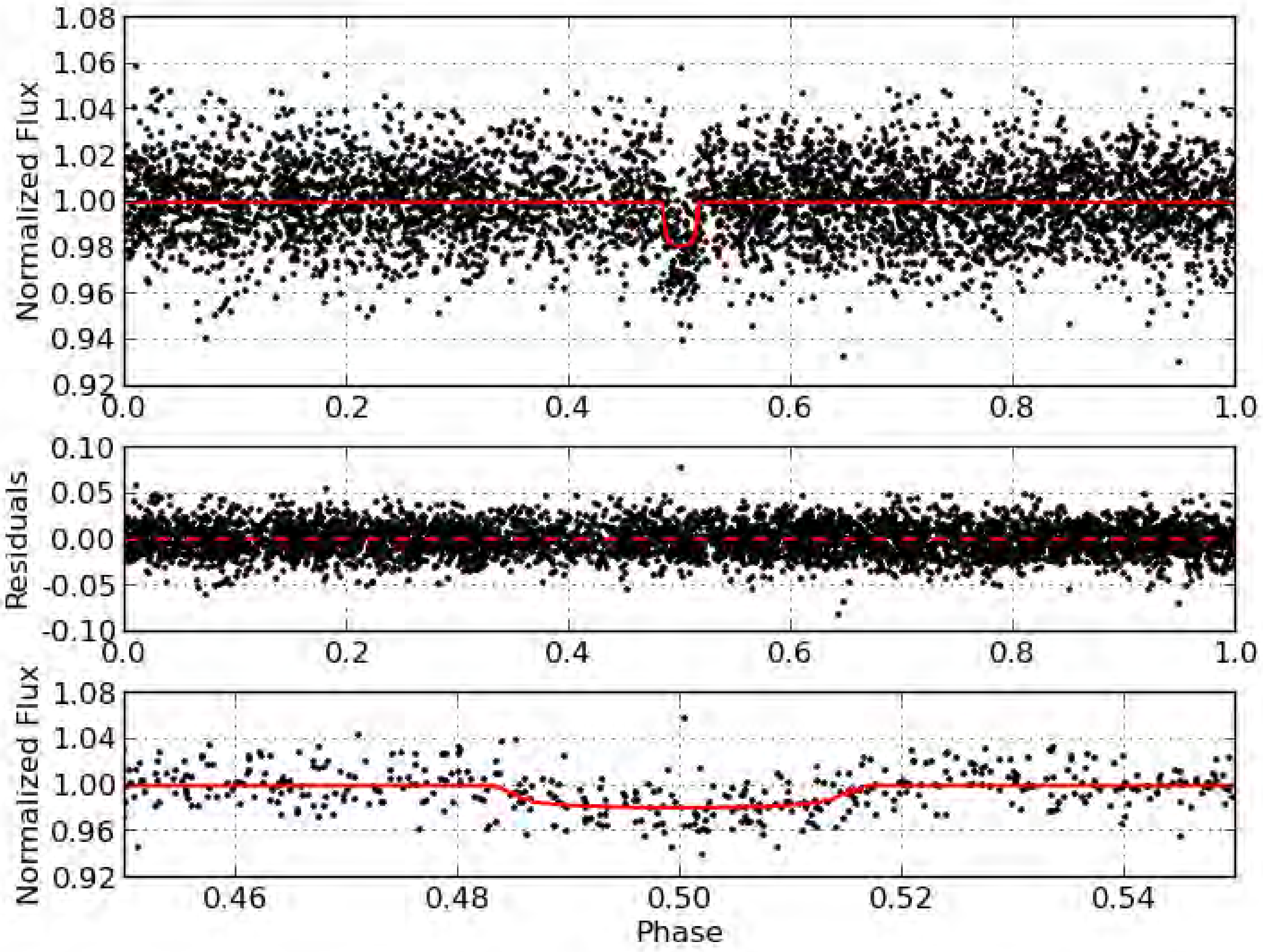

Figure A.5: KELT-South lightcurve of the exoplanet WASP-41b. *Top:* The phase folded KELT-South lightcurve with the best fit transit model as calculated by ExoFAST. *Middle:* Residuals of the best fit model. *Bottom:* Zoomed in view of the transit along with the model.

Table A.7: Table of the ExoFAST determined parameters of WASP-62b compared to the published parameters from Hellier et al. (2012).

Parameter	Units	ExoFAST Value	Published Value
M_*	Mass ($M_\odot$)	$1.22^{+0.69}_{-0.45}$	1.25 ± 0.05
R_*	Radius ($R_\odot$)	$1.29^{+0.24}_{-0.19}$	1.28 ± 0.05
$\log(g_*)$	Surface gravity (cgs)	$4.302^{+0.069}_{-0.068}$	4.316 ± 0.025
[Fe/H]	Metallicity	0.1 ± 2.2	0.04 ± 0.06
$T_{\rm eff}$	Effective temperature (K)	6232^{+98}_{-94}	6230 ± 80
P	Period (days)	$4.411945^{+0.000026}_{-0.000025}$	4.411953 ± 0.000003
a	Semi-major axis (AU)	$0.0563^{+0.0090}_{-0.0079}$	0.0567 ± 0.0007
R_P	Radius (R_J)	$1.40^{+0.24}_{-0.20}$	1.39 ± 0.06
T_{eq}	Equilibrium Temperature (K)	1438^{+39}_{-36}	1440 ± 30
T_C	Time of transit	$0.972^{+0.11}_{-0.095}$	5855.39195 ± 0.00027
i	Inclination (degrees)	90.0 (adopted)[1]	$88.3^{+0.9}_{-0.6}$
b	Impact Parameter	0.0 (adopted)[1]	$0.29^{+0.08}_{-0.14}$
δ	Transit depth	$0.01240^{+0.00077}_{-0.00075}$	0.0123 ± 0.0002
T_{14}	Total duration (days)	$0.1667^{+0.0076}_{-0.0067}$	0.1588 ± 0.0014
u_1	linear limb-darkening coefficient	$0.296^{+0.054}_{-0.030}$	
u_2	quadratic limb-darkening coefficient	$0.3118^{+0.011}_{-0.0042}$	

NOTES

1 No spectroscopic follow-up data available for KELT-South team members to better constrain the stellar parameter values, which leads to the large errors in their determined properties.

2 The ExoFAST determined "Time of transit" is listed in $\rm MBJD_{TDB}$, while the SuperWASP times are listed in MHJD.

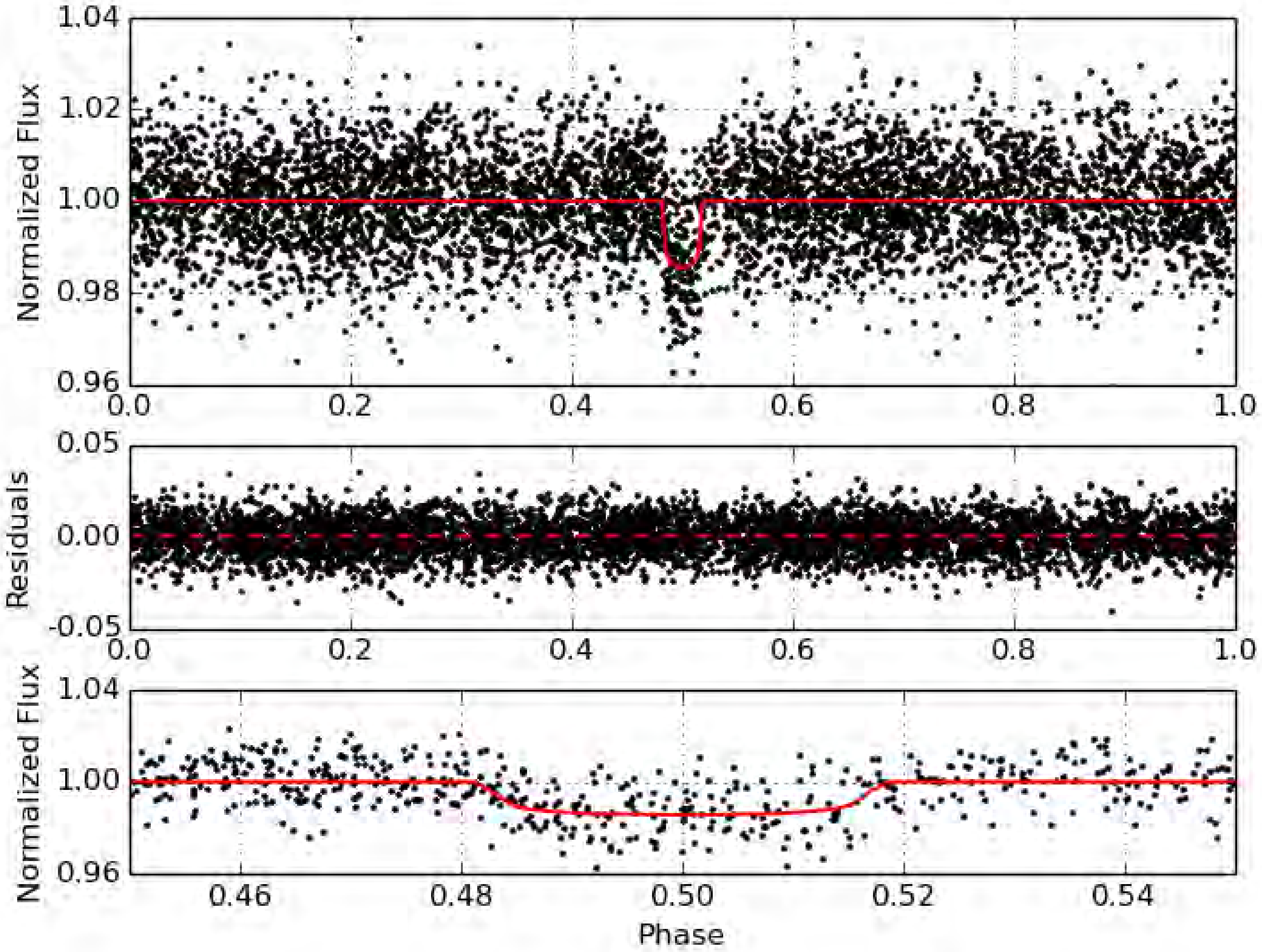

Figure A.6: KELT-South lightcurve of the exoplanet WASP-62b. *Top:* The phase folded KELT-South lightcurve with the best fit transit model as calculated by ExoFAST. *Middle:* Residuals of the best fit model. *Bottom:* Zoomed in view of the transit along with the model.

Table A.8: Table of the ExoFAST determined parameters of WASP-95b compared to the published parameters from Hellier et al. (2014).

Parameter	Units	ExoFAST Value	Published Value
M_*	Mass ($M_\odot$)	$0.81^{+0.47}_{-0.27}$	1.11 ± 0.09
R_*	Radius ($R_\odot$)	$0.98^{+0.18}_{-0.13}$	$1.13^{+0.08}_{-0.04}$
$\log(g_*)$	Surface gravity (cgs)	$4.368^{+0.059}_{-0.057}$	$4.38^{+0.02}_{-0.04}$
[Fe/H]	Metallicity	$-1.1^{+2.2}_{-1.9}$	$+0.14 \pm 0.16$
$T_{\rm eff}$	Effective temperature (K)	5633^{+96}_{-97}	5630 ± 130
P	Period (days)	$2.1846713^{+0.0000061}_{-0.0000066}$	2.1846730 ± 0.0000014
a	Semi-major axis (AU)	$0.0307^{+0.0050}_{-0.0038}$	0.03416 ± 0.00083
R_P	Radius (R_J)	$0.93^{+0.16}_{-0.12}$	1.21 ± 0.06
T_{eq}	Equilibrium Temperature (K)	1532^{+33}_{-32}	1570 ± 50
T_C	Time of transit	$6902.1015^{+0.0025}_{-0.0028}$	6338.45851 ± 0.00024
i	Inclination (degrees)	90.0 (adopted)[1]	$88.4^{+1.2}_{-2.1}$
b	Impact Parameter	0.0 (adopted)[1]	$0.19^{+0.21}_{-0.13}$
δ	Transit depth	0.00967 ± 0.00041	0.0105 ± 0.0003
T_{14}	Total duration (days)	0.1136 ± 0.0028	0.116 ± 0.001
u_1	linear limb-darkening coefficient	$0.295^{+0.16}_{-0.048}$	
u_2	quadratic limb-darkening coefficient	$0.315^{+0.024}_{-0.065}$	

NOTES

1 No spectroscopic follow-up data available for KELT-South team members to better constrain the stellar parameter values, which leads to the large errors in their determined properties.

2 The ExoFAST determined "Time of transit" is listed in $\mathrm{MBJD_{TDB}}$, while the SuperWASP times are listed in MHJD.

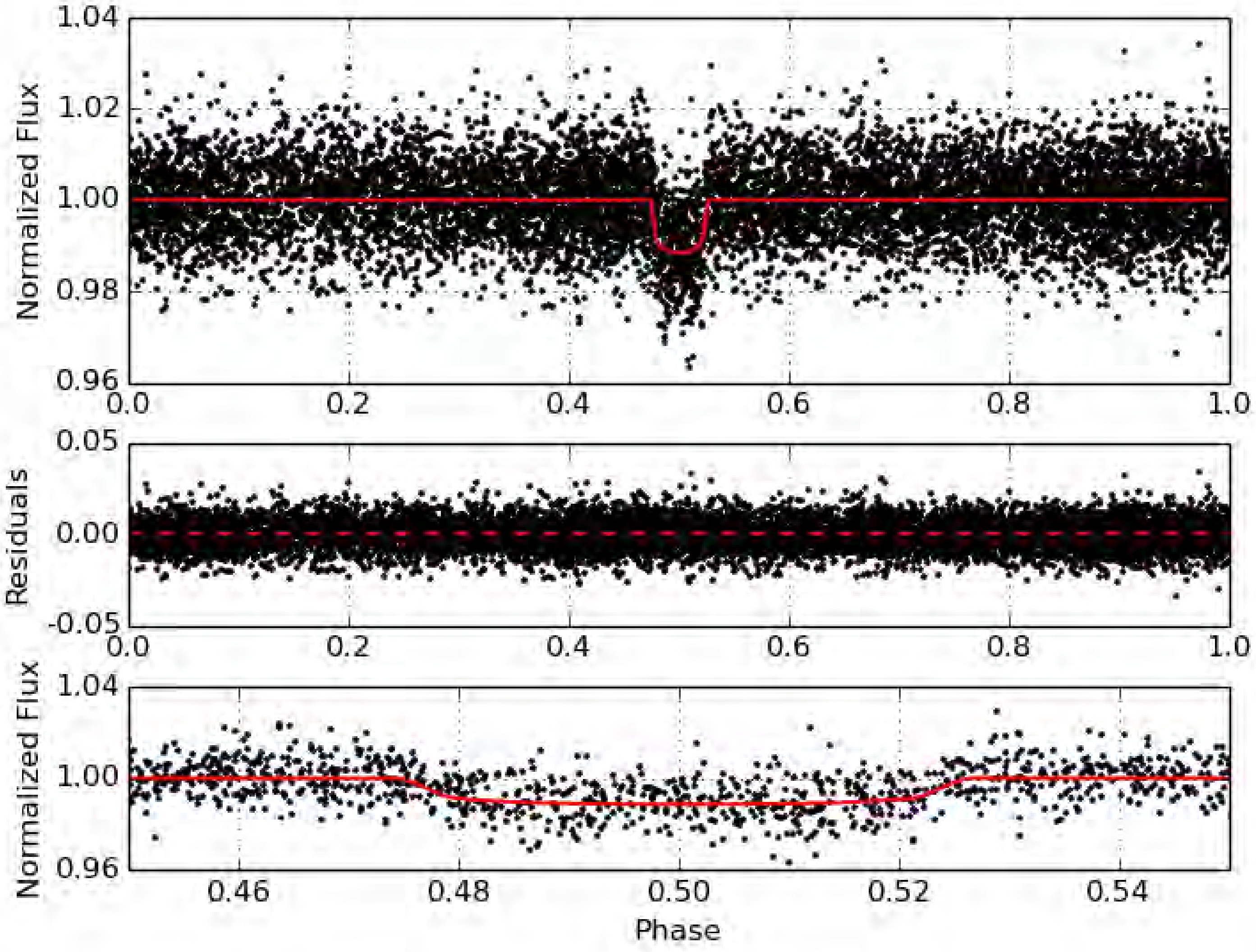

Figure A.7: KELT-South lightcurve of the exoplanet WASP-95b. *Top:* The phase folded KELT-South lightcurve with the best fit transit model as calculated by ExoFAST. *Middle:* Residuals of the best fit model. *Bottom:* Zoomed in view of the transit along with the model.

Table A.9: Table of the ExoFAST determined parameters of WASP-97b compared to the published parameters from Hellier et al. (2014).

Parameter	Units	ExoFAST Value	Published Value
M_*	Mass ($M_\odot$)	$0.95^{+0.58}_{-0.36}$	1.12 ± 0.06
R_*	Radius ($R_\odot$).......................	$0.90^{+0.17}_{-0.14}$	1.06 ± 0.04
$\log(g_*)$ ...	Surface gravity (cgs)...............	$4.509^{+0.066}_{-0.064}$	4.43 ± 0.03
[Fe/H] ...	Metallicity	$-0.2^{+2.3}_{-2.2}$	$+0.23 \pm 0.11$
T_{eff}	Effective temperature (K)	5643^{+97}_{-100}	5640 ± 100
P	Period (days).......................	$2.0727514^{+0.0000075}_{-0.0000077}$	2.072760 ± 0.000001
a	Semi-major axis (AU)	$0.0313^{+0.0054}_{-0.0046}$	0.03303 ± 0.00056
R_P	Radius (R_J)	$0.98^{+0.17}_{-0.15}$	1.13 ± 0.06
T_{eq}	Equilibrium Temperature (K)	1457^{+34}_{-33}	1555 ± 40
T_C	Time of transit	$6910.7716^{+0.0040}_{-0.0039}$	6438.18683 ± 0.00018
i	Inclination (degrees)...............	90.0 (adopted)[1]	$88.0^{+1.3}_{-1.0}$
b	Impact Parameter	0.0 (adopted)[1]	$0.23^{+0.11}_{-0.15}$
δ	Transit depth......................	0.01246 ± 0.00066	0.0119 ± 0.0002
T_{14}	Total duration (days)..............	$0.0982^{+0.0033}_{-0.0031}$	0.1076 ± 0.0008
u_1	linear limb-darkening coefficient ...	$0.375^{+0.090}_{-0.13}$	
u_2	quadratic limb-darkening coefficient	$0.275^{+0.062}_{-0.035}$	

NOTES

1 No spectroscopic follow-up data available for KELT-South team members to better constrain the stellar parameter values, which leads to the large errors in their determined properties.

2 The ExoFAST determined "Time of transit" is listed in MBJD_{TDB}, while the SuperWASP times are listed in MHJD.

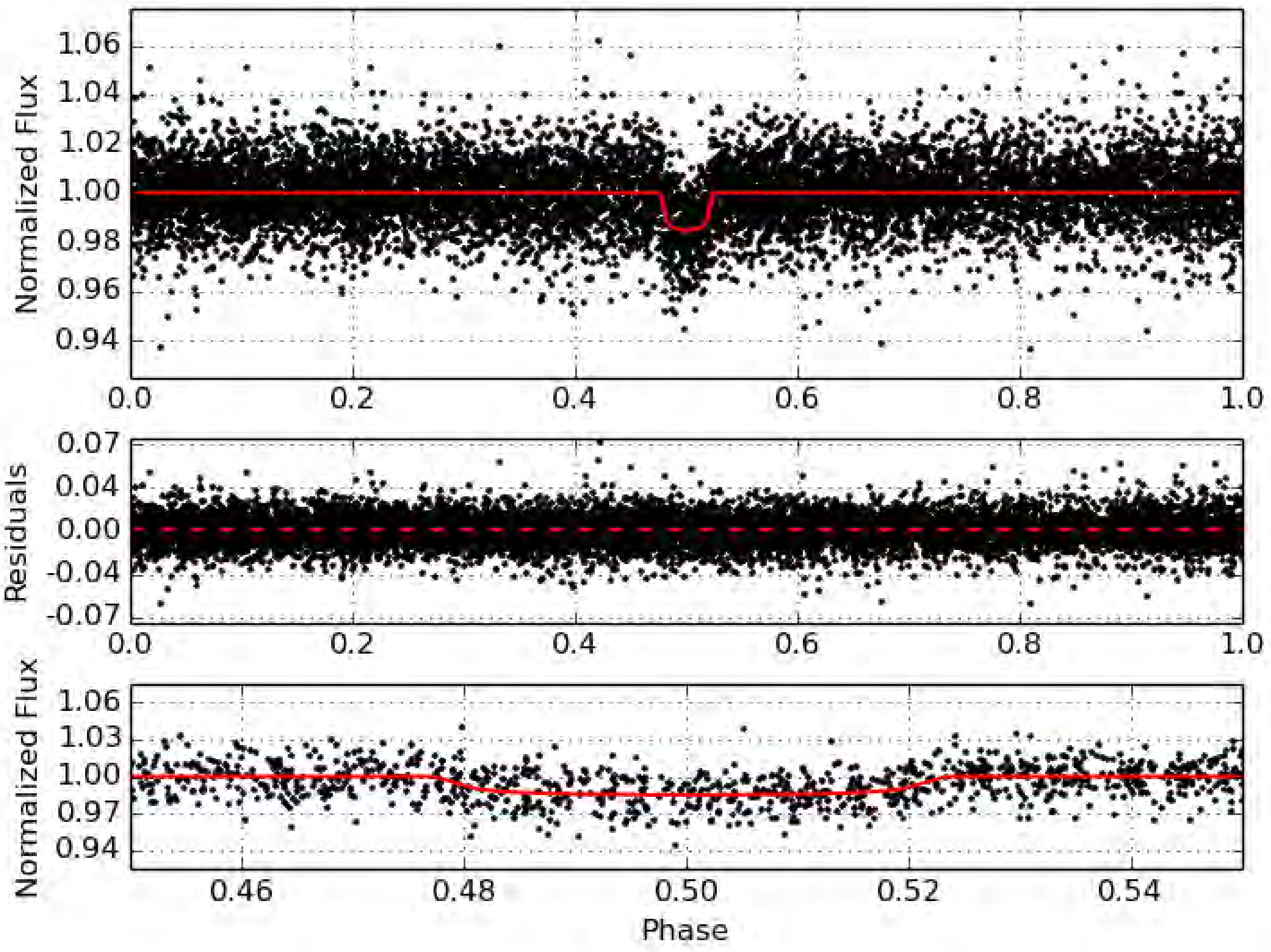

Figure A.8: KELT-South lightcurve of the exoplanet WASP-97b. *Top:* The phase folded KELT-South lightcurve with the best fit transit model as calculated by ExoFAST. *Middle:* Residuals of the best fit model. *Bottom:* Zoomed in view of the transit along with the model.

Table A.10: Table of the ExoFAST determined parameters of WASP-99b compared to the published parameters from Hellier et al. (2014).

Parameter	Units	ExoFAST Value	Published Value
M_*	Mass ($M_\odot$)	$1.29^{+0.73}_{-0.44}$	1.48 ± 0.10
R_*	Radius ($R_\odot$)	$1.54^{+0.27}_{-0.22}$	$1.76^{+0.11}_{-0.06}$
$\log(g_*)$	Surface gravity (cgs)	$4.173^{+0.068}_{-0.064}$	$4.12^{+0.02}_{-0.04}$
[Fe/H]	Metallicity	$0.2^{+2.2}_{-2.1}$	$+0.21 \pm 0.15$
T_{eff}	Effective temperature (K)	6186^{+95}_{-100}	6180 ± 100
P	Period (days)	$5.752680^{+0.000053}_{-0.000076}$	5.75251 ± 0.00004
a	Semi-major axis (AU)	$0.0684^{+0.011}_{-0.0089}$	0.0717 ± 0.0016
R_P	Radius (R_J)	$1.07^{+0.18}_{-0.15}$	$1.10^{+0.08}_{-0.05}$
T_{eq}	Equilibrium Temperature (K)	1414^{+39}_{-35}	1480 ± 40
T_C	Time of transit	$6909.5543^{+0.0088}_{-0.012}$	6224.9824 ± 0.0014
i	Inclination (degrees)	90.0 (adopted)[1]	88.8 ± 1.1
b	Impact Parameter	0.0 (adopted)[1]	0.18 ± 0.17
δ	Transit depth	$0.00508^{+0.00039}_{-0.00040}$	0.0041 ± 0.0002
T_{14}	Total duration (days)	$0.2052^{+0.0100}_{-0.0076}$	0.219 ± 0.003
u_1	linear limb-darkening coefficient	$0.306^{+0.050}_{-0.038}$	
u_2	quadratic limb-darkening coefficient	$0.3108^{+0.011}_{-0.0040}$	

NOTES

1 No spectroscopic follow-up data available for KELT-South team members to better constrain the stellar parameter values, which leads to the large errors in their determined properties.

2 The ExoFAST determined "Time of transit" is listed in $\mathrm{MBJD_{TDB}}$, while the SuperWASP times are listed in MHJD.

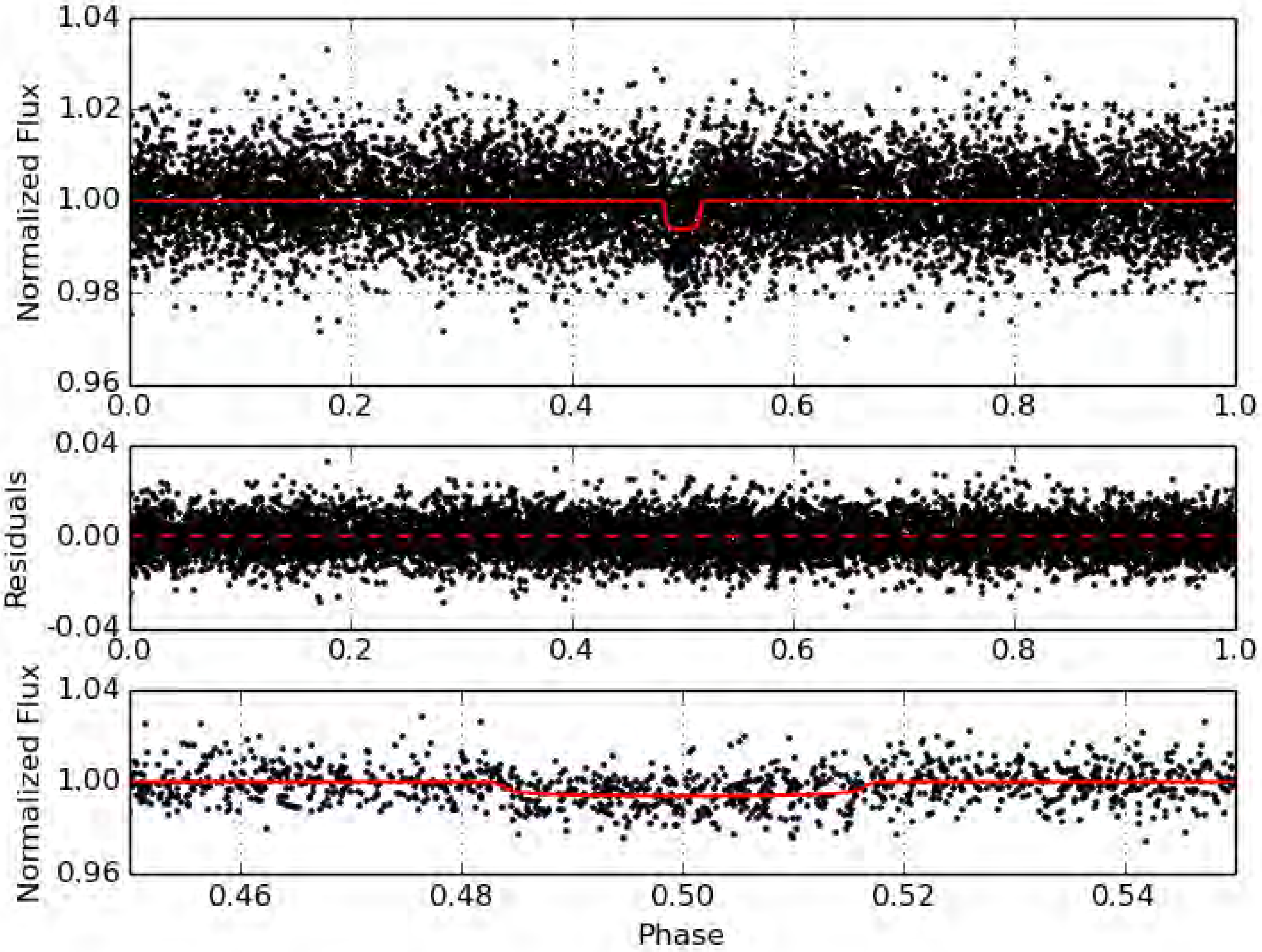

Figure A.9: KELT-South lightcurve of the exoplanet WASP-99b. *Top:* The phase folded KELT-South lightcurve with the best fit transit model as calculated by ExoFAST. *Middle:* Residuals of the best fit model. *Bottom:* Zoomed in view of the transit along with the model.

Table A.11: Table of the ExoFAST determined parameters of WASP-117b compared to the published parameters from Lendl et al. (2014).

Parameter	Units	ExoFAST Value	Published Value
M_*	Mass ($M_\odot$)	$1.16^{+0.70}_{-0.40}$	1.126 ± 0.029
R_*	Radius ($R_\odot$)	$1.33^{+0.25}_{-0.20}$	$1.170^{+0.067}_{-0.059}$
$\log(g_*)$ ...	Surface gravity (cgs)	$4.256^{+0.075}_{-0.071}$	4.28 ± 0.16
[Fe/H] ...	Metallicity	$-0.0^{+2.3}_{-2.1}$	-0.11 ± 0.14
T_{eff}	Effective temperature (K)	6040 ± 100	6040 ± 90
P	Period (days)	10.02081 ± 0.00014	10.02165 ± 0.00055
a	Semi-major axis (AU)	$0.095^{+0.016}_{-0.013}$	$0.09459^{+0.00084}_{-0.00079}$
R_P	Radius (R_J)	$1.10^{+0.20}_{-0.16}$	$1.021^{+0.076}_{-0.065}$
T_{eq}	Equilibrium Temperature (K)	1087^{+30}_{-33}	1024^{+30}_{-26}
T_C	Time of transit	$6904.610^{+0.016}_{-0.015}$	$6533.82326^{+0.00095}_{-0.00090}$
i	Inclination (degrees)	90.0 (adopted)[1]	89.14 ± 0.30
b	Impact Parameter	0.0 (adopted)[1]	$0.32^{+0.09}_{-0.11}$
δ	Transit depth	$0.00726^{+0.00058}_{-0.00055}$	$0.00803^{+0.00055}_{-0.00048}$
T_{14}	Total duration (days)	$0.2249^{+0.0089}_{-0.011}$	$0.2475^{+0.0033}_{-0.0029}$
u_1	linear limb-darkening coefficient ...	$0.315^{+0.069}_{-0.048}$	0.337 ± 0.016
u_2	quadratic limb-darkening coefficient	$0.3087^{+0.0059}_{-0.014}$	0.2997 ± 0.0058

NOTES

1 No spectroscopic follow-up data available for KELT-South team members to better constrain the stellar parameter values, which leads to the large errors in their determined properties.

2 The ExoFAST determined "Time of transit" is listed in $\mathrm{MBJD}_{\mathrm{TDB}}$, while the SuperWASP times are listed in MHJD.

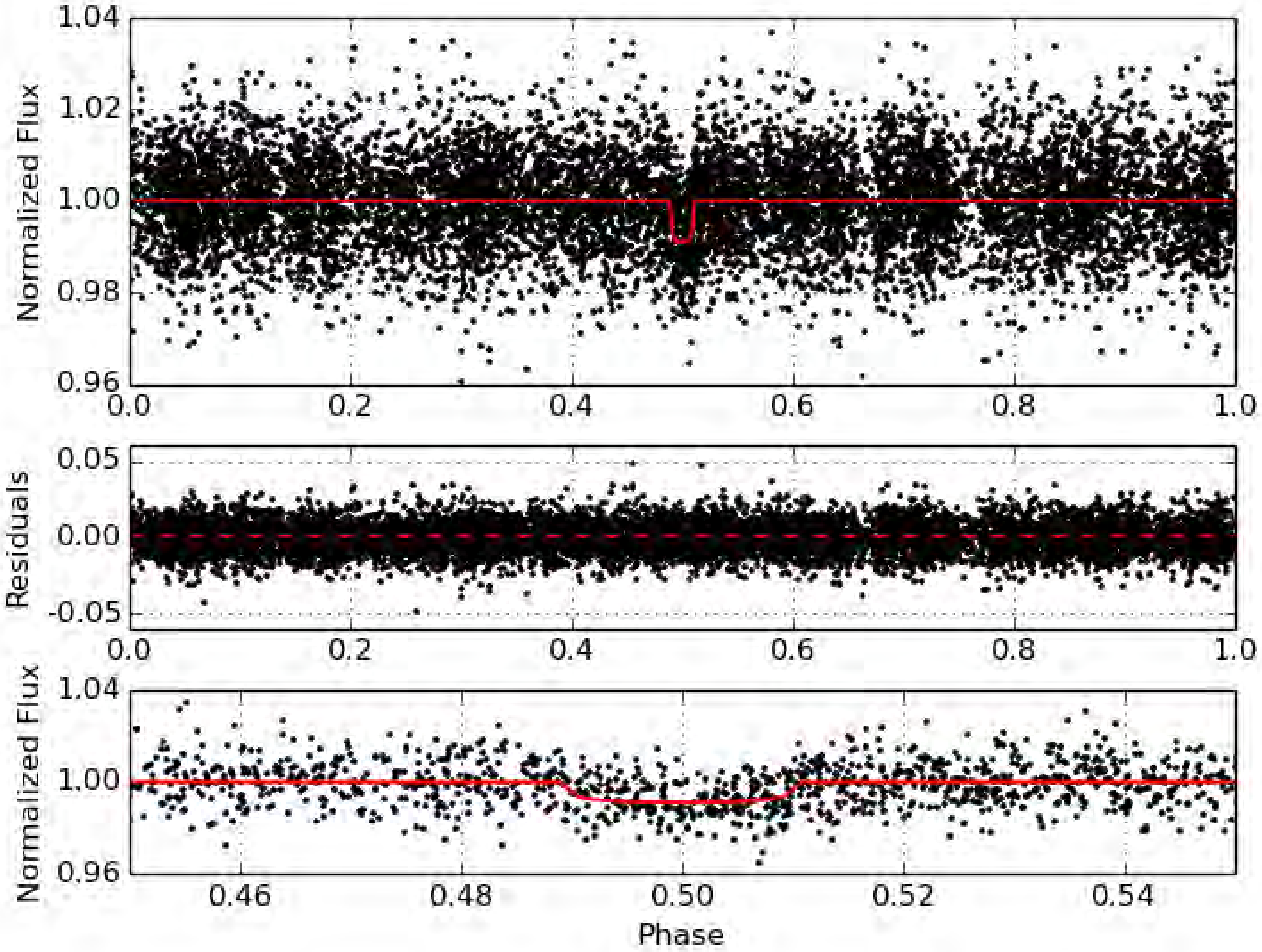

Figure A.10: KELT-South lightcurve of the exoplanet WASP-117b. *Top:* The phase folded KELT-South lightcurve with the best fit transit model as calculated by ExoFAST. *Middle:* Residuals of the best fit model. *Bottom:* Zoomed in view of the transit along with the model.

Bibliography

Addison, B. C., Tinney, C. G., Wright, D. J., Bayliss, D., Zhou, G., Hartman, J. D., Bakos, G. Á., & Schmidt, B. 2013, ArXiv e-prints

Adibekyan, V. Z., Santos, N. C., Sousa, S. G., Israelian, G., Delgado Mena, E., González Hernández, J. I., Mayor, M., Lovis, C., & Udry, S. 2012a, A&A, 543, A89

Adibekyan, V. Z., Sousa, S. G., Santos, N. C., Delgado Mena, E., González Hernández, J. I., Israelian, G., Mayor, M., & Khachatryan, G. 2012b, A&A, 545, A32

Alard, C. 2000, A&AS, 144, 363

Alard, C. & Lupton, R. H. 1998, ApJ, 503, 325

Albrecht, S., Winn, J. N., Johnson, J. A., Howard, A. W., Marcy, G. W., Butler, R. P., Arriagada, P., Crane, J. D., Shectman, S. A., Thompson, I. B., Hirano, T., Bakos, G., & Hartman, J. D. 2012, ApJ, 757, 18

Alcock, C., Allsman, R. A., Axelrod, T. S., Bennett, D. P., Cook, K. H., Park, H. S., Marshall, S. L., Stubbs, C. W., Griest, K., Perlmutter, S., Sutherland, W., Freeman, K. C., Peterson, B. A., Quinn, P. J., & Rodgers, A. W. 1993, in Astronomical Society of the Pacific Conference Series, Vol. 43, Sky Surveys. Protostars to Protogalaxies, ed. B. T. Soifer, 291

Alentiev, D., Kochukhov, O., Ryabchikova, T., Cunha, M., Tsymbal, V., & Weiss, W. 2012, MNRAS, 421, L82

Aller, K. M., Kraus, A. L., Liu, M. C., Burgett, W. S., Chambers, K. C., Hodapp, K. W., Kaiser, N., Magnier, E. A., & Price, P. A. 2013, ApJ, 773, 63

Alonso, R., Auvergne, M., Baglin, A., Ollivier, M., Moutou, C., Rouan, D., Deeg, H. J., Aigrain, S., Almenara, J. M., Barbieri, M., Barge, P., Benz, W., Bordé, P., Bouchy, F., de La Reza, R., Deleuil, M., Dvorak, R., Erikson, A., Fridlund, M., Gillon, M., Gondoin, P., Guillot, T., Hatzes, A., Hébrard, G., Kabath, P., Jorda, L., Lammer, H., Léger, A., Llebaria, A., Loeillet, B., Magain, P., Mayor, M., Mazeh, T., Pätzold, M., Pepe, F., Pont, F., Queloz, D., Rauer, H., Shporer, A., Schneider, J., Stecklum, B., Udry, S., & Wuchterl, G. 2008, A&A, 482, L21

Alonso, R., Moutou, C., Endl, M., Almenara, J.-M., Guenther, E. W., Deleuil, M., Hatzes, A., Aigrain, S., Auvergne, M., Baglin, A., Barge, P., Bonomo, A. S., Bordé, P., Bouchy, F., Cavarroc, C., Cabrera, J., Carpano, S., Csizmadia, S., Cochran, W. D., Deeg, H. J., Díaz, R. F., Dvorak, R., Erikson, A., Ferraz-Mello, S., Fridlund, M., Fruth, T., Gandolfi, D., Gillon, M., Grziwa, S., Guillot, T., Hébrard, G., Jorda, L., Léger, A., Lammer, H., Lovis, C., MacQueen, P. J., Mazeh, T., Ofir, A., Ollivier, M., Pasternacki, T., Pätzold, M., Queloz, D., Rauer, H., Rouan, D., Santerne, A., Schneider, J., Tadeu dos Santos, M., Tingley, B., Titz-Weider, R., Weingrill, J., & Wuchterl, G. 2014, A&A, 567, A112

Alsubai, K. A., Parley, N. R., Bramich, D. M., Horne, K., Collier Cameron, A., West, R. G., Sorensen, P. M., Pollacco, D., Smith, J. C., & Fors, O. 2013, Acta. Astron., 63, 465

Alsubai, K. A., Parley, N. R., Bramich, D. M., West, R. G., Sorensen, P. M., Collier Cameron, A., Latham, D. W., Horne, K., Anderson, D. R., Bakos, G. Á., Brown, D. J. A., Buchhave, L. A., Esquerdo, G. A., Everett, M. E., Fżrész, G., Hartman, J. D., Hellier, C., Miller, G. M., Pollacco, D., Quinn, S. N., Smith, J. C., Stefanik, R. P., & Szentgyorgyi, A. 2011, MNRAS, 417, 709

Anderson, D. R., Hellier, C., Gillon, M., Triaud, A. H. M. J., Smalley, B., Hebb, L., Collier Cameron, A., Maxted, P. F. L., Queloz, D., West, R. G., Bentley, S. J., Enoch, B., Horne, K., Lister, T. A., Mayor, M., Parley, N. R., Pepe, F., Pollacco, D., Ségransan, D., Udry, S., & Wilson, D. M. 2010, ApJ, 709, 159

Anderson, D. R., Smith, A. M. S., Lanotte, A. A., Barman, T. S., Collier Cameron, A., Campo, C. J., Gillon, M., Harrington, J., Hellier, C., Maxted, P. F. L., Queloz, D., Triaud, A. H. M. J., & Wheatley, P. J. 2011, MNRAS, 416, 2108

Arras, P. & Socrates, A. 2010, ApJ, 714, 1

Auvergne, M., Bodin, P., Boisnard, L., Buey, J.-T., Chaintreuil, S., Epstein, G., Jouret, M., Lam-Trong, T., Levacher, P., Magnan, A., Perez, R., Plasson, P., Plesseria, J., Peter, G., Steller, M., Tiphène, D., Baglin, A., Agogué, P., Appourchaux, T., Barbet, D., Beaufort, T., Bellenger, R., Berlin, R., Bernardi, P., Blouin, D., Boumier, P., Bonneau, F., Briet, R., Butler, B., Cautain, R., Chiavassa, F., Costes, V., Cuvilho, J., Cunha-Parro, V., de Oliveira Fialho, F., Decaudin, M., Defise, J.-M., Djalal, S., Docclo, A., Drummond, R., Dupuis, O., Exil, G., Fauré, C., Gaboriaud, A., Gamet, P., Gavalda, P., Grolleau, E., Gueguen, L., Guivarc'h, V., Guterman, P., Hasiba, J., Huntzinger, G., Hustaix, H., Imbert, C., Jeanville, G., Johlander, B., Jorda, L., Journoud, P., Karioty, F., Kerjean, L., Lafond, L., Lapeyrere, V., Landiech, P., Larqué, T., Laudet, P., Le Merrer, J., Leporati, L., Leruyet, B., Levieuge, B., Llebaria, A., Martin, L., Mazy, E., Mesnager, J.-M., Michel, J.-P., Moalic, J.-P., Monjoin, W., Naudet, D., Neukirchner, S., Nguyen-Kim, K., Ollivier, M., Orcesi, J.-L., Ottacher, H., Oulali, A., Parisot, J., Perruchot, S., Piacentino, A., Pinheiro da Silva, L., Platzer, J., Pontet, B., Pradines, A., Quentin, C., Rohbeck, U., Rolland, G., Rollenhagen, F., Romagnan, R., Russ, N., Samadi, R., Schmidt, R., Schwartz, N., Sebbag, I., Smit, H., Sunter, W., Tello, M., Toulouse, P., Ulmer, B., Vandermarcq, O., Vergnault, E., Wallner, R., Waultier, G., & Zanatta, P. 2009, A&A, 506, 411

Baglin, A. 2003, Advances in Space Research, 31, 345

Bakos, G., Noyes, R. W., Kovács, G., Stanek, K. Z., Sasselov, D. D., & Domsa, I. 2004, PASP, 116, 266

Bakos, G. Á., Csubry, Z., Penev, K., Bayliss, D., Jordán, A., Afonso, C., Hartman, J. D., Henning, T., Kovács, G., Noyes, R. W., Béky, B., Suc, V., Csák, B., Rabus, M., Lázár, J., Papp, I., Sári, P., Conroy, P., Zhou, G., Sackett, P. D., Schmidt, B., Mancini, L., Sasselov, D. D., & Ueltzhoeffer, K. 2013, PASP, 125, 154

Barclay, T., Rowe, J. F., Lissauer, J. J., Huber, D., Fressin, F., Howell, S. B., Bryson, S. T., Chaplin, W. J., Désert, J.-M., Lopez, E. D., Marcy, G. W., Mullally, F., Ragozzine, D., Torres, G., Adams, E. R., Agol, E., Barrado, D., Basu, S., Bedding, T. R., Buchhave, L. A., Charbonneau, D., Christiansen, J. L., Christensen-Dalsgaard, J., Ciardi, D., Cochran, W. D., Dupree, A. K., Elsworth, Y., Everett, M., Fischer, D. A., Ford, E. B., Fortney, J. J., Geary, J. C., Haas, M. R., Handberg, R., Hekker, S., Henze, C. E., Horch, E., Howard, A. W., Hunter, R. C., Isaacson, H., Jenkins, J. M., Karoff, C., Kawaler, S. D., Kjeldsen, H., Klaus, T. C., Latham, D. W., Li, J., Lillo-Box, J., Lund, M. N., Lundkvist, M., Metcalfe, T. S., Miglio, A., Morris, R. L., Quintana, E. V., Stello, D., Smith, J. C., Still, M., & Thompson, S. E. 2013, Nature, 494, 452

Barge, P., Baglin, A., Auvergne, M., Rauer, H., Léger, A., Schneider, J., Pont, F., Aigrain, S., Almenara, J.-M., Alonso, R., Barbieri, M., Bordé, P., Bouchy, F., Deeg, H. J., La Reza, D., Deleuil, M., Dvorak, R., Erikson, A., Fridlund, M., Gillon, M., Gondoin, P., Guillot, T., Hatzes, A., Hebrard, G., Jorda, L., Kabath, P., Lammer, H., Llebaria, A., Loeillet, B., Magain, P., Mazeh, T., Moutou, C., Ollivier, M., Pätzold, M., Queloz, D., Rouan, D., Shporer, A., & Wuchterl, G. 2008, A&A, 482, L17

Barnes, S. A. 2003, ApJ, 586, 464

—. 2007, ApJ, 669, 1167

Barrado y Navascués, D., Stauffer, J. R., & Jayawardhana, R. 2004, ApJ, 614, 386

Barros, S. C. C., Faedi, F., Collier Cameron, A., Lister, T. A., McCormac, J., Pollacco, D., Simpson, E. K., Smalley, B., Street, R. A., Todd, I., Triaud, A. H. M. J., Boisse, I., Bouchy, F., Hébrard, G., Moutou, C., Pepe, F., Queloz, D., Santerne, A., Segransan, D., Udry, S., Bento, J., Butters, O. W., Enoch, B., Haswell, C. A., Hellier, C., Keenan, F. P., Miller, G. R. M., Moulds, V., Norton, A. J., Parley, N., Skillen, I., Watson, C. A., West, R. G., & Wheatley, P. J. 2011, A&A, 525, A54

Batygin, K. & Stevenson, D. J. 2010, ApJ, 714, L238

Batygin, K., Stevenson, D. J., & Bodenheimer, P. H. 2011, ApJ, 738, 1

Bayliss, D., Zhou, G., Penev, K., Bakos, G., Hartman, J., Jordán, A., Mancini, L., Mohler, M., Suc, V., Rabus, M., Béky, B., Csubry, Z., Buchhave, L., Henning, T., Nikolov, N., Csák, B., Brahm, R., Espinoza, N., Noyes, R., Schmidt, B., Conroy, P., Wright, D., Tinney, C., Addison, B., Sackett, P., Sasselov, D., Lázár, J., Papp, I., & Sári, P. 2013, ArXiv e-prints

Bayliss, D. D. R. & Sackett, P. D. 2011, ApJ, 743, 103

Beatty, T. G. & Gaudi, B. S. 2008, ApJ, 686, 1302

Beatty, T. G., Pepper, J., Siverd, R. J., Eastman, J. D., Bieryla, A., Latham, D. W., Buchhave, L. A., Jensen, E. L. N., Manner, M., Stassun, K. G., Gaudi, B. S., Berlind, P., Calkins, M. L., Collins, K., DePoy, D. L., Esquerdo, G. A., Fulton, B. J., Fűrész, G., Geary, J. C., Gould, A., Hebb, L., Kielkopf, J. F., Marshall, J. L., Pogge, R., Stanek, K. Z., Stefanik, R. P., Street, R., Szentgyorgyi, A. H., Trueblood, M., Trueblood, P., & Stutz, A. M. 2012, ApJ, 756, L39

Beaugé, C. & Nesvorný, D. 2013, ApJ, 763, 12

Bechter, E. B., Crepp, J. R., Ngo, H., Knutson, H. A., Batygin, K., Hinkley, S., Muirhead, P. S., Johnson, J. A., Howard, A. W., Montet, B. T., Matthews, C. T., & Morton, T. D. 2014, ApJ, 788, 2

Bergfors, C., Brandner, W., Daemgen, S., Biller, B., Hippler, S., Janson, M., Kudryavtseva, N., Geißler, K., Henning, T., & Köhler, R. 2013, MNRAS, 428, 182

Bertin, E. & Arnouts, S. 1996, A&AS, 117, 393

Bessell, M. S. 2005, ARA&A, 43, 293

Beuermann, K., Buhlmann, J., Diese, J., Dreizler, S., Hessman, F. V., Husser, T.-O., Miller, G. F., Nickol, N., Pons, R., Ruhr, D., Schmülling, H., Schwope, A. D., Sorge, T., Ulrichs, L., Winget, D. E., & Winget, K. I. 2011, A&A, 526, A53

Beuermann, K., Dreizler, S., Hessman, F. V., & Deller, J. 2012, A&A, 543, A138

Beuermann, K., Hessman, F. V., Dreizler, S., Marsh, T. R., Parsons, S. G., Winget, D. E., Miller, G. F., Schreiber, M. R., Kley, W., Dhillon, V. S., Littlefair, S. P., Copperwheat, C. M., & Hermes, J. J. 2010, A&A, 521, L60

Beuzit, J.-L., Feldt, M., Dohlen, K., Mouillet, D., Puget, P., Antichi, J., Baudoz, P., Boccaletti, A., Carbillet, M., Charton, J., Claudi, R., Fusco, T., Gratton, R., Henning, T., Hubin, N., Joos, F., Kasper, M., Langlois, M., Moutou, C., Pragt, J., Rabou, P., Saisse, M., Schmid, H. M., Turatto, M., Udry, S., Vakili, F., Waters, R., & Wildi, F. 2007, in In the Spirit of Bernard Lyot: The Direct Detection of Planets and Circumstellar Disks in the 21st Century

Blomme, J., Sarro, L. M., O'Donovan, F. T., Debosscher, J., Brown, T., Lopez, M., Dubath, P., Rimoldini, L., Charbonneau, D., Dunham, E., Mandushev, G., Ciardi, D. R., De Ridder, J., & Aerts, C. 2011, MNRAS, 418, 96

Bodenheimer, P., Lin, D. N. C., & Mardling, R. A. 2001, ApJ, 548, 466

Borucki, W., Koch, D., Batalha, N., Caldwell, D., Christensen-Dalsgaard, J., Cochran, W. D., Dunham, E., Gautier, T. N., Geary, J., Gilliland, R., Jenkins, J., Kjeldsen, H., Lissauer, J. J., & Rowe, J. 2009, in IAU Symposium, Vol. 253, IAU Symposium, ed. F. Pont, D. Sasselov, & M. J. Holman, 289–299

Borucki, W. J., Koch, D. G., Batalha, N., Bryson, S. T., Rowe, J., Fressin, F., Torres, G., Caldwell, D. A., Christensen-Dalsgaard, J., Cochran, W. D., DeVore, E., Gautier, T. N., Geary, J. C., Gilliland, R., Gould, A., Howell, S. B., Jenkins, J. M., Latham, D. W., Lissauer, J. J., Marcy, G. W., Sasselov, D., Boss, A., Charbonneau, D., Ciardi, D., Kaltenegger, L., Doyle, L., Dupree, A. K., Ford, E. B., Fortney, J., Holman, M. J., Steffen, J. H., Mullally, F., Still, M., Tarter, J., Ballard, S., Buchhave, L. A., Carter, J., Christiansen, J. L., Demory, B.-O., Désert, J.-M., Dressing, C., Endl, M., Fabrycky, D., Fischer, D., Haas, M. R., Henze, C., Horch, E., Howard, A. W., Isaacson, H., Kjeldsen, H., Johnson, J. A., Klaus, T., Kolodziejczak, J., Barclay, T., Li, J., Meibom, S., Prsa, A., Quinn, S. N., Quintana, E. V., Robertson, P., Sherry, W., Shporer, A., Tenenbaum, P., Thompson, S. E., Twicken, J. D., Van Cleve, J., Welsh, W. F., Basu, S., Chaplin, W., Miglio, A., Kawaler, S. D., Arentoft, T., Stello, D., Metcalfe, T. S., Verner, G. A., Karoff, C., Lundkvist, M., Lund, M. N., Handberg, R., Elsworth, Y., Hekker, S., Huber, D., Bedding, T. R., & Rapin, W. 2012, ApJ, 745, 120

Borucki, W. J. & Summers, A. L. 1984, Icarus, 58, 121

Boss, A. P. 1997, Science, 276, 1836

Brown, T. M. 2001, ApJ, 553, 1006

Brown, T. M. & Charbonneau, D. 2000, in Astronomical Society of the Pacific Conference Series, Vol. 219, Disks, Planetesimals, and Planets, ed. G. Garzón, C. Eiroa, D. de Winter, & T. J. Mahoney, 584

Bryan, M. L., Alsubai, K. A., Latham, D. W., Parley, N. R., Collier Cameron, A., Quinn, S. N., Carter, J. A., Fulton, B. J., Berlind, P., Brown, W. R., Buchhave, L. A., Calkins, M. L., Esquerdo, G. A., Fűrész, G., Gråe Jørgensen, U., Horne, K. D., Stefanik, R. P., Street, R. A., Torres, G., West, R. G., Dominik, M., Harpsøe, K. B. W., Liebig, C., Calchi Novati, S., Ricci, D., & Skottfelt, J. F. 2012, ApJ, 750, 84

Buchhave, L. A., Latham, D. W., Johansen, A., Bizzarro, M., Torres, G., Rowe, J. F., Batalha, N. M., Borucki, W. J., Brugamyer, E., Caldwell, C., Bryson, S. T., Ciardi, D. R., Cochran, W. D., Endl, M., Esquerdo, G. A., Ford, E. B., Geary, J. C., Gilliland, R. L., Hansen, T., Isaacson, H., Laird, J. B., Lucas, P. W., Marcy, G. W., Morse, J. A., Robertson, P., Shporer, A., Stefanik, R. P., Still, M., & Quinn, S. N. 2012, Nature, 486, 375

Burke, C. J., Gaudi, B. S., DePoy, D. L., & Pogge, R. W. 2006, AJ, 132, 210

Cameron, A. C. 2012, Nature, 492, 48

Campbell, B., Walker, G. A. H., & Yang, S. 1988, ApJ, 331, 902

Cargile, P. A., James, D. J., Pepper, J., Kuhn, R. B., Siverd, R., & Stassun, K. G. 2014, ApJ, 782, 29

Catala, L., Crawford, S. M., Buckley, D. A. H., Pickering, T., Wilson, R., Butterley, T., Shepherd, H., Marang, F., Matshaya, P., & Fourie, C. 2013, ArXiv e-prints

Charbonneau, D., Brown, T. M., Latham, D. W., & Mayor, M. 2000, ApJ, 529, L45

Charbonneau, D., Brown, T. M., Noyes, R. W., & Gilliland, R. L. 2002, ApJ, 568, 377

Christiansen, J. L., Derekas, A., Kiss, L. L., Ashley, M. C. B., Curran, S. J., Hamacher, D. W., Hidas, M. G., Thompson, M. R., Webb, J. K., & Young, T. B. 2008, MNRAS, 385, 1749

Ciccarelli, A. S., Davis, W. V., Des Jardin, W., Doan, H., Meisenzahl, E. J., Pace, L. J., Putnam, G. G., Shepherd, J. E., Stevens, E. G., Summa, J. R., & Wetzel, K. 2002, in Society of Photo-Optical Instrumentation Engineers (SPIE) Conference Series, Vol. 4669, Sensors and Camera Systems for Scientific, Industrial, and Digital Photography Applications III, ed. M. M. Blouke, J. Canosa, & N. Sampat, 153–160

Claret, A. 2000, A&A, 363, 1081

—. 2004, A&A, 428, 1001

Claret, A. & Bloemen, S. 2011, A&A, 529, A75

Collier Cameron, A., Pollacco, D., Hellier, C., West, R., WASP Consortium, & SOPHIE and CORALIE Planet-Search Teams. 2009, in IAU Symposium, Vol. 253, IAU Symposium, ed. F. Pont, D. Sasselov, & M. J. Holman, 29–35

Collier Cameron, A., Wilson, D. M., West, R. G., Hebb, L., Wang, X.-B., Aigrain, S., Bouchy, F., Christian, D. J., Clarkson, W. I., Enoch, B., Esposito, M., Guenther, E., Haswell, C. A., Hébrard, G., Hellier, C., Horne, K., Irwin, J., Kane, S. R., Loeillet, B., Lister, T. A., Maxted, P., Mayor, M., Moutou, C., Parley, N., Pollacco, D., Pont, F., Queloz, D., Ryans, R., Skillen, I., Street, R. A., Udry, S., & Wheatley, P. J. 2007, MNRAS, 380, 1230

Collins, K. A., Eastman, J. D., Beatty, T. G., Siverd, R. J., Gaudi, B. S., Pepper, J., Kielkopf, J. F., Johnson, J. A., Howard, A. W., Fischer, D. A., Manner, M., Bieryla, A., Latham, D. W., Fulton, B. J., Gregorio, J., Buchhave, L. A., Jensen, E. L. N., Stassun, K. G., Penev, K., Crepp, J. R., Hinkley, S., Street, R. A., Cargile, P., Mack, C. E., Oberst, T. E., Avril, R. L., Mellon, S. N., McLeod, K. K., Penny, M. T., Stefanik, R. P., Berlind, P., Calkins, M. L., Mao, Q., Richert, A. J. W., DePoy, D. L., Esquerdo, G. A., Gould, A., Marshall, J. L., Oelkers, R. J., Pogge, R. W., Trueblood, M., & Trueblood, P. 2013, ArXiv e-prints

Cosentino, R., Lovis, C., Pepe, F., Collier Cameron, A., Latham, D. W., Molinari, E., Udry, S., Bezawada, N., Black, M., Born, A., Buchschacher, N., Charbonneau, D., Figueira, P., Fleury, M., Galli, A., Gallie, A., Gao, X., Ghedina, A., Gonzalez, C., Gonzalez, M., Guerra, J., Henry, D., Horne, K., Hughes, I., Kelly, D., Lodi, M., Lunney, D., Maire, C., Mayor, M., Micela, G., Ordway, M. P., Peacock, J., Phillips, D., Piotto, G., Pollacco, D., Queloz, D., Rice, K., Riverol, C., Riverol, L., San Juan, J., Sasselov, D., Segransan, D., Sozzetti, A., Sosnowska, D., Stobie, B., Szentgyorgyi, A., Vick, A., & Weber, L. 2012, in Society of Photo-Optical Instrumentation Engineers (SPIE) Conference Series, Vol. 8446, Society of Photo-Optical Instrumentation Engineers (SPIE) Conference Series

Cumming, A., Butler, R. P., Marcy, G. W., Vogt, S. S., Wright, J. T., & Fischer, D. A. 2008, PASP, 120, 531

Dawson, R. I. & Murray-Clay, R. A. 2013, ApJ, 767, L24

Dekany, R., Roberts, J., Burruss, R., Bouchez, A., Truong, T., Baranec, C., Guiwits, S., Hale, D., Angione, J., Trinh, T., Zolkower, J., Shelton, J. C., Palmer, D., Henning, J., Croner, E., Troy, M., McKenna, D., Tesch, J., Hildebrandt, S., & Milburn, J. 2013, ApJ, 776, 130

Des Jardin, W. & Kosman, S. L. 1999, in Society of Photo-Optical Instrumentation Engineers (SPIE) Conference Series, Vol. 3649, Sensors, Cameras, and Systems for Scientific/Industrial Applications, ed. M. M. Blouke & G. M. Williams, 74–79

Devor, J. 2005, ApJ, 628, 411

Dopita, M., Hart, J., McGregor, P., Oates, P., Bloxham, G., & Jones, D. 2007, Ap&SS, 310, 255

Doyle, L. R., Carter, J. A., Fabrycky, D. C., Slawson, R. W., Howell, S. B., Winn, J. N., Orosz, J. A., Prsa, A., Welsh, W. F., Quinn, S. N., Latham, D., Torres, G., Buchhave, L. A., Marcy, G. W., Fortney, J. J., Shporer, A., Ford, E. B., Lissauer, J. J., Ragozzine, D., Rucker, M., Batalha, N., Jenkins, J. M., Borucki, W. J., Koch, D., Middour, C. K., Hall, J. R., McCauliff, S., Fanelli, M. N., Quintana, E. V., Holman, M. J., Caldwell, D. A., Still, M., Stefanik, R. P., Brown, W. R., Esquerdo, G. A., Tang, S., Furesz, G., Geary, J. C., Berlind, P., Calkins, M. L., Short, D. R., Steffen, J. H., Sasselov, D., Dunham, E. W., Cochran, W. D., Boss, A., Haas, M. R., Buzasi, D., & Fischer, D. 2011, Science, 333, 1602

Dragomir, D., Kane, S. R., Henry, G. W., Ciardi, D. R., Fischer, D. A., Howard, A. W., Jensen, E. L. N., Laughlin, G., Mahadevan, S., Matthews, J. M., Pilyavsky, G., von Braun, K., Wang, S. X., & Wright, J. T. 2012, ApJ, 754, 37

Drake, A. J. 2003, ApJ, 589, 1020

Dunham, E. W., Mandushev, G. I., Taylor, B. W., & Oetiker, B. 2004, PASP, 116, 1072

Eastman, J., Gaudi, B. S., & Agol, E. 2013, PASP, 125, 83

Enoch, B., Cameron, A. C., Anderson, D. R., Lister, T. A., Hellier, C., Maxted, P. F. L., Queloz, D., Smalley, B., Triaud, A. H. M. J., West, R. G., Brown, D. J. A., Gillon, M., Hebb, L., Lendl, M., Parley, N., Pepe, F., Pollacco, D., Segransan, D., Simpson, E., Street, R. A., & Udry, S. 2011, MNRAS, 410, 1631

Enoch, B., Haswell, C. A., Norton, A. J., Collier-Cameron, A., West, R. G., Smith, A. M. S., & Parley, N. R. 2012, A&A, 548, A48

Faigler, S., Tal-Or, L., Mazeh, T., Latham, D. W., & Buchhave, L. A. 2013, ApJ, 771, 26

Fischer, D. A. & Valenti, J. 2005, ApJ, 622, 1102

Fischer, D. A., Vogt, S. S., Marcy, G. W., Butler, R. P., Sato, B., Henry, G. W., Robinson, S., Laughlin, G., Ida, S., Toyota, E., Omiya, M., Driscoll, P., Takeda, G., Wright, J. T., & Johnson, J. A. 2007, ApJ, 669, 1336

Ford, E. B. & Rasio, F. A. 2006, ApJ, 638, L45

—. 2008, ApJ, 686, 621

Fressin, F., Torres, G., Désert, J.-M., Charbonneau, D., Batalha, N. M., Fortney, J. J., Rowe, J. F., Allen, C., Borucki, W. J., Brown, T. M., Bryson, S. T., Ciardi, D. R., Cochran, W. D., Deming, D., Dunham, E. W., Fabrycky, D. C., Gautier, III, T. N., Gilliland, R. L., Henze, C. E., Holman, M. J., Howell, S. B., Jenkins, J. M., Kinemuchi, K., Knutson, H., Koch, D. G., Latham, D. W., Lissauer, J. J., Marcy, G. W., Ragozzine, D., Sasselov, D. D., Still, M., Tenenbaum, P., & Uddin, K. 2011, ApJS, 197, 5

Fressin, F., Torres, G., Rowe, J. F., Charbonneau, D., Rogers, L. A., Ballard, S., Batalha, N. M., Borucki, W. J., Bryson, S. T., Buchhave, L. A., Ciardi, D. R., Désert, J.-M., Dressing, C. D., Fabrycky, D. C., Ford, E. B., Gautier, III, T. N., Henze, C. E., Holman, M. J., Howard, A., Howell, S. B., Jenkins, J. M., Koch, D. G., Latham, D. W., Lissauer, J. J., Marcy, G. W., Quinn, S. N., Ragozzine, D., Sasselov, D. D., Seager, S., Barclay, T., Mullally, F., Seader, S. E., Still, M., Twicken, J. D., Thompson, S. E., & Uddin, K. 2012, Nature, 482, 195

Fruth, T., Cabrera, J., Chini, R., Csizmadia, S., Dreyer, C., Eigmüller, P., Erikson, A., Kabath, P., Kirste, S., Lemke, R., Murphy, M., Pasternacki, T., Rauer, H., & Titz-Weider, R. 2013, AJ, 146, 136

Fukugita, M., Ichikawa, T., Gunn, J. E., Doi, M., Shimasaku, K., & Schneider, D. P. 1996, AJ, 111, 1748

Gandolfi, D., Hébrard, G., Alonso, R., Deleuil, M., Guenther, E. W., Fridlund, M., Endl, M., Eigmüller, P., Csizmadia, S., Havel, M., Aigrain, S., Auvergne, M., Baglin, A., Barge, P., Bonomo, A. S., Bordé, P., Bouchy, F., Bruntt, H., Cabrera, J., Carpano, S., Carone, L., Cochran, W. D., Deeg, H. J., Dvorak, R., Eislöffel, J., Erikson, A., Ferraz-Mello, S., Gazzano, J.-C., Gibson, N. B., Gillon, M., Gondoin, P., Guillot, T., Hartmann, M., Hatzes, A., Jorda, L., Kabath, P., Léger, A., Llebaria, A., Lammer, H., MacQueen, P. J., Mayor, M., Mazeh, T., Moutou, C., Ollivier, M., Pätzold, M., Pepe, F., Queloz, D., Rauer, H., Rouan, D., Samuel, B., Schneider, J., Stecklum, B., Tingley, B., Udry, S., & Wuchterl, G. 2010, A&A, 524, A55

Gaudi, B. S. & Winn, J. N. 2007, ApJ, 655, 550

Gazak, J. Z., Johnson, J. A., Tonry, J., Dragomir, D., Eastman, J., Mann, A. W., & Agol, E. 2012, Advances in Astronomy, 2012

Ge, J., Mahadevan, S., Lee, B., Wan, X., Zhao, B., van Eyken, J., Kane, S., Guo, P., Ford, E., Fleming, S., Crepp, J., Cohen, R., Groot, J., Galvez, M. C., Liu, J., Agol, E., Gaudi, S., Ford, H., Schneider, D., Seager, S., Weinberg, D., & Eisenstein, D. 2008, in Astronomical Society of the Pacific Conference Series, Vol. 398, Extreme Solar Systems, ed. D. Fischer, F. A. Rasio, S. E. Thorsett, & A. Wolszczan, 449

Ghezzi, L., Cunha, K., Smith, V. V., de Araújo, F. X., Schuler, S. C., & de la Reza, R. 2010, ApJ, 720, 1290

Gómez Maqueo Chew, Y., Faedi, F., Pollacco, D., Brown, D. J. A., Doyle, A. P., Collier Cameron, A., Gillon, M., Lendl, M., Smalley, B., Triaud, A. H. M. J., West, R. G., Wheatley, P. J., Busuttil, R., Liebig, C., Anderson, D. R., Armstrong, D. J., Barros, S. C. C., Bento, J., Bochinski, J., Burwitz, V., Delrez, L., Enoch, B., Fumel, A., Haswell, C. A., Hébrard, G., Hellier, C., Holmes, S., Jehin, E., Kolb, U., McCormac, J., Miller, G. R. M., Norton, A. J., Pepe, F., Queloz, D., Rodríguez, J., Ségransan, D., Skillen, I., Stassun, K. G., Udry, S., & Watson, C. A. 2013, ArXiv e-prints

Gonzalez, G. 1998, A&A, 334, 221

Gonzalez, G., Laws, C., Tyagi, S., & Reddy, B. E. 2001, AJ, 121, 432

González Hernández, J. I., Delgado-Mena, E., Sousa, S. G., Israelian, G., Santos, N. C., Adibekyan, V. Z., & Udry, S. 2013, A&A, 552, A6

Gould, A., Dorsher, S., Gaudi, B. S., & Udalski, A. 2006, Acta. Astron., 56, 1

Gould, A. & Morgan, C. W. 2003, ApJ, 585, 1056

Graham, J. R., Macintosh, B., Doyon, R., Gavel, D., Larkin, J., Levine, M., Oppenheimer, B., Palmer, D., Saddlemyer, L., Sivaramakrishnan, A., Veran, J.-P., & Wallace, K. 2007, ArXiv e-prints

Grziwa, S., Pätzold, M., & Carone, L. 2012, MNRAS, 420, 1045

Guillot, T. 2005, Annual Review of Earth and Planetary Sciences, 33, 493

Hartman, J. D., Bakos, G., Stanek, K. Z., & Noyes, R. W. 2004, AJ, 128, 1761

Hartman, J. D., Bakos, G. Á., Noyes, R. W., Sipőcz, B., Kovács, G., Mazeh, T., Shporer, A., & Pál, A. 2011a, AJ, 141, 166

Hartman, J. D., Bakos, G. Á., Torres, G., Kovács, G., Johnson, J. A., Howard, A. W., Marcy, G. W., Latham, D. W., Bieryla, A., Buchhave, L. A., Bhatti, W., Béky, B., Csubry, Z., Penev, K., de Val-Borro, M., Noyes, R. W., Fischer, D. A., Esquerdo, G. A., Everett, M., Szklenár, T., Zhou, G., Bayliss, D., Shporer, A., Fulton, B. J., Sanchis-Ojeda, R., Falco, E., Lázár, J., Papp, I., & Sári, P. 2013, ArXiv e-prints

Hartman, J. D., Bakos, G. Á., Torres, G., Latham, D. W., Kovács, G., Béky, B., Quinn, S. N., Mazeh, T., Shporer, A., Marcy, G. W., Howard, A. W., Fischer, D. A., Johnson, J. A., Esquerdo, G. A., Noyes, R. W., Sasselov, D. D., Stefanik, R. P., Fernandez, J. M., Szklenár, T., Lázár, J., Papp, I., & Sári, P. 2011b, ApJ, 742, 59

Hartman, J. D., Gaudi, B. S., Holman, M. J., McLeod, B. A., Stanek, K. Z., Barranco, J. A., Pinsonneault, M. H., & Kalirai, J. S. 2008, ApJ, 675, 1254

Hatzes, A. P., Cochran, W. D., Endl, M., McArthur, B., Paulson, D. B., Walker, G. A. H., Campbell, B., & Yang, S. 2003, ApJ, 599, 1383

Hebb, L., Collier-Cameron, A., Loeillet, B., Pollacco, D., Hébrard, G., Street, R. A., Bouchy, F., Stempels, H. C., Moutou, C., Simpson, E., Udry, S., Joshi, Y. C., West, R. G., Skillen, I., Wilson, D. M., McDonald, I., Gibson, N. P., Aigrain, S., Anderson, D. R., Benn, C. R., Christian, D. J., Enoch, B., Haswell, C. A., Hellier, C., Horne, K., Irwin, J., Lister, T. A., Maxted, P., Mayor, M., Norton, A. J., Parley, N., Pont, F., Queloz, D., Smalley, B., & Wheatley, P. J. 2009, ApJ, 693, 1920

Hebb, L., Collier-Cameron, A., Triaud, A. H. M. J., Lister, T. A., Smalley, B., Maxted, P. F. L., Hellier, C., Anderson, D. R., Pollacco, D., Gillon, M., Queloz, D., West, R. G., Bentley, S., Enoch, B., Haswell, C. A., Horne, K., Mayor, M., Pepe, F., Segransan, D., Skillen, I., Udry, S., & Wheatley, P. J. 2010, ApJ, 708, 224

Hébrard, G., Ehrenreich, D., Bouchy, F., Delfosse, X., Moutou, C., Arnold, L., Boisse, I., Bonfils, X., Díaz, R. F., Eggenberger, A., Forveille, T., Lagrange, A.-M., Lovis, C., Pepe, F., Perrier, C., Queloz, D., Santerne, A., Santos, N. C., Ségransan, D., Udry, S., & Vidal-Madjar, A. 2011, A&A, 527, L11

Hellier, C., Anderson, D. R., Cameron, A. C., Delrez, L., Gillon, M., Jehin, E., Lendl, M., Maxted, P. F. L., Pepe, F., Pollacco, D., Queloz, D., Ségransan, D., Smalley, B., Smith, A. M. S., Southworth, J., Triaud, A. H. M. J., Udry, S., & West, R. G. 2014, MNRAS, 440, 1982

Hellier, C., Anderson, D. R., Collier Cameron, A., Doyle, A. P., Fumel, A., Gillon, M., Jehin, E., Lendl, M., Maxted, P. F. L., Pepe, F., Pollacco, D., Queloz, D., Ségransan, D., Smalley, B., Smith, A. M. S., Southworth, J., Triaud, A. H. M. J., Udry, S., & West, R. G. 2012, MNRAS, 426, 739

Hellier, C., Anderson, D. R., Collier Cameron, A., Gillon, M., Hebb, L., Maxted, P. F. L., Queloz, D., Smalley, B., Triaud, A. H. M. J., West, R. G., Wilson, D. M., Bentley, S. J., Enoch, B., Horne, K., Irwin, J., Lister, T. A., Mayor, M., Parley, N., Pepe, F., Pollacco, D. L., Segransan, D., Udry, S., & Wheatley, P. J. 2009, Nature, 460, 1098

Henry, G. W., Marcy, G. W., Butler, R. P., & Vogt, S. S. 2000, ApJ, 529, L41

Hessman, F. V., Dhillon, V. S., Winget, D. E., Schreiber, M. R., Horne, K., Marsh, T. R., Guenther, E., Schwope, A., & Heber, U. 2010, ArXiv e-prints

Høg, E., Fabricius, C., Makarov, V. V., Urban, S., Corbin, T., Wycoff, G., Bastian, U., Schwekendiek, P., & Wicenec, A. 2000, A&A, 355, L27

Holman, M. J., Fabrycky, D. C., Ragozzine, D., Ford, E. B., Steffen, J. H., Welsh, W. F., Lissauer, J. J., Latham, D. W., Marcy, G. W., Walkowicz, L. M., Batalha, N. M., Jenkins, J. M., Rowe, J. F., Cochran, W. D., Fressin, F., Torres, G., Buchhave, L. A., Sasselov, D. D., Borucki, W. J., Koch, D. G., Basri, G., Brown, T. M., Caldwell, D. A., Charbonneau, D., Dunham, E. W., Gautier, T. N., Geary, J. C., Gilliland, R. L., Haas, M. R., Howell, S. B., Ciardi, D. R., Endl, M., Fischer, D., Fürész, G., Hartman, J. D., Isaacson, H., Johnson, J. A., MacQueen, P. J., Moorhead, A. V., Morehead, R. C., & Orosz, J. A. 2010, Science, 330, 51

Horne, J. H. & Baliunas, S. L. 1986, ApJ, 302, 757

Horner, J., Hinse, T. C., Wittenmyer, R. A., Marshall, J. P., & Tinney, C. G. 2012, MNRAS, 427, 2812

Howard, A. W., Bakos, G. Á., Hartman, J., Torres, G., Shporer, A., Mazeh, T., Kovács, G., Latham, D. W., Noyes, R. W., Fischer, D. A., Johnson, J. A., Marcy, G. W., Esquerdo, G. A., Béky, B., Butler, R. P., Sasselov, D. D., Stefanik, R. P., Perumpilly, G., Lázár, J., Papp, I., & Sári, P. 2012a, ApJ, 749, 134

Howard, A. W., Marcy, G. W., Bryson, S. T., Jenkins, J. M., Rowe, J. F., Batalha, N. M., Borucki, W. J., Koch, D. G., Dunham, E. W., Gautier, III, T. N., Van Cleve, J., Cochran, W. D., Latham, D. W., Lissauer, J. J., Torres, G., Brown, T. M., Gilliland, R. L., Buchhave, L. A., Caldwell, D. A., Christensen-Dalsgaard, J., Ciardi, D., Fressin, F., Haas,

M. R., Howell, S. B., Kjeldsen, H., Seager, S., Rogers, L., Sasselov, D. D., Steffen, J. H., Basri, G. S., Charbonneau, D., Christiansen, J., Clarke, B., Dupree, A., Fabrycky, D. C., Fischer, D. A., Ford, E. B., Fortney, J. J., Tarter, J., Girouard, F. R., Holman, M. J., Johnson, J. A., Klaus, T. C., Machalek, P., Moorhead, A. V., Morehead, R. C., Ragozzine, D., Tenenbaum, P., Twicken, J. D., Quinn, S. N., Isaacson, H., Shporer, A., Lucas, P. W., Walkowicz, L. M., Welsh, W. F., Boss, A., Devore, E., Gould, A., Smith, J. C., Morris, R. L., Prsa, A., Morton, T. D., Still, M., Thompson, S. E., Mullally, F., Endl, M., & MacQueen, P. J. 2012b, ApJS, 201, 15

Howell, S. B., Sobeck, C., Haas, M., Still, M., Barclay, T., Mullally, F., Troeltzsch, J., Aigrain, S., Bryson, S. T., Caldwell, D., Chaplin, W. J., Cochran, W. D., Huber, D., Marcy, G. W., Miglio, A., Najita, J. R., Smith, M., Twicken, J. D., & Fortney, J. J. 2014, PASP, 126, 398

Howell, S. B., VanOutryve, C., Tonry, J. L., Everett, M. E., & Schneider, R. 2005, PASP, 117, 1187

Irwin, J., Charbonneau, D., Nutzman, P., & Falco, E. 2009, in American Institute of Physics Conference Series, Vol. 1094, 15th Cambridge Workshop on Cool Stars, Stellar Systems, and the Sun, ed. E. Stempels, 445–448

Irwin, J. M., Berta-Thompson, Z. K., Charbonneau, D., Dittmann, J., Falco, E. E., Newton, E. R., & Nutzman, P. 2014, ArXiv e-prints

Israelian, G., Delgado Mena, E., Santos, N. C., Sousa, S. G., Mayor, M., Udry, S., Domínguez Cerdeña, C., Rebolo, R., & Randich, S. 2009, Nature, 462, 189

Jackson, B., Greenberg, R., & Barnes, R. 2008, ApJ, 681, 1631

Johns-Krull, C. M., McCullough, P. R., Burke, C. J., Valenti, J. A., Janes, K. A., Heasley, J. N., Prato, L., Bissinger, R., Fleenor, M., Foote, C. N., Garcia-Melendo, E., Gary, B. L., Howell, P. J., Mallia, F., Masi, G., & Vanmunster, T. 2008, ApJ, 677, 657

Johnson, J. A., Aller, K. M., Howard, A. W., & Crepp, J. R. 2010, PASP, 122, 905

Kalas, P., Graham, J. R., Chiang, E., Fitzgerald, M. P., Clampin, M., Kite, E. S., Stapelfeldt, K., Marois, C., & Krist, J. 2008, Science, 322, 1345

Kane, S. R., Mahadevan, S., von Braun, K., Laughlin, G., & Ciardi, D. R. 2009, PASP, 121, 1386

Kawaler, S. D. 1989, ApJ, 343, L65

Kazarovets, E. V., Samus, N. N., & Durlevich, O. V. 1998, Information Bulletin on Variable Stars, 4655, 1

Kim, D.-W., Protopapas, P., Alcock, C., Byun, Y.-I., & Bianco, F. B. 2009, MNRAS, 397, 558

Konacki, M. 2014, Contributions of the Astronomical Observatory Skalnate Pleso, 43, 374

Konacki, M., Torres, G., Jha, S., & Sasselov, D. D. 2003, Nature, 421, 507

Kopparapu, R. K. 2013, ApJ, 767, L8

Kovács, G., Bakos, G., & Noyes, R. W. 2005, MNRAS, 356, 557

Kovács, G., Bakos, G. Á., Hartman, J. D., Torres, G., Noyes, R. W., Latham, D. W., Howard, A. W., Fischer, D. A., Johnson, J. A., Marcy, G. W., Isaacson, H., Sasselov, D. D., Stefanik, R. P., Esquerdo, G. A., Fernandez, J. M., Lázár, B. B. J., Papp, I., & Sári, P. 2010, ApJ, 724, 866

Kovács, G., Zucker, S., & Mazeh, T. 2002, A&A, 391, 369

Kozai, Y. 1962, AJ, 67, 591

Kukarkin, B. V., Kholopov, P. N., Artiukhina, N. M., Fedorovich, V. P., Frolov, M. S., Goranskij, V. P., Gorynya, N. A., Karitskaya, E. A., Kireeva, N. N., Kukarkina, N. P., Kurochkin, N. E., Medvedeva, G. I., Perova, N. B., Ponomareva, G. A., Samus', N. N., & Shugarov, S. Y. 1995, VizieR Online Data Catalog, 2140, 0

Lang, D., Hogg, D. W., Mierle, K., Blanton, M., & Roweis, S. 2010, AJ, 139, 1782

Latham, D. W. 2012, NewAR, 56, 16

Latham, D. W., Rowe, J. F., Quinn, S. N., Batalha, N. M., Borucki, W. J., Brown, T. M., Bryson, S. T., Buchhave, L. A., Caldwell, D. A., Carter, J. A., Christiansen, J. L., Ciardi, D. R., Cochran, W. D., Dunham, E. W., Fabrycky, D. C., Ford, E. B., Gautier, III, T. N., Gilliland, R. L., Holman, M. J., Howell, S. B., Ibrahim, K. A., Isaacson, H., Jenkins, J. M., Koch, D. G., Lissauer, J. J., Marcy, G. W., Quintana, E. V., Ragozzine, D., Sasselov, D., Shporer, A., Steffen, J. H., Welsh, W. F., & Wohler, B. 2011, ApJ, 732, L24

Latham, D. W., Stefanik, R. P., Mazeh, T., Mayor, M., & Burki, G. 1989, Nature, 339, 38

Lee, J. W., Kim, S.-L., Kim, C.-H., Koch, R. H., Lee, C.-U., Kim, H.-I., & Park, J.-H. 2009, AJ, 137, 3181

Léger, A., Rouan, D., Schneider, J., Barge, P., Fridlund, M., Samuel, B., Ollivier, M., Guenther, E., Deleuil, M., Deeg, H. J., Auvergne, M., Alonso, R., Aigrain, S., Alapini, A., Almenara, J. M., Baglin, A., Barbieri, M., Bruntt, H., Bordé, P., Bouchy, F., Cabrera, J., Catala, C., Carone, L., Carpano, S., Csizmadia, S., Dvorak, R., Erikson, A., Ferraz-Mello, S., Foing, B., Fressin, F., Gandolfi, D., Gillon, M., Gondoin, P., Grasset, O., Guillot, T., Hatzes, A., Hébrard, G., Jorda, L., Lammer, H., Llebaria, A., Loeillet, B., Mayor, M., Mazeh, T., Moutou, C., Pätzold, M., Pont, F., Queloz, D., Rauer, H., Renner, S., Samadi, R., Shporer, A., Sotin, C., Tingley, B., Wuchterl, G., Adda, M., Agogu, P., Appourchaux, T., Ballans, H., Baron, P., Beaufort, T., Bellenger, R., Berlin, R., Bernardi, P., Blouin, D., Baudin, F., Bodin, P., Boisnard, L., Boit, L., Bonneau, F., Borzeix, S., Briet, R., Buey, J.-T., Butler, B., Cailleau, D., Cautain, R., Chabaud, P.-Y., Chaintreuil, S., Chiavassa, F., Costes, V., Cuna Parrho, V., de Oliveira Fialho, F., Decaudin, M., Defise, J.-M., Djalal, S., Epstein, G., Exil, G.-E., Fauré, C., Fenouillet, T., Gaboriaud, A., Gallic, A., Gamet, P., Gavalda, P., Grolleau, E., Gruneisen, R., Gueguen, L., Guis, V., Guivarc'h, V., Guterman, P., Hallouard, D., Hasiba, J., Heuripeau, F., Huntzinger, G., Hustaix, H., Imad, C., Imbert, C., Johlander, B., Jouret, M., Journoud, P., Karioty, F., Kerjean, L., Lafaille, V., Lafond, L., Lam-Trong, T., Landiech, P., Lapeyrere, V., Larqué, T., Laudet, P., Lautier, N., Lecann, H., Lefevre, L., Leruyet, B., Levacher, P., Magnan, A., Mazy, E., Mertens, F., Mesnager, J.-M., Meunier, J.-C., Michel, J.-P., Monjoin, W., Naudet, D., Nguyen-Kim, K., Orcesi, J.-L., Ottacher, H., Perez, R., Peter, G., Plasson, P., Plesseria, J.-Y., Pontet, B., Pradines, A., Quentin, C., Reynaud, J.-L., Rolland, G., Rollenhagen, F., Romagnan, R., Russ, N., Schmidt, R., Schwartz, N., Sebbag, I., Sedes, G., Smit, H., Steller, M. B., Sunter, W., Surace, C., Tello, M., Tiphène, D., Toulouse, P., Ulmer, B., Vandermarcq, O., Vergnault, E., Vuillemin, A., & Zanatta, P. 2009, A&A, 506, 287

Lendl, M., Triaud, A. H. M. J., Anderson, D. R., Collier Cameron, A., Delrez, L., Doyle, A., Gillon, M., Hellier, C., Jehin, E., Maxted, P. F. L., Neveu-VanMalle, M., Pepe, F., Pollacco, D., Queloz, D., Segransan, D., Smalley, B., Smith, A. M. S., Udry, S., Van Grootel, V., & West, R. G. 2014, ArXiv e-prints

Lide, D. R. 1994, CRC Handbook of chemistry and physics. A ready-reference book of chemical and physical data

Lissauer, J. J., Fabrycky, D. C., Ford, E. B., Borucki, W. J., Fressin, F., Marcy, G. W., Orosz, J. A., Rowe, J. F., Torres, G., Welsh, W. F., Batalha, N. M., Bryson, S. T., Buchhave, L. A., Caldwell, D. A., Carter, J. A., Charbonneau, D., Christiansen, J. L., Cochran, W. D., Desert, J.-M., Dunham, E. W., Fanelli, M. N., Fortney, J. J., Gautier, III, T. N., Geary, J. C., Gilliland, R. L., Haas, M. R., Hall, J. R., Holman, M. J., Koch, D. G., Latham, D. W., Lopez, E., McCauliff, S., Miller, N., Morehead, R. C., Quintana, E. V., Ragozzine, D., Sasselov, D., Short, D. R., & Steffen, J. H. 2011, Nature, 470, 53

Lissauer, J. J., Marcy, G. W., Bryson, S. T., Rowe, J. F., Jontof-Hutter, D., Agol, E., Borucki, W. J., Carter, J. A., Ford, E. B., Gilliland, R. L., Kolbl, R., Star, K. M., Steffen, J. H., & Torres, G. 2014, ApJ, 784, 44

Liu, M. C., Delorme, P., Dupuy, T. J., Bowler, B. P., Albert, L., Artigau, E., Reylé, C., Forveille, T., & Delfosse, X. 2011, ApJ, 740, 108

Lomb, N. R. 1976, Ap&SS, 39, 447

Macintosh, B. A., Graham, J. R., Palmer, D. W., Doyon, R., Dunn, J., Gavel, D. T., Larkin, J., Oppenheimer, B., Saddlemyer, L., Sivaramakrishnan, A., Wallace, J. K., Bauman, B., Erickson, D. A., Marois, C., Poyneer, L. A., & Soummer, R. 2008, in Society of

Photo-Optical Instrumentation Engineers (SPIE) Conference Series, Vol. 7015, Society of Photo-Optical Instrumentation Engineers (SPIE) Conference Series

Mandel, K. & Agol, E. 2002, ApJ, 580, L171

Marcy, G., Butler, R. P., Fischer, D., Vogt, S., Wright, J. T., Tinney, C. G., & Jones, H. R. A. 2005, Progress of Theoretical Physics Supplement, 158, 24

Marcy, G. W. & Butler, R. P. 1995, in Bulletin of the American Astronomical Society, Vol. 27, Bulletin of the American Astronomical Society, 1379–+

Marois, C., Macintosh, B., Barman, T., Zuckerman, B., Song, I., Patience, J., Lafrenière, D., & Doyon, R. 2008, Science, 322, 1348

Matsumura, S., Peale, S. J., & Rasio, F. A. 2010, ApJ, 725, 1995

Maxted, P. F. L., Anderson, D. R., Collier Cameron, A., Hellier, C., Queloz, D., Smalley, B., Street, R. A., Triaud, A. H. M. J., West, R. G., Gillon, M., Lister, T. A., Pepe, F., Pollacco, D., Ségransan, D., Smith, A. M. S., & Udry, S. 2011, PASP, 123, 547

Mayor, M., Marmier, M., Lovis, C., Udry, S., Ségransan, D., Pepe, F., Benz, W., Bertaux, J. ., Bouchy, F., Dumusque, X., Lo Curto, G., Mordasini, C., Queloz, D., & Santos, N. C. 2011, ArXiv e-prints

Mayor, M., Pepe, F., Queloz, D., Bouchy, F., Rupprecht, G., Lo Curto, G., Avila, G., Benz, W., Bertaux, J.-L., Bonfils, X., dall, T., Dekker, H., Delabre, B., Eckert, W., Fleury, M., Gilliotte, A., Gojak, D., Guzman, J. C., Kohler, D., Lizon, J.-L., Longinotti, A., Lovis, C., Megevand, D., Pasquini, L., Reyes, J., Sivan, J.-P., Sosnowska, D., Soto, R., Udry, S., van Kesteren, A., Weber, L., & Weilenmann, U. 2003, The Messenger, 114, 20

Mayor, M. & Queloz, D. 1995, Nature, 378, 355

McBride, J., Graham, J. R., Macintosh, B., Beckwith, S. V. W., Marois, C., Poyneer, L. A., & Wiktorowicz, S. J. 2011, PASP, 123, 692

McCormac, J., Skillen, I., Pollacco, D., Faedi, F., Ramsay, G., Dhillon, V. S., Todd, I., & Gonzalez, A. 2014, MNRAS, 438, 3383

McCullough, P. R., Stys, J. E., Valenti, J. A., Fleming, S. W., Janes, K. A., & Heasley, J. N. 2005, PASP, 117, 783

Mink, D. J. 1999, in Astronomical Society of the Pacific Conference Series, Vol. 172, Astronomical Data Analysis Software and Systems VIII, ed. D. M. Mehringer, R. L. Plante, & D. A. Roberts, 498

Montalto, M., Piotto, G., Desidera, S., de Marchi, F., Bruntt, H., Stetson, P. B., Arellano Ferro, A., Momany, Y., Gratton, R. G., Poretti, E., Aparicio, A., Barbieri, M., Claudi, R. U., Grundahl, F., & Rosenberg, A. 2007, A&A, 470, 1137

Morton, T. D. 2012, ApJ, 761, 6

Muirhead, P. S., Johnson, J. A., Apps, K., Carter, J. A., Morton, T. D., Fabrycky, D. C., Pineda, J. S., Bottom, M., Rojas-Ayala, B., Schlawin, E., Hamren, K., Covey, K. R., Crepp, J. R., Stassun, K. G., Pepper, J., Hebb, L., Kirby, E. N., Howard, A. W., Isaacson, H. T., Marcy, G. W., Levitan, D., Diaz-Santos, T., Armus, L., & Lloyd, J. P. 2012, ApJ, 747, 144

Murakami, N., Guyon, O., Martinache, F., Matsuo, T., Yokochi, K., Nishikawa, J., Tamura, M., Kurokawa, T., Baba, N., Vogt, F., Garrel, V., & Yoshikawa, T. 2010, in Society of Photo-Optical Instrumentation Engineers (SPIE) Conference Series, Vol. 7735, Society of Photo-Optical Instrumentation Engineers (SPIE) Conference Series

Naoz, S., Farr, W. M., Lithwick, Y., Rasio, F. A., & Teyssandier, J. 2011, Nature, 473, 187

Narita, N., Sato, B., Hirano, T., & Tamura, M. 2009, PASJ, 61, L35

Neves, V., Santos, N. C., Sousa, S. G., Correia, A. C. M., & Israelian, G. 2009, A&A, 497, 563

Newberry, M. 1998, Pixel Response Effects on CCD Camera Gain Calibration, Tech. rep., Mirametrics, Inc.

Newberry, M. V. 1991, PASP, 103, 122

Nutzman, P. & Charbonneau, D. 2008, PASP, 120, 317

O'Donovan, F. T., Charbonneau, D., Bakos, G. Á., Mandushev, G., Dunham, E. W., Brown, T. M., Latham, D. W., Torres, G., Sozzetti, A., Kovács, G., Everett, M. E., Baliber, N., Hidas, M. G., Esquerdo, G. A., Rabus, M., Deeg, H. J., Belmonte, J. A., Hillenbrand, L. A., & Stefanik, R. P. 2007, ApJ, 663, L37

O'Donovan, F. T., Charbonneau, D., & Kotredes, L. 2004, in American Institute of Physics Conference Series, Vol. 713, The Search for Other Worlds, ed. S. S. Holt & D. Deming, 169–172

Oetiker, B., Kowalczyk, M., Nietfeld, B., Mandushev, G. I., & Dunham, E. W. 2010, PASP, 122, 41

Olech, A., Woźniak, P. R., Alard, C., Kaluzny, J., & Thompson, I. B. 1999, MNRAS, 310, 759

Orosz, J. A., Welsh, W. F., Carter, J. A., Fabrycky, D. C., Cochran, W. D., Endl, M., Ford, E. B., Haghighipour, N., MacQueen, P. J., Mazeh, T., Sanchis-Ojeda, R., Short, D. R., Torres, G., Agol, E., Buchhave, L. A., Doyle, L. R., Isaacson, H., Lissauer, J. J., Marcy, G. W., Shporer, A., Windmiller, G., Barclay, T., Boss, A. P., Clarke, B. D., Fortney, J., Geary, J. C., Holman, M. J., Huber, D., Jenkins, J. M., Kinemuchi, K., Kruse, E., Ragozzine, D., Sasselov, D., Still, M., Tenenbaum, P., Uddin, K., Winn, J. N., Koch, D. G., & Borucki, W. J. 2012, Science, 337, 1511

Paczyński, B., Szczygieł, D. M., Pilecki, B., & Pojmański, G. 2006, MNRAS, 368, 1311

Paegert, M., Stassun, K. G., & Burger, D. M. 2014, AJ, 148, 31

Palmer, D. M. 2009, ApJ, 695, 496

Pence, W. D., Chiappetti, L., Page, C. G., Shaw, R. A., & Stobie, E. 2010a, A&A, 524, A42

Pence, W. D., Seaman, R., & White, R. L. 2009, PASP, 121, 414

Pence, W. D., White, R. L., & Seaman, R. 2010b, PASP, 122, 1065

Pepper, J., Gould, A., & Depoy, D. L. 2003, Acta. Astron., 53, 213

Pepper, J., Kuhn, R. B., Siverd, R., James, D., & Stassun, K. 2012, PASP, 124, 230

Pepper, J., Pogge, R. W., DePoy, D. L., Marshall, J. L., Stanek, K. Z., Stutz, A. M., Poindexter, S., Siverd, R., O'Brien, T. P., Trueblood, M., & Trueblood, P. 2007, PASP, 119, 923

Pepper, J., Siverd, R. J., Beatty, T. G., Gaudi, B. S., Stassun, K. G., Eastman, J., Collins, K., Latham, D. W., Bieryla, A., Buchhave, L. A., Jensen, E. L. N., Manner, M., Penev, K., Crepp, J. R., Cargile, P. A., Dhital, S., Calkins, M. L., Esquerdo, G. A., Berlind, P., Fulton, B. J., Street, R., Ma, B., Ge, J., Wang, J., Mao, Q., Richert, A. J. W., Gould, A., DePoy, D. L., Kielkopf, J. F., Marshall, J. L., Pogge, R. W., Stefanik, R. P., Trueblood, M., & Trueblood, P. 2013, ApJ, 773, 64

Perna, R., Menou, K., & Rauscher, E. 2010, ApJ, 724, 313

Perryman, M. A. C. 2000, Reports on Progress in Physics, 63, 1209

Pietrukowicz, P., Mróz, P., Soszyński, I., Udalski, A., Poleski, R., Szymański, M. K., Kubiak, M., Pietrzyński, G., Wyrzykowski, A., Ulaczyk, K., Kozłowski, S., & Skowron, J. 2013, Acta. Astron., 63, 115

Pojmanski, G. 2000, Acta. Astron., 50, 177

Poleski, R., McCullough, P. R., Valenti, J. A., Burke, C. J., Machalek, P., & Janes, K. 2010, ApJS, 189, 134

Pollacco, D. L., Skillen, I., Collier Cameron, A., Christian, D. J., Hellier, C., Irwin, J., Lister, T. A., Street, R. A., West, R. G., Anderson, D., Clarkson, W. I., Deeg, H., Enoch, B., Evans, A., Fitzsimmons, A., Haswell, C. A., Hodgkin, S., Horne, K., Kane, S. R., Keenan, F. P., Maxted, P. F. L., Norton, A. J., Osborne, J., Parley, N. R., Ryans, R. S. I., Smalley, B., Wheatley, P. J., & Wilson, D. M. 2006, PASP, 118, 1407

Pollack, J. B., Hubickyj, O., Bodenheimer, P., Lissauer, J. J., Podolak, M., & Greenzweig, Y. 1996, Icarus, 124, 62

Pont, F., Zucker, S., & Queloz, D. 2006, MNRAS, 373, 231

Press, W. H. & Rybicki, G. B. 1989, ApJ, 338, 277

Press, W. H., Teukolsky, S. A., Vetterling, W. T., & Flannery, B. P. 1992, Numerical recipes in C. The art of scientific computing, 2nd ed. (Cambridge University Press)

Qian, S.-B., Liao, W.-P., Zhu, L.-Y., & Dai, Z.-B. 2010, ApJ, 708, L66

Queloz, D., Bouchy, F., Moutou, C., Hatzes, A., Hébrard, G., Alonso, R., Auvergne, M., Baglin, A., Barbieri, M., Barge, P., Benz, W., Bordé, P., Deeg, H. J., Deleuil, M., Dvorak, R., Erikson, A., Ferraz Mello, S., Fridlund, M., Gandolfi, D., Gillon, M., Guenther, E., Guillot, T., Jorda, L., Hartmann, M., Lammer, H., Léger, A., Llebaria, A., Lovis, C., Magain, P., Mayor, M., Mazeh, T., Ollivier, M., Pätzold, M., Pepe, F., Rauer, H., Rouan, D., Schneider, J., Segransan, D., Udry, S., & Wuchterl, G. 2009, A&A, 506, 303

Queloz, D., Eggenberger, A., Mayor, M., Perrier, C., Beuzit, J. L., Naef, D., Sivan, J. P., & Udry, S. 2000a, A&A, 359, L13

Queloz, D., Mayor, M., Weber, L., Blécha, A., Burnet, M., Confino, B., Naef, D., Pepe, F., Santos, N., & Udry, S. 2000b, A&A, 354, 99

Rabus, M., Brown, T. M., Deeg, H. J., Belmonte Avilés, J. A., Almenara Villa, J. M., & Alonso, R. 2007, in Astronomical Society of the Pacific Conference Series, Vol. 366, Transiting Extrapolar Planets Workshop, ed. C. Afonso, D. Weldrake, & T. Henning, 96

Ragozzine, D. & Wolf, A. S. 2009, ApJ, 698, 1778

Ramírez, I., Asplund, M., Baumann, P., Meléndez, J., & Bensby, T. 2010, A&A, 521, A33

Rasio, F. A. & Ford, E. B. 1996, Science, 274, 954

Rauer, H. & Catala, C. 2011, in IAU Symposium, Vol. 276, IAU Symposium, ed. A. Sozzetti, M. G. Lattanzi, & A. P. Boss, 354–358

Redfield, S., Endl, M., Cochran, W. D., & Koesterke, L. 2008, ApJ, 673, L87

Ricker, G. R. 2014, Journal of the American Association of Variable Star Observers (JAAVSO), 42, 234

Ricker, G. R., Latham, D. W., Vanderspek, R. K., Ennico, K. A., Bakos, G., Brown, T. M., Burgasser, A. J., Charbonneau, D., Clampin, M., Deming, L. D., Doty, J. P., Dunham, E. W., Elliot, J. L., Holman, M. J., Ida, S., Jenkins, J. M., Jernigan, J. G., Kawai, N., Laughlin, G. P., Lissauer, J. J., Martel, F., Sasselov, D. D., Schingler, R. H., Seager, S., Torres, G., Udry, S., Villasenor, J. N., Winn, J. N., & Worden, S. P. 2010, in Bulletin of the American Astronomical Society, Vol. 42, American Astronomical Society Meeting Abstracts 215, 450.06

Rodriguez, J. E., Pepper, J., Stassun, K. G., Siverd, R. J., Cargile, P., Beatty, T. G., & Gaudi, B. S. 2013, AJ, 146, 112

Rowe, J. F., Bryson, S. T., Marcy, G. W., Lissauer, J. J., Jontof-Hutter, D., Mullally, F., Gilliland, R. L., Issacson, H., Ford, E., Howell, S. B., Borucki, W. J., Haas, M., Huber, D., Steffen, J. H., Thompson, S. E., Quintana, E., Barclay, T., Still, M., Fortney, J., Gautier, III, T. N., Hunter, R., Caldwell, D. A., Ciardi, D. R., Devore, E., Cochran, W., Jenkins, J., Agol, E., Carter, J. A., & Geary, J. 2014, ApJ, 784, 45

Rucinski, S. M. 1998, AJ, 115, 1135

Rucinski, S. M. & Maceroni, C. 2001, AJ, 121, 254

Sackett, P. D. 1999, in NATO ASIC Proc. 532: Planets Outside the Solar System: Theory and Observations, ed. J.-M. Mariotti & D. Alloin, 189–+

Samus, N. N., Durlevich, O. V., & et al. 2009, VizieR Online Data Catalog, 1, 2025

Santerne, A., Díaz, R. F., Almenara, J.-M., Lethuillier, A., Deleuil, M., & Moutou, C. 2013, in SF2A-2013: Proceedings of the Annual meeting of the French Society of Astronomy and Astrophysics, ed. L. Cambresy, F. Martins, E. Nuss, & A. Palacios, 555–560

Santerne, A., Díaz, R. F., Moutou, C., Bouchy, F., Hébrard, G., Almenara, J.-M., Bonomo, A. S., Deleuil, M., & Santos, N. C. 2012, A&A, 545, A76

Santos, N. C., Israelian, G., & Mayor, M. 2001, A&A, 373, 1019

—. 2004, A&A, 415, 1153

Santos, N. C., Israelian, G., Mayor, M., Rebolo, R., & Udry, S. 2003, A&A, 398, 363

Scargle, J. D. 1982, ApJ, 263, 835

Schwarzenberg-Czerny, A. 1989, MNRAS, 241, 153

Seager, S. & Mallén-Ornelas, G. 2003, ApJ, 585, 1038

Showman, A. P. & Guillot, T. 2002, A&A, 385, 166

Sirko, E. & Paczyński, B. 2003, ApJ, 592, 1217

Siverd, R. J., Beatty, T. G., Pepper, J., Eastman, J. D., Collins, K., Bieryla, A., Latham, D. W., Buchhave, L. A., Jensen, E. L. N., Crepp, J. R., Street, R., Stassun, K. G., Gaudi, B. S., Berlind, P., Calkins, M. L., DePoy, D. L., Esquerdo, G. A., Fulton, B. J., Fűrész, G., Geary, J. C., Gould, A., Hebb, L., Kielkopf, J. F., Marshall, J. L., Pogge, R., Stanek, K. Z., Stefanik, R. P., Szentgyorgyi, A. H., Trueblood, M., Trueblood, P., Stutz, A. M., & van Saders, J. L. 2012, ApJ, 761, 123

Skrutskie, M. F., Cutri, R. M., Stiening, R., Weinberg, M. D., Schneider, S., Carpenter, J. M., Beichman, C., Capps, R., Chester, T., Elias, J., Huchra, J., Liebert, J., Lonsdale, C., Monet, D. G., Price, S., Seitzer, P., Jarrett, T., Kirkpatrick, J. D., Gizis, J. E., Howard, E., Evans, T., Fowler, J., Fullmer, L., Hurt, R., Light, R., Kopan, E. L., Marsh, K. A., McCallon, H. L., Tam, R., Van Dyk, S., & Wheelock, S. 2006, AJ, 131, 1163

Skumanich, A. 1972, ApJ, 171, 565

Smalley, B., Anderson, D. R., Collier-Cameron, A., Doyle, A. P., Fumel, A., Gillon, M., Hellier, C., Jehin, E., Lendl, M., Maxted, P. F. L., Pepe, F., Pollacco, D., Queloz, D., Ségransan, D., Smith, A. M. S., Southworth, J., Triaud, A. H. M. J., Udry, S., & West, R. G. 2012, A&A, 547, A61

Smith, A. M. S., Collier Cameron, A., Christian, D. J., Clarkson, W. I., Enoch, B., Evans, A., Haswell, C. A., Hellier, C., Horne, K., Irwin, J., Kane, S. R., Lister, T. A., Norton, A. J., Parley, N., Pollacco, D. L., Ryans, R., Skillen, I., Street, R. A., Triaud, A. H. M. J., West, R. G., Wheatley, P. J., & Wilson, D. M. 2006, MNRAS, 373, 1151

Socrates, A. 2013, ArXiv e-prints

Soszyński, I., Poleski, R., Udalski, A., Szymanski, M. K., Kubiak, M., Pietrzynski, G., Wyrzykowski, L., Szewczyk, O., & Ulaczyk, K. 2008, Acta. Astron., 58, 163

Soszyński, I., Udalski, A., Pietrukowicz, P., Szymański, M. K., Kubiak, M., Pietrzyński, G., Wyrzykowski, Ł., Ulaczyk, K., Poleski, R., & Kozłowski, S. 2011, Acta. Astron., 61, 285

Sousa, S. G., Fernandes, J., Israelian, G., & Santos, N. C. 2010, A&A, 512, L5

Sousa, S. G., Santos, N. C., Israelian, G., Mayor, M., & Udry, S. 2011, A&A, 533, A141

Sousa, S. G., Santos, N. C., Mayor, M., Udry, S., Casagrande, L., Israelian, G., Pepe, F., Queloz, D., & Monteiro, M. J. P. F. G. 2008, A&A, 487, 373

Southworth, J. 2008, MNRAS, 386, 1644

Sozzetti, A. 2004, MNRAS, 354, 1194

Spiegel, D. S. & Burrows, A. 2013, ApJ, 772, 76

Spiegel, D. S., Burrows, A., & Milsom, J. A. 2011, ApJ, 727, 57

Stauffer, J. R., Hartmann, L. W., Prosser, C. F., Randich, S., Balachandran, S., Patten, B. M., Simon, T., & Giampapa, M. 1997, ApJ, 479, 776

Steffen, J. H., Ragozzine, D., Fabrycky, D. C., Carter, J. A., Ford, E. B., Holman, M. J., Rowe, J. F., Welsh, W. F., Borucki, W. J., Boss, A. P., Ciardi, D. R., & Quinn, S. N. 2012, Proceedings of the National Academy of Science, 109, 7982

Stetson, P. B. 1987, PASP, 99, 191

—. 1990, PASP, 102, 932

—. 1996, PASP, 108, 851

Stetson, P. B., Davis, L. E., & Crabtree, D. R. 1990, in Astronomical Society of the Pacific Conference Series, Vol. 8, CCDs in astronomy, ed. G. H. Jacoby, 289–304

Stevenson, K. B., Bean, J. L., Madhusudhan, N., & Harrington, J. 2014, ApJ, 791, 36

Taylor, M. B. 2005, in Astronomical Society of the Pacific Conference Series, Vol. 347, Astronomical Data Analysis Software and Systems XIV, ed. P. Shopbell, M. Britton, & R. Ebert, 29

Thorsett, S. E., Arzoumanian, Z., & Taylor, J. H. 1993, ApJ, 412, L33

Tingley, B. 2004, A&A, 425, 1125

Tomaney, A. B. & Crotts, A. P. S. 1996, AJ, 112, 2872

Torres, G. 2010, AJ, 140, 1158

Torres, G., Andersen, J., & Giménez, A. 2010, A&A Rev., 18, 67

Torres, G., Fressin, F., Batalha, N. M., Borucki, W. J., Brown, T. M., Bryson, S. T., Buchhave, L. A., Charbonneau, D., Ciardi, D. R., Dunham, E. W., Fabrycky, D. C., Ford, E. B., Gautier, III, T. N., Gilliland, R. L., Holman, M. J., Howell, S. B., Isaacson, H., Jenkins, J. M., Koch, D. G., Latham, D. W., Lissauer, J. J., Marcy, G. W., Monet, D. G., Prsa, A., Quinn, S. N., Ragozzine, D., Rowe, J. F., Sasselov, D. D., Steffen, J. H., & Welsh, W. F. 2011, ApJ, 727, 24

Triaud, A. H. M. J. 2011, A&A, 534, L6

Triaud, A. H. M. J., Collier Cameron, A., Queloz, D., Anderson, D. R., Gillon, M., Hebb, L., Hellier, C., Loeillet, B., Maxted, P. F. L., Mayor, M., Pepe, F., Pollacco, D., Ségransan, D., Smalley, B., Udry, S., West, R. G., & Wheatley, P. J. 2010, A&A, 524, A25

Udalski, A., Szymanski, M., Kaluzny, J., Kubiak, M., & Mateo, M. 1992, Acta. Astron., 42, 253

Udry, S. & Santos, N. C. 2007, ARA&A, 45, 397

Walker, G. A. H., Bohlender, D. A., Walker, A. R., Irwin, A. W., Yang, S. L. S., & Larson, A. 1992, ApJ, 396, L91

Watson, C., Henden, A. A., & Price, A. 2013, VizieR Online Data Catalog, 1, 2027

Wheatley, P. J., Pollacco, D. L., Queloz, D., Rauer, H., Watson, C. A., West, R. G., Chazelas, B., Louden, T. M., Walker, S., Bannister, N., Bento, J., Burleigh, M., Cabrera, J., Eigmüller, P., Erikson, A., Genolet, L., Goad, M., Grange, A., Jordán, A., Lawrie, K., McCormac, J., & Neveu, M. 2013, in European Physical Journal Web of Conferences, Vol. 47, European Physical Journal Web of Conferences, 13002

Wilson, D. M., Gillon, M., Hellier, C., Maxted, P. F. L., Pepe, F., Queloz, D., Anderson, D. R., Collier Cameron, A., Smalley, B., Lister, T. A., Bentley, S. J., Blecha, A., Christian, D. J., Enoch, B., Haswell, C. A., Hebb, L., Horne, K., Irwin, J., Joshi, Y. C., Kane, S. R., Marmier, M., Mayor, M., Parley, N., Pollacco, D., Pont, F., Ryans, R., Segransan, D., Skillen, I., Street, R. A., Udry, S., West, R. G., & Wheatley, P. J. 2008, ApJ, 675, L113

Winn, J. N. 2007, in Astronomical Society of the Pacific Conference Series, Vol. 366, Transiting Extrapolar Planets Workshop, ed. C. Afonso, D. Weldrake, & T. Henning, 170–+

Winn, J. N., Fabrycky, D., Albrecht, S., & Johnson, J. A. 2010, ApJ, 718, L145

Winn, J. N., Johnson, J. A., Albrecht, S., Howard, A. W., Marcy, G. W., Crossfield, I. J., & Holman, M. J. 2009, ApJ, 703, L99

Wolszczan, A. & Frail, D. A. 1992, Nature, 355, 145

Wozniak, P. R. 2000, Acta. Astron., 50, 421

Wright, J. T., Marcy, G. W., Howard, A. W., Johnson, J. A., Morton, T. D., & Fischer, D. A. 2012, ApJ, 753, 160

Xie, J.-W. 2013, ApJS, 208, 22

Yi, S., Demarque, P., Kim, Y.-C., Lee, Y.-W., Ree, C. H., Lejeune, T., & Barnes, S. 2001, ApJS, 136, 417

Young, A. T. 1967, AJ, 72, 747